Towards High-Performance Organic Semiconductor Devices: Microstructure, Interlayers, and Emerging Applications

Bingjun Wang

New College

University of Oxford

A thesis submitted for the degree of

Doctor of Philosophy

Trinity 2021

Abstract

The field of organic electronics mainly focuses on the lightweight, flexible, and low-cost organic semiconductors, with ultimate goals of competing with or even substituting for the conventional silicon industries, and expanding the established success in xerography and displays to more fields. As a response to the persistent pursuit of high-performance organic semiconductor devices, in this thesis we exemplify three case studies from different perspectives, namely microstructure control, interlayer engineering, and emerging applications. First, the conformation of a light-emitting copolymer, 90F8:10BT, is regulated so that the β-phase, in which the intermonomer torsion angle of a fraction of chain segments is 180°, is generated. Recognised from its characteristic absorption peak, this typical microstructure shows significant impacts on charge transport, injection, and trapping in 90F8:10BT-based light-emitting diodes, leading to pronounced enhancements in device luminance, efficiencies, and lifetime. Second, we investigate a solution-processable hole injection/transport material, copper(I) thiocyanate (CuSCN), highlighting the effect of different solvents on its properties and applications. With a set of characterisation on thin-film topography, roughness, polymorphism, composition, and chemical bonding, as well as two critical hole-injection/transport-related properties, i.e. the surface energy and the ionisation potential, we demonstrate how CuSCN interlayers processed from six different solvents can be used in various organic semiconductor devices for improved performance. Third, we explore the possibility of using organic semiconductors to facilitate the Internet of Things, and a golden opportunity comes from organic rectifiers that can play an essential role in radio-frequency identification tags. Guided by simulation results thanks to our improved device model, we fabricate and optimise three organic rectifiers using different semiconducting materials, among which the best exhibits the potential of operating at a frequency towards the ultrahigh-frequency regime. We hope that these strategies of seeking high-performance organic semiconductor devices can make some contribution to the community of organic electronics, enriching the knowledge database and opening opportunities for the upcoming research.

Acknowledgement

It is hard to believe that my four-year study and research experience in Oxford is approaching the end when I am typing up these words. First and foremost, I would like to thank my supervisor, Prof. Donal Bradley, for offering me the chance to join probably the most prestigious university in the world; for working until 2 am on a Sunday to help me apply for the scholarship, without which my Oxford dream can never become true; for showing me from our discussions how to perform research meticulously without neglecting any seemingly unremarkable experimental results; for always encouraging me to proceed my research project even if the preliminary results look unsatisfying; for editing my paper drafts word-by-word to make them scientifically more rigorous and linguistically more idiomatic, with great patience with miscellaneous grammar mistakes made by a non-native speaker; for inviting me to visit the King Abdullah University of Science and Technology to broaden my horizons; the list seems to be endless. It is Donal's valuable guidance and painstaking efforts on my DPhil research that sometimes make me feel anxious that this thesis might let him down. I will be more than happy if this is not the case.

Joining the AFMD group and supervised by Prof. Moritz Riede are something I did not expect. Though sudden for both of us, we quickly established a very efficient and pleasant working relationship. What touched me most is that Moritz, alongside all AFMDers, never saw me as an outsider to his group, which, to be honest, worried me a little bit at the very beginning. He always tries his best to help me, from being solicitous about my mental and physical health during the difficult COVID lockdown, to continuously finding places where I can do experiments I want; from giving me plenty of suggestions on paper and thesis writing, viva, and future career, to promptly replying my emails no matter how trivial they are. I can hardly imagine how it is possible to finish my DPhil smoothly without Moritz's

efforts. His well-structured working style and optimistic personal character impressed me a lot, and all of these make our seemingly accidental encounter—maybe destined, who knows?—particularly fond memories for me.

Apart from supervisors, a great many colleagues gave me numerous help. I am especially grateful to postdocs in my group, Drs. Sungho Nam, Rick Hamilton, Chen Sun, and Hao Ye, who guided me through experimental design and operation, set up equipment for my everyday use, brought me many new ideas about both research and future life, and supported me during the difficult times. They are always the first person I think of when a problem comes into my mind, and in no circumstances they say no to my requests. My acknowledgement also belongs to postdocs, technicians, and colleagues who trained me to use a number of facilities and helped me to resolve many weird technical issues—Drs. Sameer Vajjala Kesava, Bernard Wenger, Pabitra Nayak, Grey Christoforo, James Ball, Yen-Hung Lin, Ashley Marshall, Roger Johnson, Jason Brown, Thomas Derrien, Suhas Mahesh, Jonathan Warby, and Yiren Xia, as well as Sofia Bekou, Andreas Lauritzen, Bernd Sturdza, and John Sandford O'Neill. My confidence in using multiple characterisation tools correctly and independently largely comes from their efforts. Besides, frequent discussions about various topics with my colleagues really saved me from an otherwise too boring research life. Laughs, sighs, and aha-moments comprised my chats with Drs. Nikol Lambeva, Florian Le Roux, Alice Smith, Pascal Kaienburg, Alberto Privitera, Hanyang Ye, and Ross Warren, as well as Anna Jungbluth, Irfan Habib, Helen Bristow, Mike Farrar, Yun Xiao, and Nicky Evans. Whom I should further thank are professors that kindly offered me facility access, materials, and discussion opportunities. They are Profs. Henry Snaith, Robin Nicholas, Stephen Morris, Harish Bhaskaran, SeungNam Cha, Ji-Seon Kim, Thomas Anthopoulos, Martin Heeney, and Iain McCulloch.

In addition, there are so many people who made my life in Oxford more memorable. My kind and thoughtful landlady Dr. Cynthia Harper reserved a quiet, cosy, and well-equipped room for me, where I can totally relax and, during the special COVID times,

concentrate on my tasks when I had to work from home. My friends Yao Meng, Jia'ao Wei, and Youqian Zhang, to name but a few, gave me the chance to enjoy their nice cooking every now and then, which, together with those forthright after-meal conversations, relieved my stress and cleared my mind. Another indispensable piece of comfort and support came from the other side of the Atlantic. My significant other, Miss Ru Jia, is always empathetic with me as we are having more or less similar overseas DPhil lives. Though physically far from each other, our souls have never been separated. Last but not least, the wholehearted, unconditional trust and love from my parents are constant sources of my initiative and bravery. Admittedly, they can hardly understand either the language or the contents of this thesis, but they definitely deserve a huge thank you, no matter how trivial these words are compared with their devotion to me.

Finally, I want to thank the China Scholarship Council (CSC), Pacific Alliance Group (PAG), and China Oxford Scholarship Fund (COSF) for their generous financial support, and after that, leave a small portion of acknowledgement for myself as the reward for completing the DPhil. It may or may not be a significant milestone in my whole life, but what I always believe is—

> *Reading maketh a full man; conference a ready man; and writing an exact man... Histories make men wise; poets witty; the mathematics subtle; natural philosophy deep; moral grave; logic and rhetoric able to contend. Abeunt studia in mores [Studies pass on into character].*
>
> *Francis Bacon, Of Studies, 1625*

Contents

List of Figures and Tables

Chapter 1

Chapter 2

Chapter 3

Chapter 4

Chapter 5

Chapter 6

List of Abbreviations and Symbols

Abbreviations

AC	alternating current
AFM	atomic force microscopy
APS	air-photoemission spectroscopy
BCP	bathocuproine
BHJ	bulk heterojunction
BT	2,1,3-benzothiadiazole
BuSH	1-butanethiol
CCN	C_{60}:C_{70}:N2200
CELIV	charge extraction by linearly increasing voltage
DC	direct current
DES	diethyl sulphide
DFT	density functional theory
DIM	diiodomethane
DIT	dark injection transient
DI water	de-ionised water
DMF	*N*,*N*-dimethylformamide
DMSO	dimethyl sulphoxide
DoS	density of states
DPS	dipropyl sulphide
EA	electron affinity
EBL	electron blocking layer

EL	electroluminescence
EML	emission layer
EQE	external quantum efficiency
ETL	electron transport layer
F8	9,9-dioctylfluorene
F8BT	poly(9,9-dioctylfuorene-*alt*-2,1,3-benzothiadiazole)
FTIR	Fourier-transform infrared (spectroscopy)
GIWAXS	grazing-incidence wide-angle X-ray scattering
HBL	hole blocking layer
HF	high frequency
HOMO	highest occupied molecular orbital
HTL	hole transport layer
IP	ionisation potential
ITO	indium tin oxide
LUMO	lowest unoccupied molecular orbital
MIS-CELIV	metal–insulator–semiconductor structure-based CELIV
MO	molecular orbital
N2200	poly[[*N*,*N*′-bis(2-octyldodecyl)-naphthalene-1,4,5,8-bis(dicarboximide)-2,6-diyl]-*alt*-5,5′-(2,2′-bithiophene)]
NMP	1-methyl-2-pyrrolidone
o-DCB	1,2-dichlorobenzene
OFET	organic field-effect transistor
OHD	organic heterojunction diode
OLED	organic light-emitting diode
OPV	organic solar cell (or organic photovoltaics)
OSC	organic semiconductor
OSD	organic Schottky diode
P35CPT	poly[3-(5-carboxypentyl)thiophene-2,5-diyl]

P3HT	poly(3-hexylthiophene)
$PC_{71}BM$	[6,6]-phenyl C_{71} butyric acid methyl ester
PCDTBT	poly[*N*-9′-heptadecanyl-2,7-carbazole-*alt*-5,5-(4′,7′-di-2-thienyl-2′,1′,3′-benzothiadiazole)]
PCE	power conversion efficiency
PDPPTTT	poly[[2,5-bis(2-octyldodecyl)-2,3,5,6-tetrahydro-3,6-dioxopyrrolo[3,4-*c*]-pyrrole-1,4-diyl]-*alt*-[[2,2′-(2,5-thiophene)bis-thieno[3,2-*b*]thiophen]-5,5′-diyl]]
PEDOT:PSS	poly(3,4-ethylenedioxythiophene):poly(styrene sulfonate)
PFBT	2,3,4,5,6-pentafluorothiophenol
PFO	poly(9,9-dioctylfluorene)
PhSH	thiophenol
PL	photoluminescence
PLQE	photoluminescence quantum efficiency
PMMA	poly(methyl methacrylate)
PTB7	poly[[4,8-bis[(2-ethylhexyl)oxy]benzo[1,2-*b*:4,5-*b*′]dithiophene-2,6-diyl]-[3-fluoro-2-[(2-ethylhexyl)carbonyl]thieno[3,4-*b*]thiophenediyl]]
RFID	radio-frequency identification
rpm	revolutions per minute
RR	rectification ratio
SAM	self-assembled monolayer
SCLC	space-charge-limited current
SSPL	steady-state photoluminescence
SVA	solvent vapour annealing
SY	Super Yellow copolymer
TC-SCLC	trap-controlled space-charge-limited current
TFB	poly(9,9-dioctylfluorene-*alt*-*N*-(4-*sec*-butylphenyl)diphenyl-amine)
TFL-SCLC	trap-filled-limit space-charge-limited current

TF-SCLC	trap-free space-charge-limited current
TIF-BT	dithiopheneindenofluorene–benzothiadiazole alternating copolymer
ToF	time of flight
TREL	time-resolved electroluminescence
TRPL	time-resolved photoluminescence
UHF	ultrahigh frequency
UV–vis–NIR	ultraviolet–visible–near infrared
WF	work function
XPS	X-ray photoelectron spectroscopy
XRD	X-ray diffraction

Symbols

A	absorption (or equivalently, absorptance)
a	absorbance
α	absorption coefficient
$-\Delta B$	negative differential susceptance
C	capacitance
C_{geo}	geometric capacitance
d	layer thickness
E_{B}	exciton binding energy
E_{F}	Fermi level
E_{g}	transport gap
E_{opt}	optical gap
E_{t}	trap depth
ε_0	vacuum permittivity
ε_{r}	relative permittivity
F	electric field

f	frequency
$f_{3\mathrm{dB}}$	frequency at which the output voltage gain is $-3\,\mathrm{dB}$, i.e. half the maximum
f_{T}	transition frequency for OFETs working in the transdiode mode
h	Planck constant
$h\nu$	photon energy
I	intensity
I_{DS}	drain–source current
I_{f}	current in the forward bias
J	current density
J_{r}	reverse leakage current density
J_{TC}	trap-controlled space-charge-limited current density
J_{TF}	trap-free space-charge-limited current density
k	Boltzmann constant
L	luminance
LT_{90}	time for the OLED luminance to drop to 90 % of its initial value
M_{n}	number-average molecular weight
M_{w}	weight-average molecular weight
m	mean trap depth divided by the unit energy kT for an exponential trap distribution; $m+1$ is the exponent of voltage in the trap-controlled SCLC
N	total density of transport states
N_{t}	total trap density
n	polydispersity index
q	elementary charge
q_{xy}	magnitude of the scattering vector component in the xy-plane
q_z	magnitude of the scattering vector component in the z-direction
R_{rms}	root-mean-square roughness
T	temperature
t	time

t_{rr}	reverse recovery time
τ	exciton lifetime
τ_d	delay time extracted from TREL results
τ_r	rise time extracted from TREL results
V	voltage
V_{bi}	built-in voltage
V_D	voltage across the diode
V_{DS}	drain–source voltage
V_{GS}	gate–source voltage
V_{Th}	threshold voltage
V_i	input AC voltage
V_m	amplitude of the input sinusoidal AC signal
V_o	output DC voltage
V_T	transition voltage from the injection-limited regime to the SCLC regime
V_{TC}	trap-controlled voltage, i.e. the transition voltage from the trap-controlled SCLC regime to the trap-free SCLC regime
η_L	luminous efficiency
η_{LP}	luminous power efficiency
λ	wavelength
μ	mobility
μ_e	electron mobility
μ_{eff}	effective mobility
μ_h	hole mobility
μ_{lin}	OFET mobility extracted from the linear regime
φ	intermonomer torsion angle
φ_B	total injection barrier
ω	angular frequency

Chapter 1

Introduction

1.1 Organic Compounds

For compounds studied in this thesis, the word *organic* literally means "relating to or derived from living organisms", originating from the 18$^{\text{th}}$ century when people believed that organic compounds such as starch and urea could only be created by living organisms with the help of the peculiar "vital force". Inorganic substances, on the other hand, were supposed to be sourced from minerals, entirely distinct from organics. It was not until 1828 that the German chemist F. Wöhler first converted inorganic ammonium cyanate to organic urea in the lab (Fig. 1.1(a)),[1] followed by plenty of experimental evidence to demonstrate that there was no fundamental difference between organic and inorganic compounds. In modern chemistry, organic substances are those that contain C−H bonds,[1] but there are few exceptions due to historical reasons and conventions. For example, the inorganic hydrogen cyanide (HCN) and fulminic acid (HCNO) have C−H bonds, but the organic urea ($CO(NH_2)_2$) and carbon tetrachloride (CCl_4) do not.

In 1907, the Belgian-American chemist L. Baekeland synthesised a new organic material, Bakelite,[2] which, in today's language, is a phenol-formaldehyde resin (Fig. 1.1(b)). Bakelite differed from other synthetic organic compounds at that time since it consists of many repeating units. Thirteen years later, the German chemist H. Staudinger proposed the theory of chain molecules in his famous paper *Über polymerisation* (i.e. *About polymerisation*)[3] to describe the chemical structure of compounds like Bakelite, which were named as *makromolekül* (i.e. *macromolecules*) by Staudinger in 1922. Macromolecules,

or synonymously *polymers*,[4] are large molecules composed of many small and identical structural units (the *monomers*). For each macromolecule, the number of monomers (i.e. the degree of polymerisation) may differ, leading to a distribution of molecular weight. Although in a broad sense, polymers belong to organic compounds, their statistical distribution in structure and high degree of polymerisation (usually >100)[5] distinguish themselves from the rest, which mainly includes *small molecules* (lack of repeating units), oligomers (containing 2–20 monomers),[5] long oligomers or short polymers (containing 20–100 monomers),[5] and dendrimers (monodispersed, radially symmetric molecules consisting of tree-like arms or branches).[6]

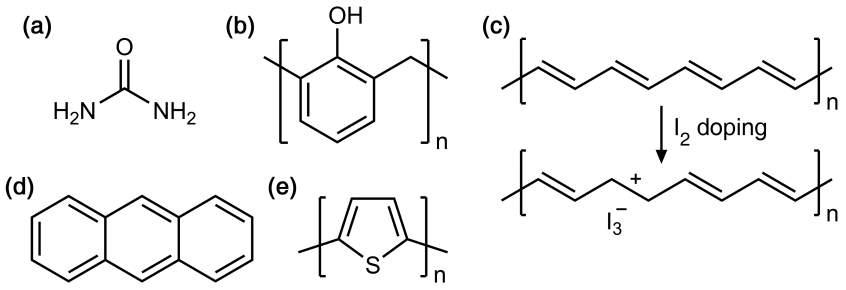

Figure 1.1 | Chemical Structures of Selected Organic Compounds. (a) Urea, the first synthesised organic compound. (b) The simplest phenol-formaldehyde resin with a linear polymer chain. The first synthesised polymer, Bakelite, is a crosslinked phenol-formaldehyde resin. (c) Polyacetylene, an electrical insulator, becomes a conductor after iodine doping. (d) Anthracene, the OSC used in the first OLED and OPV. (e) Polythiophene, the OSC used in the first OFET.

It was long believed that polymers were electrically inactive, or in other words, they were insulators. However, after some pioneering work on the electrical conductivity of organic materials,[7–10] in 1977, the serendipitous discovery of extremely high conductivity in iodine-doped polyacetylene (Fig. 1.1(c)) by A. J. Heeger, A. G. MacDiarmid, and H. Shirakawa[11] not only brought them the 2000 Nobel Prize in Chemistry, but also inspired people to commence exploring the electronic and optoelectronic properties of polymers. It is under this impetus, as well as numerous efforts made by the following researchers, that we are now standing in an active and rapidly growing community of organic electronics, a field mainly focussing on organic semiconductor physics and devices.

1.2 Organic Semiconductors (OSCs)

As the name implies, *organic semiconductors* (OSCs) are organic compounds with semiconducting properties, including light absorption and emission in the visible spectral range and moderate electrical conductivity lying between conductors and insulators. Although these characteristics can be found in inorganic semiconductors as well, e.g. silicon (Si) and gallium arsenide (GaAs), they show some differences as follows.

1. Chemical structure and bonding. Like all organic compounds, in OSCs the main interactions between molecules are van de Waals forces. Inside each molecule, atoms are bound with each other by covalent bonds, whose energy is one or two orders of magnitude higher than that of the intermolecular van de Waals forces. By contrast, atoms in Si crystals are directly held by covalent bonds, and in GaAs the bonding has a mixed covalent and ionic character; in both cases, there is no "molecule" inside.

2. Microstructure. Inorganic semiconductors usually have the tendency to form long-range order and crystallise due to the directionality and high strength of covalent bonds. However, the weak, non-directional van der Waals interactions in OSCs not only reduce the crystallinity (Section 2.2.1), but also make them prone to structural disorder, which can negatively affect the charge transport (Section 2.4.3.4).

3. Electronic structure. In inorganic semiconductor crystals, the strong covalent bond or Coulomb forces between the constituent atoms lead to strong electronic coupling, so electron wavefunctions are delocalised and the band structure results. In addition, the crystalline structure contributes to a periodic potential, allowing electrons to move coherently as a Bloch wave until being scattered by phonons, i.e. the band transport (Section 2.4.3.1).[12] For crystalline OSCs, their weak intermolecular van de Waals interactions lower the degree of electronic coupling and reduce the width of bands. What's more, the electron–phonon coupling is increased, thus at room temperature the band transport is severely interrupted by the phonon-induced scattering at almost every molecular site.[5] More commonly, for OSC materials with amorphous regions, the periodic

potential no longer exists. As a result, electrons are highly localised, and the band structure is decomposed into many localised electronic states. Electrons may hop between these states in an incoherent manner, leading to hopping transport (Section 2.4.3.2).

4. Permittivity. The majority of atoms in OSCs are carbon and hydrogen, whose atomic radii are comparatively small, so electrons are tightly held by the nucleus, resulting in a low degree of electronic polarisation. Therefore macroscopically, OSCs exhibit a much lower relative permittivity of 3–4 than inorganic semiconductors (10–15),[13] leading to reduced dielectric screening of Coulomb interactions between electrons and holes.

5. Optical gap. Traditional inorganic semiconductors typically have optical gaps less than 1.5 eV, such as 1.1 eV for Si and 1.4 eV for GaAs, depending on their band structures. In comparison, wider optical gaps of 2–3 eV are observed in many OSCs,[5] though smaller values are not rare, e.g. ~1.5 eV for zinc phthalocyanine.[14] This is caused by the π–π^* transition in single organic semiconducting molecules (Section 2.1.2) and affected by intermolecular interactions (Sections 2.2.2 and 2.2.3).

6. Intrinsic conductivity. The relatively small optical gaps in inorganic semiconductors such as Si and GaAs allow a small number of electrons to be thermally excited from the valence band to the conduction band at room temperature (~300 K). In addition, after thermal excitation and/or light absorption, the resultant electron–hole pairs are loosely bound due to the high permittivity mentioned above, leading to almost free charge carriers. Therefore, intrinsic conductivities of inorganic semiconductors are typically within 10^{-8}–10^{-2} S cm^{-1} range,[5] and can be further enhanced by doping, although after doping the conductivity is not intrinsic anymore. However in many OSCs, their larger optical gaps and lower permittivities not only prevent nearly all electrons from being thermally excited at room temperature, but also bring about a non-negligible binding energy of 0.3–1.0 eV for the Coulombically bound electron–hole pairs created by optical excitation,[13,15] which is difficult to surmount via thermal fluctuation. That is to say, pristine OSCs at room temperature are actually insulators, and their conductivity is obtained extrinsically by, for example, external charge injection (Section 2.4.2) or doping.

Except these differences, OSCs additionally exhibit some advantages over their inorganic counterparts. For example, their mechanical flexibility, light weight, and biocompatibility are crucial for wearable electronics such as health monitors and biosensors. Moreover, there are abundant strategies for chemists to engineer the molecular structures of OSCs in order to achieve desired properties. The rich choice of materials greatly promotes the development of OSC devices with high performance and/or multi-functions. Last but not least, a large number of OSCs can be dissolved in solvents, making themselves compatible with solution-processing methods, e.g. spin-coating, doctor blading, and ink-jet printing, all of which do not require high vacuum. This raises our hope for the massive, low-cost, and countinuous production of OSC devices by techniques akin to those used for printing newspapers. It is these merits that encourage us to investigate OSCs, with ultimate goals that they can compete with or even eventually substitute for inorganic semiconductors, and their established success in xerography and displays can be extended to more fields.

Corresponding to two important varieties of organic compounds, i.e. small molecules and polymers, two main categories of OSCs are small-molecule semiconductors and polymer semiconductors, though in between there are semiconducting oligomers. Generally speaking, many polymer semiconductors can be solution-processed in that solubilising side chains (e.g. alkyl, alkoxy, and phenyl) can be easily attached to the backbone to increase their solubility in certain solvents, with the rest named as *orthogonal solvents*. This strategy may also be applied to small-molecule semiconductors,[16] but for those without such engineering, their rigid and stable aromatic rings are unfavourable for significant interactions with solvent molecules, so thermal evaporation is the common method to deposit them. Besides, some polymer semiconductors are also prepared via a precursor route in which the final conjugated structure is generated by thermal treatment of a non-conjugated intermediate.[17] Therefore, due to their higher potential to be cost-effectively solution-processed, polymer semiconductors are the main target materials of this thesis.

1.3 Organic Semiconductor (OSC) Devices

In this section, we shall briefly present the functions, history, and development status of some OSC devices. Detailed working principles will be explained in Section 2.5.

1.3.1 Organic light-emitting diodes (OLEDs)

LEDs are able to emit light in response to properly applied electric fields, a process known as *electroluminescence* (EL). This effect was first observed in an inorganic material zinc sulphide (ZnS) in 1936,[18] and later in 1963, EL from organic anthracene (Fig. 1.1(d)) single crystals was first reported.[19] In the early stage, organic EL drew little attention due to the difficulty of preparing high-quality single crystals and identifying suitable injection contacts, the high voltage (~100 V) for driving devices with thick crystals, and the short device lifetime. The breakthroughs were made in the late 1980s when Tang et al. demonstrated the first practical thin-film OLEDs using vacuum-deposited tris(8-hydroxyquinoline)aluminium (Alq_3),[20] and then Bradley and co-workers successfully fabricated poly(*p*-phenylene vinylene) (PPV)-based polymer OLEDs from solution-processed precursors.[21] These seminal pieces of work signified that OLEDs are prospective candidates for large-area displays, an important motivation for pursuing high-performance and low-cost OLEDs.

During over forty years' development, the performance of OLEDs has been tremendously improved mainly owing to (i) the synthesis of highly efficient light-emitting materials, (ii) the evolution of emission principles from fluorescence to phosphorescence and then to thermally activated delayed fluorescence (TADF), and (iii) the usage of the multi-layer device structure with various functional interlayers.[22] Nowadays, the most efficient OLED can reach an external quantum efficiency (EQE) of ~56 %,[23] meaning that over half the electrons injected into the device can be converted to the emitted photons. Regarding display applications, 91.8 % coverage of the CIE 1931 (x, y) Rec. 2020 colour gamut can be achieved,[24] suggesting that the state-of-the-art OLED can

reproduce more than 90 % of the colours in nature.[25] In terms of lighting, a low operating voltage of 2.9 V is able to drive selected TADF-based OLEDs to provide an extremely high luminance of 10 000 cd m^{-2}.[26] Beyond these lab-scale accomplishments, commercialisation of OLED displays has been a great success (Fig. 1.2). Smartphones and televisions using vacuum-deposited OLEDs entered the market during the first decade of this century,[22] and recently the first commercial solution-processed OLED monitor was reported.[27] For lighting applications, it is considered that solution processing will be key in order to reach a commercially attractive price point.

Figure 1.2 | Examples of the Big Success of OLED Display Commercialisation. (a) Enormous OLED display on exhibit at the ceiling of Seoul-Incheon International Airport. (b) A transparent OLED television as part of a museum exhibit. (c) An Apple Watch with an OLED screen. (d) Rollable OLED televisions being deployed to varying heights. (e) Concept of an OLED illuminated shawl. Adapted with permission[28] under a Creative Commons Attribution (CC-BY) 4.0 International License.

1.3.2 Organic solar cells (OPVs)

On the basis of the *photovoltaic* effect, solar cells can convert the energy of light to electricity. Such a clean and renewable way to harvest energy is widely recognised as

an essential solution to both the energy and environmental issues that people are facing today. Therefore, since the first crystalline Si solar cell was reported in 1954 with 6 % efficiency,[29] extensive research has pushed that value to ~26 % and ~29 % for devices using Si and GaAs, respectively.[30] The first demonstration of organic solar cells (or organic photovoltaics, OPV) did not lag by too much; in 1959, the light-to-electricity conversion properties of anthracene (Fig. 1.1(d)) single crystals were investigated.[31] Depressingly, a negligible efficiency of 2×10^{-6} was detected, and many subsequent studies on OPVs failed in increasing this number to even 0.1 %. Before people decided to preclude OPVs from any practical applications, Tang discovered in the late 1970s[32,33] and published in 1986[34] that by using a bilayer structure, where an electron *donor* material and an electron *acceptor* material are brought together to form a planar heterojunction, 1 % efficiency OPV could result. This concept was further developed as a *bulk heterojunction* (BHJ) in the 1990s,[35–37] in which the donor and the acceptor are blended and form nanoscale domains.

The following developments in the OPV field were more about processing methods[38] and materials.[39] Within the latter category, contemporaneous with the introduction of BHJ, < 5 % efficiency can be attained using the classical polymer donors, e.g. poly[2-methoxy-5-(2-ethylhexyloxy)-1,4-phenylenevinylene] (MEH-PPV) and poly(3-hexylthiophene) (P3HT), and the fullerene derivative acceptors, e.g. [6,6]-phenyl C_{61} butyric acid methyl ester ($PC_{61}BM$) and [6,6]-phenyl C_{71} butyric acid methyl ester ($PC_{71}BM$). Since 2010, a number of donor–acceptor (D–A) copolymer donors have been synthesised,[40] and such polymer:fullerene BHJ OPVs can exhibit an efficiency as high as 11.7 %.[41] Soon after the evolution of donor materials, a new group of acceptors, non-fullerene acceptors (NFAs), plays a leading role in boosting the OPV efficiency.[16] At this moment, OPVs with ~18 % efficiency have been reported (Fig. 1.3),[42,43] thanks to the wide-gap polymer donors and the highly efficient NFAs.

Compared with the mature and commercialised photovoltaic technology using crystalline Si, OPVs are still in the process of seeking a foothold in the market. It was previously expected that the low cost of OPVs could be competitive, which was estimated

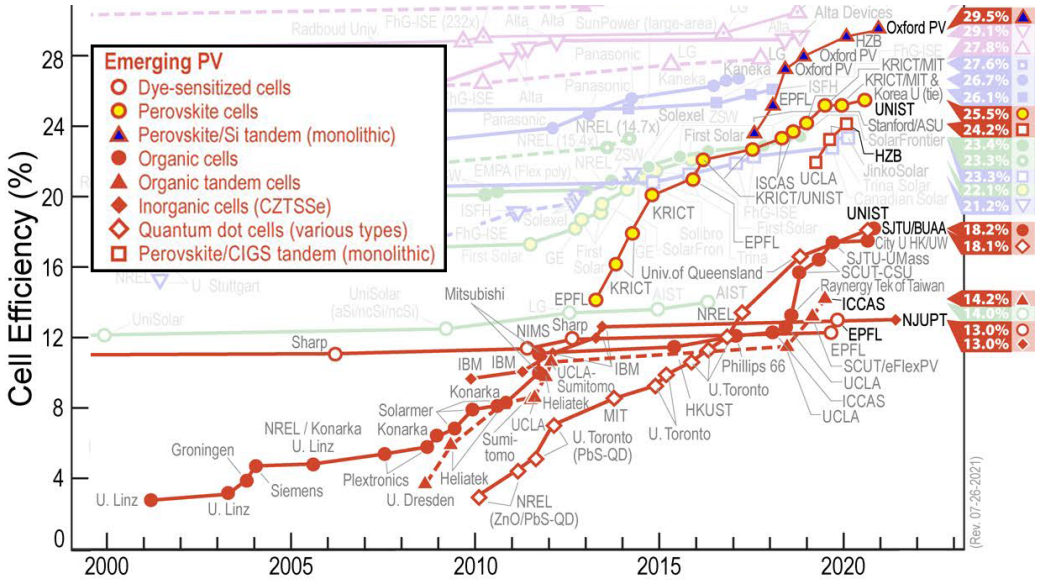

Figure 1.3 | Best OPV Efficiency Chart Since 2000. Represented by solid red dots, the OPV efficiency has risen from ~3 % at the beginning of this century to over 18 % in 2020, i.e. a six-fold increase within twenty years. Adapted with permission.[44] Copyright 2021, National Renewable Energy Laboratory (NREL).

to be \$0.28 per peak watt (Wp).[45] However the continuously dropping price of Si solar cells (~\$0.35 Wp^{-1} in 2020),[46] along with their high efficiency of $> 20\,\%$, makes it sensible for OPVs to start by filling niches where inorganic solar cells cannot serve. Examples include semi-transparent solar cells, building-integrated photovoltaics, and flexible solar cells attached to clothes.[28,46] Given the ongoing improvements in OPV stability, efficiency, and manufacturing techniques, we envisage that OPVs could be the second commercial success after OLED displays.

1.3.3 Organic field-effect transistors (OFETs)

A transistor typically contains three electrodes, and one of them is used to control the current flowing between the other two, so the input signal can be switched or amplified. Field-effect transistors (FETs) realise the current modulation by varying the applied voltage, whereas the other type of transistors, bipolar transistors, is current-controlled.[47] Since the first Si-based metal–oxide–semiconductor FET (MOSFET) was fabricated in 1960,[48] MOSFET has become probably the most prominent elementary

device in modern microelectronics, establishing the backbone of, for instance, integrated circuits, microprocessors, and active-matrix display backplanes.[49,50]

The first report on the OFET dates back to 1986.[51] Using electrochemically polymerised polythiophene (Fig. 1.1(e)), the device showed a mobility, one of the most important proxies for OFET performance, of $10^{-5}\,\mathrm{cm^2\,V^{-1}\,s^{-1}}$,[51] which was too low to have any practical application. By virtue of the evolution in organic semiconducting materials, the greater understanding of charge injection and transport, and the better control of interfacial processes, currently the mobility values of the best OFETs are claimed to reach 10^{1}–$10^{2}\,\mathrm{cm^2\,V^{-1}\,s^{-1}}$ (Fig. 1.4(a)),[52,53] comparable with that of polycrystalline Si,[54] although recently the concern about the validity of these reported high values has received increasing attention (Fig. 1.4(b) and Section 3.6.3).[52,55,56]

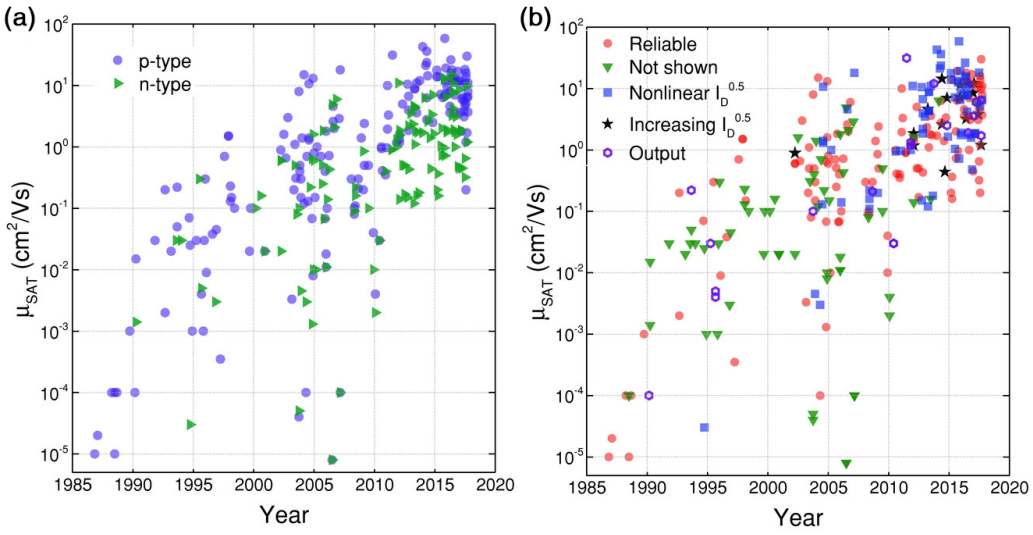

Figure 1.4 | Selected OFET Mobility Reported Since 1985. (a) The reported mobility for n- (green triangles) and p-type (violet dots) OFETs over time. (b) Re-examining the published data raises the concern about the validity of the reported values. Reliable (orange dots) and questionable results (other symbols) coexist. Adapted with permission.[52] Copyright 2018, Wiley.

Similar to the case of OPVs, the performance of OFETs still falls behind crystalline Si-based MOSFETs, which are widely used nowadays with very few shortcomings.[28] Hence, the insufficient motivation for replacing inorganic FETs with OFETs requires us to exploit the potential of using OFETs in unique and emerging applications, which may become the

springboard for their commercialisation. Such opportunities could come from bendable, foldable, or even stretchable devices, from chemical and environmental sensors, and from wearable and/or bio-compatible electronics for medical purposes.[57,58]

1.4 Survey and Scope of the Thesis

Following the discussion above, we can summarise the development tendencies of OSC devices as (i) pursuing higher efficiencies to catch up with those based on inorganic semiconductors and (ii) exploring novel functions and applications that are not easily provided by existing inorganic semiconductor devices. To this end, this thesis presents three examples of achieving high-performance OSC devices from different perspectives, namely chain conformation control of polymer semiconductors, solvent effects on hole-injection/transport interlayers, and a detailed study on the potential use of organic Schottky diodes (OSDs) in high-frequency rectifiers.

Chapter 2 provides concise theoretical backgrounds. The semiconducting properties of single organic molecules and molecule ensembles (thin films in most cases) are discussed, followed by a description of the behaviour of neutral (excitons) and charged particles (charge carriers) that dominate the physical processes in OSCs. Next, working principles of the investigated organic electronic/optoelectronic devices are explained, with some final remarks on common strategies for high-performance devices.

Chapter 3 aims to introduce experimental methods. Starting from a general description of device fabrication procedures, we then introduce the underlying principles of multiple characterisation techniques used in subsequent studies. Details of the device performance measurements are presented as well.

In Chapter 4, we report on the generation of a particular microstructure, the β-phase, in a copolymer 90F8:10BT, containing 90 % 9,9-dioctylfluorene (F8) and 10 % 2,1,3-benzothiadiazole (BT) units, and show that significant improvements in performance ensue for OLEDs with β-phase 90F8:10BT emission layers. Detailed studies addressing the underlying device physics identify higher hole mobility and correspondingly more

balanced electron and hole transport, a reduced hole injection barrier, and decreased charge carrier trapping as the dominant factors. These results confirm the effectiveness of chain conformation control for fluorene-based copolymer device optimisation.

Chapter 5 focuses on copper(I) thiocyanate (CuSCN), an attractive interlayer material used in OSC devices for improving hole injection and transport due to its favourable band structure. We demonstrate the use of two novel solvents for CuSCN, i.e. *N*,*N*-dimethylformamide (DMF) and 1-methyl-2-pyrrolidone (NMP), and perform a comparative investigation of properties and applications of CuSCN interlayers processed from six different solvents, namely diethyl sulphide (DES), dipropyl sulphide (DPS), ammonium hydroxide (NH_4OH), dimethyl sulfoxide (DMSO), DMF, and NMP, emphasising how their surface energies and energy levels affect the hole injection and transport properties. Finally, device tests on polymer OLEDs, OPVs, and OFETs confirm the success of using DMSO or DMF as the solvent for CuSCN interlayers to achieve enhanced performance. This study expands the selection range of CuSCN solvents, highlighting the significant role that interlayers can play in device optimisation.

Chapter 6 demonstrates an emerging application of OSCs, solution-processed OSD-based rectifiers. We first compare three different rectifying devices, showing the superiority of OSDs for high-frequency applications. Next, a model that describes the frequency response of OSD-based rectifiers is established on the basis of previous research, from which simulation is carried out and key factors that affect the rectifier's performance are recognised. Guided by simulation results, we then fabricate OSDs using three different OSC materials, including the benchmark PTB7, the n-type fullerene mixture, and the p-type TIF-BT. Upon proper device optimisation, the performance of their respective rectifiers are characterised, among which the best is predicted to be able to operate at ~243 MHz, a value towards the ultrahigh-frequency regime. The OSD-based high-frequency rectifiers may create another platform beyond OLEDs, OPVs, and OFETs for OSCs to manifest their multi-functionality and broad applicability.

Finally, Chapter 7 concludes the thesis and raises the outlook for subsequent research.

Chapter 2

Background Theory

In this chapter, we shall introduce the background theory of this thesis in order of length scales, i.e. from single organic semiconducting molecules (Section 2.1) to OSC thin films (Sections 2.2, 2.3, and 2.4), and finally to OSC devices (Sections 2.5 and 2.6). This structure generally follows the impressive and instructive book by Anna Köhler and Heinz Bässler.[5]

2.1 Single Organic Semiconducting Molecules

2.1.1 Atomic orbitals and bonding of carbon

Carbon, the predominant element in all organic compounds, has an electron configuration of $1s^2 2s^2 2p^2$ (Fig. 2.1(a)). Although there are only two outermost electrons, a carbon atom can usually form four chemical bonds due to the hybridisation of 2s and 2p orbitals. In detail, one 2s electron can be promoted to the empty $2p_z$ orbital, resulting in four unpaired electrons for bonding. The occurrence of this process lies in the fact that the promotion energy is small in carbon, and can be easily compensated from the energy released during the formation of chemical bonds.[59] The following hybridisation, or in plain words, mixing of orbitals, can happen in different ways; when all orbitals mix, four degenerate sp^3 hybrid orbitals pointing to the vertices of a regular tetrahedron result, which is the case in the ethane molecule (Fig. 2.1(b)). The 2s orbital can also hybrid with two 2p orbitals, $2p_x$ and $2p_y$, leading to threefold degenerate sp^2 hybrid orbitals located in the xy-plane, with an angle of 120° between them. The remaining $2p_z$ orbital is perpendicular to that plane

with a higher energy, as seen in the ethene molecule (Fig. 2.1(c)). Finally, the mixing of the 2s orbital with $2p_x$ only produces two identical sp hybrid orbitals aligned in the same line, orthogonal to both $2p_y$ and $2p_z$ orbitals. This situation is represented by the ethyne molecule (Fig. 2.1(d)).

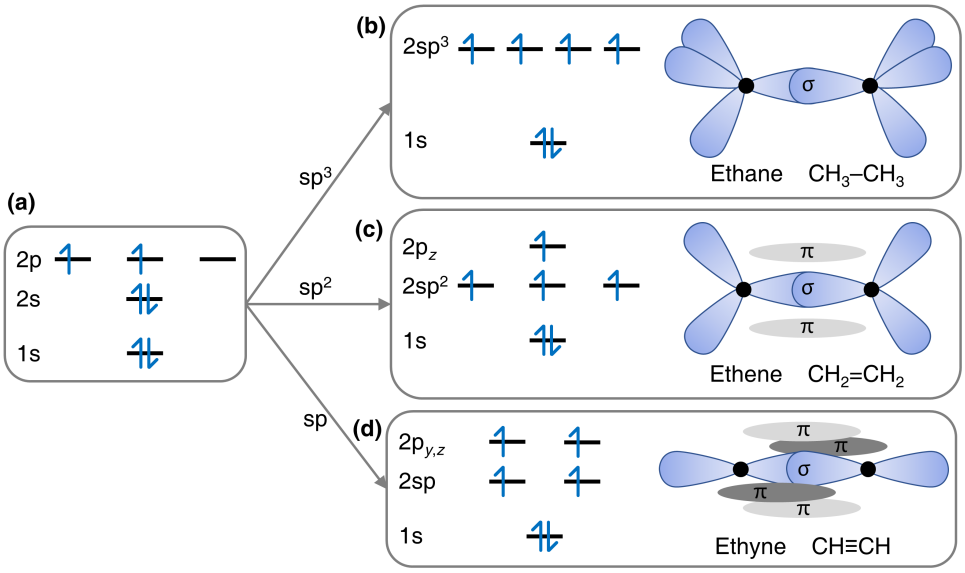

Figure 2.1 | Illustrations of the Hybridisation of Carbon. (a) Electron configuration of carbon before hybridisation. (b–d) Electron configurations of carbon after sp^3, sp^2, and sp hybridisation, respectively, with schematic diagrams of model molecules and σ- and π-bonds.

A close inspection of the C=C double bond in the ethene molecule (Fig. 2.1(c)) reveals that it contains two different bonding types. On the one hand, one carbon's sp^2 orbital overlaps the same orbital of the other in a head-to-head fashion so that in the middle of two nuclei, the electron density is the highest. This is called the *σ-bond*. On the other hand, the unhybridised $2p_z$ orbitals of two carbon atoms are paired with each other side by side. Consequently, a *π-bond* is formed with the electron density concentrated above and below the molecular plane. Similarly, the C≡C triple bond in ethyne is composed of one σ-bond and two π-bonds.

If we go beyond the compounds containing two carbon atoms, then benzene, as shown in Fig. 2.2, perfectly exemplifies the next important concept, *conjugation*. The Kekulé structure of benzene (Fig. 2.2(a)) indicates that all six carbon atoms are sp^2

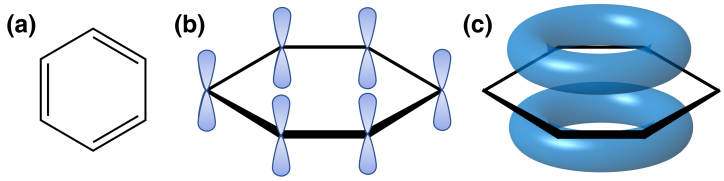

Figure 2.2 | Illustrations of the Benzene Molecule. (a) Chemical structure; (b) $2p_z$ orbitals of the constituent carbon atoms; (c) the delocalised π-bond.

hybridised, with the remaining six $2p_z$ orbitals overlap side by side (Fig. 2.2(b)). This leads to a large π-bond featured by a double-doughnut-shaped electron cloud distributed above and below the aromatic ring (Fig. 2.2(c)), allowing electrons in $2p_z$ orbitals to delocalise over the entire molecule. We refer to the structural basis of the delocalised π-bond, the alternating single and double bonds, as conjugation.[5] The importance of this concept stems from the delocalisation of electrons being a necessary, though not sufficient, condition of (semi)conducting properties of organic molecules. This is why we usually call polymer semiconductors *conjugated polymers*.

2.1.2 Molecular orbitals

The above discussion on atomic orbitals and bonding is mainly from the perspective of the valence-bond theory due to its simplicity. However, if we want to further investigate, for example, the excitation of molecules and molecular spectroscopy, a more suitable viewpoint is the molecular orbital (MO) theory, according to which electrons are not associated with specific atoms or bonds anymore but can spread throughout the whole molecule.[60] By definition, a molecular orbital ψ is the one-electron wavefunction that satisfies the Schrödinger equation $\widehat{\mathrm{H}}\psi = E\psi$,[61] where $\widehat{\mathrm{H}}$ is the Hamiltonian operator and E is the total energy as a sum of the potential and kinetic energies. The key information here is that the MO theory is based on one-electron approximation, meaning that it only considers the behaviour of *one single electron* under the influence of nuclei and a mean field of all other electrons. As a result, the MO theory ignores any electron–electron interactions such as the effects of Coulomb repulsion and electron spin.[5]

The difficulty in solving the Schrödinger equation analytically in polyatomic systems requires a more accessible way to determine MOs. A widely accepted method is to approximate the MO by a linear combination of atomic orbitals (LCAO):[60,61]

$$\psi = \sum_i c_i \varphi_i \tag{2.1}$$

where c_i is the coefficient showing the weight of the atomic orbital φ_i. This combination can produce MOs with different energies from the constituent atomic orbitals. Take a diatomic molecule AB as an example (Fig. 2.3(a)); the two atomic orbitals φ_A and φ_B, with respective energies α_A and α_B, can interfere either constructively or destructively, resulting in a MO $\psi_+ = c_\mathrm{A}\varphi_\mathrm{A} + c_\mathrm{B}\varphi_\mathrm{B}$ with a higher energy E_+ and a MO $\psi_- = c_\mathrm{A}\varphi_\mathrm{A} - c_\mathrm{B}\varphi_\mathrm{B}$ with a lower energy E_-. The energy splitting, $\Delta E = E_+ - E_-$, is primarily affected by the resonance integral (or synonymously, exchange integral) β, which can be seen as a measure of the interaction between a nucleus and the overlap of atomic orbitals.[61]

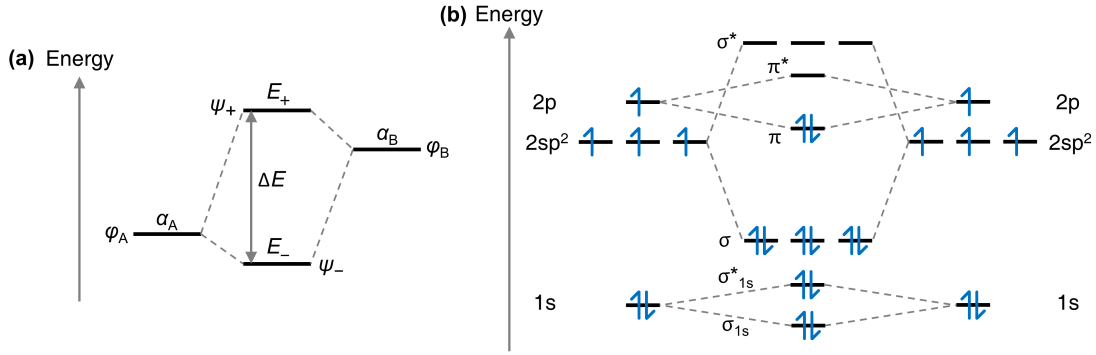

Figure 2.3 | Illustrations of Molecular Orbitals (MOs). (a) Formation of MOs ψ_+ (with energy E_+) and ψ_- (with energy E_-) by combining atomic orbitals φ_A (with energy α_A) and φ_B (with energy α_B) in a diatomic molecule AB. The energy splitting ΔE is also shown. (b) Formation of MOs and electron arrangement in ethene. Note that both the HOMO and LUMO have π-characteristics, so the lowest possible transition is the π–π^* transition.

Having shown the formation of MOs, we now try to arrange electrons into them. According to the principle of minimum energy, electrons tend to occupy MOs with

lower energies, classifying MOs into *bonding* orbitals, whose energies are lower than those of the component atomic orbitals so electron accommodation is preferred, and conversely, *antibonding* orbitals, denoted by an asterisk. In the model molecule ethene, the combination of two 1s orbitals generates a σ_{1s} bonding MO and a σ^*_{1s} antibonding MO. The threefold degenerate sp^2 hybrid orbitals in two carbon atoms lead to three σ_{2p} and three σ^*_{2p} MOs, degenerate as well in their respective cases, with a large energy splitting ΔE resulting from the highest electron density between the nuclei in σ-bonds and the concomitant large value of β. The remaining unhybridised $2p_z$ orbitals form π and π* MOs, but ΔE is smaller. This is because π-electrons concentrate at a place more distant from the nuclei, thus β becomes smaller. It is worth mentioning that here we only consider the mutual interactions of atomic orbitals with the same energy, and its rationale lies in the minor contribution from orbitals with different energies. With this analysis in mind, we can draw an illustration of MOs in ethene (Fig. 2.3(b)) and put electrons in from the bottom, i.e. the lowest-energy MO, to top, as the principle of minimum energy requires. Meanwhile, the Pauli exclusion principle (each orbital can accommodate at most two electrons with antiparallel spins) and Hund's rule (when degenerate orbitals exist, electrons prefer to occupy them singly with the same spin) need to be observed.[59]

It can be seen from Fig. 2.3(b) that the highest occupied molecular orbital (HOMO) is the π orbital, and the lowest unoccupied molecular orbital (LUMO) is the π* orbital. They are jointly referred to as the *frontier orbitals* of the molecule,[60] highlighting their vital role in determining a molecule's electronic, optoelectronic, and chemical properties. Similar to the case of ethene, HOMOs and LUMOs of organic semiconducting molecules are π and π* orbitals, respectively, because of the conjugation. Since the π–π* transition happens at a lower energy (typically in the range of 2.5 ± 0.5 eV) than the σ–σ* (~8 eV)[5] due to the difference in β and ΔE, the appropriate energy gap of the former allows organic semiconducting molecules to absorb and emit light in the visible spectral range. Fundamentally speaking, it is the conjugation and the consequent π-frontier orbitals that make organic semiconducting molecules.

2.1.3 Molecular electronic states

The *electronic state* of an organic semiconducting molecule is closely related to the way its electrons are arranged in MOs. If the electron configuration is the same as predicted from the principle of minimum energy, the Pauli exclusion principle, and Hund's rule, then the molecule is in the *ground state* S_0, which is usually taken as the reference with (arbitrarily set) zero energy. All other electron configurations have higher energies than S_0, so they are called *excited states*, among which the most important one is the first excited state, with one electron in the LUMO and one remaining in the HOMO (Fig. 2.4(a)).

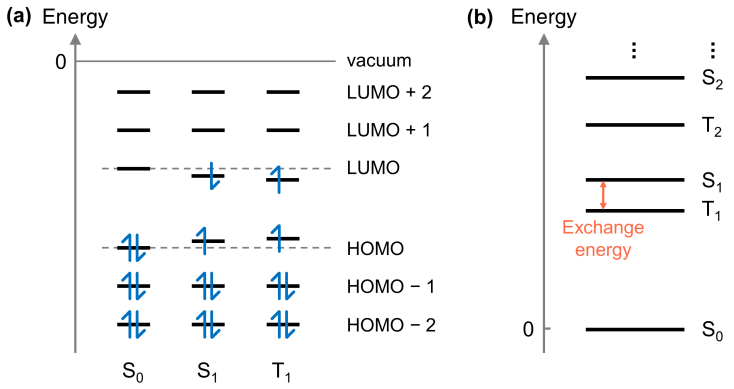

Figure 2.4 | Illustrations of Molecular Electronic States. (a) Electron configurations of S_0, S_1, and T_1 states. (b) Energies of the ground state and excited states. The energy difference between S_1 and T_1 states is the exchange energy (red arrow).

If we pause a second and recall the definition of MOs emphasised in the preceding section, then some problems arise. The main concern is that the concept of MOs is based on the one-electron wavefunction, whereas more than one electron determines the electronic state of a molecule, so the conceptual transition from the one-electron MO to the many-electron electronic state is not trivial. The discrepancy, electron–electron interactions, leads to at least two consequences. First, the description of the first excited state in the last paragraph is not accurate since it ignores the interaction between electrons. In a more precise way, the first excited state is a superposition of different electron configurations, among which the "one-in-LUMO-one-in-HOMO" manner has the major contribution. This is the basic idea of the configuration interaction method in

computational chemistry,[61] but its complexity may distract us from the physical essence we really care about. Thus as people usually do, we still stick to the simpler definition of the first excited state. Second, we have to additionally consider the spin interactions between electrons, with which the same electron configuration, e.g. one-in-LUMO-one-in-HOMO, can result in electronic states with different energies.

Upon excitation, a HOMO electron in a ground-state molecule can be promoted to the LUMO. If the spin of this electron is antiparallel with that of the electron staying in the HOMO, then their total spin cancels ($S = 0$). Hence the spin multiplicity is $2S + 1 = 1$, offering the name of this state as the *singlet* (Fig. 2.4(a)).[61] By contrast, the total spin $S = 1$, in the unit of the reduced Planck constant $\hbar$, when the π- and π*-electrons have the same spin of 1/2. The resultant multiplicity is $2S + 1 = 3$, so we refer to this state as the *triplet* (Fig. 2.4(a)).[61] With the subscripts numbering these states in energetic order, we use notations S_1 (T_1) for the first excited singlet (triplet) state, S_2 (T_2) for the second excited singlet (triplet) state, and so forth (Fig. 2.4(b)).

In an excited state, the π*-electron can correlate with the remaining hole in the HOMO via Coulomb interactions, stabilising the molecule. Therefore, the HOMO and LUMO move slightly closer to each other in excited states. Moreover, triplet states are further stabilised by the exchange interactions between the two spin-identical electrons. As a result, triplet states have lower energies than singlet, providing their electron configurations are the same. The energy difference between S_1 and T_1 states is the exchange energy, which is usually several tenths of an electronvolt.[5] All of these inferences are shown in Fig. 2.4.

2.1.4 Molecular vibrational and rotational states

So far, our discussion mainly focuses on electrons and, by implication, presumes that the nuclei are stationary (the Born–Oppenheimer approximation).[61] This is somewhat reasonable because the nucleus is way more massive than the electron, but in reality, nuclei oscillate in close proximity to their equilibrium positions. As a result, for a specific

electronic state, the motion of nuclei can differentiate it into a series of *vibrational states*. This is illustrated in Fig. 2.5, showing how the molecular potential energy is affected by the configuration coordinate Q, a measure of the internuclear separation. The two black curves represent electronic states S_0 and S_1, whose energies, when nuclei approach each other from an infinite distance, first decrease due to resonance interactions and then increase drastically as the Coulomb repulsion dominates; the minimum energy can be found at the equilibrium position Q_R. Since S_1 is an excited state, it is straightforward that its energy is higher than S_0 at all Q values. Besides, the difference in equilibrium positions between S_0 and S_1, i.e. $Q_{R0} < Q_{R1}$, can be understood from the fact that in S_1, the electron promoted to the antibonding orbital reduces the electron density between nuclei, which consequently become more loosely correlated. The blue horizontal lines in Fig. 2.5 denote vibrational states, whose energies, under the harmonic oscillator approximation, are quantised by $\hbar\omega$ (here ω is the vibrational frequency).[61] We use the quantum number ν ($= 0, 1, 2, \dots$) to symbolise different vibrational states. In passing, a particular vibrational state in an electronic state is usually abbreviated as a *vibronic state*.

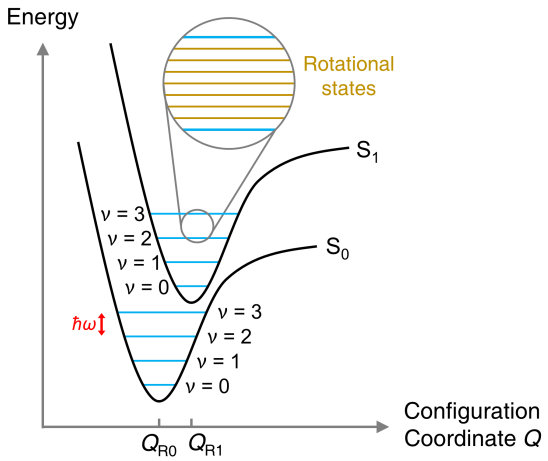

Figure 2.5 | Illustration of Molecular Vibrational and Rotational States. Black curves represent the potential energy of S_0 and S_1 states, and blue and brown horizontal lines denote vibrational and rotational states, respectively. The equilibrium configuration coordinates Q_{R0} and Q_{R1}, as well as energy quanta $\hbar\omega$ of vibrational states, are also shown.

The energy of a vibronic state can further be influenced by the molecule's rotation

around its centre of mass. Analogous to vibrational states showing the fine energetic structure of an electronic state, rotational states reveal the "sub-states" of a vibrational state. This is illustrated by the brown horizontal lines in Fig. 2.5.

2.1.5 Transition between molecular vibrionic states

Upon proper excitation, a molecule can change from its ground state to an excited state, or in the opposite way when decay occurs, releasing its excitation. These transitions can be categorised as radiative and non-radiative, depending on whether photons partake. The Jablonski diagram (Fig. 2.6) provides an overview of these processes.[5,62]

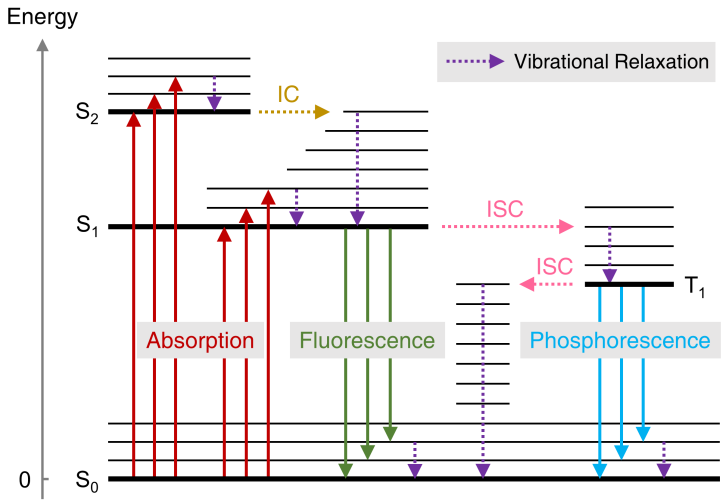

Figure 2.6 | Jablonski Diagram and Vibronic Transitions. Thick and thin black lines denote electronic and vibrational states, respectively. Solid arrows represent radiative transitions, including absorption (red), fluorescence (green), and phosphorescence (blue). Dashed arrows show non-radiative transitions, including internal conversion (IC, brown), intersystem crossing (ISC, pink), and vibrational relaxation (purple). Note that IC and ISC are isoenergetic, so their indicating arrows are horizontal.

The state a transition starts from or end with can be electronic, vibrational, or rotational. However, for organic semiconducting molecules, rotational transitions are usually ignored, since the associated energy is too small to be discerned from molecular spectroscopy.[5] Therefore, we shall concentrate on vibronic transitions. Under this consideration, the total wavefunction Ψ of a vibronic state can be approximated by

the product of the (many-electron) electronic wavefunction Ψ_{el} (depending on electron–nucleus interactions), the vibrational wavefunction Ψ_{vib} (depending on nucleus–nucleus interactions), and the spin wavefunction Ψ_{spin} (depending on electron–electron spin interactions):[5]

$$\Psi = \Psi_{\text{el}}\Psi_{\text{vib}}\Psi_{\text{spin}} \tag{2.2}$$

2.1.5.1 Radiative transitions

Radiative transitions include absorption and emission. By absorbing a photon, the molecule gains energy, and the transition from the zeroth vibrational state in S_0 to an excited vibronic state takes place. Conversely, during emission the molecule discards its excitation energy as an emitted photon and returns to a low-energy vibronic state. The energy of the lowest possible electronic transition via absorption is called the *optical gap* of a molecule ($E_{\text{opt,m}}$),[63] which usually corresponds to the $S_1 \leftarrow S_0$ transition (by conventions in molecular spectroscopy, the high-energy electronic state is always written on the left). Sometimes $E_{\text{opt,m}}$ may be confused with the HOMO–LUMO gap, the energy difference between the HOMO and LUMO of a molecule in its ground state. We note that it is inappropriate to equate these two concepts, although theoretical studies showed some positive correlations between them.[64] The main reasons are:

1. In an excited state, the promoted electron and the remaining hole are electrostatically bound, but the HOMO–LUMO gap does not reflect this binding energy;
2. As stated in Section 2.1.2, the concept of MOs is premised upon the one-electron approximation, so the HOMO–LUMO gap fails to include electron correlations during the electronic transition.

Next, we want to know which transitions between different vibronic states are feasible, and what the intensity and spectral features of the absorption and emission spectra are. To answer these questions, we can start by investigating the kinetics of radiative transitions using Fermi's golden rule,[65] which formulates the transition rate k_{if} from the initial state to the final state as a result of a weak perturbation (adding or removing a photon):[5,61]

$$k_{\mathrm{if}} = \frac{2\pi}{\hbar} \left| \left\langle \Psi_{\mathrm{f}} \middle| \widehat{\mathrm{M}} \middle| \Psi_{\mathrm{i}} \right\rangle \right|^2 \rho \tag{2.3}$$

Here Ψ_{i} and Ψ_{f} are the total wavefunctions of the initial and final states, respectively; ρ is the density of states in the molecule; and $\widehat{\mathrm{M}}$ is the electric dipole moment operator, omitting the very weak magnetic component in the electromagnetic wave. We can then expend Ψ_{i} and Ψ_{f} using Eq. (2.2), and reconstruct the expression by considering the insensitivity of both Ψ_{vib} and Ψ_{spin} to $\widehat{\mathrm{M}}$ (nuclei are too heavy to follow the oscillating electric field; spins are only affected by magnetic fields):

$$\begin{aligned} k_{\mathrm{if}} &= \frac{2\pi}{\hbar} \rho \left| \left\langle \Psi_{\mathrm{el,f}} \Psi_{\mathrm{vib,f}} \Psi_{\mathrm{spin,f}} \middle| \widehat{\mathrm{M}} \middle| \Psi_{\mathrm{el,i}} \Psi_{\mathrm{vib,i}} \Psi_{\mathrm{spin,i}} \right\rangle \right|^2 \\ &= \frac{2\pi}{\hbar} \rho \left| \left\langle \Psi_{\mathrm{el,f}} \middle| \widehat{\mathrm{M}} \middle| \Psi_{\mathrm{el,i}} \right\rangle \right|^2 \left| \left\langle \Psi_{\mathrm{vib,f}} \middle| \Psi_{\mathrm{vib,i}} \right\rangle \right|^2 \left| \left\langle \Psi_{\mathrm{spin,f}} \middle| \Psi_{\mathrm{spin,i}} \right\rangle \right|^2 \end{aligned} \tag{2.4}$$

Now we know that the rate of radiative transitions is dependent on the electronic factor (also called the dipole factor) $\left\langle \Psi_{\mathrm{el,f}} \middle| \widehat{\mathrm{M}} \middle| \Psi_{\mathrm{el,i}} \right\rangle$, the vibrational factor $\left\langle \Psi_{\mathrm{vib,f}} \middle| \Psi_{\mathrm{vib,i}} \right\rangle$, and the spin factor $\left\langle \Psi_{\mathrm{spin,f}} \middle| \Psi_{\mathrm{spin,i}} \right\rangle$. Note that if any of them is zero, then $k_{\mathrm{if}} = 0$, hence the transition is forbidden. Below we shall discuss these three factors successively.

a. the dipole factor

The dipole factor primarily affects the overall strength of a transition. First of all, the operator $\widehat{\mathrm{M}}$ has odd parity.[60] This is because the electric dipole moment $\vec{M} = q\vec{r}$ (q is the elementary charge and $\vec{r}$ is the displacement vector) has the property of $\vec{M}(-\vec{r}) = -\vec{M}(\vec{r})$. As a result, if $\Psi_{\mathrm{el,i}}$ and $\Psi_{\mathrm{el,f}}$ are of the same parity, then the dipole factor will be zero. In other words, a dipole-allowed transition is accompanied by a change of electronic wavefunction parity; otherwise the transition is dipole-forbidden. Second, the value of $\left\langle \Psi_{\mathrm{el,f}} \middle| \widehat{\mathrm{M}} \middle| \Psi_{\mathrm{el,i}} \right\rangle$ depends on the spatial overlap of $\Psi_{\mathrm{el,i}}$ and $\Psi_{\mathrm{el,f}}$. For a molecule whose HOMO and LUMO locate on a similar region, its HOMO–LUMO transitions, i.e. absorption and emission, are thus facilitated. Third, the dipole factor is also related to the value of electric dipole moment $q\vec{r}$. Therefore, molecules with well-extended orbitals can

show higher transition rates, in line with the experimental results that the absorption intensity of oligomers increases with a higher degree of polymerisation.[66] Here, it is relevant to introduce the *conjugation length* of a polymer, which is somewhat ill-defined but can be loosely described as "the length between two kinks along the conjugated path",[67] or "the length at which the π-orbitals of a unit in the polymer are no longer conjugated with the π-orbitals at the origin".[68]

To generally compare the strength of different transitions, we can adopt the concept of *oscillator strength*, a dimensionless quantity representing the intensity ratio of a transition to an electron oscillating in three dimensions in a simple harmonic way.[69] A higher oscillator strength usually implies a longer conjugation length and a stronger absorption/emission signal.

b. the vibrational factor

The vibrational factor $\langle \Psi_{\mathrm{vib,f}} | \, \Psi_{\mathrm{vib,i}} \rangle$ dominates the spectral features of the absorption and emission spectra by affecting the relative strength of different vibronic transitions according to the Franck–Condon principle.[70,71] It implies that the most probable vibronic transition happens when $\Psi_{\mathrm{vib,f}}$ and $\Psi_{\mathrm{vib,i}}$ overlap the most. Furthermore, the square of the vibrational factor, $\left| \langle \Psi_{\mathrm{vib,f}} | \, \Psi_{\mathrm{vib,i}} \rangle \right|^2$, also known as the Franck–Condon factor, gives the probability of a vibronic transition taking place.[5,60]

The Franck–Condon principle is illustrated in Fig. 2.7. At the beginning, the molecule is in S_0, $\nu = 0$ state with a bell-shaped vibrational wavefunction $\Psi_{\mathrm{vib,i}}$ (the magenta curve), whose centre locates at the equilibrium position Q_{R0}. The subsequent absorption is shown by the red arrow pointing up vertically, suggesting the assumption of immobilised nuclei during the speedy transition. To determine where the arrow terminates, i.e. the final state of absorption, we have to examine, along the vertical direction, which vibrational state in S_1 possesses a Ψ_{vib} that most resembles $\Psi_{\mathrm{vib,i}}$. In Fig. 2.7, the shape of vibrational wavefunctions (magenta curves)[60] confirms that the transition to S_1, $\nu = 2$ state dominates, denoted as the $S_1 \leftarrow S_0$ 0–2 transition. Other transitions, though possible to occur, have smaller strengths due to the less extent of wavefunction overlap.

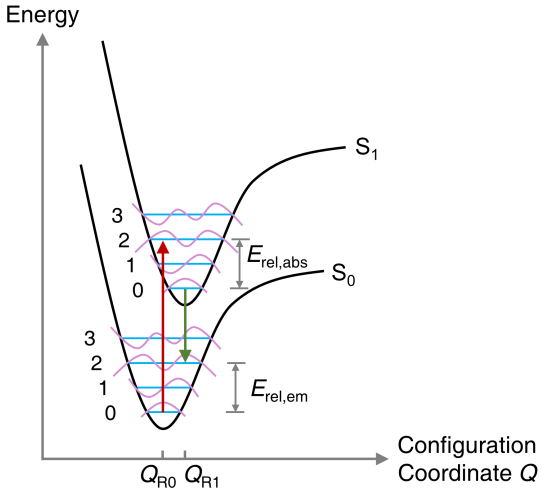

Figure 2.7 | Illustration of the Franck–Condon Principle. The overlap of vibrational wavefunctions (magenta curves) determines the most probable absorption (red arrow) and emission (green arrow). The geometric relaxation energies associated with absorption ($E_{\mathrm{rel,abs}}$) and emission ($E_{\mathrm{rel,em}}$) are shown as well.

After the $S_1 \leftarrow S_0$ 0–2 transition, the nuclei now have a chance to move to the new equilibrium position Q_{R1}, leading the molecule to reorganise its geometry with some vibrational energies dissipated to the surrounding. This non-radiative process is called vibrational relaxation, which we shall discuss later, and as an outcome, the molecule is in S_1, $\nu = 0$ state, ready for the upcoming emission (or other non-radiative transitions described below). Similar to the analysis of absorption, the emission is represented by the green arrow in Fig. 2.7; the only difference is that the arrow now points downwards along the energy coordinate. The most probable $S_1 \rightarrow S_0$ 0–2 emission brings the molecule back to the ground electronic state, and the cycle ends in another vibrational relaxation, after which the configuration coordinate returns to Q_{R0}.

From the mechanisms of absorption and emission, or more intuitively from different lengths of the red and green arrows in Fig. 2.7, it is evident that for a pair of absorption–emission transitions, the absorbed photon always has higher energy than the emitted, and the difference is the sum of *geometric relaxation energies* (E_{rel}) associated with both transitions (i.e. $E_{\mathrm{rel,abs}}$ after absorption and $E_{\mathrm{rel,em}}$ after emission). This energy difference, usually expressed in wavelength units, is referred to as the *Stokes shift*, which

macroscopically results in the bathochromic shift (i.e. to a longer wavelength) of the emission spectrum relative to the absorption for a particular organic semiconducting molecule. Since the Stokes shift is related to the geometric reorganisation process, it is possible to tune the separation between absorption and emission spectra by changing the molecular rigidity. For example, a "softer" molecule can, in principle, exhibit a larger Stokes shift, which is favourable for light-emitting purposes owing to the reduced Förster energy transfer and self-absorption (Section 2.3.2).

c. the spin factor

The spin factor, $\langle \Psi_{\mathrm{spin,f}} | \, \Psi_{\mathrm{spin,i}} \rangle$, can only take two values: it is one if the initial and final states have the same spin, and zero if not. Therefore, emission can be classified into spin-allowed *fluorescence* such as $S_1 \rightarrow S_0$, and spin-forbidden *phosphorescence* such as $T_1 \rightarrow S_0$. The reason that phosphorescence, a process that theoretically has zero possibility to occur, can sometimes be observed is the *spin–orbit coupling*, which originates from the interactions between the spin-induced magnetic momentum and the magnetic field arising from the orbital angular momentum.[60] The effect of spin–orbit coupling can be treated as a weak perturbation, under which the triplet state wavefunction contains some singlet component, and vice versa for the singlet state wavefunction.[5] Thus, the spin-forbidden $T_1 \rightarrow S_0$ transition can happen, though with limited strength, between the singlet components and between the triplet components of two states, both spin-allowed.

The phosphorescence intensity is normally weak in OSCs since the spin–orbit coupling is not strong enough. To increase the strength of spin–orbit coupling and phosphorescence, a common strategy is to incorporate heavy atoms, such as Pt and Ir, into organic semiconducting molecules to form organometallic complexes. This is because the orbital magnetic field is caused by the circular current when the electron moves around the nucleus, so in a heavy atom with more nuclear charges, the current becomes larger, and a stronger spin–orbit coupling results.

2.1.5.2 Non-radiative transitions

Non-radiative transitions include internal conversion (IC), intersystem crossing (ISC), and vibrational relaxation. The first two are isoenergetic processes, meaning that the initial and the final vibronic states have the same energy. Hence in the Jablonski diagram, IC and ISC are represented by horizontal dashed arrows (Fig. 2.6). Their main difference lies in whether the spin multiplicity of the initial and final states is conserved; IC takes places between two states with the same multiplicity (e.g. $S_2 \rightarrow S_1$, $T_3 \rightarrow T_2$), whereas those between singlet and triplet states are termed as ISC (e.g. $S_1 \rightarrow T_1$, $T_2 \rightarrow S_1$). Therefore, ISC is spin-forbidden, and a strong spin–orbit coupling is usually the prerequisite to observing it. In passing, a situation drawing particular research interest is the emission following the $T_1 \rightarrow S_1$ ISC. Such luminance is referred to as *thermally activated delayed fluorescence* (TADF),[72] based on which the high-efficient blue OLEDs become possible.

The vibrational relaxation occurs from a high-energy vibrational state to a low-energy one within the same electronic state, usually simultaneous with geometric reorganisation of the molecule and thermal dissipation. Denoted by downward dashed arrows in the Jablonski diagram (Fig. 2.6), vibrational relaxation is more like a process accompanying others—absorption, emission, IC, and ISC—to bring the molecule to the lowest-energy vibrational state.

2.1.6 Molecular ionised states

The charge neutrality of the molecule is implicit in the aforementioned molecular vibronic states and their transitions, since the studied molecule is isolated and there is no intermolecular charge transfer. However, if we, by some means, add or remove electrons to or from a molecule, then it will be negatively or positively charged, forming an anion or cation, respectively. In this subsection we shall discuss the energy related to molecular ionised states, and how these states can be generated.

The first thing we need to do is to select an energy reference. Recall that when we

talk about vibronic states, the energy of S_0 serves as the reference and is set to zero. All excited states thus have a positive energy in Fig. 2.4(b), which can be referred to as a *state* energy level diagram. For ionised states, what matters is the energy associated with their formation, because the energy discrepancy between different ionised states, containing different numbers of electrons, is trivial. The common practice is to adopt the local vacuum level, namely the energy of an electron at rest just outside the molecule, as the zero-energy reference ($E_{\text{vac}} = 0$).[73,74] This should be distinguished with the vacuum level at infinity ($E_{\text{vac}}(\infty)$), which is not experimentally accessible and only has theoretical significance.[73,74] The stabilisation effect of electrons in a molecule being bound to nuclei reduces their energy from E_{vac}. Therefore, in an *orbital* energy level diagram, all energies are negative (Figs. 2.4(a) and 2.8).

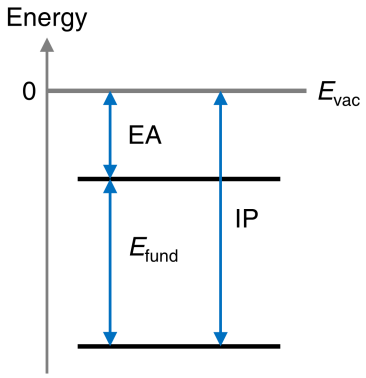

Figure 2.8 | Illustration of Energies Related to Molecular Ionised States. The local vacuum level E_{vac} is set to zero, and the relationship between electron affinity (EA), ionisation potential (IP), and fundamental gap (E_{fund}) is shown.

The formation of ionised states is associated with adding or removing electrons to or from the molecule. Thus, two relevant concepts are the *electron affinity* (EA), the energy released when an additional electron is attached to an originally neutral, ground-state molecule, and the *ionisation potential* (IP), the minimum energy required to eject an electron out of an originally neutral, ground-state molecule.[75] The energy difference between IP and EA is the *fundamental gap* of a molecule (E_{fund}).[74] If we look back to the definition of frontier orbitals, it seems plausible that the absolute energies of the LUMO

and HOMO is the same as the EA and IP, respectively, so E_{fund} should equal to the HOMO–LUMO gap. Nevertheless, we note that these relationships, though widely used, is incorrect in a strict sense, because the concept of MOs overlooks (i) electron correlations in a molecule due to its one-electron approximation, and (ii) the geometric relaxation of a molecule upon an electron being added or removed. Admittedly, the HOMO energy may be seen as a crude estimation of the IP, as stated by Koopmans' theorem:[61,76] in the Hartree–Fock method (i.e. one-electron approximation),

$$\text{IP} \approx -E_{\text{HOMO}} \tag{2.5}$$

It has been shown that the mean error between these two energies was ~0.74 eV for single organic semiconducting molecules.[77] Thus Koopmans' theorem should be regarded as a qualitative, rather than quantitative, conclusion. Besides, in Koopmans' original work[76] there was nothing to do with the relationship between E_{LUMO} and EA, so any attempt to correlate them is actually an overgeneralisation of Koopmans' theorem.

If we bring the three "gaps" of a molecule together, namely $E_{\text{opt,m}}$, E_{fund}, and the HOMO–LUMO gap, it should be aware that none of them is synonymous with another. Besides, the first two can be determined by experiments, while the last one is commonly used in theoretical calculations and is never observable. For $E_{\text{opt,m}}$ and E_{fund} of a molecule, their difference is the electron–hole binding energy E_{B}:[74]

$$E_{\text{fund}} = E_{\text{opt,m}} + E_{\text{B}} \tag{2.6}$$

An additional comment is that this relationship cannot be expressed meaningfully in a single schematic diagram as Brédas did,[63] since $E_{\text{opt,m}}$ is state-based and E_{fund} is orbital-based; they have different zero-energy references.

Equation (2.6) provides us with an insight into the generation of molecular ionised states, i.e. by an optically excited molecule overcoming E_{B}. As a result, an electron is emitted to the vacuum, leaving the molecule carrying a positive charge. This process is

called photoionisation,[5] and it requires the incident photon to have a higher energy than $E_{\mathrm{opt,m}}$, with E_{B} being the minimum excess. It turns out that photons with energies close to the molecule's absorption edge are not responsible for creating ionised states.

2.2 Organic Semiconductor (OSC) Thin Films

2.2.1 Molecular arrangements

When going from a single organic semiconducting molecule to molecule ensembles, for example, thin films in most cases, first we need to consider how these molecules arrange themselves. The main interaction between organic molecules is the van der Waals force, consisting of the orientation force between polar molecules, the induction force between polar and non-polar molecules, and the dispersion force between any molecules, all of which are attractive. Besides, the Coulomb repulsive force prevents two molecules from being too close to each other.

The non-directionality and weakness of the van der Waals force make it more difficult for organic materials to form long-range order, i.e. crystallise, than inorganics. Although both single-crystalline[78] and polycrystalline[79] OSCs have been reported, they are mostly restricted to small molecules due to their structural simplicity. Conjugated polymers, on the other hand, are usually semicrystalline with short-range order, and microscopically consist of many nanoscale crystallites embedded in amorphous matrices.[80] Different materials can exhibit varied degrees of crystallinity; P3HT, as the most famous semicrystalline conjugated polymer, can show millimetre-sized spherulites,[81] while at the other extreme, high degrees of conformational freedom lead some polymer semiconductors to be almost or completely amorphous.[82] Another consideration stems from the deposition methods of conjugated polymers, which are usually solution-processed. Achieving controllable microstructure of conjugated polymers via using different solution-processing conditions is now an active research topic, but for the simplest spin-coating process, the fast evaporation of solvents within few seconds can substantially increase the randomness

of polymer chain arrangements, leaving the obtained microstructure containing a high amount of static disorder that worsens the charge transport (Section 2.4.3.2). By and large, in conjugated polymers, the nature of their long, soft, and sometimes coiled chains, along with the way they are processed, results in great complexity of molecular arrangements.

2.2.2 Environmental effects: polarisation

Upon molecules being brought together, every constituent molecule is in an environment composed of all the others. Due to the environmental effects, energies of molecular vibronic states, as well as of the formation of molecular ionised states, are different from the case when only one isolated molecule exists, as we have already seen in Sections 2.1.5 and 2.1.6. Here we shall discuss the polarisation effect in OSC thin films; another important topic, the statistical averaging, will be presented in the next subsection.

The polarisation effect in neutral molecules is related to the intermolecular van der Waals force, which is known to lower the potential energy due to the interactions of molecular dipole moment. This results in the decrease in energy of both the ground and excited states, yet to different extents. The excited states are more stabilised by dipole moment interactions, since their slightly expended molecular size, as shown in Fig. 2.5 by the increased value of equilibrium configuration coordinate Q_{R}, and consequently the higher degree of polarisation increase their dipole moment. This is illustrated in Fig. 2.9(a) by a larger potential energy reduction for the excited state (V_{ES}) than for the ground state (V_{GS}) when molecules are put together, leading to a smaller condensed-phase optical gap $E_{\mathrm{opt,c}}$, or simply E_{opt}. This explains the bathochromic shift of thin-film absorption/emission spectra compared with single molecules in the gas phase.[83,84]

For molecules carrying charges, i.e. in ionised states, their neighbouring molecules will polarise under their local electric fields. Thus as shown in Fig. 2.9(b), both molecular cations and anions are stabilised by their polarisation energies, P_+ and P_-, respectively,[63,85,86] causing the shrink of the *transport gap* (E_{g}),[63] a condensed-phase analogue to E_{fund} of a molecule. In addition, when charge carriers move between molecules,

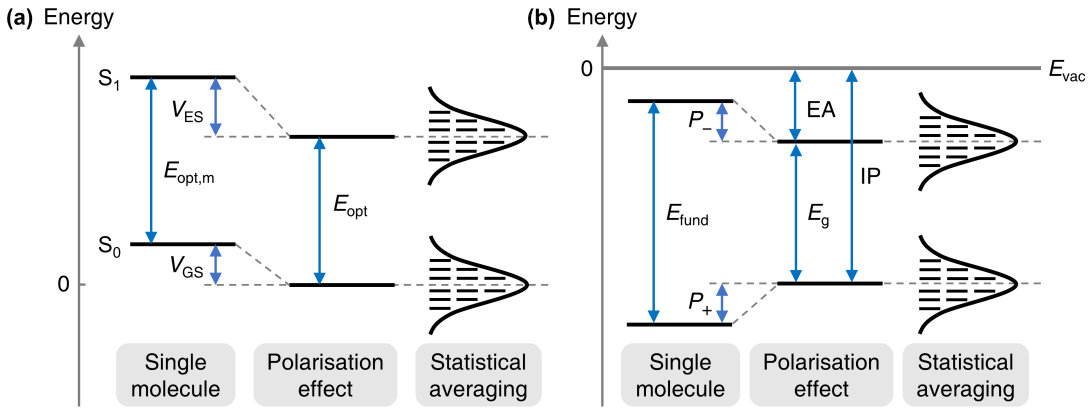

Figure 2.9 | Illustrations of Environmental Effects on OSC Thin Films. Upon molecules being brought together, the polarisation and statistical averaging effects on (a) electronic state energies in neutral molecules and (b) formation energies of ionised molecules are shown.

the conformational change of adjacent molecules induced by the polarisation effect follows, inspiring us to define *polarons*,[75] a quasiparticle comprising a charge carrier and the associated molecular distortion.

2.2.3 Environmental effects: statistical averaging

The statistical averaging results from the randomness of molecular arrangements, such as the diverse orientations of crystallites in semicrystalline conjugated polymers, and the amorphous regions in both semicrystalline and non-crystalline OSC thin films. The varied intermolecular distances and dipole moment orientations lead different molecules to sense the polarisation effect with different strengths from different directions. Consequently, in OSC thin films the molecular vibronic and ionised states do not have fixed energies anymore, but their *density of states* (DoS) follow some distribution (Fig. 2.9). In statistics, the central limit theorem helps us to identify such a distribution to be Gaussian, whose probability density function g is given by:[5]

$$g(\epsilon) = \frac{1}{\sqrt{2\pi}\sigma} \exp\left(-\frac{(\epsilon - \epsilon_0)^2}{2\sigma^2}\right) \tag{2.7}$$

where ϵ can represent the energy of a vibronic state, EA, or IP; σ is the standard deviation of the distribution, and is often referred to as the disorder parameter; ϵ_0 is the mean value of the distribution.

The statistical averaging effect accounts for, for example, the broadened absorption and emission spectra for OSC thin films[84] relative to the discrete spectral lines for single molecules in the gas phase.[83] Hence, the signal of some fine vibrational transitions in the condensed phase is buried under the broadened peaks, spectroscopically undistinguishable.

Having introduced how energies of molecular vibronic and ionised states change when molecules are gathered together, we shall then discuss in OSC thin films, how neutral and charged excitations, that is, excitons (Section 2.3) and charge carriers (Section 2.4), behave.

2.3 Behaviours of Excitons: Generation, Energy Transfer, and Decay

An exciton, the Coulomb-bound electron–hole pair, is a neutral quasiparticle capable of transporting energy in OSCs.[87] Depending on the electron–hole separation (i.e. Bohr radius), excitons can be classified into Frenkel excitons (< 5 Å),[88,89] Wannier excitons (40–100 Å),[90] and charge-transfer (CT) excitons (5–40 Å)[91] (Fig. 2.10). The size of an exciton is related to the material's relative permittivity ε_r. As mentioned in Section 1.2, for inorganic semiconductors such as Si and GaAs, their high ε_r of > 10 leads to well-screened electron–hole Coulomb interactions, so excitons are loosely bound and can encompass several crystal lattice spacings, i.e. they are of the Wannier type. By contrast, OSCs exhibit lower ε_r of 3–4, so tightly bound Frenkel excitons with smaller radii result, usually located on single molecules. Finally, the CT exciton, an intermediate case between the Frenkel and the Wannier, has a spatial extent of two neighbouring molecules correlated electrostatically.[92] In all, the different exciton Bohr radii and material permittivities give rise to varied *exciton binding energies* E_B, defined as the Coulomb interaction energy

between the electron and hole in an exciton.[13]

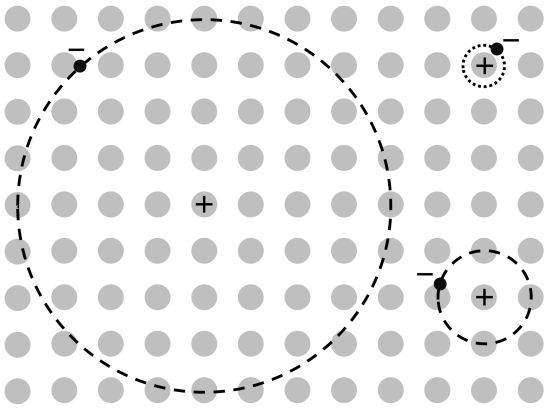

Figure 2.10 | Illustration of Different Excitons. Left, a Wannier exciton with a relatively large radius of several lattice constants. Right top, a Frenkel exciton located on a single molecule. Right bottom, a charge-transfer (CT) exciton residing in two adjacent molecules.

2.3.1 Exciton generation

Excitons can be populated by primary processes including optical and electrical excitation, or by secondary processes involving other existing excitons (e.g. $S_1 \rightarrow T_1$ intersystem crossing).[5] Here we shall mainly discuss primary processes.

As described in Section 2.1.5, a molecule in its ground state can be converted to an excited state by optical means, i.e. absorbing photons, thus the promoted electron and the remaining hole form excitons. The conservation of spin during this process indicates that the obtained excitons are singlets. Triplet excitons, however, can only be populated via subsequent intersystem crossing with a substantially low rate.

Another possible way to create excitons is electrical excitation, that is, injecting electrons and holes from the cathode and anode, respectively, to OSCs (Section 2.4.2). The two types of charge carriers can travel towards each other inside OSC thin films, during which some can be captured by those with the opposite charge through Coulomb attraction. This leads to the recombination of charge carriers and the generation of excitons. The recombination, a neutralising process for charge carriers, is widely assumed to be irrelevant to the spin of charge carriers. Thus the ratio of the resultant singlet

and triplet excitons statistically follows their spin multiplicities, i.e. 25 % vs 75 %.[93] It is worth mentioning that in some conjugated polymers, this relationship is broken and the proportion of singlet excitons can be considerably higher;[94] in an extreme case, over 80 % electrically generated excitons are singlets.[95] It has been proposed that this spin-dependent recombination might be related to different singlet and triplet forming rates and some spin-randomising processes, e.g. intersystem crossing.[96] Besides, triplet–triplet annihilation (Section 2.3.3) may also play a role in reducing the triplet fraction.[97]

As a brief summary, the optical and electrical methods mainly differ in the ratio of populated singlet and triplet excitons. The former mechanism is important for OPVs (Section 2.5.2), whereas the latter is a crucial step during OLED operation (Section 2.5.1).

2.3.2 Energy transfer

A key feature of excitons is that their movements give rise to the transport of energy, with no need for charge carriers to participate.[87] In OSCs, the structural and energetic disorder hinders the energy transfer from occurring in a wavelike manner, which is the case in crystalline inorganic semiconductors.[5] Rather, two representative modes in OSCs are Förster energy transfer[98] and Dexter energy transfer.[99] The former is typically for singlet excitons and in competition with the fluorescence process, while the latter prevails in triplet excitons and competes with the phosphorescence process.[100]

Both Förster and Dexter energy transfers can be generally described as an exciton donor molecule, D*, passing the exciton to an acceptor molecule, A, so that the donor is de-excited to D and the acceptor is in the excited state A*. The two pathways, nonetheless, have different underlying principles: Förster energy transfer is based on dipole–dipole interactions of two molecules, whilst Dexter energy transfer involves electron exchange between D* and A.[86]

As Fig. 2.11(a) illustrates, in the Förster-type process, the electron in the LUMO of molecule D* returns to its HOMO, and simultaneously, an electron in the HOMO of molecule A is promoted to its LUMO. It can also be understood by imagining a

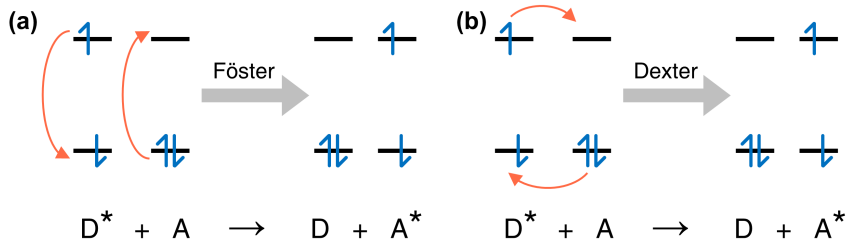

Figure 2.11 | Schematic Mechanisms of Energy Transfer. (a) Förster energy transfer; (b) Dexter energy transfer. Red arrows indicate how electrons move.

virtue photon; molecule A absorbs this photon before molecule D* emits it.[86] Therefore, efficient Förster energy transfer requires a good overlap between molecular absorption and emission spectra, and owing to its dipole–dipole coupling mechanism, the distance between two molecules can be comparatively long (1–10 nm),[100] provided that they are still correlated by the Coulomb force.

In comparison, during Dexter energy transfer the donor and acceptor exchange their electrons (Fig. 2.11(b)): the one in the LUMO hops from D* to A, and in turn, one electron in molecule A's HOMO hops to the same orbital of D*. Such an exchange process entails good wavefunction overlap, thus only takes over at short intermolecular distances (< 1 nm).[100]

2.3.3 Exciton decay

The decay processes can convert excitons to other particles, such as photons, phonons, charges, and new excitons. Four main categories of decay are:

1. *Intramolecular radiative and non-radiative decay.* Similar to what has been shown in Section 2.1.5, an exciton can discard its excitation by emitting a photon, resulting in florescence (for a singlet exciton) or phosphorescence (for a triplet exciton). This is how OLEDs become luminescent (Section 2.5.1). Additionally, the non-radiative decay may also take place, e.g. $S_1 \rightarrow T_1$ intersystem crossing.
2. *Dissociation.* An exciton can dissociate into an electron and a hole that are not electrostatically correlated anymore, as long as the exciton binding energy E_B

can be overcome. The dissociation of CT excitons is the essence of the light-to-electricity conversion in OPVs (Section 2.5.2).

3. *Exciton–exciton interactions.*[5,86,92] This includes singlet–singlet annihilation ($S_1 + S_1 \rightarrow S_n + S_0 \rightarrow S_1 + S_0 + \text{phonon}$), triplet–triplet annihilation ($T_1 + T_1 \rightarrow S_n + S_0 \rightarrow S_1 + S_0 + \text{phonon}$, or $T_1 + T_1 \rightarrow T_n + S_0 \rightarrow T_1 + S_0 + \text{phonon}$), singlet–triplet annihilation ($S_1 + T_1 \rightarrow S_0 + T_n \rightarrow S_0 + T_1 + \text{phonon}$), and singlet fission ($S_1 + S_0 \rightarrow T_1 + T_1$).
4. *Exciton–charge interactions.*[5,86,92] Excitons can also interact with charge carriers, i.e. electrons (e^-) and holes (h^+), thereby losing their excitation (S_1 or $T_1 + e^-/h^+ \rightarrow S_0 + e^-/h^+ + \text{phonon}$). This process is detrimental to OLED lifetime.[101]

2.4 Behaviours of Charge Carriers: Injection and Transport

2.4.1 Basic concepts

Charge carriers, including electrons and holes, are responsible for the formation of current in OSCs. If their accompanying molecular distortion is also taken into account, the resulting quasiparticles are negative and positive polarons, respectively. In addition, two similar polarons can pair up to form a (negative or positive) bipolaron. Microscopically, the current density J can be expressed as:[5]

$$J = qn\mu F \tag{2.8}$$

where q is the elementary charge; n is the charge carrier density; μ represents the charge carrier mobility, a crucial, material-based parameter describing how fast charge carriers can be transported under a certain electric field F. The product of $qn\mu$ are refered to as the conductivity σ of OSCs.

As stated in Section 1.2, there are very few thermally excited charge carriers in OSCs at room temperature. Therefore, charge carriers have to be introduced by some additional

processes. The main three ways are (i) optical excitation and exciton dissociation, which have been mentioned for the single-molecule case in Section 2.1.6, and will be discussed in conjunction with the working principles of OPVs in Section 2.5.2 for molecule ensembles, especially for the electron donor–acceptor blend; (ii) charge injection via electrodes, which will be elaborated in the following subsection; and (iii) doping, whose principles are beyond the scope of this thesis and can be found from pertinent reviews.[102,103]

The dark current density in an OSC device is largely affected by two processes, namely charge injection and transport. Consider the simplest device with the sandwich structure, that is, an OSC thin film positioned amid two electrodes. During the injection, electrodes provide the intrinsically insulating OSC, usually referred to as the *active material*, with external charge carriers, which can subsequently flow in the device under the electric field, resulting in a current. Therefore, the magnitude of the dark current density can be limited by either the efficiency of charge injection, or the ability of the active material to transport the injected charges, i.e. the mobility. In the former case, the metal–OSC contact is a *Schottky contact* and the current density is *injection-limited* in that the injection process does not provide enough charge carriers for the active material to transport. By contrast, if the injection barrier is small enough, then the electrode is able to inject more charges than the active material can transport. In this *Ohmic contact*, the electrode is akin to an infinite charge carrier reservoir, and the device current density is limited by the accumulated charges close to the injection electrode, i.e. space charges, as they can shield the electric field for injection thereabouts. This situation leads to the *space-charge-limited current* (SCLC), which follows the Mott–Gurney law,[104] a generalisation of the Child's law in vacuum:[105]

$$J = \frac{9}{8}\varepsilon_0\varepsilon_\mathrm{r}\mu\frac{V^2}{d^3} \tag{2.9}$$

Here V is the voltage across the active layer; d is the layer thickness; ε_0 and ε_r are the vacuum and relative permittivities, respectively. In the following two subsections, we shall discuss the charge injection and transport processes, and use the HOMO and the LUMO as analogues to the valance and the conduction band edges in inorganic

semiconductors, respectively, to represent energy levels relevant to hole and electron injection. Therefore, IP $\approx -E_{\mathrm{HOMO}}$, and EA $\approx -E_{\mathrm{LUMO}}$. Note that this treatment is not rigorous (Section 2.1.6), but can greatly facilitate our discussion before more suitable terminologies are widely accepted by the community.

2.4.2 Charge injection

2.4.2.1 Metal–organic semiconductor contact: the ideal case

Charge injection is a process during which electrons (or holes) originally settling at the Fermi level E_{F} of the metal electrode are transferred to the LUMO (or the HOMO) of the OSC. Thus the energy difference between metal's work function (WF), i.e. the absolute energy of E_{F}, and OSC's EA (or IP) is a measure of the electron injection barrier φ_{e} (or the hole injection barrier φ_{h}):

$$\varphi_{\mathrm{e}} = \mathrm{WF_c} - \mathrm{EA} \tag{2.10}$$

$$\varphi_{\mathrm{h}} = \mathrm{IP} - \mathrm{WF_a} \tag{2.11}$$

The subscripts "c" and "a" of WF denote the cathode and anode, respectively. This is for the sandwich-structured device with its electrodes unconnected (Fig. 2.12(a)).

If we connect the electrodes with an external circuit, then some electrons will move from the cathode to the anode through the wire to equilibrate the E_{F} of electrodes. As a result, the cathode effectively brings positive charges while the anode brings negative, leading to the formation of a built-in electric field F_{bi}:

$$F_{\mathrm{bi}} = \frac{\mathrm{WF_a} - \mathrm{WF_c}}{qd} = \frac{V_{\mathrm{bi}}}{d} \tag{2.12}$$

where V_{bi}, the electrodes' work function difference divided by q, is referred to as the *built-in potential*, causing energy levels of the active material to incline in the simplest picture (Fig. 2.12(b)).

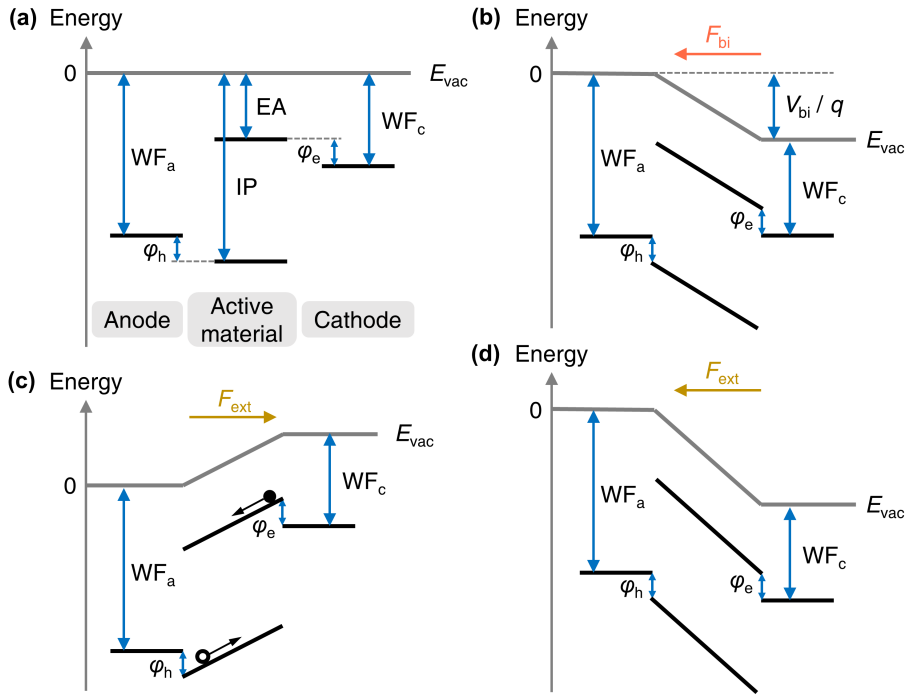

Figure 2.12 | Energy Level Diagrams of a Sandwich-Structured Device. (a) Before and (b) after electrodes being connected by an external circuit, with illustrations of the built-in voltage V_{bi} and the direction of the built-in field $\overrightarrow{F_{bi}}$. (c) In the forward and (d) reverse biases under the external electric field $\overrightarrow{F_{ext}}$.

When the device is in the forward bias, that is, the anode has a higher potential than the cathode, the direction of the external electric field $\overrightarrow{F_{ext}}$ is opposite to that of $\overrightarrow{F_{bi}}$. As the applied voltage V_{app} increases, F_{bi} is first weakened and then cancelled when $V_{app} = V_{bi}$, followed by the conversion of the electric field direction in the active layer (Fig. 2.12(c)). Therefore, the difference between V_{app} and V_{bi} is the actual voltage drop V across the active layer, and only if $V_{app} - V_{bi} > q\varphi_e$ (or $q\varphi_h$), electrons (or holes) can be successfully injected. In other words, the injection barrier in devices (φ_D) is, in principle, the sum of φ_e (or φ_h) and V_{bi}/q:

$$\varphi_D = \varphi_{e/h} + \frac{V_{bi}}{q} \tag{2.13}$$

In addition, when $V_{app} > V_{bi}$, energy levels of the active material tilt in a thermodynamically favourable manner for injected electrons to move downwards in the energy space,

and for holes to move upwards. This provides the injected charge carriers with driving forces to be subsequently transported.

By contrast, in the reverse bias the F_{bi} is continuously enhanced by F_{ext} when V_{app} increases, and the unfavourable tilt of energy levels becomes much steeper, preventing charge carriers from being injected until the device is broken down (Fig. 2.12(d)).

2.4.2.2 Metal–organic semiconductor contact: in reality

From the previous discussion, it seems that injection barriers can be easily calculated and predicted if energy levels of electrodes and active materials are known. However, in reality some interfacial effects significantly complicate the analysis. The two most pronounced effects are interface dipole and band bending.

a. interface dipole

Upon depositing an OSC layer on top of the metal surface, we can investigate their interface from the perspective of adsorption, be it physisorption or chemisorption, depending on whether chemical bonds are formed between the substrate (metal) and the adsorbate (OSC).

If the substrate is passivated or chemically inactive, and the adsorbate molecule does not have an intrinsic dipole or anchoring group, then physisorption will occur.[106] For a clean, bare metal substrate, there are dangling bonds just outside the surface, meaning that some electrons are spilled out of the bulk. These electrons make it more difficult to move a surface electron of the metal to the vacuum, a process whose energy is defined as the metal's WF.[74] Therefore, the physisorption of organic semiconducting molecules on the metal surface can push these electrons back, forming a push-back dipole Δ_{PB} that reduces the metal's WF.[107] For example, it has been measured that by covering the Au surface with a 2,2′-dimethyl-*N*,*N*′-di-[(1-naphthyl)-*N*,*N*′-diphenyl]-1,1′-biphenyl-4,4′-diamine (α-NPD) monolayer, its WF decreased significantly from 5.2 eV to 4.0 eV.[108] Furthermore, despite the lack of chemical bonds between the metal and the OSC, integer

charge transfer can still happen via tunnelling.[106] This leads to an integer-charge-transfer dipole Δ_{ICT}.[107]

On the other hand, chemisorption can induce a through-bond charge transfer that creates an interface dipole Δ_{CT}.[107] Besides, the intrinsic dipole Δ_{int} carried by adsorbate molecules also contributes. This is the main reason why self-assembled monolayers (SAMs) can regulate the metal's WF (Section 2.6.2).[109] Moreover, the adsorbed molecules themselves, such as polyelectrolytes and doped OSCs, may contain charges to polarise the metal surface. The resultant image charges in the metal can attract the organic semiconducting molecules, so they have the tendency to move towards each other. During the movement, the large size and the deformability of organic molecules result in varied extents to which different parts of the molecule approach the metal surface. This produces a net dipole Δ_{IDD} since it is related to an "induced double dipole" in both the OSC layer and the metal.[110,111]

Summing all these interface dipoles up, we can achieve a total interface dipole Δ:[107]

$$\Delta = \Delta_{\mathrm{PB}} + \Delta_{\mathrm{ICT}} + \Delta_{\mathrm{CT}} + \Delta_{\mathrm{int}} + \Delta_{\mathrm{IDD}} \tag{2.14}$$

Note that the effect of each component on the sum can be productive or counterproductive, depending on their individual dipole orientations. The total interface dipole Δ can affect the injection barrier by shifting the local vacuum level (Fig. 2.13(b)) by a magnitude of φ_{Δ}:[112]

$$\varphi_{\Delta} = \frac{q\Delta}{\varepsilon_0 \varepsilon_{\mathrm{r}} A} \tag{2.15}$$

Here A is the unit area.

b. band bending

The term "band bending" comes from inorganic semiconductor physics. It describes the scenario where an additional electric field is produced by the local deviation from neutrality after electrons being transferred from the semiconductor to the metal.[113] The

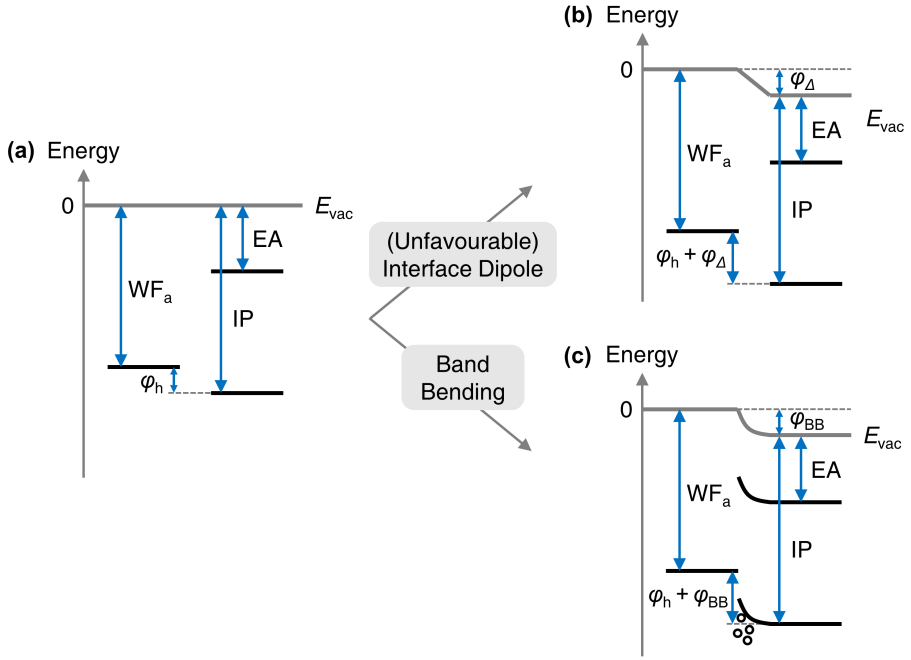

Figure 2.13 | Illustrations of the Impact of Interface Dipole and Band Bending on the Injection Barrier. Here we take (a) hole injection from the anode to the OSC layer as an example. (b) The unfavourable interface dipole increases the hole injection barrier by φ_Δ. (c) The band bending effect induced by hole accumulation (black circles) at the metal–OSC interface leads to an additional barrier φ_{BB}.

potential energy of this field bends the semiconductor's energy bands in the vicinity of the metal–semiconductor interface, that is, the depletion region.[106] For OSCs, this term may not be appropriate since there is no band structure but only localised electronic states. However, we shall still use it due to the similar physical essence.

Owing to the extremely low intrinsic charge carrier density, the band bending effect in OSCs is less prominent than in their inorganic counterparts. It can be caused by the integer or though-bond charge transfer discussed above, but is only relevant to molecules residing very close to the interface. Besides, it can also be observed in doped OSCs. The result of band bending is an extra injection barrier φ_{BB} (Fig. 2.13(c)).[112]

Finally, we can obtain the total injection barrier (φ_B) for a metal–OSC contact by considering the energy level difference (Eqs. (2.10) and (2.11)), the interface dipole-

induced barrier (Eq. (2.15)), and the band bending effect together:[112]

$$\varphi_{\mathrm{B}} = \varphi_{\mathrm{e/h}} + \varphi_{\Delta} + \varphi_{\mathrm{BB}} \tag{2.16}$$

It turns out that φ_{B} can hardly be accurately predicted. Therefore, the energy level difference calculated from an energy level diagram, i.e. φ_{e} or φ_{h}, is only a rough estimation of φ_{B}. Practically, if $\varphi_{\mathrm{e/h}} < 0.3\,\mathrm{eV}$, the metal–OSC contact may be regarded as Ohmic.[114] In addition, for a sandwich-structured device consisting of two metal–OSC contacts, another built-in potential term should be added to φ_{B} (Eq. (2.13)).

2.4.2.3 Charge injection models

Two classical models explaining how charge carriers overcome the injection barrier φ_{B} at the metal–OSC interface are the Richardson–Schottky (RS) thermionic injection[47] and the Fowler–Nordheim (FN) tunnelling injection.[115]

The RS thermionic emission model points out that during the charge injection under an external electric field F_{ext}, the barrier φ_{B} will be lowered by $\Delta\varphi = \beta_{\mathrm{RS}}\sqrt{F_{\mathrm{ext}}}$ due to the interactions between image charges and F_{ext}, a phenomenon known as the Schottky effect.[116] Here $\beta_{\mathrm{RS}} = \sqrt{q^3/4\pi\varepsilon_0\varepsilon_{\mathrm{r}}}$ is the RS factor.[47] The basic assumption of this model is that once an electron in the metal acquires enough thermal energy to surmount the potential barrier of $\varphi_{\mathrm{B}} - \Delta\varphi$, it can traverse this barrier in an elastic way.[5] The injection current density J_{RS} is given by[47,117]

$$J_{\mathrm{RS}} = A^* T^2 \exp\left(-\frac{\varphi_{\mathrm{B}} - \Delta\varphi}{kT}\right) \tag{2.17}$$

with $A^* = 4\pi q m^* k^2/h^3$ being the Richardson constant (m^*: electron effective mass; h: the Planck constant),[118] and k and T being the Boltzmann constant and the temperature, respectively. Therefore, the RS model is characterised by the $\ln(J/T^2) \propto 1/T$ relationship. The applicability of the RS model to the metal–OSC contact is mediocre in that some electrons are prone to be inelastically scattered before crossing the potential barrier, with

no contribution to the current density.[5]

The FN model, on the other hand, is premised upon the idea that the tunnelling injection to vacuum can occur if the electron's de Broglie wavelength is larger than the width of the triangular potential barrier at the metal–vacuum interface.[5] The FN injection current density J_{FN} can be expressed as[115,117]

$$J_{\mathrm{FN}} = \frac{q^3}{8\pi h\varphi_{\mathrm{B}}} F^2 \exp\left(-\frac{8\pi\sqrt{2m^*\varphi_{\mathrm{B}}^3}}{3hqF}\right) \tag{2.18}$$

which exhibits a $\ln(J/F^2) \propto 1/F$ dependence, with F being the electric field. This mechanism, however, is unlikely to be the main pathway of charge injection at the metal–OSC contact, mainly because (i) it was originally proposed to study the electron emission to the vacuum without considering the Schottky effect; and (ii) the tunnelling length under typical electric field in sandwich-structured devices is too large for electrons to go across elastically.[5]

A final remark is that some new models have been developed, from both experimental results[117] and theoretical analysis,[119,120] to better describe the charge injection process at the metal–OSC contact, though none of them has become the consensus yet.

2.4.3 Charge transport

2.4.3.1 Band transport

After charge carriers are injected into OSCs, they will then be transported, a process macroscopically characterised by the mobility μ. However, its microscopic mechanisms can hardly be covered simply by a figure of merit, so various models have been proposed. We shall start our discussion with the band transport, which is typically found in inorganic semiconductors.

In an ideal crystalline inorganic semiconductor, its periodic potential leads the electron wavefunction to follow the Bloch function. As a result, electrons are delocalised in the

entire volume, propagating in the form of Bloch wave coherently (Fig. 2.14(a)).[12] Such band transport may be interrupted by structural defects or crystal lattice vibrations (Fig. 2.14(a)), but in essence the electronic interaction energy between two neighbouring transport sites is significantly larger than the energy related to disorder.[5,92] With an increasing temperature, the Bloch wave has a higher possibility to be scattered, thus the mobility drops:[5,86]

$$\mu \propto T^{-n} \quad (n > 1) \tag{2.19}$$

The highly efficient band transport endows inorganic semiconductors with high mobility, e.g. electron mobility $\mu_e > 10^3\,\mathrm{cm^2\,V^{-1}\,s^{-1}}$ for single-crystalline Si.[121] In OSCs, only high-purity single crystals at low temperatures show band-like transport characteristics,[122] as Eq. (2.19) indicates.

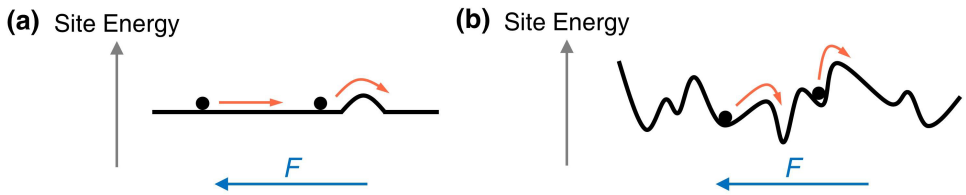

Figure 2.14 | Illustrations of Band Transport and Hopping Transport. (a) For band transport, delocalised electrons move within energy bands in the form of Bloch wave, and may be scattered by phonons, shown as the local energy bump. (b) For hopping transport, electrons are localised due to the dynamic- and static-disorder-induced rough energy landscape, so their transport is completed via site-to-site hopping. Red arrows indicate how electrons (block dots) move, and blue arrows represent the direction of the external electric field $\vec{F}$.

2.4.3.2 Hopping transport

A more common physical picture of charge transport in OSCs is that the effect of disorder prevails against the electronic coupling of neighbouring sites. Consequently, each charge carrier is localised in a specific site, and their transport is completed via incoherent site-to-site transfer.[5] This is the so-called hopping transport (Fig. 2.14(b)).

Concerning the disorder, it can be *dynamic* due to electron–vibration interactions, since their influence on transport parameters is time-dependent. Here the vibration can

be intramolecular (i.e. geometric relaxations) or intermolecular (i.e. phonons). Otherwise the disorder is *static*, that is, the effect caused by energetic and structural irregularities in OSCs, usually described by a time-independent Gaussian distribution (Eq. (2.7)). The hopping transport in which dynamic disorder dominates is referred to as *polaronic transport*, whereas when static disorder takes over, it becomes *disorder transport*. Note that by convention and as we shall adhere to in the following discussion, the term "polaronic effect" is used exchangeably with dynamic disorder, and the word "disorder" without an attribute is related to static disorder.

a. polaronic transport

The basic idea of polaronic transport is that the hopping of a charge carrier is associated with the distortion of the molecule and its environment (i.e. polaron hopping), thus an activation energy of geometric reorganisation is required. Such energy is found to be half the polaron binding energy E_{pol},[123] which is defined as the energy difference of a molecule before and after carrying a polaron. The analytical insight into polaronic transport was first provided by Holstein,[124,125] who derived the hopping rate by introducing the inter-site electronic coupling as a weak perturbation. This enables us to write down the mobility for polaronic transport:[5,126]

$$\mu = \frac{\pi q a^2 J^2}{3\hbar k T} \sqrt{\frac{\pi}{2 E_{\mathrm{pol}} k T}} \exp\left(-\frac{E_{\mathrm{pol}}}{2kT}\right) \tag{2.20}$$

where a is the intermolecular distance and J is the electronic transfer integral.

The μ–T relationship of polaronic transport can be inferred from Eq. (2.20). At relatively low temperatures, say, below ~600 K,[5] the exponential term is the determining factor, leading the mobility to follow an Arrhenius-type temperature dependence, i.e. $\ln(\mu) \propto -1/T$. This positive μ–T correlation is indicative of a phonon-activated hopping mechanism. At higher temperatures, the pre-exponential term dominates, hence $\mu \propto T^{-3/2}$. Its resemblance to Eq. (2.19) suggests that the electron–phonon coupling now functions as the scattering to the hopping, though the high temperature may cause

chemical decomposition of many OSCs.

b. disorder transport

In most conjugated polymers, the (static) disorder has a significant impact on charge transport. The disorder can be classified as *diagonal* and *off-diagonal*, which originates from expressing the Hamiltonian of the electron being transported in matrix notations.[92] The diagonal disorder represents the energy variation of transport sites, induced by both the statistical averaging effect (Section 2.2.3) and the conformation-related distribution of conjugation lengths.[5,126] The off-diagonal disorder reflects the electronic coupling variation of adjacent sites. This primarily arises from the non-uniform intermolecular spacing and orientation.[5,126]

One of the main consequences of diagonal and off-diagonal disorder is that electron hopping becomes asymmetric. In other words, the jumping rate w_{ij} from site i to site j is different from w_{ji}. Under this circumstance, the hopping process can be described by a probability function:[127]

$$\frac{\partial}{\partial t}p_i(t) = -\sum_{j\neq i} w_{ij}p_i(t)[1-p_j(t)] + \sum_{j\neq i} w_{ji}p_j(t)[1-p_i(t)] - \lambda_i p_i(t) \tag{2.21}$$

where $p_i(t)$ is the probability of site i being occupied by a charge carrier at time t, so $1-p_i(t)$ is the probability of an unoccupied site i; λ_i is the decay rate of the charge carrier at site i, as it has a finite lifetime before recombining with the other type of charge carrier or being discharged at the electrode. Now the task is to solve this equation, and its complexity picks the Monte–Carlo simulation as one of the most reasonable approaches. The resultant model is called the Gaussian disorder model (GDM), or the Bässler model, named after its developer.[128]

To perform Monte–Carlo simulation, one has to input two important parameters, namely the hopping rate w_{ij} and the density of transport sites.[126] For the former, the GDM adopts the Miller–Abrahams expression,[129] which assumes that a downward hopping in energy space is spontaneous and has a constant probability, whereas an upward transition

entails Arrhenius-type thermal activation. For the latter, a Gaussian DoS is used, as shown by Eq. (2.7). The simulation results indicate that[128]

$$\mu = \mu_0 \exp\left[-\left(\frac{2\sigma}{3kT}\right)^2\right] \times \begin{cases} \exp\left\{C\sqrt{F}\left[\left(\frac{\sigma}{kT}\right)^2 - \Sigma^2\right]\right\} & \text{for } \Sigma \geqslant 1.5 \\ \exp\left\{C\sqrt{F}\left[\left(\frac{\sigma}{kT}\right)^2 - 1.5^2\right]\right\} & \text{for } \Sigma < 1.5 \end{cases} \tag{2.22}$$

with σ and Σ being the energetic and positional disorder parameters, respectively, and C a numerical constant depending on the inter-site distance. Under low electric fields, the GDM predicts the μ–T relationship to be

$$\mu \propto \exp\left[-\left(\frac{T_0}{T}\right)^2\right] \tag{2.23}$$

Note that it does not exhibit an Arrhenius-type characteristic.

Following Bässler's pioneering work, researchers have proposed some revised models to improve the GDM, such as the correlated-GDM.[130] In addition, efforts have been made to combine the polaronic effect and disorder together to achieve unified models.[131,132] Nevertheless, similar to the case for charge injection, at the moment it would be too formidable a task to use a single model to describe the charge transport in OSCs universally and precisely.

2.4.3.3 Factors influencing charge carrier mobility

The transport models shown above may be more attractive to theorists. From the experimental side, it is helpful to grasp the idea of which factors can influence the mobility of an OSC and how. Here we shall present perhaps the most important four, namely crystallite orientation, temperature, electric field, and charge carrier density; the discussion mostly appertains to semicrystalline conjugated polymers. Trap states, as a much broader topic, will be separately discussed later.

a. crystallite orientation

Crystallites in semicrystalline conjugated polymers show strong charge transport anisotropy, thus their orientation distribution, also referred to as the *texture*,[133] can affect the mobility. The anisotropy comes from the different inter-site electronic coupling at the crystallographic a, b, and c directions of a crystallite (Fig. 2.15(a), in which P3HT is used as the model material).[134] The c axis parallels with the polymer backbone, along which the intrachain charge transport is highly efficient thanks to the presence of conjugation. In the b direction, π-orbitals on different molecules stack up, leading to an interchain overlap of electron wavefunctions. This π–π stacking allows charge carriers to delocalise between adjacent polymer chains, so the charge transport along the b axis is efficient as well, though inferior to the backbone direction. The a axis, however, is the direction where side chains, e.g. alkyl, alkoxy, and phenyl, pile up. These segments are attached to the polymer backbone to increase the solubility, and have an insulating nature due to the lack of conjugation. As a result, charge transport along this lamellar stacking direction encounters hindrance.

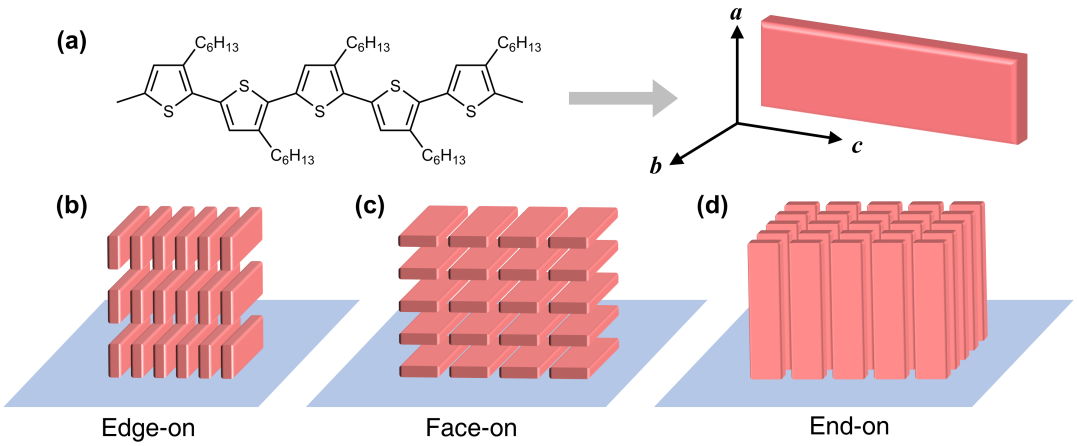

Figure 2.15 | Illustrations of Crystallite Orientations. (a) The chemical structure of the model semicrystalline conjugated polymer, P3HT (containing only five monomers for simplicity), and the way it can be represented by a brick-like cuboid with crystallographic directions a, b, and c. (b–d) The edge-on, face-on, and end-on orientations, respectively.

The way a crystallite orientates with respect to the substrate plane can be described

as edge-on, face-on, or end-on, depending on which axis is parallel with the plane (i.e. in-plane) and which is perpendicular to (i.e. out-of-plane).[134] If the π–π stacking is in-plane and the lamellar stacking is out-of-plane, then the crystallite is *edge-on* orientated (Fig. 2.15(b)). Conversely, the *face-on* orientation is characterised by the in-plane lamellar stacking and the out-of-plane π–π stacking (Fig. 2.15(c)). The *end-on* orientation, as a very rare case, requires the polymer backbone to be aligned in the out-of-plane direction, that is, polymer chains to stand up (Fig. 2.15(d)).

It now becomes evident that the horizontal charge transport, as in OFETs, can be facilitated by the edge-on orientation, whereas face-on orientated crystallites can assist the vertical charge transport in diodes, e.g. OLEDs and OPVs. Therefore, a feasible way to improve the mobility is to tune the edge-on-to-face-on ratio contingent upon the charge flowing direction. Although the end-on orientation is, in principle, the most advantageous texture for both in-plane and out-of-plane charge transport, the great difficulty in its construction excludes itself as a practical strategy for high mobility.

It is worth emphasising that the crystallite orientation is not the whole story; in a semicrystalline conjugated polymer thin film, these crystallites are embedded in an otherwise amorphous matrix (Section 2.2.1). It is the hopping transport in the non-crystalline region that restricts the overall mobility. Indeed, regulating the texture can affect the mobility to some extent, but a more effective way is to connect the crystallites with some tie chains, leading to a percolating network where amorphous regions are "short-circuited".[135] This can be achieved by using high-molecular-weight materials.[136]

b. temperature

The mobility–temperature dependence has been discussed along with the introduction of transport models, so here we just make a conclusive comment. For highly disordered materials such as conjugated polymers, the mobility increases with higher temperatures, although different models can give different mathematical expressions (Eqs. (2.20) and (2.22)). Correctness of these equations may be verified by experimental results; however, data from the relatively narrow temperature window, limited by the poor thermal

stability of polymers, can be fitted by both expressions reasonably well.[137]

c. electric field

The mobility for conjugated polymers is field-dependent, and generally shows the Poole–Frenkel-type behaviour in the range of 10^4–$10^6\,\mathrm{V\,cm^{-1}}$:[126,138]

$$\mu = \mu_0 \exp\left(\gamma\sqrt{F}\right) \tag{2.24}$$

Here the prefactor μ_0 is the zero-field mobility, and γ is a temperature-dependent factor that can be either positive or negative. For $\gamma > 0$, the mobility rises with an increasing electric field F, which can be understood from a trap-controlled charge transport process.[138] Under a high electric field, the activation energy of detrapping is reduced, hence more trapped charge carriers are released and able to participate in charge transport. However, γ can be negative as well, e.g. when $T > 250\,\mathrm{K}$ for P3HT.[139] This implies that the mobility will drop when the field becomes stronger. A possible explanation is that at low fields, charge carriers manage to find optimum pathways along which they have the minimum possibility to be captured by trap states. As the electric field becomes higher, they are forced to move directionally regardless of the presence of traps, so more charge carriers are captured and, concomitantly, the mobility decreases.[126]

d. charge carrier density

One of the best demonstrations of the mobility–charge-carrier-density dependence is given by Tanase et al.,[140] who observed that the mobility difference in OFETs and diodes based on the same conjugated polymer could be as large as three orders of magnitude, with the OFET mobility being higher. They ascribed this discrepancy to the distinct charge carrier density p in these two types of devices, and summarised that μ was barely affected for $p < 10^{16}\,\mathrm{cm^{-3}}$, whereas beyond this threshold μ would increase with a power law. The reasons are twofold. First, in the low-p regime, the energy of starting sites in the hopping process is independent of the charge carrier density, whereas the Fermi–Dirac statistics

in the high-p regime lead to an increase of this energy.[141] The result is that in the latter case, hopping requires less activation energy with an increasing p, so the mobility rises. Second, during charge transport the existence of energetic and structural defects can trap charge carriers and influence the mobility adversely. This can affect all charge carriers when p is low, but in the high-p regime only a portion of charge carriers are captured before all trap states are filled, so the remaining can go through a more efficient trap-free transport.[126]

This effect largely accounts for why the state-of-the-art OFETs with claimed mobility $\mu > 10^1\,\mathrm{cm^2\,V^{-1}\,s^{-1}}$ are contemporary with organic diodes whose typical mobility is $\sim 10^{-4}\,\mathrm{cm^2\,V^{-1}\,s^{-1}}$.[52,53] Interestingly, some conjugated polymers with purely amorphous microstructure were found to exhibit charge-carrier-density-independent mobility.[82]

2.4.3.4 *Trap states*

Traps are localised electronic states within the transport gap (Fig. 2.16),[142] and are donor-like (or acceptor-like) if they are in the vicinity of the HOMO (or the LUMO). Depending on their energy offsets to the HOMO or the LUMO, i.e. the trap depth E_t, traps can be shallow if E_t is a few kT, or deep if $E_\mathrm{t} \approx E_\mathrm{g}/2$. In OSCs, there are a number of possible mechanisms of trap formation.[142] For example, the dynamic and static disorder is the main source of intrinsic traps, and the so-called extrinsic traps can be induced by (intentionally or unintentionally) doping, interfacial effects, chemical reactions with water and oxygen, long-term electrical bias stress, to name but a few. Therefore, trap states are pervasive in OSCs.

The ubiquity of traps is, unfortunately, detrimental to charge transport, since charge carriers can be captured and held back. For shallow trap states, charge carriers may have chances of overcoming the small E_t by thermal fluctuation or the assistance of external electric fields, thereby being released. This trapping–detrapping process effectively slows down the charge transport. On the other hand, if charge carriers are caught by deep traps, they will have a negligible possibility to liberate themselves via thermal activation. The

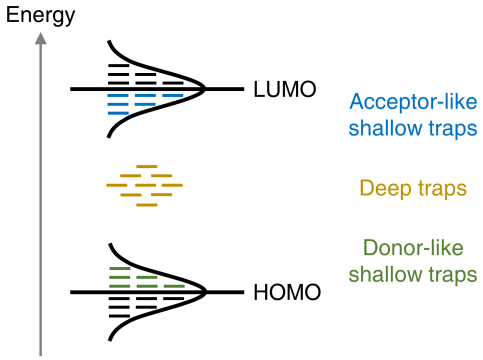

Figure 2.16 | Illustration of Trap States. The donor-like (or acceptor-like) shallow trap states close to the HOMO (or the LUMO) are represented by green (or blue) bars. Deep traps, located around the transport gap centre, are denoted by brown bars.

consequence is that deep traps function as recombination centres and reduce the lifetime of charge carriers. In all, the existence of traps decreases the mobility; what's more, it leads to the deviation of SCLC from the Mott–Gurney law (Eq. (2.9)).

When we discuss trap effects, Eq. (2.9) is usually referred to as the trap-free SCLC (TF-SCLC), and the current density is denoted as J_{TF}. Upon traps being considered, the simplest situation is that all trap states are shallow with the same depth E_{t}, resulting in the trap-filled-limit SCLC (TFL-SCLC):[143]

$$J_{\mathrm{TFL}} = \frac{9}{8}\varepsilon_0\varepsilon_{\mathrm{r}}\mu\theta\frac{V^2}{d^3} = \theta \cdot J_{\mathrm{TF}} \tag{2.25}$$

with θ being the ratio of the free charge carrier density (n_{f}) to the total charge carrier density, i.e. the sum of n_{f} and the trapped charge carrier density n_{t}:

$$\theta = \frac{n_{\mathrm{f}}}{n_{\mathrm{f}} + n_{\mathrm{t}}} = \frac{N}{N_{\mathrm{t}}}\exp\left(-\frac{E_{\mathrm{t}}}{kT}\right) \tag{2.26}$$

Here N and N_{t} represent the density of transport states and trap states, respectively. Note that all traps can be filled above a trap-filled-limit voltage V_{TFL}, and beyond V_{TFL} the TF-SCLC characteristics appear. Since $\theta < 1$, J_{TFL} is always smaller than J_{TF}, so an abrupt increase in current density at V_{TFL} is the key feature of TFL-SCLC. However,

this discrete distribution of shallow traps is the exception rather than the rule for most OSCs and mainly applies to single crystals.[144,145]

In most OSCs including conjugated polymers, E_t is not a fixed value but follows some distribution, among which the two most widely studied are the exponential and Gaussian distributions. For the former, the density of trap states (t-DoS) per unit depth range can be written as[146]

$$h(E_t) = \frac{N_t}{E_t^0} \exp\left(-\frac{E_t}{E_t^0}\right) \tag{2.27}$$

where E_t^0 is the mean trap depth. The resultant trap-controlled SCLC (TC-SCLC) is given by[146]

$$J_{TC} = N\mu q^{1-m} \left(\frac{\varepsilon_0 \varepsilon_r m}{N_t(m+1)}\right)^m \left(\frac{2m+1}{m+1}\right)^{m+1} \frac{V^{m+1}}{d^{2m+1}} \tag{2.28}$$

Here the key parameter $m = E_t^0/kT > 1$. Compared with J_{TF} (Eq. (2.9)), the exponent of voltage in this equation is always bigger than 2, suggesting a much steeper J–V dependence. As the voltage rises, traps will eventually be filled, and consequently J_{TC} will merge with J_{TF}. This takes place above the trap-controlled voltage V_{TC}:[146]

$$V_{TC} = \frac{qd^2}{\varepsilon_0 \varepsilon_r} \left[\frac{9}{8} \cdot \frac{N_t^m}{N} \left(\frac{m+1}{m}\right)^m \left(\frac{m+1}{2m+1}\right)^{m+1}\right]^{\frac{1}{m-1}} \tag{2.29}$$

For the Gaussian distribution, the t-DoS can be described by Eq. (2.7), provided that the density of trap states N_t is multiplied to both sides. However, a unified analytical model for the current density, akin to Eq. (2.28), is not possible;[86] instead, all existing equations have specific validity conditions.[147] In practice, it is acceptable to assume the t-DoS of conjugated polymers to be exponential if we only care about the J–V relationship rather than the detailed trapping physics. This approximation is not simply motivated by the mathematical convenience in dealing with the exponentially distributed t-DoS, but more fundamentally owing to the generation of indistinguishable J–V curves when two distributions with appropriate parameters are used, according to both theoretical simulation[148] and experimental results.[149]

2.5 Device Physics

2.5.1 Organic light-emitting diodes (OLEDs)

Equipped with the understanding of intra- and inter-molecular electronic and optoelectronic processes, we are now ready to discuss how OSC devices work, with OLEDs as the starting point. The simplest OLED consists of a thin emission layer (EML) of ~100 nm sandwiched between two electrodes, one of which is transparent so that the emitted photons can escape from the device. Normally this electrode is the indium tin oxide (ITO) anode (Fig. 2.17(a)). Under an external electric field that is strong enough to drive the device, an OLED can operate through four steps (Fig. 2.17(b)):[86]

1. *Charge injection.* Electrons and holes are injected from the cathode and the anode, respectively (Section 2.4.2);
2. *Charge transport.* Injected electrons and holes move towards each other in the EML under the applied electric field (Section 2.4.3);
3. *Electron–hole recombination and exciton generation.* During the transport in the EML, electrons and holes have the possibility to recombine and form excitons (Section 2.3.1);
4. *Exciton radiative decay and light emission.* Some excitons can decay in a radiative way with photons emitted from the transparent electrode (Section 2.1.5.1).

On the basis of this sandwich structure, it is now a common practice to insert some interlayers between electrodes and the EML in order to promote the injection of one type of charge carriers and/or block the other.[5] This is achieved by choosing interlayer materials with proper energy levels. For example, a hole injection/transport layer (HIL/HTL) with its HOMO lying between the anode's WF and the active material's HOMO can facilitate hole injection due to the graded energy levels, and an electron injection/transport layer (EIL/ETL) works in an analogous way. Sometimes the HIL/HTL can also function as the electron blocking layer (EBL) if its LUMO is very much shallower than the active material's, so that the injected electrons are unlikely to leave the EML

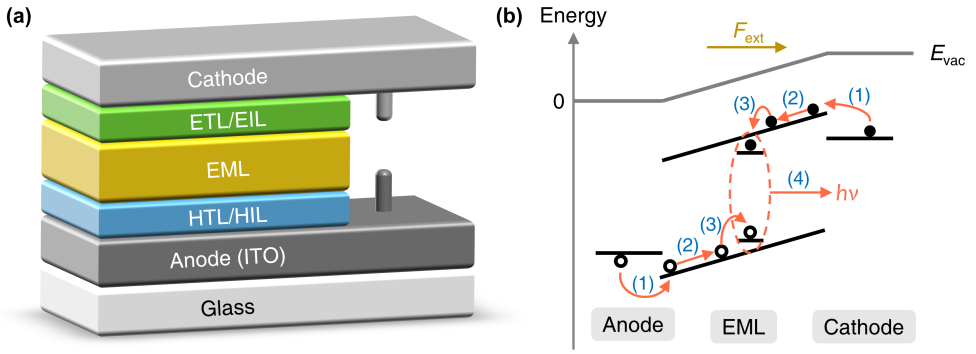

Figure 2.17 | Schematic Device Structure and Working Principles of OLEDs. (a) Illustration of the multilayer structure. (b) Energy level diagram showing the four steps of OLED operation (see the main text for details). Black dots and circles represent electrons and holes, respectively. For simplicity, the ETL/EIL and HTL/HIL are omitted.

before recombining with holes. Similarly, an EIL/ETL can be a hole blocking layer (HBL) as well. This multilayer structure is illustrated in Fig. 2.17(a).

2.5.2 Organic solar cells (OPVs)

The most common OPVs nowadays contain a BHJ active layer with nanoscopically well-mixed electron donor (D) and acceptor (A) materials that differ in their energy levels. Two electrodes are attached to the BHJ layer, and one of them, usually the ITO anode, needs to be transparent to allow light absorption (Fig. 2.18(a)). When electrodes are connected through an external circuit and the device is illuminated, light can be converted to current via five steps (Fig. 2.18(b)):[86]

1. *Light absorption and exciton generation.* Photons with higher energies than E_{opt} can be absorbed by active materials, so some of their molecules are in excited states, i.e. excitons are created (Sections 2.1.5 and 2.3.1). The generated electron–hole pair is usually located on the same molecule (Frenkel excitons);
2. *Exciton diffusion.* Most excitons (ideally all) can diffuse to the D–A interface via energy transfer within their lifetime before any decay happens (Section 2.3.2);
3. *Charge transfer.* At the D–A interface, the Frenkel exciton on a donor molecule may be converted to a CT exciton by transferring its LUMO electron to the LUMO

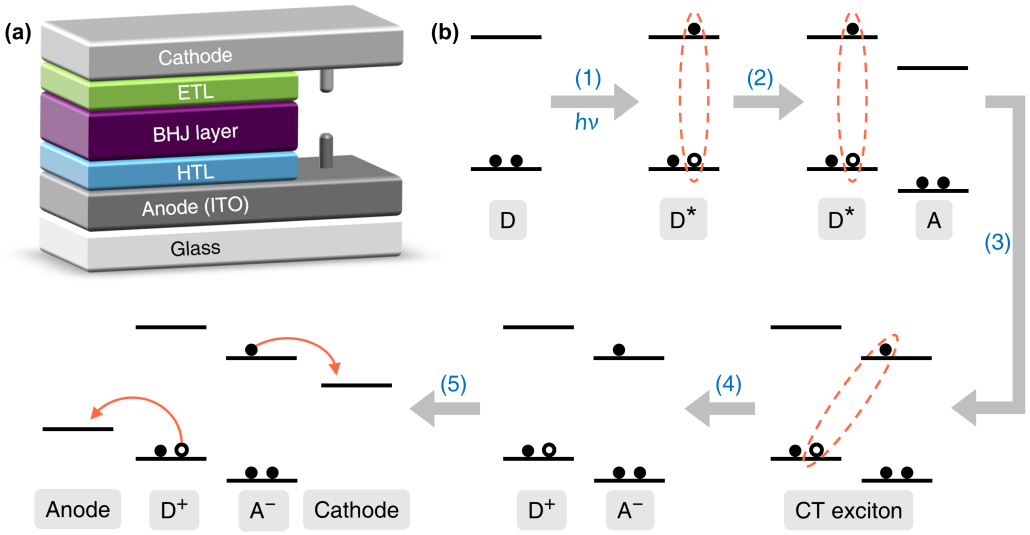

Figure 2.18 | Schematic Device Structure and Working Principles of OPVs. (a) Illustration of the multilayer structure. (b) Schematic diagram showing the five steps of OPV operation (see the main text for details). Black dots and circles represent electrons and holes, respectively.

of an adjacent, unexcited acceptor molecule (vice versa for an excited acceptor molecule). This charge transfer process can occur as long as both kinetic and thermodynamic conditions are fulfilled.[5] Kinetically, the difference in EA (ΔEA) between the donor and acceptor should be larger than the energy required to move the electron away from the hole in the donor molecule against the Coulomb attraction (E_{Cou}). Thermodynamically, the energy of the formed CT exciton, $E_{\mathrm{CT}} = \mathrm{IP_D} - \mathrm{EA_A} - E_{\mathrm{B,CT}}$, with $E_{\mathrm{B,CT}}$ being the CT exciton binding energy (around 0.5 eV for CT excitons with 1 nm electron–hole separation),[150] ought to be smaller than that of the Frenkel excitons on both donor and acceptor molecules, that is, $E_{\mathrm{opt,D}}$ and $E_{\mathrm{opt,A}}$. Otherwise, if $E_{\mathrm{CT}} > E_{\mathrm{opt,D}}$, the charge transfer will not happen at all; if $E_{\mathrm{opt,D}} > E_{\mathrm{CT}} > E_{\mathrm{opt,A}}$, there will only be energy transfer yet no charge transfer;[5]

4. *CT exciton dissociation and charge generation.* The CT excitons can then dissociate into electrons and holes that are not electrostatically correlated, hence free charge carriers emerge. The activation energy of this process comes from $\Delta\mathrm{EA} - E_{\mathrm{Cou}}$,

which then becomes the kinetic energy of electrons and holes so that they can get rid of the Coulomb interactions.[151] Therefore, charge transfer and CT exciton dissociation may be regarded as one step, since both are activated by ΔEA;[86]

5. *Charge transport and collection.* The photogenerated free charge carriers are then transported in the active layer, and some of them, if not being trapped or recombined, are finally collected by respective electrodes. There are two driving forces for charge transport in the absence of an external electric field.[86] The first is the internal built-in field resulting from the difference in WF between the anode and cathode (Section 2.4.2.1), which gives rise to the drift photocurrent. Second, the concentration of free charge carriers at the D–A interface is higher than that at electrodes. This concentration gradient forces charge carriers to move away from the interface and produces the diffusion photocurrent. In BHJ OPVs, what additionally requires for efficient charge transport is the sufficient percolation pathways to ensure that electrons (or holes) can move within the acceptor (or the donor) material before being collected.

The working principles of OPVs explain why the morphology control for BHJ active layers is so crucial. For one thing, well-mixed D:A nano-domains are essential for improved interface area and more dissociated CT excitons. This accounts for the superiority of the BHJ over the planar heterojunction. For another, continuous material networks are important for efficient charge transport. Besides, similar to OLEDs, interlayers are widely used in OPVs. The difference is that here the main purpose is not for charge injection (since there is no injection process at all) but for selectively and effectively extracting charge carriers from the BHJ layer.

2.5.3 Organic field-effect transistors (OFETs)

An OFET has (at least) three electrodes, namely the source, the drain, and the gate, therefore its working principles are different from diodes. Apart from electrodes, an OFET further contains an organic semiconducting active layer (contact with the source

and drain) and an insulating dielectric layer (contact with the gate). The way these components are structured determines the configuration of an OFET (Fig. 2.19(a)).

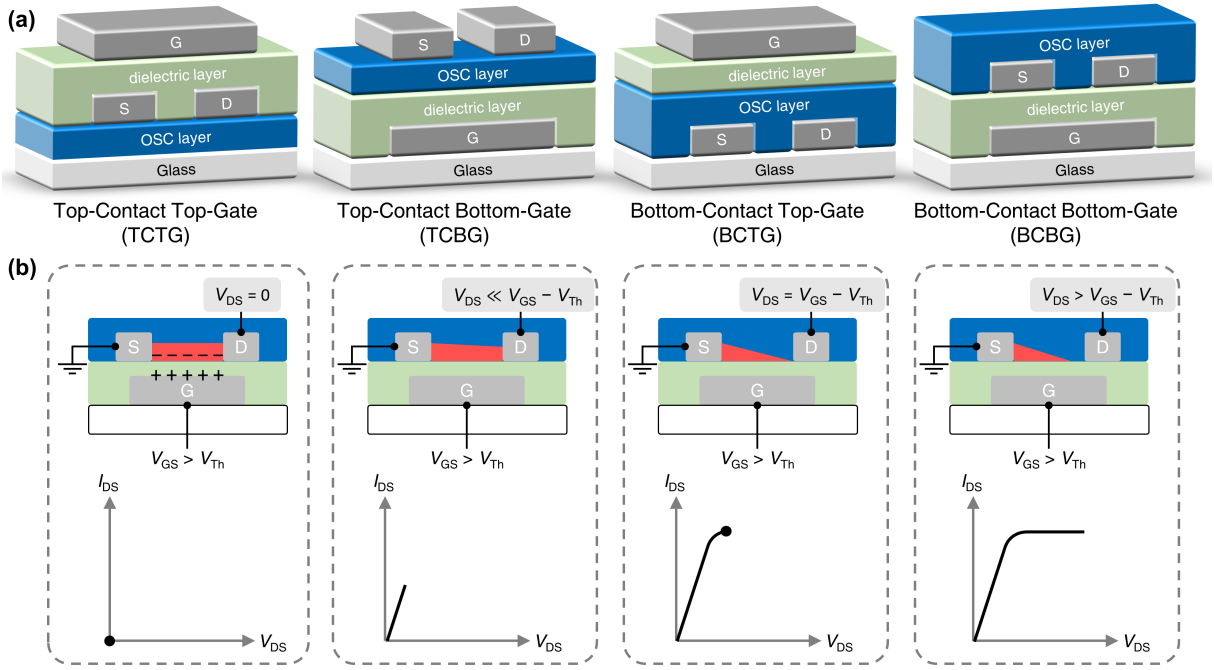

Figure 2.19 | Schematic Device Structure and Working Principles of OFETs. (a) Illustrations of different OFET configurations. (b) Illustrations of the mobile charge carrier density (red areas) and the drain–source current I_{DS} of a bottom-contact bottom-gate OFET when different drain–source voltages V_{DS} are applied, assuming V_{GS} is positive.

The main function of OFETs is to control the drain–source current I_{DS} by varying the drain–source voltage V_{DS} and the gate–source voltage V_{GS}. During operation, the source is grounded ($V_S = 0$) and acts as the charge injection electrode. If, for example, a positive V_{GS} is applied, the dielectric layer will be polarised, inducing electrons to be injected from the source and uniformly accumulated at the OSC–dielectric interface (Fig. 2.19(b), leftmost). These free charge carriers are responsible for the formation of I_{DS}. In reality, however, a small V_{GS} is not able to create mobile charges due to the injection barrier from the source to the OSC layer and the intrinsic traps that need to be filled first.[86,152] These result in a threshold voltage V_{Th}, and the effective gate voltage becomes $V_{GS} - V_{Th}$.

When $V_{GS} - V_{Th} > 0$, electrons are injected and distributed between the source and drain, that is, within the channel, and can move if a positive V_{DS} is applied. As long as

$V_{DS} \ll V_{GS} - V_{Th}$, electrons are almost uniformly distributed in the channel, and I_{DS} is proportional to V_{DS} (Fig. 2.19(b), second left). In this *linear regime*, the OFET can be regarded as a V_{GS}-controlled variable resistor that obeys Ohm's law.[153] If V_{DS} increases to be equal to $V_{GS} - V_{Th}$, the area beside the drain will be depleted of free charge carriers in that the drain voltage cancels out the effective gate voltage. This situation is referred to as the pinch-off of the channel (Fig. 2.19(b), second right). Further increasing V_{DS} only leads to the movement of the pinch-off point towards the source, but I_{DS} remains unchanged, which is the characteristic of the *saturation regime* (Fig. 2.19(b), rightmost).

The working principles of OFETs indicate that the charge injection and transport processes take place in a very narrow region (~5 nm)[5,86] in the OSC layer next to the OSC–dielectric interface. As a result, the charge carrier density in OFETs is substantially higher than that in diodes, which is one of the main reasons for the mobility difference in these two types of devices (Section 2.4.3.3). Moreover, any factor that affects interface properties, e.g. device configurations, layer deposition protocols, and the chemical nature of dielectric materials, can contribute to a significant variance in I_{DS}.

2.6 Strategies for High-Performance Devices

As the conclusion of this theory chapter, we shall briefly present some strategies for high-performance OSC devices from both the material and device sides. Some of these strategies will be reflected in the following chapters.

2.6.1 Material side: structure–property relationships

From the perspective of polymer physics, polymer materials can exhibit hierarchical structures at different length scales.[154,155] This very fact reveals the richness of polymers' structural characteristics, motivating us to fine-tune the multilevel structures of conjugated polymers for desired material properties and OSC device performance. Below we shall introduce four kinds of structures in order of length scales, and show how different structural features can be regulated for device optimisation.

The primary structure of conjugated polymers is intramonomer at the scale of atoms or chemical groups. This mainly refers to the chemical structures, including composition, configuration, and monomer copolymerisation. For example, changing the composition of a polymer donor, poly[[4,8-bis[5-(2-ethylhexyl)-4-fluoro-2-thienyl]benzo[1,2-*b*:4,5-*b*′]dithiophene-2,6-diyl]-2,5-thiophenediyl[5,7-bis(2-ethylhexyl)-4,8-dioxo-4*H*,8*H*-benzo[1,2-*c*:4,5-*c*′]-dithiophene-1,3-diyl]-2,5-thiophenediyl] (PM6), by replacing its fluorine atoms with chlorine leads to a smaller IP and concomitantly higher open-circuit voltage and efficiencies for OPVs.[156] Regarding configuration, which is the spatial arrangement of side groups, the regioregularity of P3HT has been shown to be relevant to its absorption spectrum and hole mobility.[157] In addition, the highly-efficient and widely-used D–A copolymer donors in OPVs might be the best illustration of copolymerisation. The primary structure fundamentally determines the electronic and optoelectronic properties of conjugated polymers, and is the basis of other types of structures at higher levels. With the help of chemists, we are now, to some extent, capable of designing and synthesising new materials with expected properties.[158]

The secondary structure is intermonomer or intramolecular, and is mainly represented by the conformation of conjugated polymers. The conformation specifies the spatial relationship between neighbouring chain segments that may change due to the rotations about C−C single bonds.[4] In the famous light-emitting polymer, poly(9,9-dioctylfluorene) (PFO), its intermonomer torsion angle can change from ~135° to 180°, resulting in a transition from the glassy phase to the chain-extended planar β-phase.[159] The latter shows abundant photophysical[160] and spectroscopic properties,[161] and is advantageous to highly efficient blue OLEDs with excellent spectral stability,[162] as well as many other applications.[163,164] The ability to exhibit various conformations under different environments and processing conditions is a unique feature of polymer materials because of their chain flexibility. Therefore, exploiting the secondary structure of conjugated polymers can give rise to novel pathways of device optimisation.

The tertiary structure is relevant to intermolecular packing and assembly, such

as crystallinity, texture (i.e. crystallite orientation distribution), liquid-crystalline, and chain alignment. As stated in Section 2.4.3.3, crystallinity and crystallite orientation have impacts on charge transport and the resultant mobility. For instance, in an n-type semicrystalline conjugated polymer poly[[*N*,*N*′-bis(2-octyldodecyl)-naphthalene-1,4,5,8-bis(dicarboximide)-2,6-diyl]-*alt*-5,5′-(2,2′-bithiophene)] (N2200), crystallites were found to mainly adopt the face-on orientation.[165] Surprisingly, this material is conducive to top-gate OFET operation and can show high field-effect electron mobility of ~0.45 $cm^2 V^{-1} s^{-1}$.[166] Upon careful structural examination, the answer lies in a very thin edge-on surface layer covering the face-on bulk.[167] This unusual character makes N2200 suitable for both diode and OFET applications. Besides, conjugated polymers in the liquid-crystalline phase and/or after chain alignment can exhibit strong anisotropy in (opto)electronic properties, enabling high-mobility OFETs[168,169] and polarised OLEDs.[170,171] The tertiary structure goes beyond single polymer chains to the condensed phase, hence it has a close connection with physical processes, especially charge transport, happening in OSC devices.

Finally, the quaternary structure may be regarded as an inter-component character for conjugated polymer blends. This is the particular case for the BHJ active layer in OPVs, in which the domain size and interpenetration, phase separation, and vertical composition distribution are all important structural features of the D–A mixture, directly dictating the resultant OPV performance.[172,173]

2.6.2 Device side: interface engineering

Most OSC devices are composed of stacked layers (Figs. 2.17, 2.18, and 2.19). Therefore, judicious engineering of the interface plays a crucial role in device optimisation. This can be realised by inserting functional interlayers, or by controlling the properties of the surface onto which the active layer is deposited, as discussed below.

The use of interlayers, such as HTLs and ETLs, has been introduced in Section 2.5.1, and the main purpose is to change the energy level of electrodes so that they can

match well with active materials' to minimise the charge injection/extraction barrier. These interlayers can be conjugated polymers,[174] polyelectrolytes,[175] small molecules,[176] inorganic materials,[177] and interestingly, self-assembled monolayers (SAMs).[178] SAM molecules are characterised by anchoring groups that can form strong chemisorption onto metal surfaces. For example, the thiol group (−SH) can attach to Au robustly,[179] and phosphonates have a good affinity to transparent conducting oxides such as ITO.[180] Since SAM molecules can exhibit a wide range of molecular dipoles, their adsorption on electrodes can modify the latter's WFs to a large extent. Another very important feature of SAMs is that their monolayer nature has little hindrance to charge transport, even if the SAM molecules themselves are insulating, as charge carriers can tunnel through such a thin layer.[181] As a result, SAMs have been successfully incorporated into OSC devices to ensure a quasi-Ohmic metal–OSC contact.[178,182]

Finally, concerning surface properties, we would like to emphasise two of them, namely the roughness and the surface energy. First, a rough surface is generally unfavourable to OSC device lifetime, since it can lead to high local electric fields and shorts. In OLEDs, for example, such roughness-induced local failure can be observed as dark spots on the EML.[183] Therefore, a smooth surface is usually desirable. Second, the surface energy can affect both the solution-processability and the texture of conjugated polymers. For the former, the formation of uniform thin films requires the substrate surface energy to be higher than the solution's, thus dewetting can be avoided. This accounts for the common practice of treating ITO substrates in UV-ozone or oxygen plasma atmosphere to increase their surface energies, and adding surfactants into gravure-printing inks to lower their surface energies and improve the thin-film quality.[184] For the latter (crystallite orientation), it has been shown that low-energy surfaces favour the formation of edge-on orientated crystallites, while the face-on orientation is promoted when the substrate surface energy increases.[134,185,186] This relationship allows us to regulate the texture and mobility of semicrystalline conjugated polymers via modifying the surface energy of the layer underneath, a strategy already manifesting its effectiveness in OPV optimisation.[187]

Chapter 3

Experimental Methods

In this chapter, we shall first present general sample fabrication procedures (Section 3.1), and then discuss the main principles of characterisation techniques used in the following chapters (Sections 3.2, 3.3, 3.4, and 3.5). Finally, descriptions of device performance measurements are given in Section 3.6. Further experimental details will be shown along with the main text of Chapters 4, 5, and 6. Unless stated otherwise, all sample preparation, device fabrication, property/performance characterisation, and data analysis were completed by the author.

3.1 Sample Fabrication

The sample fabrication procedures generally contain substrate cleaning and layer deposition. The substrate used in our studies includes pre-patterned ITO on glass, bare soda–lime glass, fused silica, and silicon, depending on the purposes of experiments and how samples/devices will be characterised. All substrates were cleaned in ultrasonic baths first with acetone and then isopropanol for 10 min each, followed by UV-ozone treatment for 10 min in an Ossila E511 UV-ozone cleaner.

Layers in samples and devices can be deposited by spin-coating or thermal evaporation. For the former (Fig. 3.1(a)), the substrate is placed on the spin-coater chuck and is held in place by vacuum. Then drops of solutions drip onto the substrate, which rotates with the chuck at a certain speed, measured in units of revolutions per minute (rpm), spreading the solution and spinning the excess solution off. Meanwhile, airflow above the substrate makes the solvent quickly evaporated, so a solid thin film is obtained. Normally the

resulting layer is then thermally annealed to completely remove the solvent residue. Since in our studies, OSCs are sensitive to oxygen and moisture, their thin films were spin-coated in a nitrogen-filled glovebox using a Specialty Coating Systems G3P-8 spin-coater. Otherwise for solution-processed interlayers, a Laurell WS-650-MZ-23NPPB spin-coater in the fume hood was used.

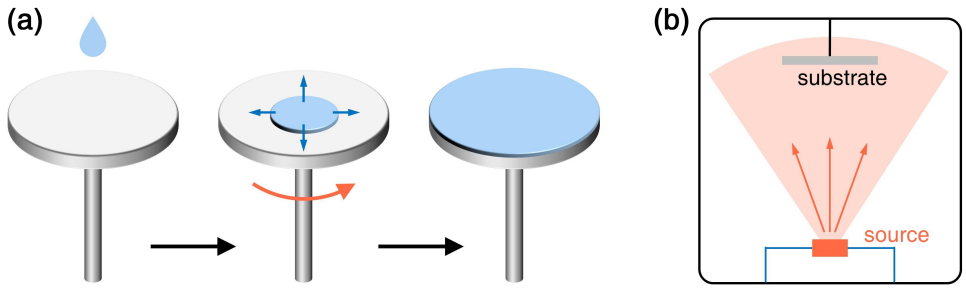

Figure 3.1 | Illustrations of Spin-Coating and Thermal Evaporation. (a) During spin-coating, the solution is dropped onto the substrate, which then rotates to spread the solution and spin the excess solution off. A thin film is obtained after solvent evaporation. (b) During thermal evaporation, the source material is heated electrically in a chamber under high vacuum, and its vapour is deposited on the substrate positioned above to form thin films.

Thermal evaporation (Fig. 3.1(b)) is a physical vapour deposition (PVD) process, during which the source material is heated electrically under high vacuum to a temperature higher than its melting or sublimation point using a resistive heat support. The vapour of the source material is then deposited onto the substrate located above to form thin films. By adjusting the heating power, the deposition rate (in $\text{Å}\,\text{s}^{-1}$) can change as needed. In our studies, metal electrodes and some inorganic interlayers were evaporated in an LC Technology high-vacuum chamber (pressure $p < 10^{-6}\,\text{Pa}$, source–substrate distance $d \approx 60\,\text{cm}$) controlled by an Inficon SQC-310 thin film deposition controller. The chamber is placed inside the glovebox, so the spin-coated active layer can be transferred to the evaporator with no need to contact with air.

3.2 Energy Level Characterisation

3.2.1 Ionisation potential (IP): air-photoemission spectroscopy (APS)

Air-photoemission spectroscopy (APS) is based on the photoelectric effect. For the measurement, the sample is placed into the setup in air, and a beam of monochromatic light with varying energies is incident on the sample. The detector then records the photocurrent between the sample surface and a metal tip just above, so the relationship between the photoelectron yield and the incident photon energy is obtained. According to Fowler's analysis of photoemission,[188] the onset energy of the cube root of the photoelectron yield corresponds to the IP of a semiconductor.[189] Compared with the more commonly used ultraviolet photoemission spectroscopy (UPS)[190,191] which requires high vacuum, APS is conveniently performed in ambient pressure, closer to the actual device fabrication and working conditions.

In Chapter 5, APS was employed to determine the IP of different CuSCN interlayers on a KP Technology APS04 system in Prof. Ji-Seon Kim's group in Imperial College London with the help of Dr. Saurav Limbu. The tip potential was set to be 10 V, and data analysis was completed on APS04 software by Dr. Saurav Limbu.

3.2.2 Optical gap (E_{opt}): the Tauc plot

For inorganic semiconductors such as CuSCN, one of the methods that can accurately extract their optical gap E_{opt} was given by Tauc et al.[192] In detail, after the photon-energy-dependent absorption coefficient α is obtained from the sample's absorbance spectrum (Section 3.3.1), a plot of $(\alpha h\nu)^n$–$h\nu$ can be drawn, with $h\nu$ being the incident photon energy and n a constant: $n = 2$ for semiconductors with direct band gaps, and $n = 1/2$ for indirect.[12] The onset photon energy of $(\alpha h\nu)^n$ is the E_{opt} of the sample.

The Tauc plot was used to determine the E_{opt} of different CuSCN interlayers in Chapter 5. Details of the absorbance measurement are given in Section 3.3.1.

3.2.3 Electron affinity (EA)

It should be clarified that the common practice of determining the OSC's EA by subtracting the E_{opt} from its IP is not correct since the exciton binding energy E_{B} fails to be considered (Eq. (2.6)). Alternatively, EA can be measured by inverse photoelectron spectroscopy (IPES),[191] although the relevant equipment is very uncommon in most labs. In passing, another popular way to acquire IPs and EAs of OSCs, cyclic voltammetry (CV), requires much caution for data interpretation. The conversion from the measured redox potentials to the IP and EA can be accomplished by different approaches, and none of them is universally applied to OSCs, leading to poor results comparability.[63] Besides, most CV measurements are performed in OSC solutions, where the solvation free energy is difficult to predict and quantify, resulting in the deviation from thin-film energy levels.[5,74]

In Chapter 5, we try to obtain the EA of CuSCN, an inorganic semiconductor, in which E_{B} is usually negligible (a few meV).[63] This allows us to approximate its E_{g} to E_{opt}, and calculate its EA by EA $\approx$ IP $- E_{\mathrm{opt}}$. We note that excitonic effects on some inorganic alkali halides[12] and low-dimensional semiconductors[193] were previously reported, but as far as we know, no pertinent studies have been explicitly performed on CuSCN, though the question on whether it has some excitonic nature was once raised.[194]

3.2.4 Work function (WF): the Kelvin probe

The WF of metals and (inorganic) semiconductors can be measured using the Kelvin probe. A vibrating metallic tip with a known WF is placed very close above the sample so that electron tunnelling can occur. Hence the tip and the sample surface are electrically connected, though physically non-contact, enabling their Fermi levels to equilibrate. As a result, their local vacuum levels exhibit an energy difference, which can be compensated by an external potential V_{CPD} (here "CPD" denotes "contact potential difference"). The sample's WF can be calculated as:[195]

$$\mathrm{WF}_{\mathrm{sample}} = \mathrm{WF}_{\mathrm{tip}} + \frac{V_{\mathrm{CPD}}}{q} \tag{3.1}$$

In Chapters 5 and 6, WFs of CuSCN interlayers and SAM-modified Au electrodes, respectively, were determined on a KP Technology KP020 Kelvin probe with a 2-mm-diameter gold disk tip in Prof. Henry Snaith's group in the Department of Physics. Measurements were performed in air, and the $\mathrm{WF}_{\mathrm{tip}}$ was calibrated using a highly orientated pyrolytic graphite (HOPG) reference whose WF is 4.650 eV. For each sample, over 50 data points of V_{CPD} were recorded and averaged.

3.3 Optical Property Characterisation

3.3.1 Absorption

When a beam of light is incident on a thin-film sample, phenomenologically it can be absorbed by, reflected from, or transmitted through the sample. The reflection and the transmission can further be classified as specular and diffuse, depending on the directional relationship between the reflected/transmitted light and the incident (Fig. 3.2).[196] Their respective intensities relative to that of the incident light, all of which are wavelength λ-dependent, are called the absorptance (or more commonly, the absorption) $A(\lambda)$, the reflectance $R(\lambda)$, and the transmittance $T(\lambda)$. Decidedly,[196]

$$A(\lambda) + R(\lambda) + T(\lambda) = A(\lambda) + R_{\mathrm{S}}(\lambda) + R_{\mathrm{D}}(\lambda) + T_{\mathrm{S}}(\lambda) + T_{\mathrm{D}}(\lambda) = 1 \tag{3.2}$$

where subscripts "S" and "D" represent "specular" and "diffuse", respectively. Therefore, in order to obtain the absorption spectrum of a sample, both the total reflectance $R(\lambda) = R_{\mathrm{S}}(\lambda) + R_{\mathrm{D}}(\lambda)$ and the total transmittance $T(\lambda) = T_{\mathrm{S}}(\lambda) + T_{\mathrm{D}}(\lambda)$ spectra need to be measured.

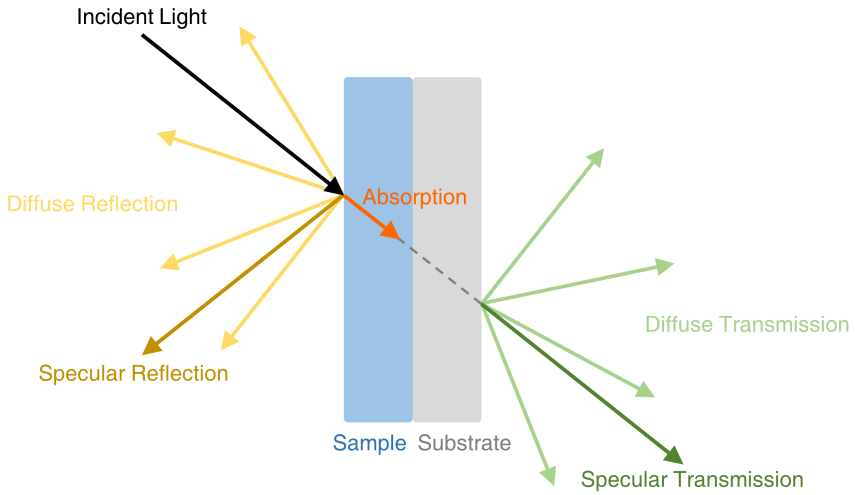

Figure 3.2 | Illustration of Absorption (red), Reflection (brown), and Transmission (green). Both specular (in deeper colours) and diffuse (in lighter colours) reflection and transmission are shown. Note that here the refraction at interfaces is ignored.

Another relevant concept is the absorbance (or optical density) $a(\lambda)$, defined as[196]

$$a(\lambda) = -\lg(T(\lambda)) \tag{3.3}$$

The absorbance $a(\lambda)$ is correlated with the absorption coefficient $\alpha(\lambda)$ by[196]

$$\alpha(\lambda) = \frac{a(\lambda)\ln 10}{d} \approx \frac{2.303a(\lambda)}{d} \tag{3.4}$$

where d is the sample thickness. It is worth emphasising that $a(\lambda)$ and $\alpha(\lambda)$ have no relationship with $A(\lambda)$, since their extraction is irrelevant with $R(\lambda)$ and only requires $T(\lambda)$. This is because these two physical quantities were originally defined to describe the absorption in solutions, where the reflection is insignificant.[197] In other words, the absorbance and the absorption coefficient cannot provide complete descriptions of a thin-film sample's absorption properties. They should only be used in limited cases, e.g. the Tauc plot (Section 3.2.2).

From the discussion above, $R(\lambda)$ and/or $T(\lambda)$ spectra are the data we need to derive $A(\lambda)$ or $\alpha(\lambda)$. During their measurements, the thin-film sample has to be deposited on a

transparent substrate, which, in principle, has no influence on $R(\lambda)$ in that the reflection occurs at the sample surface. However, the substrate we usually use in the near UV and the visible spectral range (250–800 nm), the fused silica, is not entirely transparent and can exhibit an absorption of ~5 %. Therefore, the measured transmittance $T_{\mathrm{meas}}(\lambda)$ has to be normalised by the substrate transmittance $T_{\mathrm{sub}}(\lambda)$ to obtain the sample transmittance $T(\lambda)$:

$$T(\lambda) = \frac{T_{\mathrm{meas}}(\lambda)}{T_{\mathrm{sub}}(\lambda)} \tag{3.5}$$

Note that this treatment ignores the possible reflection at the sample–substrate interface.

The collection of $R(\lambda)$ and $T(\lambda)$ spectra is completed on a ultraviolet–visible–near infrared (UV–vis–NIR) spectrometer. Take the one we used in this thesis as an example; radiation from the light source, be it a deuterium lamp for the UV range or a halogen lamp for the vis–NIR range, passes through the monochromator to achieve the desired wavelength, and is then separated into a reference and a sample beam. The former serves as the intensity reference, and the latter interacts with the sample. Their intensities are recorded by a photomultiplier tube, so the reflectance or transmittance at this wavelength can be determined. Repeating these steps for all wavelengths allows us to construct a spectrum. In order to collect the reflected or transmitted light at all angles, i.e. the total reflectance and transmittance, an integrating sphere, containing diffusely reflective inner coating and small holes for light entrance and exit, is used to redistribute the light inside, so the intensity becomes angle-independent. By detecting the photon number N_Ω over a solid angle Ω at the exit port, we can infer the total number N of photons in the sphere to be[198]

$$N = \frac{4\pi}{\Omega} N_\Omega \tag{3.6}$$

Therefore, $R(\lambda)$ or $T(\lambda)$ spectrum can be acquired by placing the integrating sphere at a position just before or after the beam hitting the sample, respectively.

In Chapter 4, absorption spectra of glassy and β-phase 90F8:10BT thin films were obtained using Eqs. (3.2) and (3.5). In Chapter 5, absorption coefficients of different

CuSCN interlayers were derived from Eqs. (3.3), (3.4), and (3.5), based on which Tauc plots can be yielded (Section 3.2.2). Both $R(\lambda)$ and $T(\lambda)$ spectra were measured in air on a PerkinElmer Lambda 1050 UV–vis–NIR spectrometer, with a 100-mm-diameter integrating sphere accessory coated with the Spectralon material.

3.3.2 Emission

3.3.2.1 Steady-state photoluminescence (SSPL)

PL describes the light emission of a material excited by another beam of light. For most fluorescent materials, this process happens in the nanosecond range,[5] so SSPL refers to the situation where the illumination duration is longer than several nanoseconds, usually continuous, so the material's emission spectrum can be obtained.

SSPL measurements are carried out on a spectrofluorometer. For the one we used, the high-intensity light source, a xenon lamp, shines light onto an excitation monochromator to select the excitation wavelength. Then photons with the same energy bombard the sample to induce the $S_1 \leftarrow S_0$ transition, followed by a radiative decay during which the emitted photons are directed to an emission monochromator. Changing the rotation angle of the grating inside this second monochromator enables the photomultiplier tube behind to detect the emission intensity at different wavelengths. Thus an SSPL spectrum is achieved.

In Chapter 4, SSPL spectra of glassy and β-phase 90F8:10BT thin films were collected in air using a HORIBA FluoroMax-4 spectrofluorometer, with the excitation wavelength being 380 nm.

3.3.2.2 Time-resolved photoluminescence (TRPL)

A TRPL measurement involves exciting the sample by a fast light pulse (laser in most cases) whose duration is shorter than the radiative decay time and is usually in the picosecond range. The result is a decay curve, in which the PL intensity I is plotted

against the time t after the excitation, and can be fitted by[5]

$$I(t) = I_0 \exp\left(-\frac{t}{\tau}\right) + C \tag{3.7}$$

Here τ is the exciton lifetime, and I_0 and C are constants. Note that this single exponential equation applies to materials with only one radiative decay channel, and more exponential terms are needed to describe a multi-channel radiative decay.

In TRPL measurements, the high temporal resolution entails a specially designed signal detection technique, e.g. time-correlated single photon counting (TCSPC). The sample is excited by a relatively weak laser pulse, so less than one photon is detected per excitation period. A timer records the time between the arrival of the laser pulse at the sample and the observation of the first emitted photon. Repeating this procedure numerous times results in a histogram of the count of photons within a series of "time bins". If the timer's resolution is high enough, the width of time bins becomes so small that the histogram turns into the I–t decay curve we need.

TRPL results of glassy and β-phase 90F8:10BT thin films are shown in Chapter 4. Data were acquired in air using a PicoQuant FluoTime 300 TCSPC setup in Prof. Henry Snaith's group in the Department of Physics with the help of Dr. Hao Ye. Samples were photoexcited by a 398-nm, 16-ps-pulsed PicoQuant LDH-D-C-405M diode laser, with a Sepia PDL 820 laser driver at a repetition rate of 5 MHz. The PL emission was collected by a lens coupled into a Princeton Instruments SP-2558 grating spectrometer, equipped with a Micro Photon Devices PDM photon counting detector. The setup was controlled electronically using a PicoQuant PicoHarp 300 TCSPC event timer.

3.3.2.3 Photoluminescence quantum efficiency (PLQE)

The PLQE of an emissive material is defined as the number ratio of the emitted photons to the absorbed photons during the PL process,[199] and is an indication of the material's emission efficiency. A common way to determine the PLQE was proposed by de Mello et

al.[199] using a spectrofluorometer and an integrating sphere. The measurement consists of three steps (Fig. 3.3): (i) the incident light is directed to an empty integrating sphere; (ii) the sample is placed in the sphere, but the incident beam hits the sphere wall rather than the sample; (iii) the sample is placed in the sphere and is directly illuminated by the incident beam. In the collected spectra, areas under the incident beam profile (L_1, L_2, and L_3) and the sample emission profile (P_2 and P_3) are proportional to the photon numbers (subscripts denote the corresponding measurement step). These areas can be used to extract the PLQE as:[199]

$$\mathrm{PLQE} = \frac{L_2 P_3 - L_3 P_2}{L_1 L_2 - L_1 L_3} \times 100\,\% \tag{3.8}$$

The uncertainty of this method was shown to be ~5 %.[199,200]

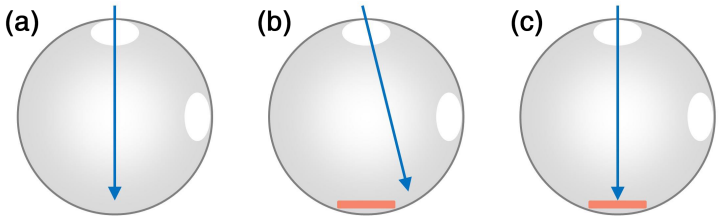

Figure 3.3 | Illustrations of the PLQE Measurement Steps. (a) Step 1: the incident light (blue) is directed to an empty integrating sphere. (b) Step 2: the sample (red) is placed in the sphere, but the incident beam hits the sphere wall rather than the sample. (c) Step 3: the sample is placed in the sphere and is directly illuminated by the incident beam.

In Chapter 4, PLQEs of glassy and β-phase 90F8:10BT thin films were measured in air using a HORIBA FluoroMax-4 spectrofluorometer with a Quanta-φ F-3029 integrating sphere coated with the Spectralon material. The excitation wavelength was 380 nm.

3.4 Electrical Property Characterisation

3.4.1 Current density–voltage (J–V) characteristics

As the most basic electrical characteristic, the J–V relationship for unipolar diodes in Chapters 4, 5, and 6 were measured on a Keithley 2400 sourcemeter in air. For OLEDs,

OPVs, and OFETs, their J–V curves were obtained using different setups, as described in Section 3.6.

3.4.2 Mobility

The mobility μ of an OSC can be measured by various methods. Below we shall first provide a brief overview of some common techniques, and then discuss two methods employed in this thesis.

3.4.2.1 Overview

A classical way to measure the mobility for OSCs is the time of flight (ToF) method. A sandwich-structured device is photoexcited by a laser pulse through a transparent electrode, creating a sheet of free charge carriers therefrom. Under an external electric field, these carriers move towards the counter-electrode, so in principle, a constant photocurrent can be observed from the connected oscilloscope. When they arrive at the electrode, the photocurrent drops and a transit time can be extracted to calculate the mobility. In this ideal case, the photocurrent–time curve exhibits a plateau-and-downhill character, and the charge transport is *non-dispersive* since the sheet of charge carriers moves together. In reality, however, the existence of traps with different depths usually leads to a continuous fall of the photocurrent and *dispersive* charge transport. The ToF technique was widely used in early studies, but it has some disadvantages,[5,201] such as (i) the OSC layer has to be much thicker (~1 µm) than in OLEDs or OPVs (~100 nm), so the microstructure may differ; (ii) the OSC is required to have relatively strong absorption at the excitation wavelength to generate enough numbers of charge carriers, which may not always be feasible; and (iii) the metal–OSC contact has to block the charge injection effectively, otherwise the electric field inside the OSC layer is no longer uniform.

Another common method is to calculate μ from Eq. (2.9) by assuming trap-free SCLC in the device. This is straightforward in terms of performing experiments, as only the J–V curve needs to be measured. Nonetheless, its prerequisites, the Ohmic contact and

the trap-free charge transport, can hardly be fulfilled. A recent study has shown that unfavourable injection barriers, as well as inappropriate OSC layer thickness d, may result in the measured J–V characteristics deviating significantly from the Mott–Gurney law.[202] Thus, it is crucial to check if both the $J \propto V^2$ and $J \propto d^{-3}$ relationships are valid to ensure the SCLC method is applicable.[203] Besides, the accurate determination of d is also important for the reliable and reproducible extraction of the SCLC-mobility.[204]

The dark injection transient (DIT) method involves applying a step voltage to a sandwich-type device, in which one of the contacts is Ohmic. The measured transient current ideally shows a peak, and the corresponding time can be employed to calculate the mobility. In practice, this technique does not always work, mainly because (i) the OSC layer thickness needs to be fine-tuned to make sure that it is neither too thin to exhibit a longer transit time than the device's RC constant, nor too thick to distinguish the peak from the background noise; and (ii) the presence of the peak is dependent on the nature of charge transport; it may disappear if the transport is highly dispersive.[205]

The working principles of OFETs also allow us to extract the mobility from the linear or saturation regime (Section 3.6.3). However, as stated in Section 2.4.3.3, the charge carrier density in OFETs is very different from that in diodes, thus their mobility differs. Additionally, current in OFETs can be easily affected by the properties of the OSC–dielectric interface as the charge transport primarily takes place thereabout (Section 2.5.3). Thus the OFET-mobility is more device-dependent than material-dependent.

Finally, some techniques that work on the ultra-fast timescales can determine the backbone mobility for conjugated polymers with no need to fabricate devices. For example, terahertz-probe spectroscopy showed that the hole mobility for P3HT backbones was $\sim 30\,\mathrm{cm^2\,V^{-1}\,s^{-1}}$.[206] Evidently, this molecular-scale, intrachain mobility is different from the interchain mobility in thin films for our macroscopic devices.

3.4.2.2 Charge extraction by linearly increasing voltage (CELIV) and variants

CELIV technique was first proposed in 2000 to determine the mobility for microcrystalline Si,[207] but soon gained popularity in the OSC field. During the measurement, a linearly increasing voltage pulse is applied to a sandwich-type device with non-injecting contacts. The time at which the resultant transient current peaks is used to derive the mobility. The superiority of CELIV mainly comes from its wide applicability to both dispersive and non-dispersive transport,[208] to both low and high mobility regimes, and to both doped and undoped materials,[5] as well as the achievable experimental conditions of the OSC layer thickness (~100 nm) and the applied voltage (usually < 10 V).[201] However, a major drawback of CELIV is that the hole and electron mobility cannot be clearly discerned, so one typically ends up with the "combined" mobility dominated by the faster charge carriers. Besides, for undoped OSCs, the extracted current is originated from the intrinsic charge carriers therein, which are usually not abundant enough to support a distinguishable transient current peak.

These problems can be resolved by one of the variants of CELIV, the metal–insulator–semiconductor structure-based CELIV (MIS-CELIV).[209] This improved technique functions through inserting an insulating dielectric layer between the anode (or the cathode) and the OSC layer to minimise the hole (or the electron) injection thereabout. Hence the device becomes electron-only (or hole-only), and the electron (or the hole) mobility can be unambiguously measured. Meanwhile, the other electrode has a small injection barrier, so the desired type of charge carriers can be injected and then accumulated at the OSC–dielectric interface. When a linearly increasing voltage of the appropriate polarity is then applied, injected charge carriers can be extracted, resulting in transient current for electron (or hole) transport. The key parameter used to calculate the mobility is t_{2j_0}, which is the time for the output current density to rise to twice the displacement current density j_0. The mobility μ is given by[210]

$$\mu = \frac{\pi^2 d_s^2}{8 A t_{2j_0}^2} \left(1 + \frac{\varepsilon_s d_i}{\varepsilon_i d_s}\right) \tag{3.9}$$

where d_s (d_i) is the thickness of the OSC (insulator) layer; ε_s (ε_i) is the relative permittivity of the OSC (insulator); and A is the changing rate of the linearly increasing voltage (in $\mathrm{V\,s^{-1}}$).

In Chapters 4 and 5, the MIS-CELIV method was used to determine the electron and hole mobility for glassy and β-phase 90F8:10BT, as well as the hole mobility for a conjugated polymer (PTB7) deposited on top of CuSCN interlayers. Measurements were performed in air on the Fluxim PAIOS measurement platform with Characterization Suite 4.2 software. The rate A was changed from 200 to 1000 $\mathrm{V\,ms^{-1}}$ with 200 $\mathrm{V\,ms^{-1}}$ steps.

3.4.2.3 Impedance-spectroscopy-based methods

The impedance spectroscopy reveals how a sample's complex impedance Z varies with the frequency f. The reciprocal of Z is referred to as the complex admittance Y, whose real and imaginary parts are the conductance G and the susceptance B, respectively. The impedance spectroscopy is related to charge transport kinetics and relaxation processes in OSCs, and both G and B can be used to derive the mobility.[211,212] Since their underlying principles are different from the techniques mentioned above, impedance-spectroscopy-based methods are good cross-checks of the validity of the mobility measured otherwise. Below we shall introduce the impedance-spectroscopy-based negative differential susceptance ($-\Delta B$) method.

A small alternating voltage V_A with the frequency f is superimposed on a direct bias voltage V_D. They are applied to a unipolar diode, and V_D enables the device to operate in the SCLC regime. The $-\Delta B$ varies with f as follows:[213]

$$-\Delta B = 2\pi f \left(C - C_{geo}\right) \tag{3.10}$$

where C is the frequency-dependent capacitance, and C_{geo} is the geometric capacitance

of the device. The obtained $-\Delta B$ vs f curve is expected to exhibit a peak, which defines the peak frequency f_{p}. Depending on the nature of charge carriers in the unipolar device, the electron or the hole mobility can be calculated as:[214]

$$\mu = \frac{d^2 f_{\mathrm{p}}}{0.54(V_{\mathrm{D}} - V_{\mathrm{bi}})} \tag{3.11}$$

where d is the OSC layer thickness, and V_{bi} is the built-in voltage.

In Chapter 4, the $-\Delta B$ method was used as a second technique to determine the electron and hole mobility for glassy and β-phase 90F8:10BT. Measurements were carried out in air on the Fluxim PAIOS measurement platform with Characterization Suite 4.2 software. The V_{A} was set to be 0.05 V, and V_{D} was varied from 5 to 7 V with 1 V steps.

3.5 Thin-Film Characterisation

3.5.1 Atomic force microscopy (AFM)

Atomic force microscopy (AFM) is a high-resolution scanning probe microscopy capable of imaging the surface topography of thin-film samples. When working in the tapping mode (Fig. 3.4), a probe consisting of a cantilever and a tiny sharp tip oscillates at its fundamental frequency just above (~10 nm) the sample surface. During the scanning over a certain area, a proportional–integral–derivative (PID) feedback controller communicates

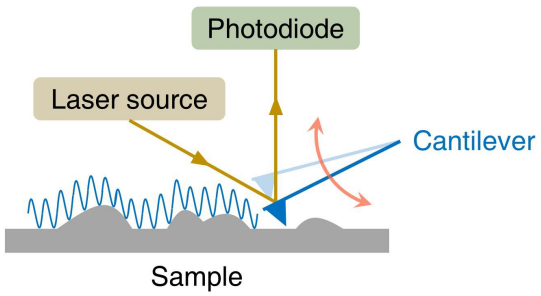

Figure 3.4 | Illustration of the AFM Tapping Mode. When the vibrating cantilever scans through the sample surface, its amplitude remains constant by changing the cantilever's height, which is monitored by a photodiode using the reflected laser beam.

with the mechanical system to move the cantilever up and down so that the oscillation amplitude remains constant. This motion is monitored by a laser beam directed at the cantilever; any change in the laser reflection, tracked by a photodiode, can be translated to the vertical movement of the cantilever. Hence the variance of the cantilever's height provides a replica of the sample's topography, whose lateral resolution depends on the tip radius.

In addition, with the measured height data, the surface roughness can be calculated. The commonly used root-mean-square roughness R_{rms} is defined as:[215]

$$R_{\text{rms}} = \sqrt{\frac{1}{N}\sum_{i=1}^{N}(z_i - \bar{z})^2} \tag{3.12}$$

where z_i is the height at the i^{th} data point; $\bar{z}$ is the mean height of N data points.

In Chapter 4, the surface topography of glassy and β-phase 90F8:10BT thin films was measured over a $5 \times 5\,\mu\text{m}^2$ area in air using a Nanosurf CoreAFM atomic force microscope in Prof. Stephen Morris' group in the Department of Engineering Science. In Chapter 5, CuSCN thin film topography was characterised over a $2 \times 2\,\mu\text{m}^2$ area in air on an Asylum Research MFP-3D atomic force microscope in Prof. Harish Bhaskaran's group in the Department of Materials with the help of Miss Yu Shu. In both cases the Budget Sensors TAP300Al-G probes were used, and the tip radius was $< 10\,\text{nm}$. All data were processed using Gwyddion software.[216]

3.5.2 Raman and Fourier-transform infrared (FTIR) spectroscopy

Both Raman and Fourier-transform infrared (FTIR) spectroscopy can provide information about molecular vibrational transitions but with different underlying principles. Raman spectroscopy is based on Raman scattering, a process in which incident photons interact inelastically with the molecule, resulting in the scattered photons having different energies with the incident. This energy discrepancy, usually called the Raman shift in wavenumber units, corresponds to a specific vibrational transition mode of the molecule. The Raman-

active transitions must involve a change in the molecule's polarisability. On the other hand, FTIR spectroscopy relies on the molecule absorbing the infrared photons to initiate vibrational transitions, associated with an altered molecular dipole moment.

A Raman spectrometer usually contains a laser source to excite the sample, a filter to collect Raman signals by blocking photons with unchanged energy, a dispersive element (e.g. the grating), and a high-sensitive charge-coupled device (CCD) detector. In comparison, an FTIR spectrometer uses an IR light source (e.g. SiC), and the light passes through a Michelson interferometer before striking the sample. The interferometer can split the incident light into two beams with different optical paths, and then combine them to produce a particular interference pattern. The pattern changes after the light interacts with the sample, so the detector can collect a characteristic interferogram, from which the computer can decode the IR spectrum using the Fourier transform algorithm.

In Chapter 5, the polymorphism of CuSCN layers was investigated using both Raman and FTIR spectroscopy. The former was carried out in air with a Jobin Yvon T64000 triple spectrometer in Prof. Robin Nicholas' group in the Department of Physics. Samples were excited by a 532-nm Ventus Solo Nd:YAG laser, and the incident radiation on the sample was controlled to be $< 1\,\mathrm{mW}$. The triple spectrometer was calibrated by a Si substrate before each measurement, with its first two gratings rejecting the light at the excitation wavelength and the third resolving the Raman signal from the sample. An Andor DU420A-OE CCD was used as the detector. FTIR spectra were recorded in air with a Thermo Scientific Nicolet iS 5 spectrometer in Prof. Henry Snaith's group in the Department of Physics. Measurements were performed in the reflection mode with an iD5 reflection accessory. Signals from air and the substrate were subtracted, and for each sample 32 scans were collected and averaged.

3.5.3 Thin-film X-ray diffraction (XRD)

When X-ray photons hit atoms in a crystalline material, the resultant coherent scattering can interfere. At certain incident angles θ (between the incident beam and the sample),

the interference is constructive, leading to a diffracted beam. These characteristic angles θ are described by Bragg's law:[217]

$$2d \sin\theta = n\lambda \tag{3.13}$$

where d is the crystal's interplanar spacing; λ is the X-ray wavelength; and n is a positive integer. Scanning the diffraction intensity at different angles gives us a characteristic pattern, which is helpful in, for example, identifying the material and its polymorph.

In an X-ray diffractometer, the radiation generated by the X-ray source is first monochromated, followed by the adjustment of its beam shape through the incident slits. Then the X-ray illuminates the sample, and diffracted signals are collected by a detector. The angular scan of the intensity can be performed in the θ–θ configuration, in which the sample is stationary, and the X-ray tube and detector rotate simultaneously towards each other at the same angular speed, leading to identical angles with respect to the sample.

In Chapter 5, polymorphs of CuSCN samples were additionally characterised by thin-film XRD. Measurements were carried out in air on a Rigaku SmartLab diffractometer with Cu Kα radiation ($\lambda = 1.5406$ Å) and a HyPix-3000 detector. The incident optics were in the parallel beam geometry, and a 2.5° incident slit was used. In the θ–θ configuration, the rotation rate was set to be $1° \,\mathrm{min}^{-1}$. Background signals from the substrate were collected and subtracted.

3.5.4 Grazing-incidence wide-angle X-ray scattering (GIWAXS)

Grazing-incidence wide-angle X-ray scattering (GIWAXS) technique can be employed to characterise the crystallite orientation distribution (i.e. the texture) of semicrystalline conjugated polymers. The use of the word "scattering" is in accordance with the poorer crystallinity of conjugated polymers compared with crystalline materials, where "diffraction" patterns usually result. In a GIWAXS setup, the incident beam grazes the sample, meaning the incident angle α_i is very small (usually $< 0.5°$). Consequently,

the illumination area is significantly larger than that in normal XRD measurements, which is favourable for not only collecting more scattering data but also reducing the sample degradation under the X-ray radiation. At the detection side, photons with wide scattering angles are collected. This usually refers to 1°–45°, but there is no unambiguous definition. Using Eq. (3.13), it turns out that this range corresponds to crystallite interplanar spacings of 0.1–4.5 nm, assuming the most common Cu Kα radiation for lab-scale equipment is used as the X-ray source. For the classic semicrystalline conjugated polymer P3HT, its crystallites exhibit a lamellar and a π–π stacking distances of 1.66 nm and 3.90 nm, respectively,[218] both detectable by GIWAXS. Therefore, GIWAXS is a suitable tool to characterise the texture of semicrystalline conjugated polymers.

During the measurement, a 2D detector is used to collect the scattered X-ray photons within the exposure time, and the light source, sample, and detector are all fixed. The resultant 2D figure shows the intensity at different scattering vectors $\vec{q}$, whose magnitude q is defined as[219]

$$q = \frac{4\pi \sin\theta}{\lambda} = \frac{2\pi}{d} \tag{3.14}$$

Here θ is the scattering angle; λ and d have the same meanings as in the previous subsection. Thus q correlates with different interplanar spacings and stacking manners (i.e. lamellar or π–π). How these stackings orientate themselves in the 3D space is reflected by the direction of $\vec{q}$, which can be described by its respective components in the x, y, and z directions, $\vec{q_x}$, $\vec{q_y}$, and $\vec{q_z}$, with x and y defining the sample plane and z perpendicular to that plane. Hence,

$$\begin{cases} \vec{q} = \vec{q_x} + \vec{q_y} + \vec{q_z} \\ q = \sqrt{q_x^2 + q_y^2 + q_z^2} \end{cases} \tag{3.15}$$

Since the crystallite orientation is determined by the in-plane and out-of-plane stacking manners (Section 2.4.3.3), an in-plane scattering vector $\overrightarrow{q_{xy}} = \vec{q_x} + \vec{q_y}$ and an out-of-plane vector $\vec{q_z}$ are enough to depict the distribution of different orientations, i.e. edge-on and face-on. Therefore, a 2D GIWAXS plot demonstrates the texture of semicrystalline

conjugated polymers by showing the scattering intensity at different q_{xy} and q_z.

Measuring the scattering intensity is trivial; however, correlating the intensity with specific q_{xy} and q_z requires some extra conversions from the 2D coordinates in the detector plane to the 3D coordinates in the q-space. This is accomplished using the incident angle α_i, in-plane scattering angle $2\theta_\mathrm{f}$, and out-of-plane scattering angle α_f (Fig. 3.5):[220]

$$\begin{cases} q_x = \dfrac{2\pi}{\lambda}\cos\alpha_\mathrm{f}\sin 2\theta_\mathrm{f} \\ q_y = \dfrac{2\pi}{\lambda}(\cos\alpha_\mathrm{f}\cos 2\theta_\mathrm{f} - \cos\alpha_\mathrm{i}) \\ q_z = \dfrac{2\pi}{\lambda}(\sin\alpha_\mathrm{f} + \sin\alpha_\mathrm{i}) \end{cases} \tag{3.16}$$

Moreover, it is worth mentioning that the scattering intensity in the vicinity of the $\vec{q_z}$ direction is non-detectable by GIWAXS, leading to a missing wedge in the resulting plot. This can be understood from the Ewald construction of the scattering process; only the space within the intersection of the Ewald sphere and the crystallite orientation sphere is observable.[133]

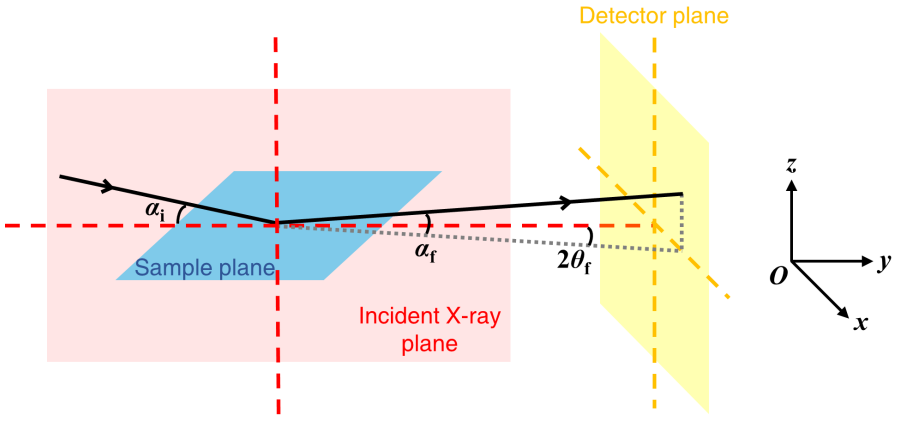

Figure 3.5 | Illustration of the GIWAXS Measurement Geometry. Planes containing the sample (blue), the incident X-ray (red), and the detector (yellow) are perpendicular to each other. The incident angle α_i, in-plane scattering angle $2\theta_\mathrm{f}$, out-of-plane scattering angle α_f, and the 3D coordinate system are shown.

In Chapters 5 and 6, the texture of conjugated polymer thin films deposited on various CuSCN interlayers and SAM-modified Au electrodes, respectively, was investigated using

GIWAXS. Measurements were performed in air on a Rigaku SmartLab diffractometer with Cu Kα radiation ($\lambda = 1.5406\,\text{Å}$) and a HyPix-3000 2D detector. The incident angle was 0.2°, and the exposure time was 30 min. Background signals from air and the substrate were recorded and subtracted. Data analysis was completed using a MATLAB program written by the author, and the code can be found on the GitHub repository.[221]

3.5.5 X-ray photoelectron spectroscopy (XPS)

X-ray photoelectron spectroscopy (XPS) is a surface-sensitive technique based on the photoelectric effect. When a beam of monochromatic X-ray illuminates the sample surface, some electrons in surface atoms can absorb the incident photon energy $h\nu$ and then escape from the sample with kinetic energies E_k. Thus the binding energy E_b between the electron and its host atomic nucleus is given by[222]

$$E_\text{b} = h\nu - E_\text{k} \tag{3.17}$$

It has been demonstrated that E_b is closely related to the atomic element, the orbital the electron originally residing, and the orbital's chemical environment. For example, for a specific atom, electrons in s-orbitals only exhibit one E_b, whereas those in p-orbitals show split double peaks in the energy spectrum, e.g. the $2p_{1/2}$ and $2p_{3/2}$ peaks. By comparing the measured E_b with values in the database or previous publications, we are able to reveal the sample's surface chemical characteristics, including composition, bonding, and chemical states of the constituent elements.

The XPS measurement is performed under high vacuum to slow down the surface adsorption of gas atoms and prevent the ejected electrons from being scattered. As Fig. 3.6 shows, the monochromated X-ray strikes the sample surface, and the generated photoelectrons are focussed by a lens system before their E_k being examined by a hemispherical electron energy analyser, which can scan over either a large energy range with lower resolution (i.e. a survey scan), or a small range with higher resolution (i.e. a

core level scan for a particular atomic orbital). During the measurement, an electron flood gun is placed next to the insulating sample to compensate for the positive charges on the surface due to the loss of electrons. Finally, E_b can be calculated using Eq. (3.17), and is usually further calibrated by locating the C 1s peak of adventitious carbon, present in all samples because of the accidental contamination in air during sample transfer, to a standard value.

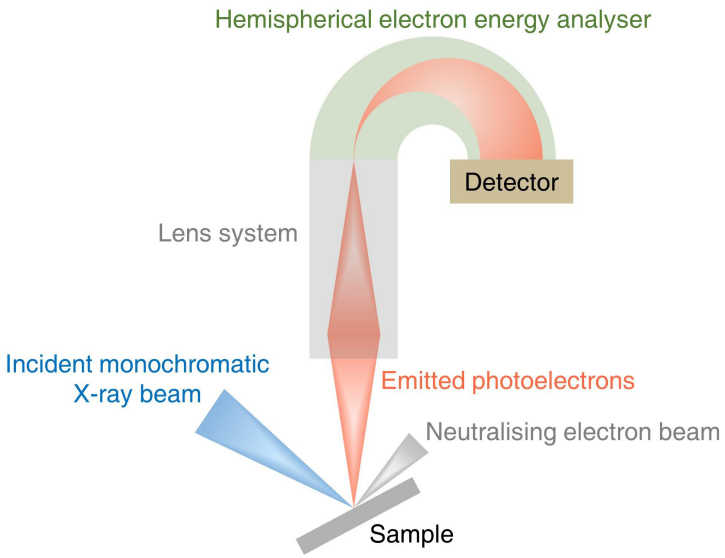

Figure 3.6 | Illustration of the XPS Instrument. The photoelectrons are ejected from the sample surface upon X-ray striking, and then focussed by the lens system. The hemispherical analyser can distinguish electrons with different kinetic energies. A neutralising beam is used to compensate the loss of electrons.

In Chapter 5, XPS spectra of CuSCN thin films were measured on a Thermo Scientific K-Alpha X-ray photoelectron spectrometer by Oxford Materials Characterisation Service (OMCS). The energy of the micro-focussed monochromated Al Kα X-ray source was 1486.6 eV, and the spot size was 400 µm^2. The analyser operated at a constant pass energy of 200 eV for survey scans and 50 eV for core level scans. Charge neutralisation was applied using a dual-beam low energy electron/ion flood source. The data acquisition was performed on Thermo Scientific Avantage software, and analysis was completed using CasaXPS software. All spectra were calibrated by the adventitious carbon 1s peak at E_b = 284.80 eV.[222] Backgrounds were recognised and removed using Shirley's

algorithm,[223] except when sloping backgrounds were detected, a linear interpretation was chosen.[224]

3.5.6 Contact angle and surface energy measurements

When a drop of liquid falls onto a solid surface in air, a contact angle θ exists at the solid–liquid–gas triple point, tangential to and enclosing the drop (Fig. 3.7).[225] As a measure of the wettability of a solid by a liquid, θ correlates the solid's surface energy γ_S, the liquid's surface tension γ_L, and the interfacial tension γ_{SL} via Young's equation:[226]

$$\gamma_S = \gamma_{SL} + \gamma_L \cos\theta \tag{3.18}$$

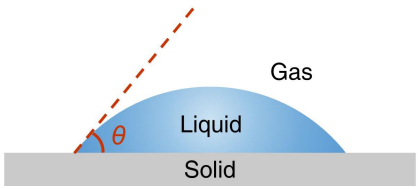

Figure 3.7 | Illustration of the Conatct Angle. The contact angle θ at the solid–liquid–gas triple point is tangential to and encloses the liquid drop.

The solid's surface energy γ_S can be measured according to the Fowkes theory premised on the assumption that γ_S comprises a dispersive (i.e. non-polar) component γ_S^D and a polar component γ_S^P. Similarly, the liquid's surface tension γ_L consists of a dispersive part γ_L^D and a polar part γ_L^P. Apparently $\gamma_S = \gamma_S^D + \gamma_S^P$, and $\gamma_L = \gamma_L^D + \gamma_L^P$. Fowkes pointed out that[227]

$$I_{SL} = 2\sqrt{\gamma_S^D \gamma_L^D} + 2\sqrt{\gamma_S^P \gamma_L^P} \tag{3.19}$$

where I_{SL} is the interfacial adhesion energy per unit area, and can be formulated by Dupre's equation:[226]

$$I_{SL} = \gamma_S + \gamma_L - \gamma_{SL} \tag{3.20}$$

Combining Eqs. (3.18), (3.19), and (3.20) gives us the principle of determining γ_S via the

Fowkes method:

$$\sqrt{\gamma_S^D \gamma_L^D} + \sqrt{\gamma_S^P \gamma_L^P} = \frac{\gamma_L(1+\cos\theta)}{2} \tag{3.21}$$

Here γ_L, γ_L^D, and γ_L^P of certain test liquids can be obtained from the database,[225] and resolving two unknown variables, γ_S^D and γ_S^P, entails measuring the contact angle between the solid and two different liquids.

In Chapter 5, surface energies of CuSCN interlayers were determined using Eq. (3.21). Two test liquids, de-ionised (DI) water and diiodomethane (DIM), were dropped on the sample surface. The process was recorded by the camera on the Ossila L2004A1 contact angle goniometer in Prof. Henry Snaith's group in the Department of Physics. Values of θ were then extracted using Ossila Contact Angle software to derive γ_S.

3.5.7 Thickness

The thin-film thickness was measured by three different methods in this thesis depending on the nature of the sample. First, spin-coated polymer thin films were deliberately scratched, and the local topography around the scratch was detected by a Veeco Daktak 150 profilometer in Prof. Henry Snaith's group in the Department of Physics. A profilometer is equipped with a sensitive stylus, which physically contacts the sample and draws across the scratch to reveal the hill-and-valley topography. The layer thickness can be obtained from the height difference within and outside the scratch. Attention needs to be paid to the appropriate setting of the stylus force; for soft materials such as polymers, a large force may lead to additional scratches and wrong thickness values. In our measurements, a relatively small force of 3 mg (= 29.4 µN) was used.

Second, the thickness of all evaporated layers, including metal electrodes and inorganic interlayers, was calibrated by X-ray reflectivity (XRR) measurements on a Rigaku SmartLab diffractometer. Compared with the profilometer-based method, XRR is a non-damaging technique and can provide higher thickness accuracy, especially suitable for samples with ultra-smooth surfaces. During the measurement, the interference of

reflected beams leads to the characteristic Kiessig fringes[228] in the resultant reflection intensity–incident angle curve, from which the layer thickness can be acquired.[229]

Finally, in Chapter 5, the spin-coated CuSCN thin films were neither soft enough to be vulnerable to scratches nor smooth enough to be measured by XRR. Their thickness was determined by spectroscopic ellipsometry using a J.A. Woollam RC2 ellipsometer. The polarisation change of the light before and after interacting with the sample was recorded, and the thickness was extracted by fitting the data in the transparent region into a multilayer model using the Cauchy equation of the refractive index.[230] This was completed on J.A. Woollam CompleteEASE software.

3.6 Device Characterisation

3.6.1 Organic light-emitting diodes (OLEDs)

3.6.1.1 Radiometry and photometry

Before we discuss how OLEDs are characterised, it is helpful to introduce and compare radiometric and photometric quantities. Radiometry is the physical measurement of radiant energies including light.[196] For example, the radiant flux Φ_e (the subscript "e" denotes "electromagnetic") is the radiant energy per unit time, so its unit is watt.[5] By contrast, photometry measures the light energy based on how human eyes perceive it.[196] Therefore, the photometric counterpart of Φ_e, the luminous flux Φ_v (the subscript "v" represents "vision"), involves the correction of the sensitivity of human eyes to different wavelengths λ:[5]

$$\Phi_v = K \int \Phi_e(\lambda) V(\lambda)\, \mathrm{d}\lambda \tag{3.22}$$

Here the unit of Φ_v is lumen (lm); $V(\lambda)$ is the luminous efficiency function; and K is a constant called the absolute luminous efficiency. Note that $V(\lambda)$ and K have different values when the light intensity changes, in line with different modes of human vision (e.g. photopic, scotopic, and mesopic).[5] With Φ_v, the luminance L is defined as the luminous

flux per solid angle Ω per unit area A:[196]

$$L = \frac{\partial^2 \Phi_v}{\partial \Omega \, \partial A} \tag{3.23}$$

The unit of L is thus $\mathrm{lm\,sr^{-1}\,m^{-2}}$, or equivalently $\mathrm{cd\,m^{-2}}$ in SI units.

3.6.1.2 OLED measurements

A basic OLED characterisation setup (Fig. 3.8) consists of a sourcemeter to supply the voltage V and measure the device current I (usually converted to the current density J), an integrating sphere to collect the emitted photons in all directions, and a pre-calibrated spectrometer to determine the number of photons at each wavelength. Typical results for evaluating OLED performance include the J–V and L–V characteristics; the external quantum efficiency (EQE), luminous efficiency (η_L), and luminous power efficiency (η_{LP}) as a function of luminance; and the electroluminescence (EL) spectrum.

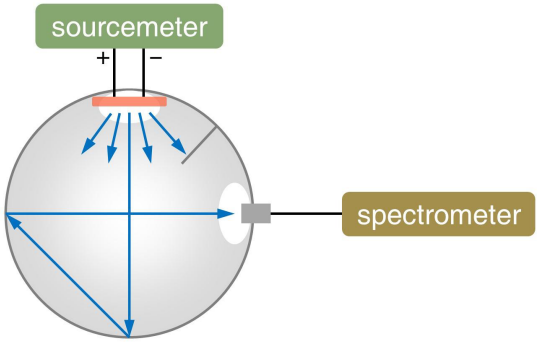

Figure 3.8 | Illustration the Typical OLED Measurement Setup. The device is driven by the sourcemeter, which also records the device current. The emitted light is redistributed in the integrating sphere and then detected by the spectrometer.

The J–V curve is measured using the sourcemeter. The luminance L is determined based on the assumption that the OLED is a Lambertian emitter, i.e. its luminance is independent of the direction, though this often-used assumption is not always true due

to interference effects.[231] Therefore,[196]

$$L = \frac{\Phi_{\mathrm{v}}}{\pi A} \tag{3.24}$$

with A being the device's active area. Since the spectrometer records the spectral radiant flux $\Phi_{\mathrm{e}}(\lambda)$, L can be extracted using Eqs. (3.22) and (3.24).

The EQE is the number ratio of the emitted photons to the injected electrons.[231] The former is obtained from the spectrometer, and the latter can be derived from the current density. The η_{L} (in $\mathrm{cd\,A^{-1}}$) and η_{LP} (in $\mathrm{lm\,W^{-1}}$) are defined as[231]

$$\eta_{\mathrm{L}} = \frac{L}{J} \tag{3.25}$$

$$\eta_{\mathrm{LP}} = \frac{\Phi_{\mathrm{v}}}{IV} \tag{3.26}$$

Finally, EL spectra at different driving voltages are collected by the spectrometer.

In Chapters 4 and 5, OLEDs were characterised using a custom-built setup comprising a Keithley 2636 sourcemeter, a Newport Oriel Instruments 70682NS integrating sphere, and an Ocean Optics Maya2000 Pro spectrometer in Prof. Henry Snaith's group in the Department of Physics. The setup was calibrated by a reference Si LED and a Konica LS-150 luminance meter. Bespoke software was used to choose the device under test, perform measurements, and collect data. The active area was $15\,\mathrm{mm^2}$, and devices were encapsulated using UV-cured epoxy adhesive (LT-U001, Lumtec) and glass coverslips before being measured in air.

3.6.2 Organic solar cells (OPVs)

Characterisation of OPVs involves illuminating the sample by a solar simulator to determine the power conversion efficiency (PCE). For the solar simulator, the light it provides has to meet specific requirements for the irradiance E_{e}, which is a radiometric quantity and is defined as the radiant flux Φ_{e} per unit area A:[196]

$$E_{\mathrm{e}} = \frac{\partial \Phi_{\mathrm{e}}}{\partial A} \tag{3.27}$$

so its unit is $\mathrm{W\,m^{-2}}$. The standard condition requires that the spectral irradiance $E_{\mathrm{e}}(\lambda)$ follows the AM1.5 spectrum, and the total irradiance $\int E_{\mathrm{e}}(\lambda)\,\mathrm{d}\lambda$ is $1000\,\mathrm{W\,m^{-2}}$.[232] Here "AM" means "air mass", and the solar spectrum outside the earth's atmosphere is AM0 since there is no air. The solar radiation received at the equator is AM1 in that the optical path of this normal incidence is exactly the atmosphere's thickness. Similarly, the AM1.5 spectrum (Fig. 3.9(a)) describes the sunlight received on the earth at an angle of ~48° with respect to the vertical, so the optical path is 1.5 times the thickness of the atmosphere.[5]

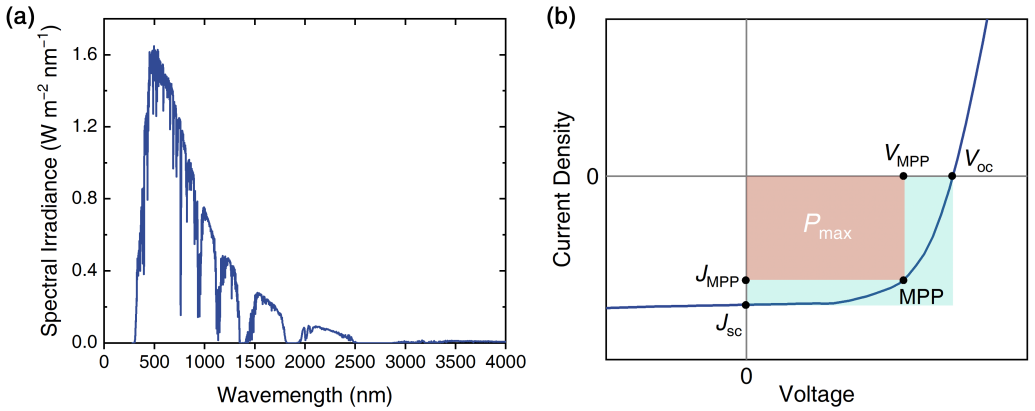

Figure 3.9 | The AM1.5 Solar Radiation Spectrum and Typical *J*–*V* Characteristics for an OPV under Illumination. (a) The spectral irradiance of AM1.5 spectrum. Data were obtained from the National Renewable Energy Laboratory (NREL) website.[233] (b) Typical J–V curve for an illuminated OPV. The short-circuit current density J_{sc}, open-circuit voltage V_{oc}, and maximum power point (MPP) are shown. The fill factor (FF) is the area ratio of the red rectangle to the green (Eq. (3.28)).

The PCE of an OPV can be derived from its short-circuit current density J_{sc}, open-circuit voltage V_{oc}, and fill factor FF. Under the AM1.5 illumination, if we connect the anode and cathode, the resultant current density is J_{sc}, but the output power is zero since $V = 0$. On the other hand, if electrodes are unconnected, then the voltage across the device is V_{oc}, but $J = 0$ nullifies the output power as well. Thus in between, as Fig. 3.9(b)

shows, a maximum power P_{max} can result when $J = J_{\text{MPP}}$ and $V = V_{\text{MPP}}$ (the subscript "MPP" denotes the "maximum power point"; $0 < J_{\text{MPP}} < J_{\text{sc}}$; $0 < V_{\text{MPP}} < V_{\text{oc}}$). The FF is defined as[232]

$$\text{FF} = \frac{P_{\text{max}}}{A \cdot J_{\text{sc}} V_{\text{oc}}} = \frac{J_{\text{MPP}} V_{\text{MPP}}}{J_{\text{sc}} V_{\text{oc}}} \tag{3.28}$$

where A is the device's active area. The PCE is given by[232]

$$\text{PCE} = \frac{P_{\text{max}}}{A \int E_{\text{e}}(\lambda)\,\mathrm{d}\lambda} = \frac{J_{\text{sc}} \cdot V_{\text{oc}} \cdot \text{FF}}{\int E_{\text{e}}(\lambda)\,\mathrm{d}\lambda} \tag{3.29}$$

During the OPV measurement, the J_{sc} and V_{oc} are recorded by the sourcemeter, followed by a J–V scan to determine the P_{max}, FF, and finally PCE.

In Chapter 5, OPV characterisation was completed in air using a Keithley 2401 sourcemeter and a Wavelabs SINUS-220 solar simulator in Prof. Henry Snaith's group in the Department of Physics. The irradiance of the incident light was calibrated using a reference Si photodiode, and all devices were masked by 25 mm^2 metal apertures to define the active area and avoid edge effects.[234] Note that here a possible source of error is the difference in spectral response between the Si-based reference and OPV devices.[235] Bespoke software was used to choose the device under test, perform measurements, and collect data.

3.6.3 Organic field-effect transistors (OFETs)

The performance of an OFET can be reflected in the output and transfer characteristics.[5] The former gives the relationship between the drain–source current I_{DS} and drain–source voltage V_{DS} at different gate–source voltages V_{GS}, so the linear and saturation regimes are clearly shown (Fig. 3.10(a)). The latter is an I_{DS}–V_{GS} plot at certain V_{DS}; the device may operate in the linear or saturation regime (Fig. 3.10(b–c)). The transfer characteristics can be used to extract the OFET-mobility μ. In the linear regime,[52]

$$\mu_{\text{lin}} = \frac{\partial I_{\text{DS}}}{\partial V_{\text{GS}}} \cdot \frac{L}{W C_{\text{i}} V_{\text{DS}}} \tag{3.30}$$

where L is the channel length, i.e. the distance between the source and drain; W denotes the channel width; and C_i represents the capacitance per unit area of the dielectric layer. In the saturation regime,[52]

$$\mu_\mathrm{sat} = \left(\frac{\partial \sqrt{I_\mathrm{DS}}}{\partial V_\mathrm{GS}} \right)^2 \cdot \frac{2L}{WC_\mathrm{i}} \tag{3.31}$$

It is noteworthy that as the critical proxy for OFET performance, the mobility should be carefully extracted to avoid the possible overestimation due to the contact resistance and other interface non-idealities. Several reviews[52,55,56] have discussed this topic in detail and proposed instructions on determining the OFET mobility properly and convincingly. Following these procedures can be helpful in increasing the reliability of the reported OFET mobility values.

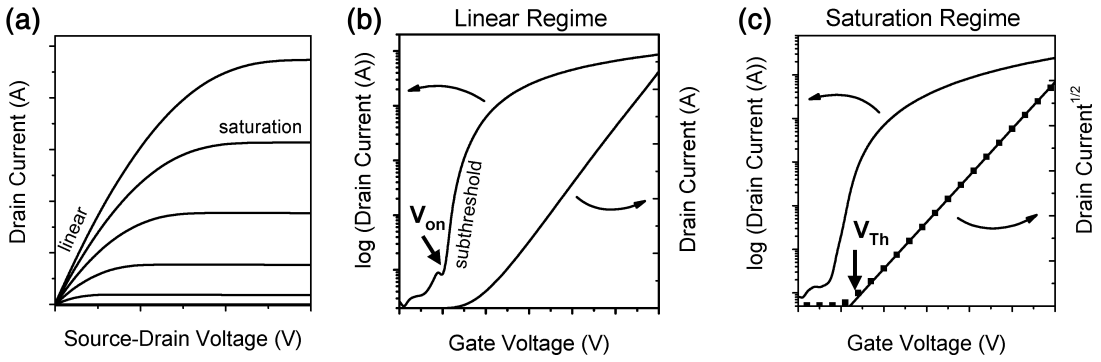

Figure 3.10 | Typical OFET Output and Transfer Characteristics. (a) Output characteristics. (b–c) Transfer characteristics in the (b) linear and (c) saturation regimes. Adapted with permission.[152] Copyright 2007, American Chemical Society.

In Chapter 5, OFETs were measured in air on a Keithley 4200-SCS semiconductor parameter analyser, which is connected to a Cascade Microtech probe station to allow the selection of the device under test, in Prof. SeungNam Cha's group in the Department of Engineering Science with the help of Dr. Sungho Nam, who also analysed the data.

Chapter 4

Chain Conformation Control of Fluorene–Benzothiadiazole Copolymer Light-Emitting Diode Efficiency and Lifetime

4.1 Introduction

Following the first report of a solution-processed conjugated polymer LED in 1990,[21] the past three decades have seen the successful commercial development of ink-jet-printed high-resolution LED displays, with these devices also expected to play an increasing role in solid-state lighting applications where high throughput manufacturing at suitably low cost is required. In addition to their solution processability, polymer semiconductors lend themselves to physical structure control via manipulation of chain conformation,[236] liquid crystalline,[170,237] and crystalline ordering.[238] This provides novel possibilities to optimise structure–property–device-performance relationships and with the right processing methods yields innovative patterning approaches for electronic, optoelectronic, and photonic devices.[164,239–242] Among such polymers, poly(9,9-dioctylfluorene) (PFO) is one of the most widely studied, and it has proven to be an excellent model system which allows the exploration of physical structure control. This, combined with a relatively short wavelength luminescence emission, has made PFO the baseline emission material of blue polymer LEDs.[240,243,244]

The β-phase microstructure of PFO[159,164,241] comprises a fraction of chain segments for which the intermonomer torsion angle, φ, approaches 180°, resulting in the adoption of a chain-extended planar conformation with alkyl substituent groups for neighbouring

fluorene units on opposite sides of the chain (Fig. 4.1(a)). It differs from the normal glassy phase obtained by spin-coating from a good solvent, where the average angle $\langle\varphi\rangle \approx 135°$.[245] Generation of the β-phase requires different fabrication conditions either during film deposition or via additional treatment of glassy samples (spin-coated or quenched from the nematic melt). Examples of the former include using moderate/poor[159,237] and/or high-boiling-point[246] solvents, inclusion of high-boiling-point additives,[247,248] and Langmuir–Blodgett deposition.[249] The latter category includes thermal cycling to liquid nitrogen temperature and back to room temperature,[159,160,237] solvent vapour annealing (SVA),[161,250] writing solvent on top of the film,[163] and dipping the glassy sample in a solvent/non-solvent mixture (or simply "dipping" for short).[161,162] The presence of the β-phase can be readily confirmed from characteristic changes in optical properties,[159–161,245,246] comprising the appearance of a new narrow-linewidth absorption peak at ~435 nm, and a red-shift and relative intensity enhancement of the main ($S_1 \rightarrow S_0$ 0–0) photoluminescence (PL) peak. This shift from ~420 nm to ~440 nm is also accompanied by an increase in vibronic peak resolution due to a narrowing of the peaks. We emphasise that for "β-phase samples" or "β-phase devices", a fraction of $\varphi = 180°$ chain-extended segments are embedded within an otherwise glassy matrix, where the fraction can be varied from 0 % (i.e. fully glassy) to about 45 %,[247] although at this latter percentage scattering films with poor optical quality typically result. In our own experience, ~25 % is the limit to maintain good film quality.[161]

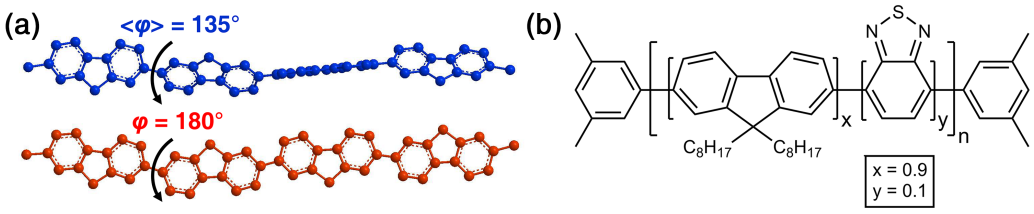

Figure 4.1 | (a) Schematic PFO chain conformations in the glassy (blue) and β- (red) phases. Note that hydrogen atoms and dioctyl side chains have been omitted for clarity. (b) The chemical structure of 90F8:10BT.

Initial interest in the β-phase in PFO was from the perspective of better understanding

the influence of physical structure on photophysical properties[160,161,238,251] and as a "self-doped" donor–acceptor system,[237] which provides an excellent platform to investigate fundamental topics in energy transfer and excitation dynamics.[246,252,253] Subsequent interest broadened to include refractive index patterning[163,241,250] for photonic structure fabrication and also device optimisation. In the latter category, a small β-phase fraction of ~1.3 % was shown to lead to a large increase in the luminance and external quantum efficiency (EQE) of PFO LEDs.[162] In addition, β-phase PFO was found to be a promising gain medium to control the polariton physics of metal–PFO–metal microcavities.[164]

Motivated by the attractive features of β-phase conformational control of electronic, optoelectronic, and photonic properties in PFO, researchers have sought to broaden the range of materials within which a β-phase-like change in microstructure might be induced. PFO homologs with heptyl and nonyl substituents were shown to support β-phase formation whilst hexyl and decyl substituents suppressed.[254] Copolymers of 9,9-dioctylfluorene (F8) with low fractions ($\leqslant$ 10–15 %) of dibenzothiophene-*S*,*S*-dioxide and dibenzothiophene also showed β-phase formation but have been little studied.[255] Likewise the β-phase was observed in electron-beam crosslinkable alternating copolymers of dihexylfluorene and vinyl-ether-functionalised dialkyl fluorene.[256] More recently, the β-phase was generated successfully in F8-based copolymers 97F8:3BSP, 95F8:5BSP and 90F8:10BSP, containing, respectively, 3 %, 5 %, and 10 % butyl-substituted phenylene-diamine (BSP) units.[200] In contrast, 80F8:20BSP did not allow β-phase generation because the F8 sequence length was too short. The key benefit of forming the β-phase in 95F8:5BSP emission layer (EML) LEDs was to improve the device Commission Internationale de L'Éclairage (CIE) (x, y) colour coordinates from (0.149, 0.175) to (0.145, 0.123), achieving a significantly deeper-blue emission with outstanding spectral stability. This results from the localisation of excited states on the β-phase F8 segments instead of arylamine moieties, thereby changing the emission from a broad, red-shifted CT-exciton-like band to predominantly being a vibronically-structured neutral exciton emission, characteristic of β-phase PFO.

In the current study, we investigate β-phase generation and LED performance for a 90F8:10BT copolymer consisting of 90 % F8 and 10 % 2,1,3-benzothiadiazole (BT) units (Fig. 4.1(b)). In this copolymer the lowest-lying BT absorption band overlaps the emission spectrum of the F8 segments, leading to efficient Förster energy transfer prior to luminescence emission, just as also observed for LED-optimised "5BT:95F8" polymer blends which comprise 5 % poly(9,9-dioctylfuorene-*alt*-2,1,3-benzothiadiazole) (F8BT) and 95 % PFO, yielding an overall 2.5 % fraction of BT units.[257] The resulting emission then lies in the green spectral range, characteristic of BT-containing polymers and starburst molecules.[258] The 90F8:10BT copolymer has previously been used in optically pumped lasers,[259] optical amplifiers,[260] and quantum-dot-enhanced LEDs,[261] but in none of those studies was consideration given to the effects of β-phase formation.

Herein, we report on the generation of β-phase F8 chain segments in 90F8:10BT (Section 4.2) and demonstrate resulting improvements in performance for 90F8:10BT EML LEDs (Section 4.3). For devices with a ~5 % β-phase fraction induced by dipping, the luminance (at 10 V) and the maximum EQE were improved by 25 % and 61 % to 5940 cd m^{-2} and 1.91 %, respectively. In addition, the device stability was significantly enhanced, yielding 90 % luminance retention after 20-hour continuous operation from a starting luminance of ~3700 cd m^{-2}. The basis for these improvements was studied in detail, and it was found that an increase in hole mobility leading to correspondingly more balanced charge transport (Section 4.4), lowering of the hole injection barrier (Section 4.5), and a reduced trap density during device operation (Section 4.6) all contribute. Results shown in this chapter have been published elsewhere.[262]

4.2 β-Phase Generation and Resulting Optical Spectra

The β-phase was induced in 90F8:10BT thin films by both SVA and dipping. 90F8:10BT (weight-average molecular weight M_w = 55 000, polydispersity index n = 3.6, product name ADS233YE, American Dye Source) was dissolved in toluene (99.8 %, anhydrous, Sigma-Aldrich) at a concentration of 10 mg ml^{-1}, and the solution was spin-coated on

fused silica (Bright Crystals Technology) at 1000 rpm, giving us ~80 nm glassy 90F8:10BT thin films. For the SVA method, the sample was placed together with ~5 ml toluene in a vial (to induce a saturated toluene vapour) within a sealed container and kept there at room temperature for 24 hours in the dark. For the dipping method, the sample was immersed in a ~5 ml cyclohexane/isopropanol mixture (volume ratio = 1 : 1, both 99.5 % from Sigma-Aldrich) for 90 s and then dried under flowing nitrogen. The sample remained intact during dipping, but its thickness reduced, suggesting partial dissolution. Taking this into account, to achieve comparable thickness samples, the starting films for dipping were deliberately fabricated thicker by adjusting the spin-coating speed to 770 rpm in order that the final thickness would be the same as for glassy and SVA samples.

Table 4.1 | β-Phase Fraction and PLQE Values of Glassy and β-Phase 90F8:10BT Thin Films.

Sample	β-Phase Fraction (%)	PLQE (%)
Glassy	0	80 ± 5
β-Phase (SVA)	8 ± 1	80 ± 5
β-Phase (dipping)	5 ± 1	80 ± 5

Formation of the β-phase is confirmed by appearance of the characteristic peak at ~430 nm[159,161,246] in the absorption spectra (Fig. 4.2(a)) following both SVA and dipping. The difference spectra between glassy and β-phase samples (red areas in Fig. 4.2(b–c)) thus correspond to the absorption of β-phase chain segments, and can be used to estimate the β-phase fraction:[161,263]

$$\beta\text{-phase fraction} = \frac{A_\beta}{A_\beta + 1.08 A_\mathrm{g}} \tag{4.1}$$

where A_β is the area under the difference spectra, and A_g corresponds to the absorption of glassy F8 chain segments, obtained by integrating the glassy spectra (blue in Fig. 4.2(a–c)) in the 350–400 nm range. The factor 1.08 is the oscillator strength ratio of β- to glassy phases determined by density functional theory (DFT) calculations.[264] The achieved β-

phase fractions are listed in Table 4.1. We note that these numbers (8 ± 1 % and 5 ± 1 % for SVA- and dipping-induced β-phase samples, respectively) may have compromised accuracy due to the difficulty in precisely determining the area for glassy F8 chain segment absorption; the spectral range of 350–400 nm is a rough estimation. Nevertheless, the qualitative conclusion is clear: the SVA method yields a higher fraction of β-phase segments than dipping, although in both cases the glassy phase remains predominant.

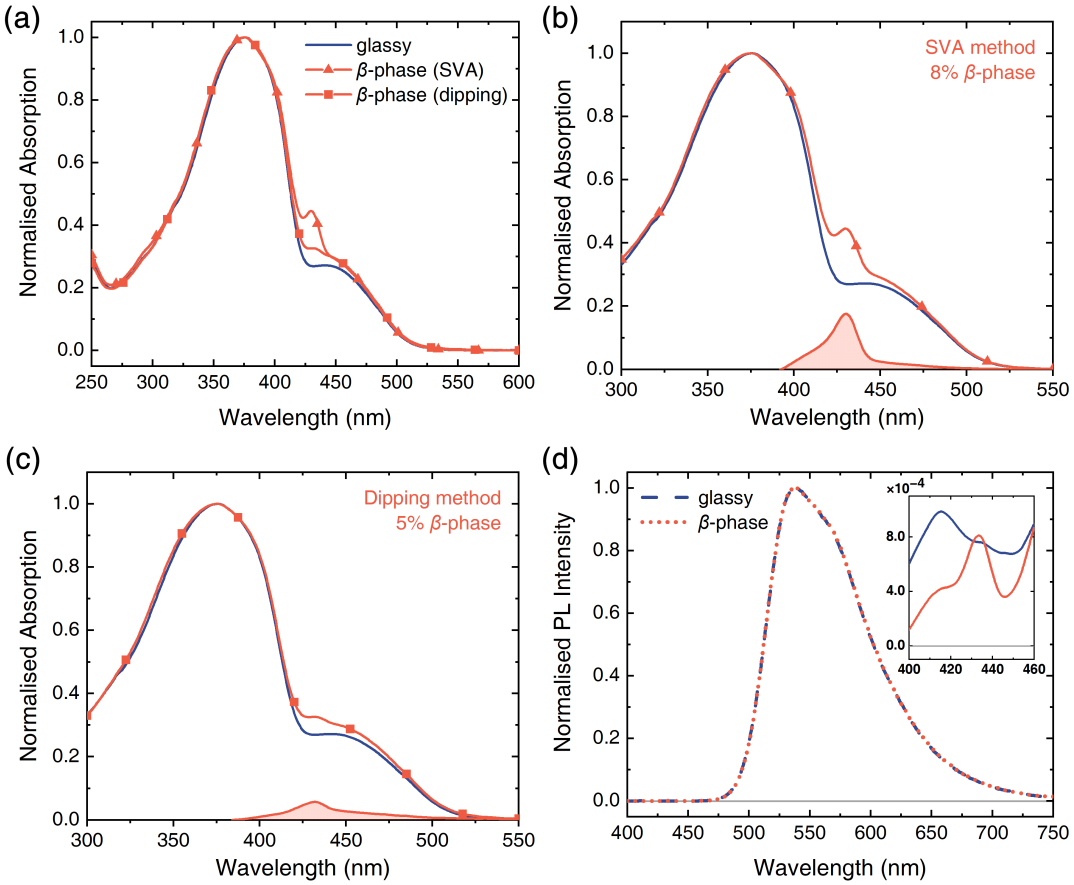

Figure 4.2 | Optical Spectra of Glassy and β-Phase 90F8:10BT Thin Films. (a) Normalised absorption spectra for glassy (blue) and β-phase 90F8:10BT samples (red) induced by SVA (with triangles) and dipping (with squares) methods. (b–c) Absorption spectra deconvolution of (b) SVA- and (c) dipping-induced β-phase samples to determine the β-phase fraction. The absorption spectra of β-phase (red) and glassy (blue) samples are overlaid, and the difference spectra (light red areas) represent the absorption of β-phase chain segments. (d) Normalised SSPL spectra for glassy (dashed blue line) and SVA-induced β-phase 90F8:10BT samples (dotted red line) excited at 380 nm, with the grey line indicating the zero PL intensity level. The inset to (d) shows the PL spectra from 400 nm to 460 nm on an expanded scale.

For glassy 90F8:10BT thin films, the main absorption peak locates at ~375 nm, close to the lowest energy $S_1 \leftarrow S_0$ absorption band in PFO (390 nm).[159,161] The second, longer wavelength peak at ~445 nm is attributed to the presence of the BT units, consistent with the 455 nm peak in F8BT absorption spectra.[265,266] This BT-moiety-centred contribution is also seen in truxene-cored starburst molecules with 20 % BT/ 80 % 9,9-dihexylfluorene side arms, appearing as a long-wavelength peak/shoulder close to 450 nm.[258] It is associated with the dipole-allowed optical transition between a delocalised HOMO and a BT-localised LUMO.[267] At low BT moiety content the LUMO is relatively destabilised, through there being little BT-to-BT interaction, and as a consequence the band is blue-shifted relative to F8BT.[267]

The 375 nm absorption band derives instead from the same delocalised HOMO but the transition is to higher-lying unoccupied molecular orbitals that have electron density largely on the fluorene moieties. The observed blue-shift of this peak relative to PFO has been postulated, in light of quantum-chemical calculations, to arise from a destabilisation of the associated unoccupied molecular orbitals through the effect that the BT moieties have on limiting the F8 sequence/conjugation length, just as occurs for oligomers with lower repeating unit numbers.[267]

Figure 4.2(d) shows the steady-state PL (SSPL) spectra of glassy and β-phase 90F8:10BT thin film samples excited at 380 nm, close to the extended-F8-sequence-centred absorption peak. The PL emission spectra are largely independent of the presence of β-phase chain segments and their generation method; the data shown here are for a thin film subjected to SVA. There is a single dominant emission band peaked at 538 nm which is very similar to that of F8BT (540 nm peak).[265,266] Expanding the intensity scale in the 400 nm to 460 nm spectral region (Fig. 4.2(d) inset) reveals weak features that show a dependence on the presence or otherwise of β-phase chain segments. For the glassy sample there is a peak located at ~415 nm, whereas for the β-phase sample the strongest peak is at ~435 nm with a shoulder at ~415 nm. These are close to the characteristic emission peaks for glassy and β-phase PFO at ~420 nm and ~440 nm[159,161,251] and are, therefore,

assigned to residual emission from a small fraction of excitons that avoid transfer to BT-centred excited states. The F8-to-BT excited-state energy transfer process is evidently very efficient, leading to a three orders of magnitude higher PL emission intensity from BT-centred states. This is despite the BT moieties comprising only 10 % of the polymer backbone units. As a result, whether the extended F8 backbone sequences in a 90F8:10BT film are in the glassy or β-phase does not significantly alter the SSPL spectrum. This contrasts with previous results[267] for a range of $F8_{(1-x)}$–$BT_{(x)}$ copolymers where F8 emission is still clearly visible in the SSPL spectrum for BT fractions up to 26 % ($x = 0.26$), but it should be noted that those measurements were performed for dilute solution samples. It is evident that energy transfer is much more effective in the solid state, likely a combined effect of more extended, rigid, and densely packed polymer chains.

One of the important parameters for EML materials is the photoluminescence quantum efficiency (PLQE), which enumerates the relative efficiency of radiative decay. Table 4.1 summarises the 90F8:10BT thin-film PLQE values for glassy and β-phase samples (generated by both SVA and dipping), which all show a high PLQE of 80 ± 5 %. This is reasonably consistent with reported values[267] although in that case the measurements were performed for dilute solutions and the consequent less-efficient energy transfer yields PLQE values that are closer to PFO than F8BT. For PFO thin films the PLQE ranges from 50 % to 80 % depending on the state of order (spin-coated glassy, nematic glassy, β-phase, or crystalline).[161,238] For F8BT, the PLQE has been reported to lie between 58 ± 5 % for thin films,[268] and 78 % for dilute solutions.[267]

In addition to measuring the PLQE values, we have also recorded PL decay transients to assess the radiative exciton lifetimes for thin film samples with and without the β-phase. Figure 4.3 shows the time-resolved PL (TRPL) results as well as the extracted lifetimes, derived from single exponential fits, with the coefficient of determination $R^2 > 0.995$. The lifetimes, 2.502 ns and 2.286 ns for glassy and β-phase 90F8:10BT thin films, respectively, are close to but slightly longer than that for F8BT (2.03 ns) and substantially longer than for PFO (227 ps).[268] The single exponential decay and the long lifetime is consistent

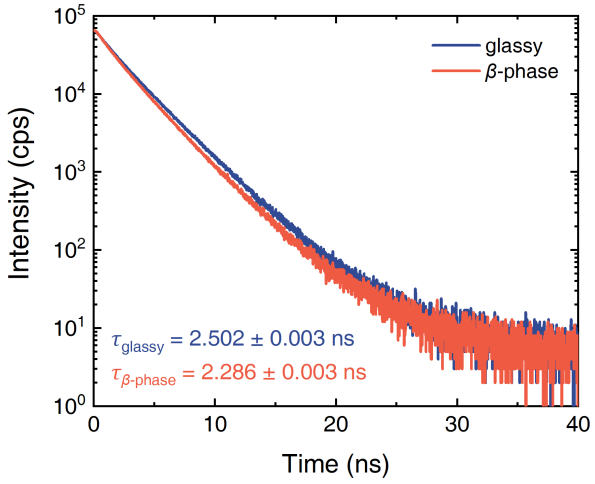

Figure 4.3 | TRPL Decay Curves of Glassy (blue) and β-Phase (red) 90F8:10BT Thin Films. The exciton lifetimes were extracted from single exponential fits ($R^2 > 0.995$).

with (i) the exciton being localised in the vicinity of the BT units (as also deduced from the spectral data) and (ii) energy transfer from extended F8 sequences to BT sites being highly efficient and much more rapid than the subsequent decay. The excitons in 90F8:10BT additionally have a ~9 % shorter lifetime when the β-phase is present. Given that the PLQE values show no significant difference between glassy and β-phase samples (Table 4.1), the decrease in lifetime is likely due to an increase in oscillator strength, consistent with the expected increase in conjugation length.[5]

Given again that there is no change in PLQE when the β-phase is generated, it might be expected that no improvement in LED performance would be engendered by this conformation change. However, as shown in the next section, generation of β-phase chain segments is significantly advantageous to the performance of 90F8:10BT-based LEDs.

4.3 Polymer Light-Emitting Diode Performance

To examine the influence of the β-phase in 90F8:10BT on LED performance, we fabricated devices with a conventional bottom emission structure (Fig. 4.4(a)), i.e. ITO / PEDOT:PSS (30 nm) / TFB (15 nm) / 90F8:10BT (80 nm) / LiF (1 nm) / Al (100 nm). The expected energy level diagram is shown in Fig. 4.4(b) using literature

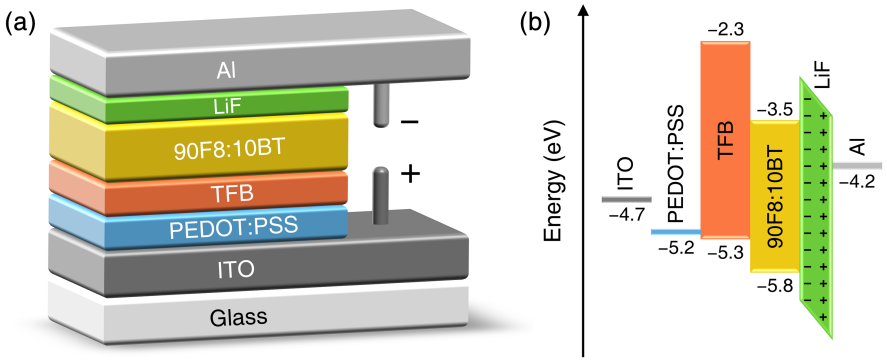

Figure 4.4 | (a) Schematic 90F8:10BT bottom emission LED structure and (b) nominal device energy level diagram.

values for the electron affinities (EAs), ionisation potentials (IPs), and work functions (WFs).[200,261,269–271] On the pre-patterned ITO-coated glass substrates (sheet resistance = 10 Ω sq^{-1}, Thin Film Devices), PEDOT:PSS solution (Clevios™ PVP AI4083, Heraeus) was spin-coated at 2500 rpm, and then annealed at 150 °C for 15 min in air to remove residual moisture. Next, a poly(9,9-dioctylfluorene-*alt*-*N*-(4-*sec*-butylphenyl)diphenylamine) (TFB, $M_w > 30\,000$, Sigma-Aldrich) layer, functioning as blocking electrons and reducing exciton quenching,[174] was spin-coated in the glovebox from 2 mg ml^{-1} toluene solution at 1000 rpm, and then annealed at 180 °C for 60 min to enable partial crosslinking,[272] thus preventing damage from the same toluene solvent used to deposit 90F8:10BT film on top.

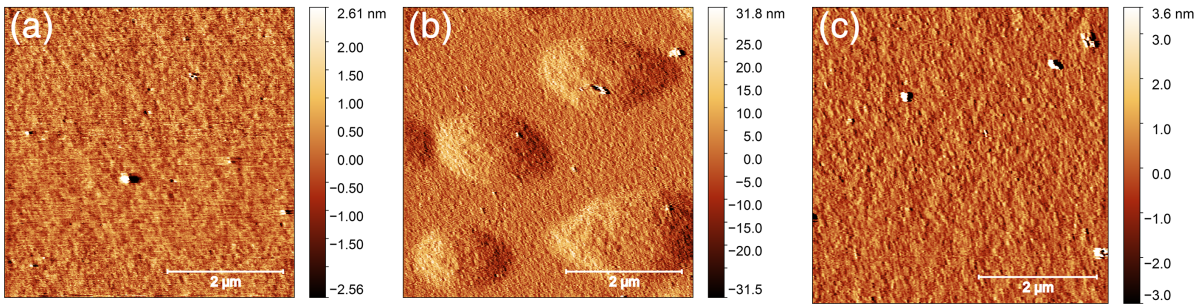

Figure 4.5 | AFM Images of Glassy and *β*-Phase 90F8:10BT Thin Films on Fused Silica. (a) Glassy sample (as spin-coated). (b–c) *β*-phase samples subjected to (b) SVA and (c) dipping. Scale bars in all figures represent 2 µm. The root-mean-square roughness (R_{rms}) is 1.02 nm, 11.57 nm, and 2.40 nm, respectively.

Concerning the EML, 90F8:10BT thin films, we chose the dipping method to generate β-phase chain segments owing to the resultant smoother surface compared with the sample subjected to SVA, as shown by AFM images in Fig. 4.5. The high roughness of the latter ($R_{\mathrm{rms}} = 11.57\,\mathrm{nm}$) is undesirable as it can lead to non-uniform emission and a greater tendency for dielectric breakdown (Section 2.6.2). EMLs were deposited on the partly crosslinked TFB layer using the same protocol mentioned in the preceding section. The LED fabrication was completed by transferring the 90F8:10BT coated samples to a thermal evaporator where LiF (at $0.2\,\mathrm{Å\,s^{-1}}$, 99.99 %, Testbourne) and Al (at $1\,\mathrm{Å\,s^{-1}}$, 99.99 %, Kurt J. Lesker) were deposited to form the top cathode.

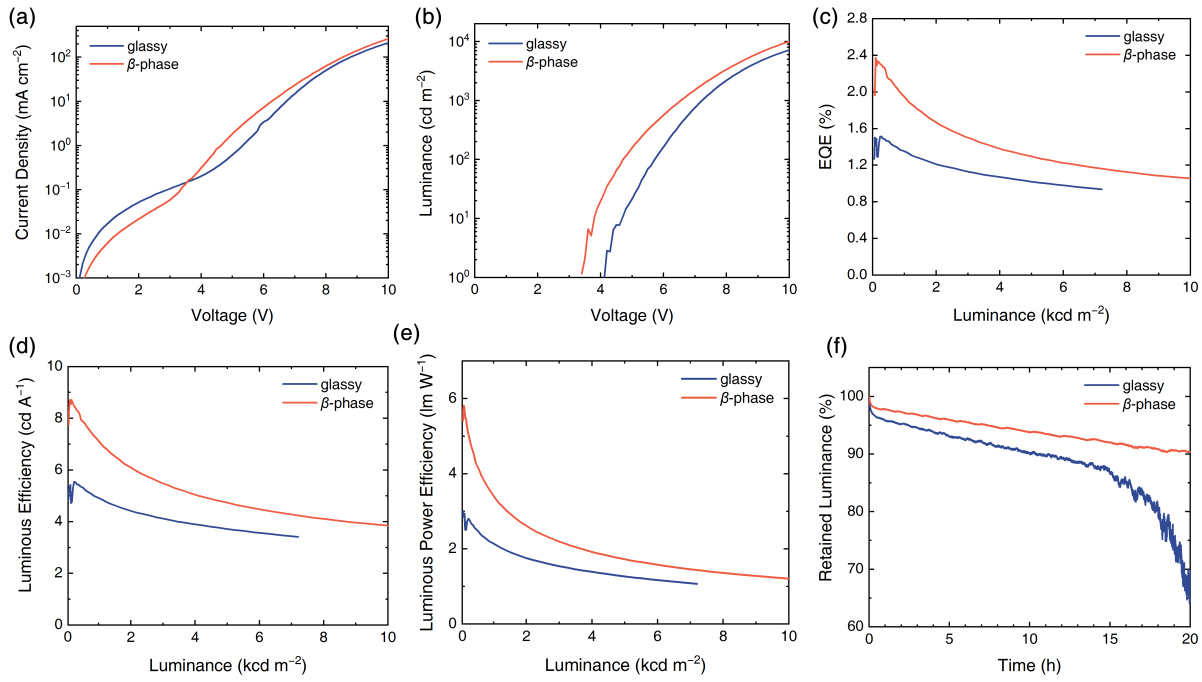

Figure 4.6 | Typical Device Performance and Operational Stability of Glassy (blue) and β-Phase (red) 90F8:10BT LEDs. (a) J–V characteristics; (b) L–V characteristics; (c) EQE, (d) luminous efficiency, and (e) luminous power efficiency, as a function of luminance; (f) accelerated device lifetime test results, performed on encapsulated devices held at constant current density $J = 80\,\mathrm{mA\,cm^{-2}}$.

Figure 4.6 presents device characteristics for both glassy (blue) and β-phase (red) 90F8:10BT LEDs sharing the same emission spectrum (Fig. 4.12) peaked at ~535 nm in green. Figure 4.6(a–b) shows the current density (J) and luminance (L) versus voltage (V)

data, respectively. The current densities at 10 V are similar, with a slightly higher value for the β-phase LEDs, but the current turns on strongly at a significantly lower voltage in the latter case. The L–V curves show that the strong current turn-on correlates with light emission and the β-phase 90F8:10BT LEDs have higher luminance all the way up to 10 V. The turn-on voltage (the voltage at which $L = 1\,\mathrm{cd\,m^{-2}}$) drops from 4.1 V for glassy to 3.4 V for β-phase and the luminance at 10 V increases from ~7000 to $> 10\,000\,\mathrm{cd\,m^{-2}}$.

Figure 4.6(c–e) shows the EQE, luminous efficiency (η_L), and luminous power efficiency (η_LP), respectively, as a function of luminance for both devices. The peak EQE values for β-phase LEDs reach ~2.4 % for low luminance and remain above 1 % for luminance up to $> 10\,000\,\mathrm{cd\,m^{-2}}$. For glassy devices the maximum EQE, also at low luminance, is ~1.5 %. The η_L and η_LP exhibit similar trends; for β-phase devices the peak $\eta_\mathrm{L} \approx 8.6\,\mathrm{cd\,A^{-1}}$ and the peak $\eta_\mathrm{LP} \approx 5.8\,\mathrm{lm\,W^{-1}}$ whilst for glassy devices maximum values are ~5.5 $\mathrm{cd\,A^{-1}}$ and ~2.9 $\mathrm{lm\,W^{-1}}$, respectively.

Generation of the β-phase in another PFO-based copolymer[200] and PFO itself[273] has been reported to improve the LED operational stability, so we have also undertaken an accelerated device lifetime test for the 90F8:10BT LEDs. The measurement was carried out using encapsulated devices held at constant current density $J = 80\,\mathrm{mA\,cm^{-2}}$ under ambient conditions. The initial luminance for glassy and β-phase devices were ~2800 and ~3700 $\mathrm{cd\,m^{-2}}$, respectively.

Figure 4.6(f) shows fractional luminance retention as a function of time. After 20-hour continuous operation, the luminance of β-phase devices still exceeds 90 % of their initial value. However, for glassy devices, ~35 % of the starting luminance is lost over the same period. Both devices see a fast, initial decay followed by a more gradual decay with an approximately constant slope. The β-phase devices decay less during the initial rapid drop and show a shallower slope thereafter. In addition, after about 14 hours the glassy devices abruptly degrade with a noisy luminance fluctuation superimposed on top of the sharp decay. The time for the device luminance to drop to 90 % of its initial value is denoted $\mathrm{LT_{90}}$, and we find $\mathrm{LT_{90}} = 10.4\,\mathrm{h}$ for the glassy devices and $> 20\,\mathrm{h}$ for β-phase

devices. Therefore, we conclude that, as previously reported, device operational stability is significantly improved by the introduction of β-phase chain segments.

Table 4.2 | Summary of the Device Performance and Lifetime of Glassy and β-Phase 90F8:10BT LEDs.

	Glassy device	β-Phase device	Improvement
Luminance at 10 V ($\mathrm{cd\,m^{-2}}$)[a]	4750 ± 470	5940 ± 610	25.1 %
Maximum EQE (%)[a]	1.19 ± 0.12	1.91 ± 0.11	60.5 %
Maxumum η_L ($\mathrm{cd\,A^{-1}}$)[a]	4.10 ± 0.34	6.18 ± 0.50	50.7 %
Maxumum η_LP ($\mathrm{lm\,W^{-1}}$)[a]	2.22 ± 0.22	3.69 ± 0.39	66.3 %
$\mathrm{LT_{90}}$ (h)[b]	10.4	> 20	> 92.3 %

[a] Averaged values from more than 20 devices of each type;
[b] Time for device luminance to drop to 90 % of its original value at constant current density $J = 80\,\mathrm{mA\,cm^{-2}}$.

Table 4.2 summarises the average performance parameters for more than 20 devices of each type. It is evident that generating the β-phase in 90F8:10BT systematically boosts LED performance in luminance, efficiencies (EQE, η_L, and η_LP), and operational stability ($\mathrm{LT_{90}}$). In the following three sections we shall successively discuss the factors that contribute to the observed improvement in EQE, luminance, and operational stability.

4.4 External Quantum Efficiency (EQE) Enhancement

The EQE of LEDs using fluorescent EMLs can be described as a product of terms that relate to the physical processes involved:[5]

$$\mathrm{EQE} = \eta_\mathrm{CC} \times \eta_\mathrm{S/T} \times \mathrm{PLQE} \times \eta_\mathrm{out} \tag{4.2}$$

where (i) η_CC is the probability that injected holes and electrons Coulombically capture to form an exciton; (ii) $\eta_\mathrm{S/T}$ is the ratio of singlet to triplet excitons that form; (iii) PLQE is the radiative probability for singlet exciton decay; and (iv) η_out is the out-coupling

efficiency, namely the fraction of photons emitted within the device that escape to the exterior. For glassy and β-phase 90F8:10BT EMLs within an otherwise identical device structure, $\eta_{S/T}$ and η_{out} are expected to be largely similar. Moreover, since their PLQEs were also found to be the same (Table 4.1), the improvement in EQE is most probably related to the Coulomb capture probability η_{CC}. An effective way to increase η_{CC} is to tune the position of the recombination zone, which ideally should be at the centre of the EML, or in other words, away from the interfaces that favour non-radiative quenching of the excitons generated. This can be realised by balanced charge injection and transport, ideally through the achievement of Ohmic contacts and comparably high hole and electron mobilities. To investigate this further, we measured the hole and electron mobilities in both glassy and β-phase samples using two different methods, namely (i) metal–insulator–semiconductor structure-based charge carrier extraction by linearly increasing voltage (MIS-CELIV) and (ii) negative differential susceptance ($-\Delta B$) measurements.

Samples for MIS-CELIV measurements were fabricated with the structures ITO / PEDOT:PSS / 90F8:10BT / MgF_2 (10 nm) / Al for hole mobility and ITO / MgF_2 (10 nm) / 90F8:10BT / LiF / Al for electron mobility measurements. For the $-\Delta B$ method, test samples were either an ITO / PEDOT:PSS / 90F8:10BT / MoO_3 (10 nm) / Al hole-only device or an ITO / ZnO (30 nm) / 90F8:10BT / LiF / Al electron-only device. Here MgF_2 (99.99 %, Kurt J. Lesker) and MoO_3 (99.95 %, Testbourne) were thermally evaporated (both at 0.2 Å s^{-1}) while ZnO was solution-processed following the published method.[274] All other layers were fabricated using the same protocols as in LED devices.

Representative MIS-CELIV current density transients are shown in Fig. 4.7(a–b), and the mobility values extracted from the full set of measurements according to Eq. (3.9) are presented in Fig. 4.7(c). Glassy samples have an electron mobility (4.9×10^{-7} cm^2 V^{-1} s^{-1}) that is more than twice the hole mobility (2.2×10^{-7} cm^2 V^{-1} s^{-1}). Generation of β-phase chain segments resolves this imbalance, yielding a more than two-fold (118 %) mobility increase for holes to 4.7×10^{-7} cm^2 V^{-1} s^{-1}, without significantly affecting the electron mobility other than by desirably reducing its spread. β-phase-enhanced hole transport

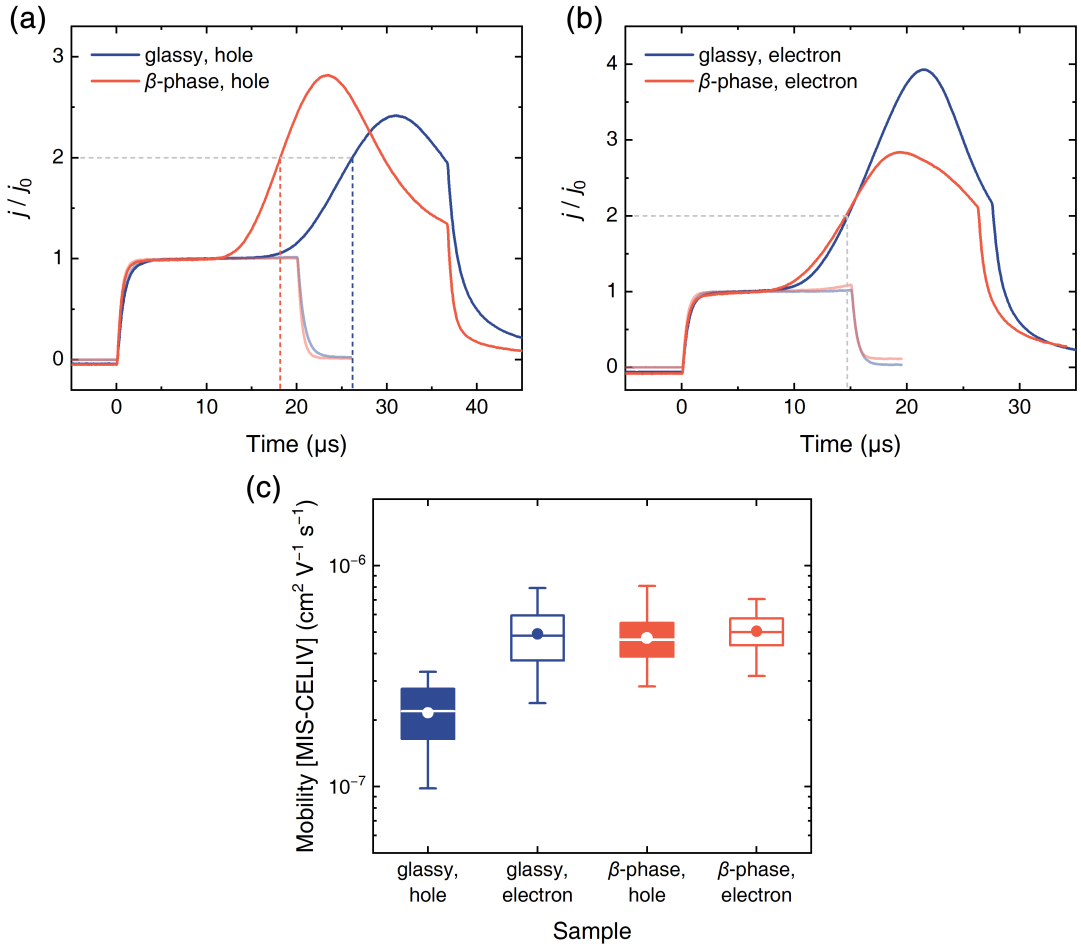

Figure 4.7 | MIS-CELIV-Derived Hole and Electron Mobilities for Glassy and β-Phase 90F8:10BT. (a) Typical hole and (b) electron MIS-CELIV transients for glassy (blue) and dipping-induced β-phase (red) 90F8:10BT thin films. The corresponding transients in the absence of injection (offset voltage = 0 V) are shown by the faint curves that turn off at ~20 µs. The dashed lines highlight the $j = 2j_0$ condition. Results in (a) were obtained with a voltage increasing rate of 600 V ms^{-1}, whereas in (b) the rate was 800 V ms^{-1}. (c) Extracted mobility from more than 10 samples for each measurement, with symbols displaying the minimum to maximum value range (vertical lines with end caps), the first and third quartiles (the bottom and top boundaries of the box, respectively), and the median and mean values (horizontal line and circle inside the box, respectively).

has already been observed in PFO,[162,275] likely due to the longer conjugation length of β-phase chain segments, a more ordered and energetically favourable environment for hole transport, and a more interchain-connected microstructure. With β-phase chain segments present, hole and electron mobilities in 90F8:10BT become very closely matched, which is supportive of a favourable η_{CC}.

The MIS-CELIV mobilities are relatively low compared with typical time-of-flight (ToF) or dark injection transient (DIT) measurement values on PFO and F8BT[276,277] but not dissimilar to what is found for the copolymer 90F8:10BSP in which 10 % of BSP moieties are included in an otherwise F8 backbone.[200] Different measurements can yield different mobility values in the case that trapping effects occur and the measurements involve a large difference in charge carrier density, e.g. OFET mobility (high density) versus SCLC- or ToF-mobility measured in diode structures (low density),[140] although there are also conjugated polymers for which the mobility is charge-carrier-density-independent (Section 2.4.3.3).[82]

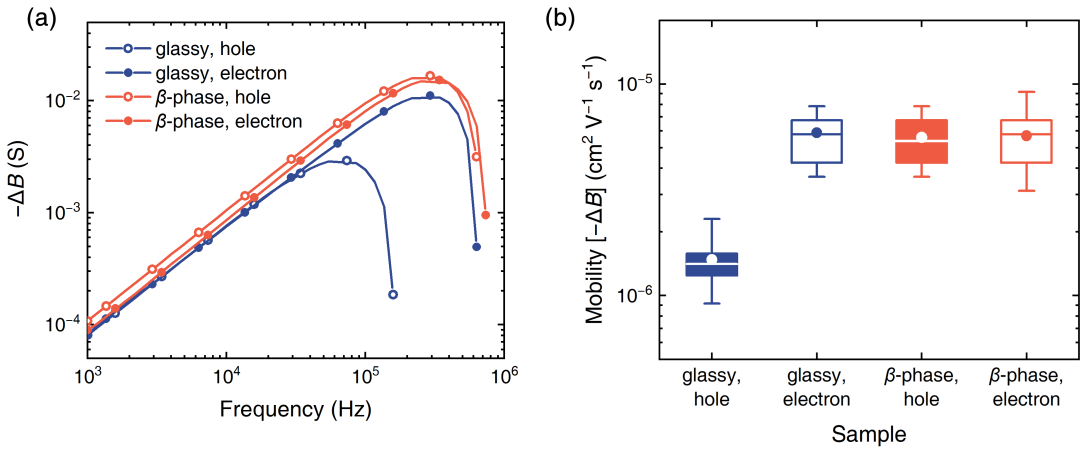

Figure 4.8 | $-\Delta B$-Derived Hole and Electron Mobilities for Glassy and β-Phase 90F8:10BT. (a) Typical $-\Delta B$ measurement data for hole (with open circles) and electron (with solid circles) mobilities of glassy (blue) and β-phase (red) 90F8:10BT thin films with the applied direct voltage $V_D = 7\,V$. (b) Extracted mobility from more than 10 samples for each measurement, with symbols displaying the minimum to maximum value range (vertical lines with end caps), the first and third quartiles (the bottom and top boundaries of the box, respectively), and the median and mean values (horizontal line and circle inside the box, respectively).

To check the reliability of the MIS-CELIV mobilities, we employed a second $-\Delta B$ method. The typical $-\Delta B$ vs f curves are presented in Fig. 4.8(a), and the $-\Delta B$-derived mobility values according to Eq. (3.11) are shown in Fig. 4.8(b). The same qualitative changes are observed, albeit with higher derived mobility values for $-\Delta B$ than MIS-CELIV (Table 4.3). Glassy 90F8:10BT has hole mobility that is significantly lower than

its electron mobility. Balanced charge transport then ensues following β-phase generation with the hole mobility increasing from 1.5×10^{-6} to $5.6\times10^{-6}\,\mathrm{cm^2\,V^{-1}\,s^{-1}}$ and the electron mobility marginally decreasing from 5.9×10^{-6} to $5.7\times10^{-6}\,\mathrm{cm^2\,V^{-1}\,s^{-1}}$.

Table 4.3 | Summary of the hole (μ_h) and electron (μ_e) mobilities for glassy and β-phase 90F8:10BT samples extracted from MIS-CELIV and $-\Delta B$ measurements.[a]

	MIS-CELIV			$-\Delta B$		
	μ_h ($\mathrm{cm^2\,V^{-1}\,s^{-1}}$)	μ_e ($\mathrm{cm^2\,V^{-1}\,s^{-1}}$)	$\mu_\mathrm{h}/\mu_\mathrm{e}$	μ_h ($\mathrm{cm^2\,V^{-1}\,s^{-1}}$)	μ_e ($\mathrm{cm^2\,V^{-1}\,s^{-1}}$)	$\mu_\mathrm{h}/\mu_\mathrm{e}$
Glassy	$(2.16\pm0.67)\times10^{-7}$	$(4.91\pm1.37)\times10^{-7}$	0.44	$(1.48\pm0.47)\times10^{-6}$	$(5.88\pm1.57)\times10^{-6}$	0.25
β-Phase	$(4.71\pm1.23)\times10^{-7}$	$(5.06\pm1.02)\times10^{-7}$	0.93	$(5.59\pm1.45)\times10^{-6}$	$(5.69\pm1.96)\times10^{-6}$	0.98
Improvement	118.1 %	3.1 %	—	277.7 %	−3.2 %	—

[a] Averaged values from more than 10 samples for each type.

Factors that may influence the difference between MIS-CELIV and $-\Delta B$ absolute mobility values (Table 4.3) are expected to be related to the assumptions that underpin the mobility derivations in two methods, leading to their respective systematic errors. It has been previously shown that the MIS-CELIV method can result in overestimation of the mobility when the metal and the OSC form an Ohmic contact, whereas for an injection barrier larger than ~0.47 eV the mobility may be underestimated.[278] Here, the nominal energy levels (Fig. 4.4(b)) would lead to an injection barrier of 0.5 eV, meaning the acquired MIS-CELIV mobilities are likely to be slightly lower than the true values. Likewise, for the $-\Delta B$ measurement, the numerical factor 0.54 in its principle, Eq. (3.11), was obtained from a case study of a poly(*p*-phenylene vinylene) derivative.[211,213] Whilst this value has been shown to be valid for different conjugated polymers, a deviation of ±0.1 is still possible when the charge transport is subject to different degrees of dispersion.[279] If we assume the charge transport is highly dispersive in 90F8:10BT films, i.e. the factor should be larger than 0.54, then $-\Delta B$ mobilities presented here slightly overestimate the true values. This hypothesis is supported by dark injection transient (DIT) results for

90F8:10BT samples (data not shown here), where no distinct maximum in the transient current density can be observed, indicating a high degree of charge carrier dispersion.[205] This offers an interesting topic for future research on the charge transport nature in 90F8:10BT, but the discussion here has indeed reduced the gap between the measured MIS-CELIV and $-\Delta B$ mobilities.

The qualitative effect of β-phase chain segment formation in leading to balanced electron and hole mobility in these LEDs, confirmed by two independent methods, explains the observed improvement in EQE, with the resulting more centred recombination zone reducing interfacial quenching and any tendency to charge carrier leakage.

4.5 Luminance Enhancement

As noted in Section 4.3 and shown in Fig. 4.6(b), the turn-on voltage in β-phase LEDs is lower than that for glassy devices, and β-phase LEDs yield higher luminance at a given voltage, from turn-on all the way up to 10 V. The measured turn-on voltage is composed of the built-in voltage V_{bi} required to equilibrate the Fermi levels of the anode and cathode, and the additional voltage needed to assist charge carriers to overcome the electron/hole injection barriers (Section 2.4.2.1).[5] Since the glassy and β-phase LEDs are identical other than their 90F8:10BT EML microstructure, V_{bi} should be the same for both. The lower turn-on voltage in β-phase LEDs thus indicates that one or both of the charge injection barriers must be lower. To further explore this behaviour, both J–V and C–V (i.e. capacitance–voltage) measurements were performed on unipolar diodes (with the same device structure as in $-\Delta B$ measurements) and LEDs, respectively.

Given that the J–V curves for electron-only glassy and β-phase diodes are almost identical (Fig. 4.9(a)), as also are their electron mobilities (Table 4.3), we can conclude that the β-phase does not greatly affect electron injection and transport properties. This is somewhat predictable since the BT moieties provide the dominant contribution to the LUMO.[267] In contrast, the hole current densities for glassy and β-phase diodes show significantly different voltage dependences (Fig. 4.9(b)). At low voltages, for both devices

$J \propto V$, as expected for Ohmic transport associated with a background density of charge carriers within the film; for most conjugated polymers, as here, the background charge is p-type, potentially linked to oxidative doping by catalyst residues. The inverse film thickness and the conductivity are expected to determine the magnitude of the current density in this Ohmic regime (Eq. (2.8)).

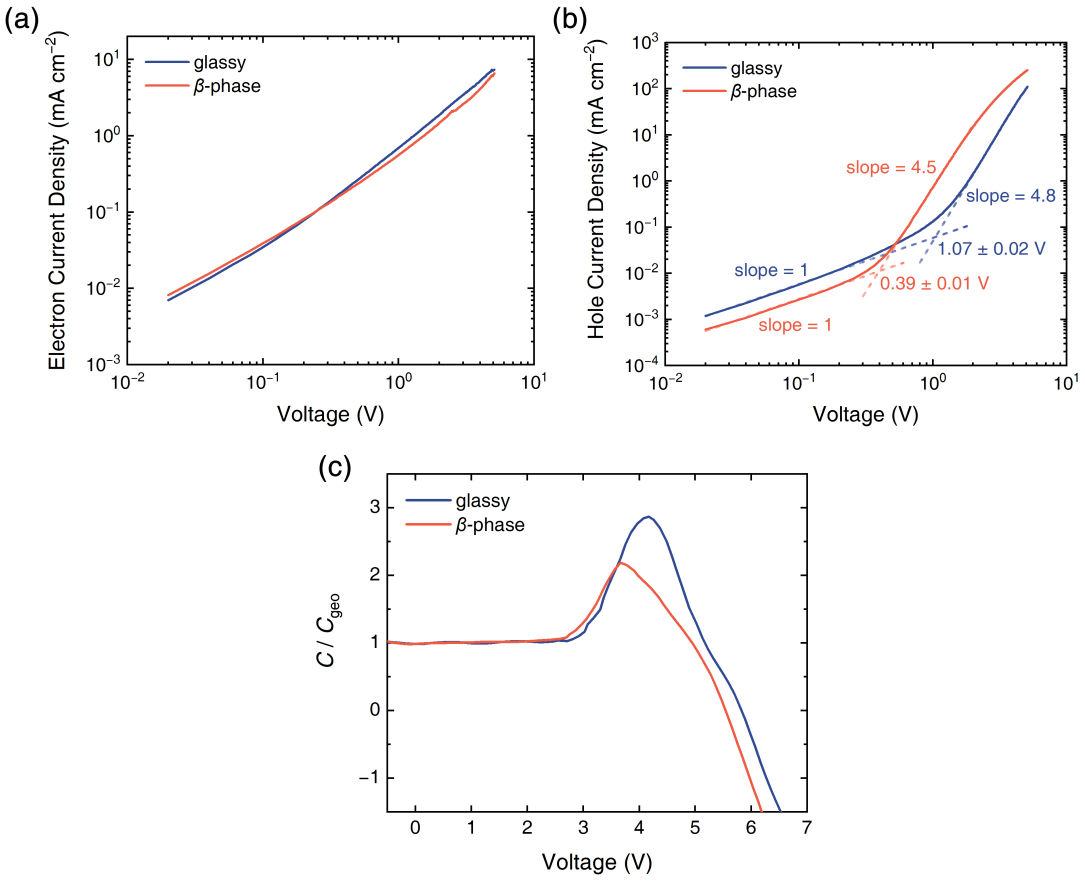

Figure 4.9 | (a–b) J–V characteristics for (a) electron-only and (b) hole-only glassy (blue) and β-phase (red) 90F8:10BT unipolar diodes plotted on a double logarithmic scale. In (b), linear fits (dashed lines) are shown to the Ohmic and TC-SCLC regimes for both microstructures. The transition voltage between these two regimes is estimated from the intercept of the linear fits. (c) C–V characteristics for glassy (blue) and β-phase (red) 90F8:10BT LEDs.

At higher voltages, above a threshold, the slope becomes much steeper, indicative of trap-controlled SCLC (TC-SCLC) with $J \propto V^{m+1}$ (Section 2.4.3.4).[280] Here $m = 3.8$ for glassy and $m = 3.5$ for β-phase devices. In the case of an exponential trap distribution, the lower value of m would suggest a narrower trap distribution for the β-phase 90F8:10BT,

consistent with a higher degree of molecular order. However, in order to investigate the trap distribution in detail, a full temperature- and film thickness-dependent study would be required,[280] which is beyond the scope of this work. The transition from the Ohmic to TC-SCLC regime, estimated from the intercept of linear fits to the two regimes, is seen at (1.07 ± 0.02) V and (0.39 ± 0.01) V for glassy and β-phase devices, respectively. The lower transition voltage in β-phase diodes confirms that their hole injection barriers must be lower. The transition is also significantly more abrupt for β-phase diodes, again consistent with a narrower trap distribution. The lower injection barrier for β-phase devices is further in line with prior results for PFO where β-phase formation was also seen to reduce the turn-on voltage.[200] The chain-extended β-phase conformation is expected to reduce the IP (more delocalised π-electron density),[160,238,252,281] and calculations for fluorene octamers yield a ~120 to 140 meV rise in the HOMO level.[282] The optical gap is correspondingly ~160 meV smaller for β-phase, compared with glassy PFO.[283] An additional reference point (upper bound) for the HOMO of β-phase chain segments is that they are deeper-lying than the cyclic-voltammetry-determined IP of 95F8:5BSP, namely ~5.5 eV; β-phase formation does not alter the turn-on voltage of 95F8:5BSP LEDs.[200]

The injection barriers were also investigated by measuring the C–V characteristics for glassy and β-phase 90F8:10BT LEDs on the Fluxim PAIOS measurement platform with Characterization Suite 4.2 software. The capacitance was determined by applying the superposition of a small alternating voltage (amplitude $V_A = 0.05$ V, frequency $f = 1$ kHz) and a varying direct bias voltage V_D to the device. Figure 4.9(c) shows a plot of the capacitance normalised to the geometric capacitance, C_{geo}, as a function of V_D. When V_D is small, there is no significant charge carrier density present within the device, so the ratio $C/C_{geo} = 1$. An increase in capacitance is then observed from ~2.7 V for both devices due to the injection of electrons and/or holes and their accumulation within the structure. From the energy level diagram (Fig. 4.4(b)), hole injection is expected to have a 0.5 eV barrier height whilst the LiF / Al cathode with a work function of ~2.75 eV should form an Ohmic contact to 90F8:10BT.[271] It is, therefore, expected that electrons will be

injected first (at 2.7 V), with very similar behaviour for both 90F8:10BT microstructures, as is indeed seen. At higher voltages, holes will also be able to surmount their associated barrier and be injected, resulting in charge carrier recombination to form excitons and concomitantly a fall in capacitance. The voltage, V_{p}, at peak capacitance has previously been shown by numerical simulation to be a measure of the second injection barrier.[284] In Fig. 4.9(c), the V_{p} values for glassy and β-phase devices are (4.2 ± 0.1) V and (3.7 ± 0.1) V, respectively, confirming again that the hole injection barrier is reduced by β-phase chain segment formation.

The sensitivity of hole-related and the contrasting insensitivity of electron-related injection and transport to β-phase formation can be understood from previous quantum-chemical calculations. Winfield et al.[267] have shown that for F8–BT oligomers with BT ratio varying from 8.3 % to 50 %, the LUMO is always highly localised on the BT moieties, whereas the HOMO delocalises to the degree allowed by the chain geometry. Torsional twists limit wavefunction spread and, therefore, during β-phase formation where the change in conformation is to a chain-extended planar structure, the HOMO rises in energy and the hole injection barrier lowers. In contrast, the BT-dominated LUMO is barely affected by the change in F8-sequence conformation, leaving the electron injection barrier largely unchanged. In addition, Cornil et al.[281] have calculated the geometry-dependent interchain transfer integrals, critical to mobility in the hopping transport regime. In F8BT (the alternating copolymer) when two neighbouring polymer chains translate relative to each other along their long-chain axis, it was found that the transfer integral for hole transport undulates as a function of the degree of translation whilst that for electron transport is fairly constant when the BT units on one chain face F8 units on the other. Here in 90F8:10BT, only 10 % of the chain is comprised of BT units but a cautious generalisation should still be possible. This would suggest that adoption of the β-phase should alter the transfer integral for hole transport, and thus the hole mobility. However, the low BT content makes it highly likely that BT units on one polymer chain will face F8 units on neighbouring chains, making the transfer integral for electron transport, as

well as the electron mobility, rather insensitive to the conformation change.

The reduced hole injection barrier engendered by β-phase chain segment formation, in conjunction with more balanced charge transport, leads to an increased exciton formation rate and explains the higher luminance observed. One question that may arise here is whether the dipping process can result in any significant changes in the interface between the TFB and 90F8:10BT layers due to intermixing. We note, however, in this context that the TFB layer was crosslinked at 180 °C for 1 h before the 90F8:10BT films were spin-coated on top. In a previous paper[272] it was shown that after crosslinking treatment used here, the TFB layer is highly solvent resistant, so significant mixing is not expected. Furthermore, the same spin-coating parameters were used for both the films that subsequently remained in the glassy state and those that were dipped to generate the β-phase. Any intermixing at the interface might be expected to more readily occur during this step, given the solvents used, than during the dipping step and thus to be the same for both device types (glassy and β-phase). Finally, intermixing is even less likely to occur exclusively in the presence of poor solvents (cyclohexane and isopropanol) used for dipping.

4.6 Operational Stability Enhancement

Time-resolved electroluminescence (TREL) measurements were performed on glassy and β-phase LEDs to investigate the operational stability differences shown in Fig. 4.6(f). Before being tested, the encapsulated devices were continuously stressed in air under constant current density $J = 80\,\mathrm{mA\,cm^{-2}}$ for different durations t, be it 0 (fresh), 10, or 20 hours. Measurements were carried out on the Fluxim PAIOS measurement platform with Characterization Suite 4.2 software, and a 10 V, 500 µs voltage pulse was applied to the device, with the resultant time-dependent EL intensity recorded. Typical TREL curves comprise four features (Fig. 4.10(a)): (i) A delayed onset of EL intensity following the application of the voltage pulse, with a characteristic delay time τ_d (Fig. 4.10(b) inset). This time can be used to extract the effective mobility μ_eff that combines the contribution

from the hole and electron mobilities:[285]

$$\mu_{\text{eff}} = \frac{d^2}{\tau_{\text{d}}(V - V_{\text{bi}})} \tag{4.3}$$

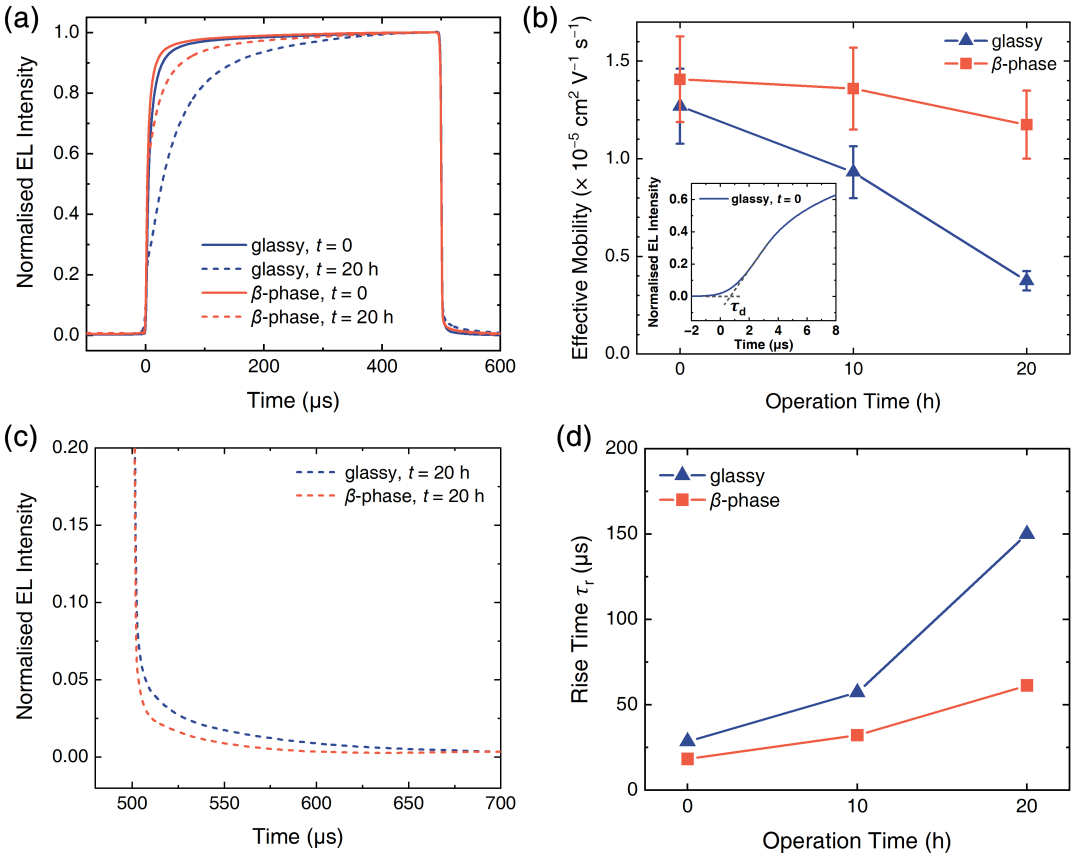

Figure 4.10 | TREL Curves and the Deduced Effective Mobilities and EL Rise Times for Glassy and β-Phase 90F8:10BT LEDs during Extended Operation. (a) TREL curves for glassy (blue) and β-phase (red) 90F8:10BT LEDs before (solid lines) and after (dashed lines) 20-hour continuous operation at constant current density $J = 80\,\text{mA}\,\text{cm}^{-2}$, with starting luminance values of ~2800 and ~3700 $\text{cd}\,\text{m}^{-2}$ for glassy and β-phase devices, respectively. (b) Deduced effective mobilities for glassy (blue triangles) and β-phase (red squares) 90F8:10BT LEDs during extended operation using the delay time τ_{d}; the inset shows a typical data set (a fresh glassy device) used in the extraction of τ_{d}. (c) Enlarged turn-off response ($t > 500\,\mu\text{s}$) for glassy (blue) and β-phase (red) 90F8:10BT LEDs after 20-hour operation. (d) EL rise times τ_{r} for glassy (blue triangles) and β-phase (red square) 90F8:10BT LEDs during extended operation. The lines joining data points in (b) and (d) are a guide to the eye. The TREL curves after 10-hour operation are omitted for clarity in (a) and (c).

where V_{bi} is the built-in voltage and, assuming the charges transit the whole device (i.e. none is trapped within it), d is the thickness of the active layer. (ii) The rise in EL intensity to its steady-state value, with a characteristic rise time τ_r to reach 90 % of the maximum luminance. A longer τ_r signals lower mobility and/or higher trap density. (iii) Steady-state EL whilst the voltage pulse is on. (iv) The EL decay after turning the applied voltage off. During the decay, oppositely charged carriers can de-trap and recombine to yield delayed EL emission. Slow decays therefore indicate higher trap densities. The first and fourth features, respectively, reflect charge carrier mobility and trap density, and the second is representative of both.

Figure 4.10(b) shows the effective mobility values extracted from τ_d. The measurement on the initial β-phase device yields higher mobility than that for the glassy device, consistent with the results from MIS-CELIV and $-\Delta B$ measurements (Table 4.3). During continuous operation, the effective mobility for both devices reduces and the difference between them increases, especially after 10 hours, signaling a significant degradation in charge transport for the glassy LED. After 20-hour operation, the effective mobility in the β-phase device drops to $1.17 \times 10^{-5}\,\mathrm{cm^2\,V^{-1}\,s^{-1}}$, i.e. 84 % of its initial value, but for the glassy one only 29 % of the initial effective mobility, $3.74 \times 10^{-6}\,\mathrm{cm^2\,V^{-1}\,s^{-1}}$, remains. The higher μ_{eff} for the β-phase LED after extended operation, relative to the glassy, was also confirmed by additional $-\Delta B$ measurements on LED structures before and after continuous ageing (Fig. 4.11), though the absolute mobility values are not exactly the same as derived from TREL results due to their different underlying principles.

The EL decay curves after 20-hour operation, shown on an expanded intensity scale in Fig. 4.10(c), have a correspondingly slower drop-off in luminance for glassy devices, suggesting that a higher trap density is present. Such traps are expected to partly account for the lower and faster-worsened μ_{eff} for glassy LEDs. The origin of the traps in this case remains unknown, but a variety of chemical and physical changes are known to contribute.[286,287] Influenced by both charge carrier mobility and trapping, the deduced rise times τ_r, shown in Fig. 4.10(d), follow the trends reported above, namely that β-

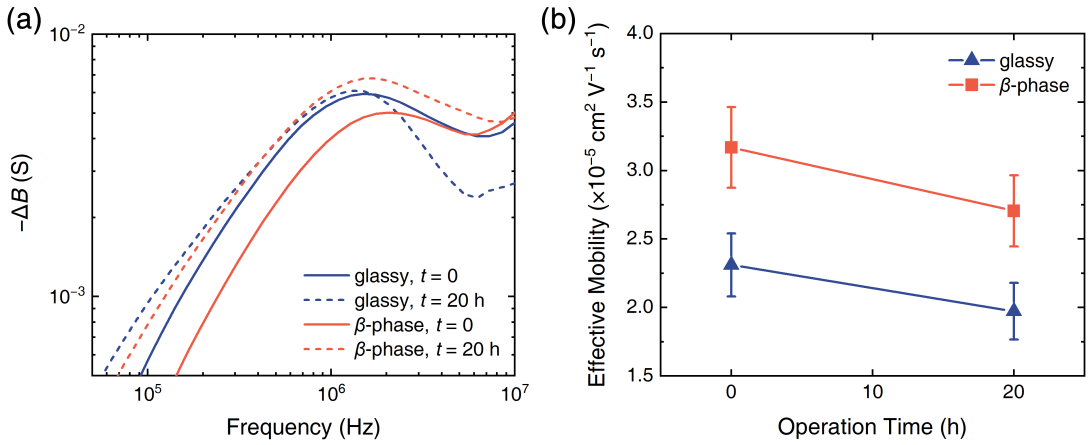

Figure 4.11 | $-\Delta B$-Derived Effective Mobilities for Glassy and β-Phase 90F8:10BT LEDs Before and After 20-Hour Continuous Operation. (a) Typical results of glassy (blue) and β-phase (red) 90F8:10BT LEDs before (solid lines) and after (dashed lines) 20-hour operation at constant current density $J = 80\,\mathrm{mA\,cm^{-2}}$, with the applied direct voltage $V_\mathrm{D} = 7\,\mathrm{V}$. (b) Extracted effective mobilities for glassy (blue triangles) and β-phase (red squares) 90F8:10BT LEDs. The joining lines are a guide to the eye.

phase devices are less prone to forms of degradation that lead to increased trap densities and/or other negative impacts on mobility. In this context, we also note that during the operation of an LED, the shorter exciton radiative lifetime following β-phase generation (Fig. 4.3) means that there is less chance for excitons to interact with charge carriers and each other, potentially helping to reduce trap formation.[101]

As the final characterisation, the EL spectra for glassy and β-phase LEDs were recorded before and after 20-hour continuous operation (Fig. 4.12). The change in EL spectra is rather modest with a slight broadening of the peak on its red edge whilst the short wavelength side is essentially unchanged. The changes are more noticeable, but certainly not pronounced, for glassy devices with a slight increase in relative emission strength at ~560 nm. The relative weighting of F8BT spectral components has been reported to depend on inter-chain, inter-BT unit packing, with an increase in direct BT-to-BT contacts between chains increasing the strength of the longer wavelength shoulder.[288] More generally, aggregation effects often yield red-shifted and broadened PL and EL spectra, and certain chemical species formed during photo-oxidation of fluorene units can

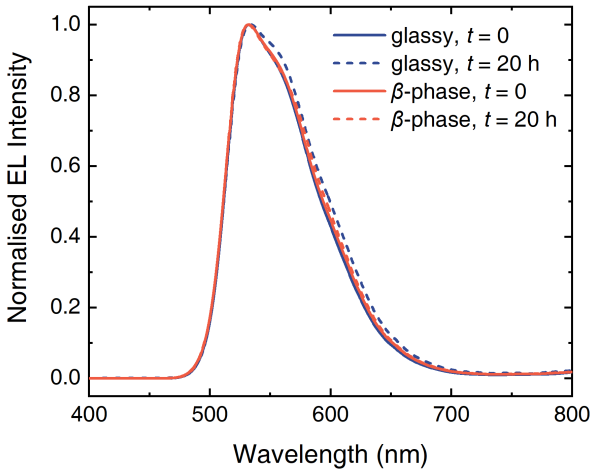

Figure 4.12 | Changes in EL Spectra for Glassy (blue) and β-Phase (red) 90F8:10BT LEDs Following 20-Hour Continuous Operation. Initial spectra are shown by solid lines and those following 20-hour operation by dashed lines. All devices were operated at constant current density $J = 80\,\mathrm{mA\,cm^{-2}}$.

also contribute, with the resulting fluorenone excimer emission at ~535 nm.[289] However, no equivalent of such green-band emission around this wavelength, which downgrades the blue emission colour of PFO LEDs, is observed here, albeit that if it appeared in the same spectral position as for PFO it would strongly overlap with the observed undegraded 90F8:10BT emission spectrum. A more detailed study of the chemical- and photo-stability of β-phase 90F8:10BT would be an interesting topic for future research.

4.7 Conclusions and Outlook

The research reported in this chapter demonstrates a successful generalisation of the use of chain conformation to enhance the device performance of conjugated polymer LEDs. Generation of the β-phase conformation for PFO has been shown previously to improve the performance of LEDs fabricated therefrom. Here, we use the similar strategy of introducing β-phase chain segments into a commercially available 10 % BT-containing F8-based copolymer, 90F8:10BT, to yield significantly enhanced LED efficiency and lifetime. A detailed investigation of device-related material properties and the performance of LEDs with and without the β-phase allows an understanding of the role that this conformation

change plays.

The absorption spectra of 90F8:10BT combine the spectral features of PFO and the alternating copolymer F8BT, and generation of β-phase chain segments via SVA or dipping yields the characteristic β-phase peak at ~430 nm. Spectral deconvolution allows estimation of the β-phase content, typically in the range 5–10 %. Unlike absorption spectra, the luminescence emission is dominated by the green-yellow BT-localised exciton with the residual F8-related blue emission having a steady-state peak intensity of $\leqslant 0.1$ % of the green-yellow emission. Efficient and rapid energy transfer occurs from F8-localised excitons, and the emission then proceeds with a single exponential decay with a time constant that is very close to, but slightly longer than that of F8BT. The emission efficiency is also high (~80 %) and independent of β-phase fraction (for the range studied). The shorter decay time with the same PLQE implies a higher oscillator strength for the more ordered β-phase films.

A detailed investigation (using MIS-CELIV, $-\Delta B$, C–V, J–V, and TREL measurements) of the charge injection, transport, and trapping, as well as LED electrical and optical characteristics for 90F8:10BT shows that glassy films give rise to imbalanced charge carrier injection and transport with significantly lower hole than electron mobility and a higher LED turn-on voltage. With the β-phase, the hole mobility rises to become close to the electron mobility, and the injection barrier is reduced. This is evident from the MIS-CELIV, $-\Delta B$, and C–V measurements. β-phase 90F8:10BT LEDs consequently yield higher luminance, and exhibit higher EQE, η_{L}, and η_{LP} values. Both glassy and β-phase devices show the effects of trapping but they are more pronounced for the glassy. This is particularly clear from J–V characteristics and TREL measurements. Moreover, β-phase formation significantly enhances LED's operational stability relative to glassy 90F8:10BT devices under continuous operation at $J = 80\,\mathrm{mA\,cm^{-2}}$. The glassy devices show strongly increased trapping effects leading to reduced TREL effective mobilities, as well as longer TREL rise and turn-off times. The corresponding performance changes for β-phase devices are significantly weaker, such that, for example, the average $\mathrm{LT_{90}}$ value

is more than double the ~10 hours found for glassy devices. Finally, EL spectra show relatively little and not very distinct change, with a red-edge broadening that is larger for glassy phase but not major in either case.

90F8:10BT has proven to be an interesting test case with which to study the influence of conformation on the fundamental and applied properties of fluorene-based conjugated copolymer emission materials. It provides a system within which charge carrier injection, transport, and exciton characteristics can be tuned as a function of the microstructure. This broadens the applicability range of conformation-imparted improvements to LED performance, an intervention level that lies between chemical modification and device engineering. Thus, it is worthwhile to investigate if this optimisation strategy can be further generalised to other F8-based copolymers, other conjugated polymer families, and other types of OSC devices. Also, in terms of 90F8:10BT itself, how β-phase affects the energy level, charge transport, and trap formation and distribution, as well as its chemical- and photo-stability during LED operation, remains for future studies.

Chapter 5

Properties and Applications of Copper(I) Thiocyanate (CuSCN) Hole-Transport Interlayers Processed from Different Solvents

5.1 Introduction

OSC devices have witnessed rapid developments across multiple device types in recent years, and these achievements largely originate from an evolution in OSC materials, deeper understanding of the associated device physics, and a proliferation of device engineering expertise. One widely applied element of device engineering is the insertion of appropriate interlayers within the device stack,[290,291] in order to tune interfacial physical and chemical processes and the heterojunction energy structure.[107]

Conventionally, interlayers in OSC devices are broadly categorised as electron-injection/transport layers (EILs/ETLs) or hole-injection/transport layers (HILs/HTLs),[291] depending on the charge carrier type for which injection and/or transport is facilitated. These injection and transport layers can also serve, importantly, as blocking layers for the opposite sign of charge carrier,[292] and in some OLEDs separate charge blocking layers are used.[293] Both injecting and blocking properties are determined by the energy level alignments between the interlayers and active materials, also taking into account any dipole-induced offsets in the vacuum level (Section 2.4.2.2).[107,294] In addition, an optical gap larger than that of the active materials in the device is generally important for interlayers in OPVs and OLEDs since competing light absorption is, respectively, unfavourable to their light harvesting and emission efficiencies. Last but not least, facile

deposition with good film forming characteristics (even at low layer thickness) is a serious practical concern. This requires that the deposition does not damage any underlying layers, avoids formation of pinholes and other defects, results in spatially uniform surface properties, and yields good adhesion to materials both below and on top.

Compared with a large number of available EILs/ETLs,[295–298] choices for solution-processable HILs/HTLs primarily focus on poly(3,4-ethylenedioxythiophene):poly(styrene sulfonate) (PEDOT:PSS) and materials developed therefrom,[299] together with various inorganic materials such as transition metal oxides.[300] As a mixture of conductive PEDOT-decorated PSS chains and insulating undecorated PSS chains,[299] PEDOT:PSS combines good solubility and processability, tuneable conductivity[301], and a work function (WF) of ~5.2 eV,[270] comparable to or higher than that of typical ITO.[269] These desirable features, which have driven very widespread utilisation, are offset to some degree by the acidity and chemical reactivity of the films[302,303] and the potential for de-doping accompanied by detachment of the PEDOT segments from their PSS carrier chains. This is further compounded by a non-negligible absorption in the visible spectral range.[304] In addition, the electron-blocking properties of PEDOT:PSS are not ideal,[305] and the tendency for electrons to be trapped by PEDOT:PSS (also leading to dedoping) can cause changes in device performance over time.[277] The PEDOT:PSS WF is also insufficient to generally support Ohmic injection into materials with larger ionisation potentials (IPs), leading to hole-injection-limited electrode function,[203] albeit that in certain circumstances Fermi level pinning at the interface can remove this barrier.[306] Moreover, the WF of PEDOT:PSS is found to be sensitive to processing protocols,[270] as its microstructure and surface composition may vary.[307] All of these considerations have led, over a number of years, to an active search for PEDOT:PSS replacements, with efforts mainly focussed on inorganic HILs/HTLs. It has not, however, proven straightforward to achieve this objective.

Commonly used examples of inorganic HILs/HTLs include MoO_3, WO_3, and V_2O_5, all with higher WFs than PEDOT:PSS.[308] The limiting factors then change to processing conditions, since these metal oxides can hardly be dissolved in solvents without chemical

reactions, so thermal evaporation is usually preferred. Admittedly, solution-based methods are not impossible,[309] but the mechanism of in-situ thermal decomposition of precursor layers[310] normally requires high annealing temperatures,[300] with the possibility of ending up with an interlayer showing unfavourable stoichiometry and, consequently, energetics if, for example, substrate temperature limits intervene.[311,312] A more recent option for use as an HIL/HTL in OSC devices is copper(I) thiocyanate (CuSCN), which is inexpensive, abundantly available,[177] and readily soluble in di-*n*-alkyl sulphides such as diethyl sulphide (DES) and dipropyl sulphide (DPS).[313] The calculated band structure of CuSCN[314,315] supports its potential for use as a hole-injection/transport material, with its large band gap (~3.9 eV) yielding high transparency, a deep-lying valence band edge (around −5.8 eV) for effective hole injection, and a low-lying conduction band edge (around −2.1 eV) for good electron blocking. Solution-processed CuSCN interlayers have been used to good effect in OLEDs,[177,316] OPVs,[317–319], and transistors.[320,321] The limited choices of solvent for CuSCN are, however, an impediment to its wider application. In particular, organic sulphides such as DES and DPS are hazardous chemicals of long-lasting, obnoxious odour, and their use demands extra care and strict control.

To overcome this limitation, researchers have sought to find new solvents for CuSCN which need both to be more benign and to ensure that the deposited CuSCN interlayers have hole injection/transport properties as good as, if not better than, films processed from the benchmark solvents, DES and DPS. Wijeyasinghe et al.[322] reported on using ammonium hydroxide (NH_4OH) to dissolve CuSCN. The resulting thin films showed lower surface roughness, deeper valence band edge, and better environmental stability than the DES-based counterparts. In comparison with PEDOT:PSS, improved efficiencies were observed for both OPVs and perovskite solar cells using NH_4OH-processed CuSCN as a substitute interlayer. Chaudhary et al.[323] further showed that dimethyl sulphoxide (DMSO) can also dissolve CuSCN, and reported the use of DMSO-processed CuSCN interlayers in OPVs. To date, DES, DPS, NH_4OH, and DMSO appear to be the only solvents that have been employed to solution-process CuSCN interlayers for OSC devices.

In this chapter we present a side-by-side comparison of these known solvents with two new promising candidates, namely *N*,*N*-dimethylformamide (DMF) and 1-methyl-2-pyrrolidone (NMP), which are polar aprotic solvents sharing similar properties to DMSO but have not been explored as solvents for CuSCN so far. The coloration of six CuSCN solutions indicates significant differences between oxidation state and solvation of the Cu metal sites, and the resulting surface roughness for spin-coated thin films are characterised (Section 5.2). Next, the polymorphism found in drop-cast thick films is investigated in Section 5.3, and X-ray photoelectron spectroscopy (XPS) is used in Section 5.4 to analyse the chemical composition and bonding of the deposited CuSCN thin films. We then discuss two important features of CuSCN interlayers that can affect the hole injection/transport properties, namely the surface energy (Section 5.5), playing an important role in tuning the crystallite orientation of semicrystalline conjugated polymers deposited atop the interlayer and thereby influencing their charge carrier mobility, and the energy level (Section 5.6) that determines hole injection barriers. For the former, CuSCN thin films processed from NH_4OH, DMSO, DMF, and NMP exhibit higher surface energies ($\sim$75 mJ m^{-2}) than those from DES and DPS ($\sim$60 mJ m^{-2}), resulting in $\sim$40 % improved hole mobility of $\sim 5 \times 10^{-5}$ cm^2 V^{-1} s^{-1} for the PTB7 conjugated polymer deposited on top. For the latter, the measured IPs of the CuSCN interlayers vary significantly from 5.19 to 5.91 eV across the sequence NMP < DMF < DMSO < DES < DPS < NH_4OH, thereby allowing tuning of the hole injection barrier height for different active materials via solvent selection. Finally, in Section 5.7, device tests on OLEDs, OPVs, and OFETs are carried out, and their performance when using various CuSCN interlayers is referenced to devices with a PEDOT:PSS interlayer or simply no interlayer. For devices studied here, DMSO and DMF, two more common, benign, and eco-friendly chemicals than the conventional DES and DPS, allow the resulting CuSCN interlayers to considerably boost the device performance. This study helps to broaden the applicability of CuSCN as a highly efficient hole injection/transport material for OSC devices by expanding the documented range of suitable CuSCN solvents.

5.2 Solutions and Thin Films

5.2.1 Solutions

CuSCN (99 %, Sigma-Aldrich) was mixed with six solvents, namely DES, DPS, NH_4OH, DMSO, DMF, and NMP; details of these solvents can be found in Table 5.1. All solutions were made at a concentration of 10 mg ml^{-1} and were filtered through 0.45 µm polytetrafluoroethylene (PTFE) filters before use. For DES, DPS, and NH_4OH, the solutions were stirred at room temperature for over 12 h, whereas for DMSO, DMF, and NMP, dissolution required heating at 120 °C for over 24 h with vigorous stirring. In the case of DMF and NMP, the added CuSCN did not fully dissolve; the actual concentration (listed in Table 5.1) was determined by decanting a fixed portion of the solution, evaporating the solvent, and weighing the resulting precipitate.

Table 5.1 | Details of Solvents and Solutions Used in This Study.

Solvent	Full Name, Purity, and Source	Chemical Structure	Boiling Point (°C)	Solution Concentration (mg ml^{-1})
DES	Diethyl sulphide, 98 %, Sigma-Aldrich	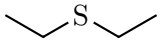	91	10
DPS	Dipropyl sulphide, 97 %, Sigma-Aldrich	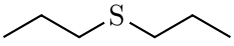	142	10
NH_4OH	Ammonium hydroxide, 50 % v/v aqueous solution, Alfa Aesar	—	38	10
DMSO	Dimethyl sulphoxide, 99.9 % anhydrous, Sigma-Aldrich		189	10
DMF	*N*,*N*-Dimethylformamide, 99.8 % anhydrous, Sigma-Aldrich	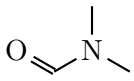	153	2.1 (max.)
NMP	1-Methyl-2-pyrrolidinone, 99.5 % anhydrous, Sigma-Aldrich	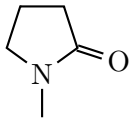	203	2.8 (max.)

According to Pearson's Hard and Soft Acids and Bases theory,[324] Cu^+ as a soft acid interacts more easily with soft bases, which is the case for the sulphur-containing DES, DPS, and DMSO. In comparison, the inclusion of the nitrogen atom in DMF and NMP makes them much "harder", leading to reduced solubility (Table 5.1). An exception here is NH_4OH, which is a hard base but can dissolve CuSCN readily. This may be related to the quick oxidation of Cu^+ in the presence of NH_4OH (see discussion below), with the product Cu^{2+} a much "harder" acid.[325] Figure 5.1 shows the photograph of typical solutions; the DES and DPS solutions are colourless, while the NH_4OH solution is in deep blue, all in line with previous reports.[322] A dark brown solution is obtained when DMSO is used as the solvent, and DMF and NMP solutions are light green and greenish yellow, respectively.

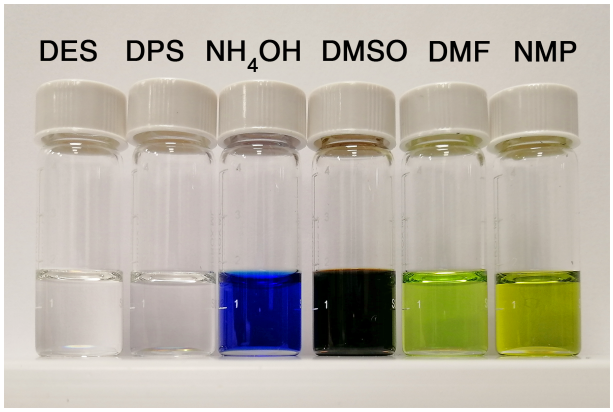

Figure 5.1 | Photograph of CuSCN Solutions. The strong colour changes for different solvents is evident, indicative of varied ionic states and complex formation. The concentration is 10 mg ml^{-1} for the first four, and 2.1 and 2.8 mg ml^{-1} for DMF and NMP solutions, respectively, which are saturated.

When CuSCN is dissolved in a solvent, usually the solvent molecules can form complexes with Cu^+ and thereby breaking the ionic bond to SCN^-.[313] Therefore, the solution colour differences give an indication of the changes in chemical state and bonding of the copper in these solutions. For example, Cu(I)-amine complexes are generally colourless,[326] so the deep blue CuSCN-NH_4OH solution is likely caused by at least partial formation of a [Cu(II)-amine]$^{2+}$ complex ion. This oxidation is confirmed by XPS analysis

(see Section 5.4). Besides, the colours of Cu(I) complexes are very dependent on their organic ligands;[326] the similar colours for DMF and NMP solutions suggest that the copper is present in a broadly similar chemical environment therein, as might be expected from the similarity of DMF and NMP chemical structures (Table 5.1). By contrast, the very different colour of the CuSCN-DMSO solution indicates different coordination in the presence of the sulphoxide moiety.

5.2.2 Thin-film topography and roughness

The solutions were deposited on ITO-coated glass substrates (sheet resistance = $5\,\Omega\,\mathrm{sq}^{-1}$, Lumtec) to yield CuSCN thin films. To achieve a comparable thickness for all samples, CuSCN-DES and -DPS solutions were diluted to 3 and $4\,\mathrm{mg\,ml}^{-1}$, respectively. Then all solutions were spin-coated at 1000 rpm. For high-boiling-point solvents, i.e. DMSO, DMF, and NMP, a long spinning time (3 min) was used to provide sufficient time for evaporation. Finally, the samples were annealed at 100 °C for 10 min in air, leading to ~10 nm thickness films for all solvents except DMF and NMP where ~6 nm thickness resulted.

Atomic force microscopy (AFM) was applied to characterise the surface topography and roughness of CuSCN thin films in an area of $2 \times 2\,\mu\mathrm{m}^2$ (Fig. 5.2). Here we also include the ITO substrate and ITO / PEDOT:PSS (~30 nm) as references. PEDOT:PSS (Clevios™ PVP AI4083, Heraeus) was spin-coated at 2500 rpm and annealed at 150 °C for 15 min in air; this protocol of PEDOT:PSS deposition keeps unchanged throughout this chapter. Figure 5.2(a) for the bare ITO substrate reveals the characteristic polycrystalline grain microstructure[177,322] with grain sizes of several hundred nanometres; the root-mean-square roughness (R_{rms}) is 3.00 nm. When coated with PEDOT:PSS (Fig. 5.2(b)), the substrate becomes smoother ($R_{\mathrm{rms}} = 1.84$ nm), one of the well-documented benefits of the PEDOT:PSS HTL.[177,317,322] CuSCN thin films processed from DES and DPS solutions comprise ~50 nm crystalline grains (Fig. 5.2(c–d)) with $R_{\mathrm{rms}} = 2.58$ nm and 2.83 nm, respectively, somewhat smoother than for bare ITO but rougher than when PEDOT:PSS is used. In earlier publications, thicker CuSCN-DES and -DPS films around 50 nm have

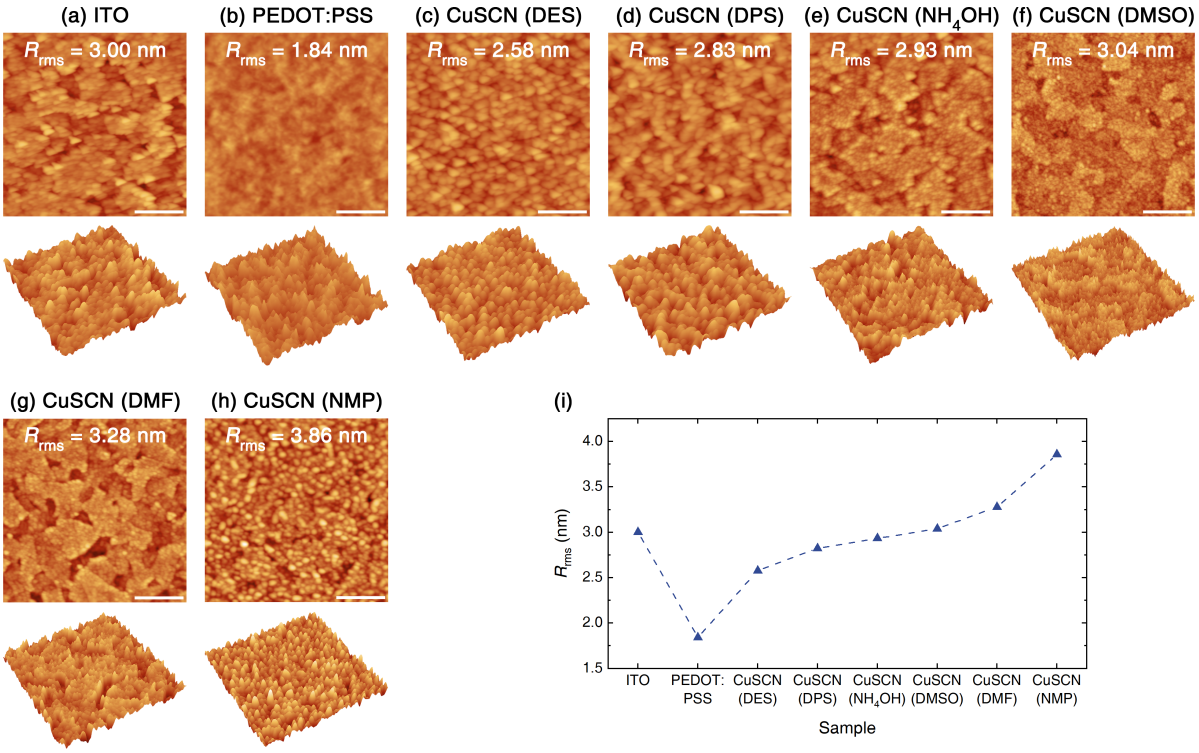

Figure 5.2 | AFM Images and Deduced Roughness for ITO and Interlayer-coated ITO Substrates. (a–h) Two-dimensional (upper panels) and three-dimensional (lower panels) topography for: (a) bare ITO; (b) ITO / PEDOT:PSS; (c) ITO / CuSCN (from DES solution); (d) ITO / CuSCN (DPS solution); (e) ITO / CuSCN (NH_4OH solution); (f) ITO / CuSCN (DMSO solution); (g) ITO / CuSCN (DMF solution); and (h) ITO / CuSCN (NMP solution). The scale bars in 2-D images represent 500 nm. The root-mean-square roughness (R_{rms}) values are collected together in (i) for all samples. The dashed connection line is a guide to the eye.

been reported to have a higher R_{rms} than ITO.[317,322] In this study, all spin-coated CuSCN thin films were controlled to be ~10 nm thickness in order to be able to compare the six solvents side by side; the limited solubility of CuSCN in DMF and NMP (Table 5.1) precludes the straightforward preparation of spin-coated thicker films.

The CuSCN thin film topography resulting from NH_4OH, DMSO, and DMF solutions is similar to that of bare ITO (Fig. 5.2(e–g)), possibly due to the thinness of the films and the lack of significant crystalline grain formation. The R_{rms} for these three samples is also close to that of ITO. Finally, for the CuSCN-NMP film (Fig. 5.2(h)), a much rougher surface with R_{rms} = 3.86 nm is observed, and its topological characters differ a lot from the CuSCN-DMF sample. Considering the chemical similarity between the two solvents,

we propose that during spin-coating, the higher boiling point of NMP (203 °C) makes it much slower to evaporate, facilitating crystallisation and leading to a rougher surface. Figure 5.2(i) summarises the R_{rms} values for all eight surfaces, among which PEDOT:PSS shows the best smoothening effect. For all bar the NMP-processed, the CuSCN thin films show a similar surface roughness to that of ITO; in the latter case R_{rms} is ~30 % larger.

5.3 Polymorphism

Crystalline CuSCN can exhibit at least two polymorphs, namely α- and β-CuSCN. The former has an orthorhombic crystal lattice,[327] whilst the latter can be either rhombohedral (the $3R$ polytype) or hexagonal (the $2H$ polytype).[328] Theoretical calculations show that the unit cell of β-CuSCN has ~60 meV lower energy than that of the α-phase,[329] confirming β-CuSCN to be thermodynamically the most stable polymorph. This is consistent with previous experimental reports that β-CuSCN films were widely obtained by drop-casting,[314] electrodeposition,[330] and successive ionic layer adsorption and reaction (SILAR),[331] whereas α-CuSCN films can only be achieved under some non-equilibrium conditions, for example during electrodeposition in the presence of selected organic additives.[332] Other polymorphs, e.g. γ-, δ-, and ε-CuSCN, have been predicted by density functional theory (DFT) calculations[333] yet not been experimentally observed.

To investigate the polymorphism of our CuSCN samples processed from different solvents, we performed Raman and Fourier-transform infrared (FTIR) spectroscopy as well as X-ray diffraction (XRD) measurements. Since much thicker films are required for crystallographic structure determination, samples were deposited by drop-casting on silicon substrates (n-doped by As, with 200 ± 10 nm SiO_2 oxidation layer, Active Business Company GmbH) for Raman and FTIR, or on soda–lime glass (Lumtec) for XRD.

Figure 5.3 shows the Raman spectra of CuSCN films under the excitation of 532 nm. Similar peaks are observed for all samples at lower Raman shifts, i.e. ~205 cm^{-1} for Cu−S stretching, ~244 cm^{-1} for Cu−N stretching, ~433 cm^{-1} for S−C≡N scissoring, and ~749 cm^{-1} for C−S stretching.[334,335] At higher Raman shifts, all samples exhibit

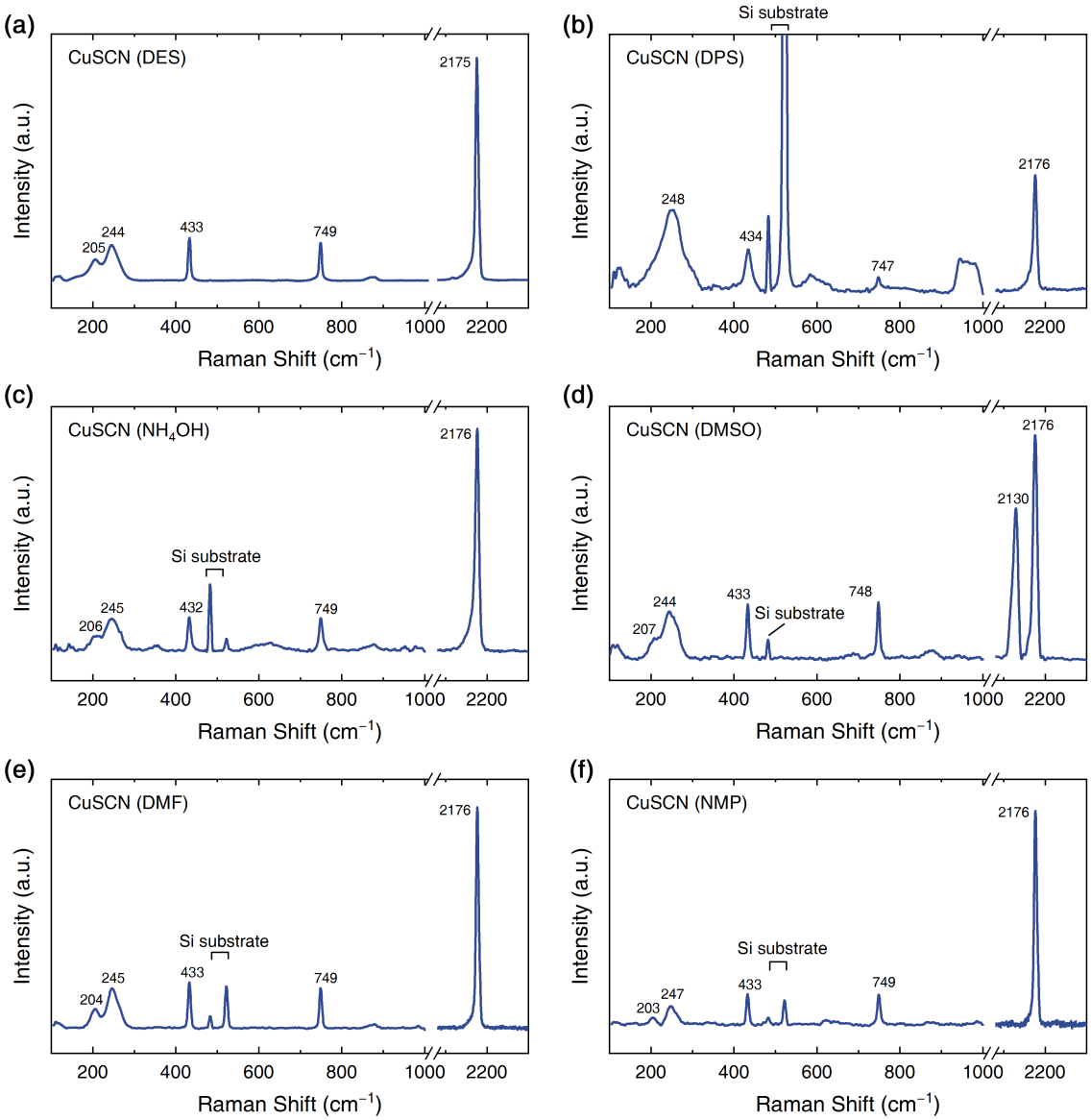

Figure 5.3 | Raman Spectra of CuSCN Thick Films. Samples were drop-cast from (a) DES, (b) DPS, (c) NH_4OH, (d) DMSO, (e) DMF, and (f) NMP solutions. Peaks from CuSCN are labelled by the corresponding Raman shift values, and those from Si substrates are denoted as well. The ~2176 cm^{-1} peaks for all samples correspond to the C≡N stretching mode in β-CuSCN, whereas the additional peak at 2130 cm^{-1} for (d) CuSCN-DMSO sample represents the same mode in α-CuSCN. The excitation wavelength was 532 nm.

a peak at ~2176 cm^{-1} corresponding to the C≡N stretching mode in β-CuSCN.[328,335] However for the CuSCN-DMSO film, in addition to the 2176 cm^{-1} peak, a new peak at 2130 cm^{-1} was detected (Fig. 5.3(d)), which can be assigned to the C≡N stretching mode in α-CuSCN.[328,335] That is to say, with DMSO as the solvent, both α- and β-CuSCN

polymorphs coexist in the drop-cast films, whilst all other samples contain pure β-CuSCN. The different C≡N stretching mode energies in various CuSCN films engendered by different polymorphs can also be observed in their FTIR spectra (Fig. 5.4), complementing the Raman data and confirming this conclusion.

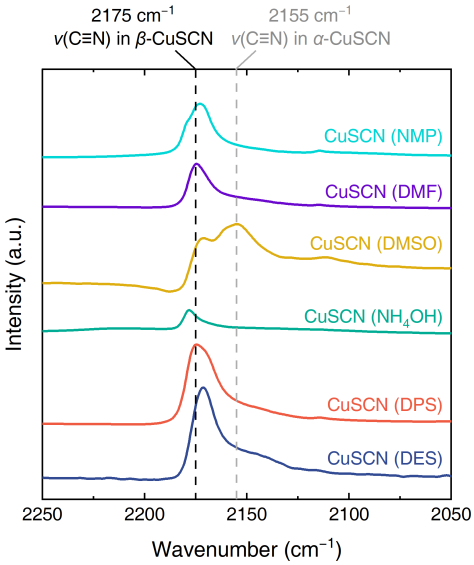

Figure 5.4 | FTIR Spectra of CuSCN Thick Films. Samples were drop-cast from different solvents, i.e. DES, DPS, NH_4OH, DMSO, DMF, and NMP (from bottom to top). The characteristic peaks of C≡N stretching modes ν(C≡N) in α- and β-CuSCN are labelled.

The polymorphism of various CuSCN films is further examined by XRD measurements (Fig. 5.5). While all samples exhibit (003) and (101) peaks for the β-phase, the one processed from DMSO additionally shows (121), (211), and (112) α-phase peaks.[336] The coexistence of both polymorphs was previously reported in a 14 nm thick CuSCN film processed from DPS using transmission electron microscopy (TEM) and selected area electron diffraction (SAED) techniques.[320] For our CuSCN-DMSO sample, the way Cu(I) coordinates with DMSO molecules may affect the crystallisation process, leading to a mixture of the most stable and the metastable phases; the detailed mechanism still remains open and is an interesting topic for future research. Nonetheless, this finding provides us with a useful platform with which the relationship between CuSCN polymorphs and electronic properties can be experimentally investigated, complementing previous

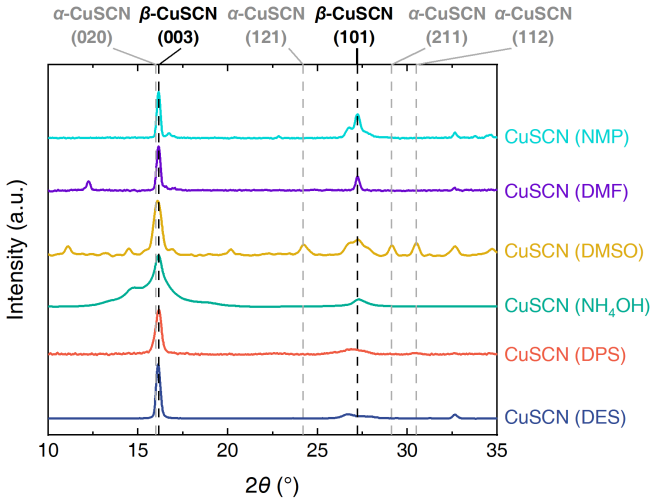

Figure 5.5 | XRD Patterns of CuSCN Thick Films. Samples were drop-cast from different solvents, i.e. DES, DPS, NH_4OH, DMSO, DMF, and NMP (from bottom to top). Characteristic diffraction peaks for α- and β-CuSCN are indicated; their positions are sourced from the Powder Diffraction File 29-0581 and 29-0582, respectively.[336]

theoretical studies.[329] We note the caveat, however, that the samples used here are several micrometres in thickness, whereas thin films of ~10 nm are used in the devices reported below (Section 5.7). How much the variation in thickness and associated processing conditions lead to a change in polymorphism remains unclear.

5.4 Surface Chemistry

The surface chemistry features of CuSCN samples, including the composition, chemical bonding, and states of the constituent elements, are investigated by XPS. Unlike the thick, drop-cast layers used in Raman, FTIR, and XRD measurements, CuSCN thin films for XPS, as used in devices (Section 5.7), were spin-coated on fused silica substrates (Bright Crystals Technology) using the same parameters as for AFM samples; these processing conditions remain unchanged in the rest of this chapter. Survey spectra (Fig. 5.6) confirm the existence of Cu, S, C, and N in all samples, with signals of Si from the substrates. Peaks for O originate from the substrates, contaminants, and oxidation products.

High-resolution C 1s core level spectra of all samples (Fig. 5.7) show, as expected,

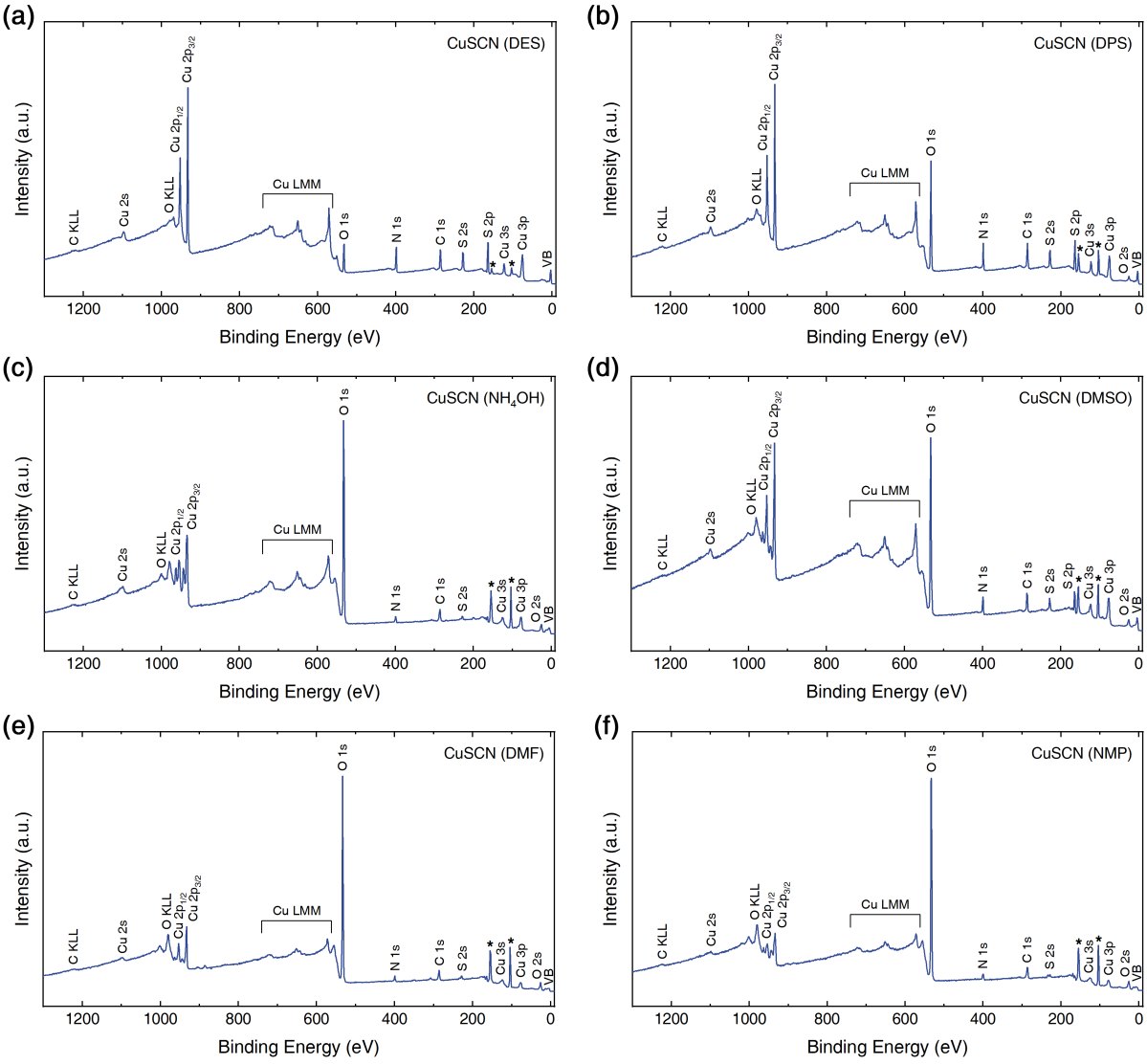

Figure 5.6 | XPS Survey Spectra of CuSCN Thin Films. Samples were spin-coated from (a) DES, (b) DPS, (c) NH_4OH, (d) DMSO, (e) DMF, and (f) NMP solutions. The origin of each peak is assigned, and those at ~100 and ~150 eV, marked with asterisks, correspond to the Si 2p and 2s core levels, respectively, from the substrate. The "VB" denotes "valance band".

peaks associated with S−C≡N bond at ~286.4 eV and adventitious carbon at 284.8 eV.[314,322] Traces of residual solvent are also observed, namely C−S peaks for DES-, DPS-, and DMSO-processed samples and C−N peaks for DMF- and NMP-processed. The case of NH_4OH will be discussed separately below; N 1s spectra are needed since there is no C present in the solvent. It has been reported that DES and DPS molecules are easily trapped inside the CuSCN thin film, even after annealing at temperatures higher

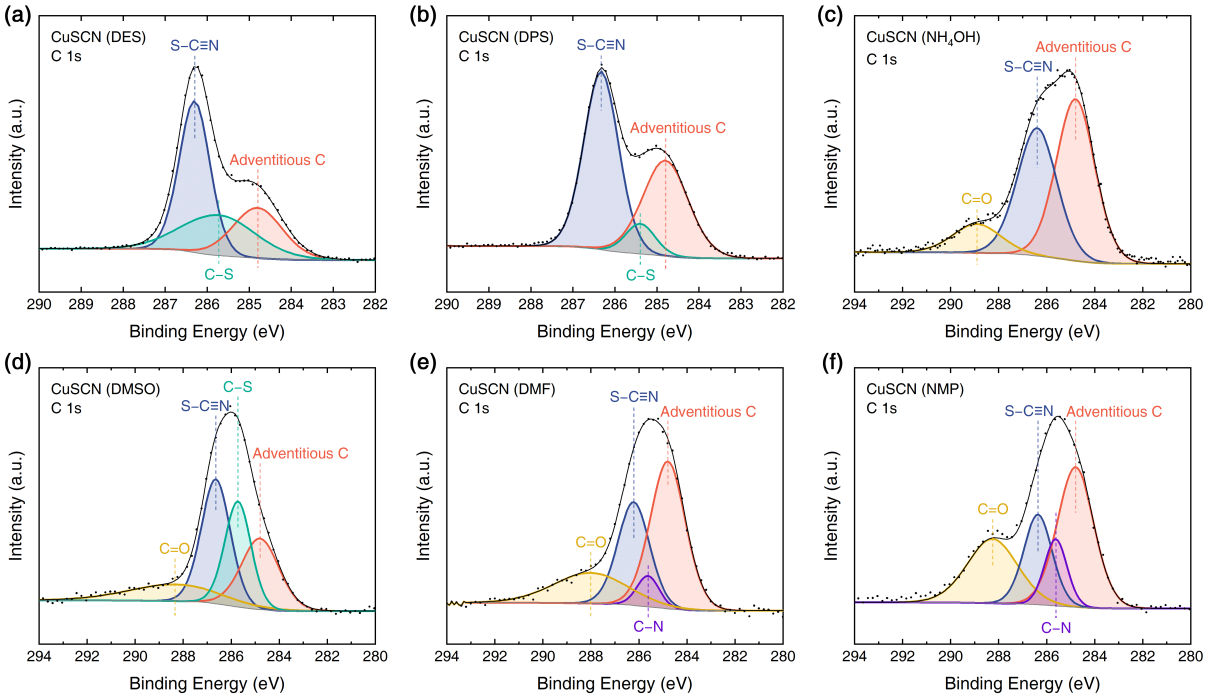

Figure 5.7 | XPS C 1s Core Level Spectra of CuSCN Thin Films. Samples were spin-coated from (a) DES, (b) DPS, (c) NH_4OH, (d) DMSO, (e) DMF, and (f) NMP solutions. Data points are shown by black dots, and the envelopes from the peak fitting analysis are shown by black curves. Fitted peaks and assigned chemical bonds are colour coded: S−C≡N (blue), C−S (green), C=O (yellow), C−N (purple), and adventitious C (red).

than their boiling points, due to the strong coordination between Cu(I) and di-*n*-alkyl sulphides.[337,338] In terms of DMSO, DMF, and NMP, their high boiling points (Table 5.1) may additionally hinder their removal during thermal annealing. Furthermore, C=O peaks at ~288.5 eV[339] are also observed for the samples processed from NH_4OH, DMSO, DMF, and NMP, indicating the presence of adventitious oxidation products.

The N 1s core level spectra of all samples (Fig. 5.8) show a characteristic S−C≡N peak at ~398.9 eV, consistent with previous reports.[320,322] Additional N−H peaks at ~400.2 eV in the DES- and DPS-processed thin films, as observed before,[322] can be attributed to partial hydrogeneration of some of the nitrogen atoms. A much stronger N−H peak is seen for NH_4OH-processed samples, probably stemming from solvent residues bound to CuSCN.[322] C−N peaks appear at ~399.9 eV[340] for DMF- and NMP-processed samples, confirming the evidence from the C 1s spectra that there is residual solvent present.

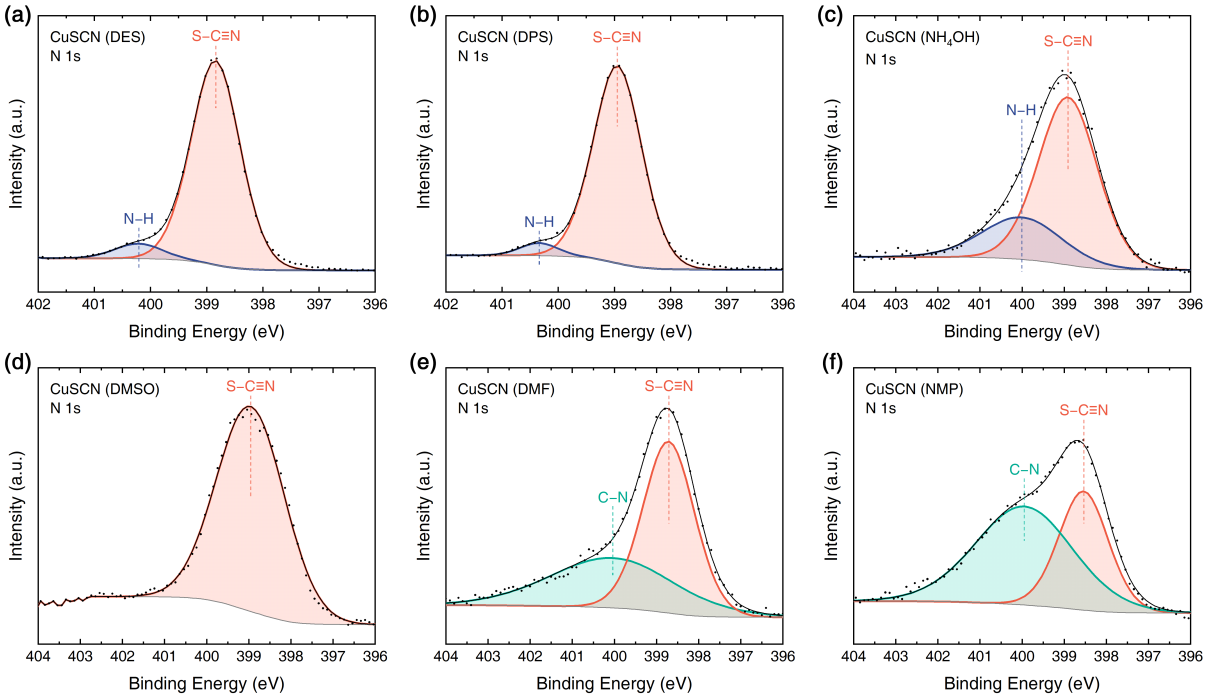

Figure 5.8 | XPS N 1s Core Level Spectra of CuSCN Thin Films. Samples were spin-coated from (a) DES, (b) DPS, (c) NH_4OH, (d) DMSO, (e) DMF, and (f) NMP solutions. Data points are shown by black dots, and the envelopes from the peak fitting analysis are shown by black curves. Fitted peaks and assigned chemical bonds are colour coded: S−C≡N (red), N−H (blue), and C−N (green).

Figure 5.9 presents the S 2p core level spectra, with S−C≡N peaks evident for all samples, located at ~163.8 eV for S $2p_{3/2}$.[341] Thin films processed from DES and DPS exhibit C−S peaks around 163.6 eV ($2p_{3/2}$),[342] again arising from residual solvent molecules. These two samples further show very weak S−O peaks at ~169.6 eV ($2p_{3/2}$), suggesting a marginal degree of oxidation of sulphur, as reported previously.[322] This oxidation is more pronounced in the last four samples (Fig. 5.9(c–f)) and may lead to a shift in the CuSCN valence band edge due to a change in the configuration of the outermost 3p electrons, as predicted by DFT calculations.[314] The oxidation process may result in sulphate ions SO_4^{2-} being formed, producing S vacancies in the CuSCN lattice. However, this type of defect has been reported to be electrically inactive.[314]

High-resolution spectra of Cu 2p core levels are displayed in Fig. 5.10. While all samples show Cu^+ peaks at ~933.0 eV,[314,322] thin films processed from NH_4OH, DMSO,

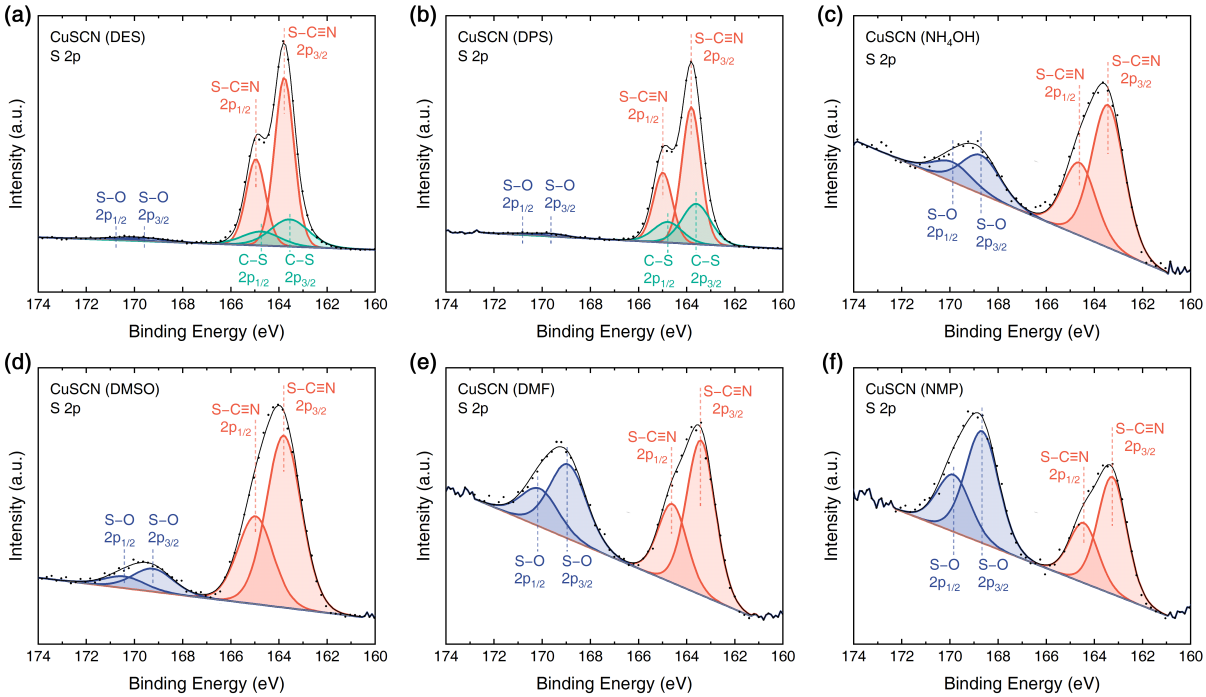

Figure 5.9 | XPS S 2p Core Level Spectra of CuSCN Thin Films. Samples were spin-coated from (a) DES, (b) DPS, (c) NH_4OH, (d) DMSO, (e) DMF, and (f) NMP solutions. Data points are shown by black dots, and the envelopes from the peak fitting analysis are shown by black curves. Fitted peaks and assigned chemical bonds are colour coded: S−C≡N (red), S−O (blue), and C−S (green).

DMF, and NMP exhibit an additional peak at ~934.6 eV, which can be assigned to Cu^{2+}.[343] This is further corroborated by the characteristic Cu^{2+} satellite peaks around 943 eV.[344] Similar to the case of sulphur, the partial oxidation of Cu^{+} can affect the position of CuSCN valence band edges in the last four samples through the change in 3d electrons.[314] Moreover, the oxidation product, Cu^{2+} ions, may act as p-dopants to CuSCN if Cu^{2+} can replace Cu^{+} in the lattice, or lead to Cu vacancies if Cu^{2+} cannot. In the latter case, Cu^{2+} are likely to exist in the form of Cu^{2+}-ammine complexes (for NH_4OH-processed) or $CuSO_4$ (for DMSO-, DMF-, and NMP-processed). Both possibilities can cause CuSCN Fermi level shift, and will be discussed further in Section 5.6.

Finally, we measured the O 1s core level spectra (Fig. 5.11). Oxygen is not expected to appear in pure CuSCN thin films, however oxidation products, the adsorption of moisture, and the background signal from the substrates can all contribute. These sources lead to

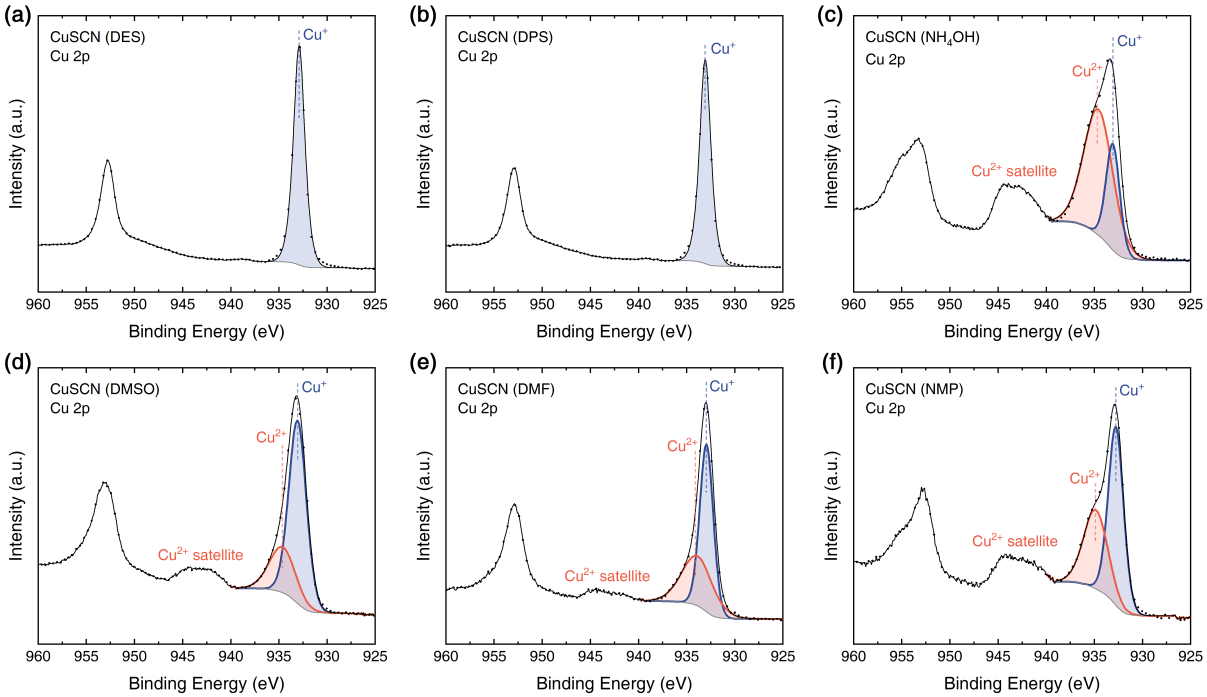

Figure 5.10 | XPS Cu 2p Core Level Spectra of CuSCN Thin Films. Samples were spin-coated from (a) DES, (b) DPS, (c) NH_4OH, (d) DMSO, (e) DMF, and (f) NMP solutions. Data points are shown by black dots, and the envelopes from the peak fitting analysis are shown by black curves. Fitted peaks and assigned Cu chemical states are colour coded: Cu^{+} (blue) and Cu^{2+} (red).

C=O, S−O, O−H, and Si−O peaks for various samples. Interestingly, in the CuSCN-DMSO thin film, a peak at 530.2 eV shows up (Fig. 5.11(d)), which possibly originates from the existence of Cu_2O.[345] The latter has a smaller IP (~5.3 eV)[346] than CuSCN and has been used as a hole injection/transport material in its own right.[194] A mixture of both may result in a cascaded hole injection/extraction interface, provided that a favourable composition gradient can be formed normal to the sample plane. Such a Cu_2O/CuSCN composite HTL has already been used in perovskite solar cells to enhance charge transport and inhibit interfacial degradation,[347] but with different processing methods from us. Therefore, further investigations are needed on the origin and applications of this effect. By and large, CuSCN thin films studied here exhibit some complexity in the chemistry related to the different solvents, leading to a variation in the chemical composition and bonding of the resulting films.

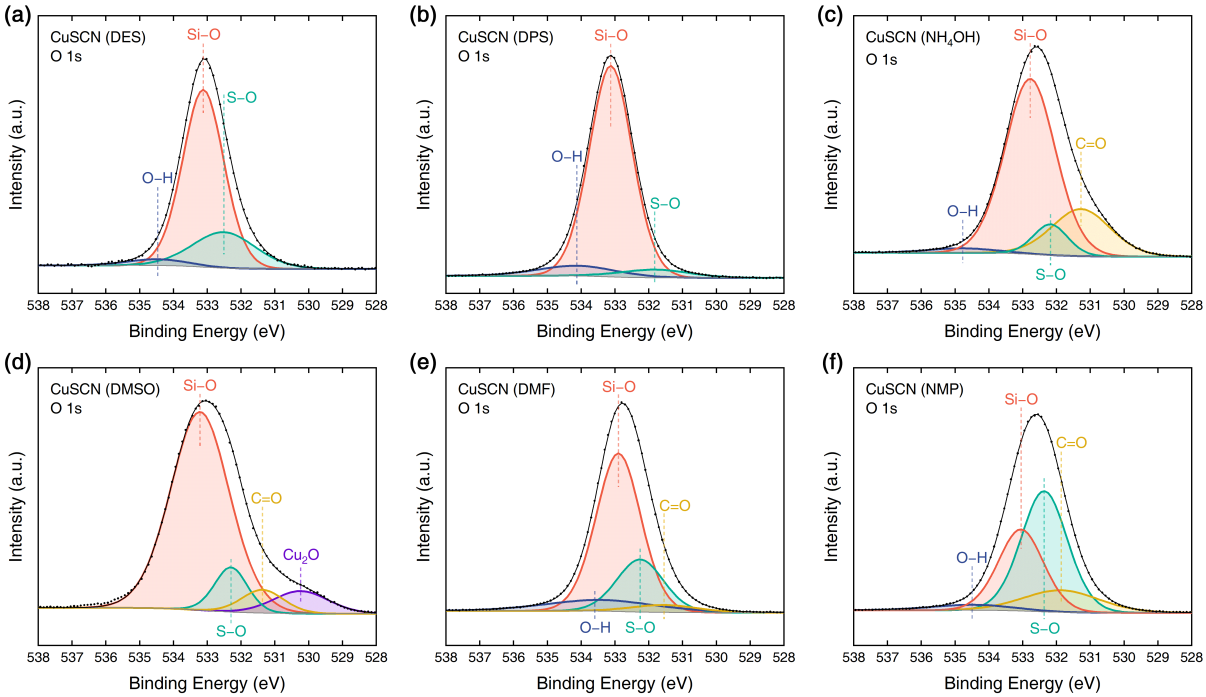

Figure 5.11 | XPS O 1s Core Level Spectra of CuSCN Thin Films. Samples were spin-coated from (a) DES, (b) DPS, (c) NH_4OH, (d) DMSO, (e) DMF, and (f) NMP solutions. Data points are shown by black dots, and the envelopes from the peak fitting analysis are shown by black curves. Fitted peaks and assigned chemical bonds are colour coded: Si−O (red), O−H (blue), S−O (green), C=O (yellow), and Cu−O in Cu_2O (purple).

5.5 Surface Energy, Polymer Orientation, and Mobility

In addition to the surface chemistry of the interlayer, its surface energy will have an impact on the crystallite orientation of a semicrystalline conjugated polymer spin-coated on top, influencing the charge transport properties. Specifically, interlayers with low surface energies tend to favour the edge-on crystallite orientation, while face-on is often promoted when the interlayer surface energy increases (Section 2.6.2).[134,185,186] For diode structures where charge carriers flow in the normal-to-plane direction, face-on orientated chain packing is beneficial for charge transport as their π–π stackings align in the normal-to-plane direction as well, leading to improved mobility (Section 2.4.3.3). These two relationships are well-demonstrated in Fig. 5.12(a) by the results from CuSCN interlayers processed from different solvents and a semicrystalline conjugated

polymer, poly[[4,8-bis[(2-ethylhexyl)oxy]benzo[1,2-*b*:4,5-*b*′]dithiophene-2,6-diyl][3-fluoro-2-[(2-ethylhexyl)carbonyl]thieno[3,4-*b*]thiophenediyl]] (PTB7, Fig. 5.12(b)). Below we shall discuss the relevant experimental data in detail.

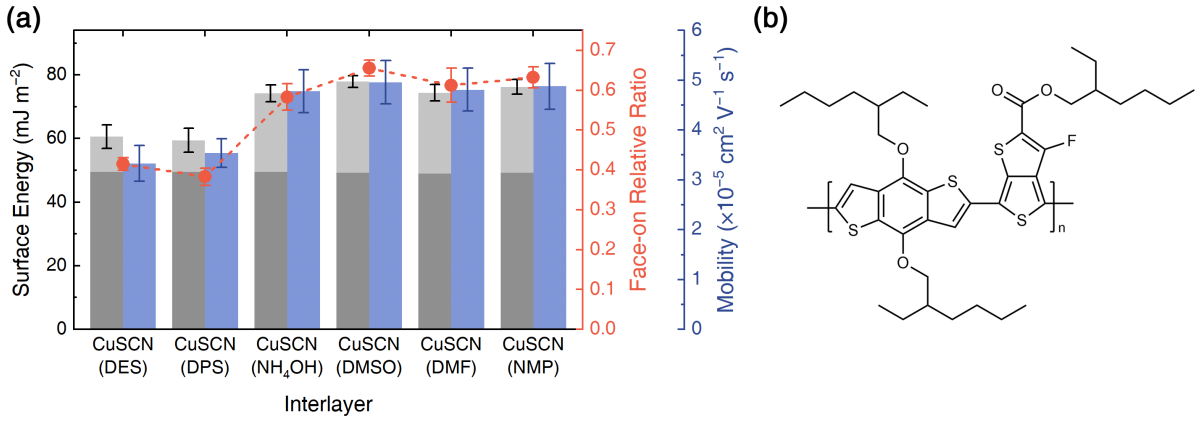

Figure 5.12 | (a) Summary of the relationship between CuSCN surface energies (grey bars), PTB7 crystallite face-on relative ratios (red dots), and PTB7 hole mobility (blue bars). The deep grey (lower) and light grey (upper) parts represent the dispersive and polar surface energies, respectively. The face-on relative ratio is calculated as the intensity ratio of the $q_{xy} \approx 0.38\,\text{Å}^{-1}$ peak (face-on) to the $q_z \approx 0.38\,\text{Å}^{-1}$ peak (edge-on) in GIWAXS patterns. Hole mobility is measured by the MIS-CELIV technique. Dashed connection lines are a guide to the eye. (b) Chemical structure of PTB7.

We first measured the contact angles of de-ionised (DI) water (conductivity $< 5.00\,\mu\text{S}\,\text{cm}^{-1}$ at 25 °C, Scientific Laboratory Supplies) and diiodomethane (DIM, 99 %, Alfa Aesar) on six CuSCN thin films spin-coated on ITO substrates, as shown in Fig. 5.13. With contact angle values, the surface energy of CuSCN interlayers can be extracted according to the Fowkes theory (Eq. (3.21)). The results are presented in Fig. 5.12(a) by grey bars, of which the lower parts (in deeper grey) and upper parts (in lighter grey) indicate the dispersive and polar components, respectively. All CuSCN thin films are found to have similar dispersive surface energies around $50\,\text{mJ}\,\text{m}^{-2}$, yet samples processed from NH_4OH, DMSO, DMF, and NMP show significantly higher polar surface energies ($\sim 25\,\text{mJ}\,\text{m}^{-2}$) than those from DES and DPS ($\sim 10\,\text{mJ}\,\text{m}^{-2}$), leading to higher total surface energies of the former group. DFT calculations revealed that for β-CuSCN, polar surfaces such as (101) and (001) have higher energies than the non-polar, e.g. (110) and (100),

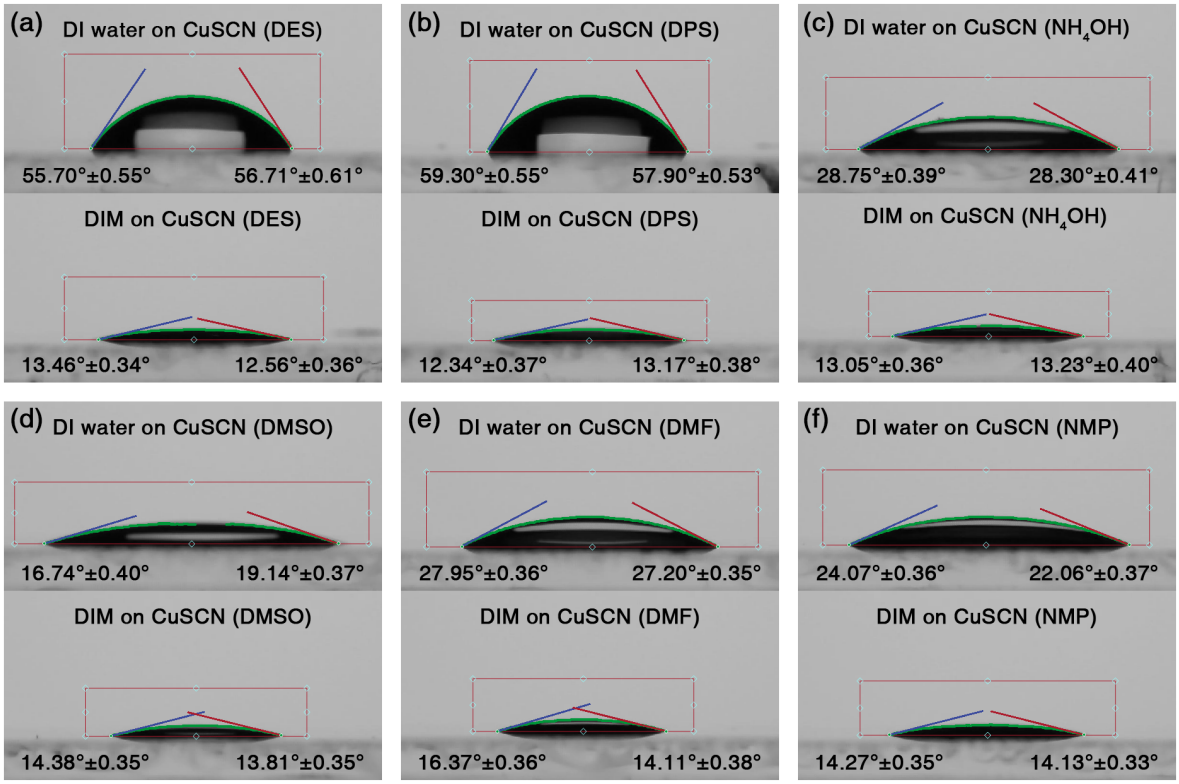

Figure 5.13 | Contact Angle Measurements of DI Water (upper panels) and DIM (lower panels) on CuSCN Thin Films. Samples were spin-coated from (a) DES, (b) DPS, (c) NH_4OH, (d) DMSO, (e) DMF, and (f) NMP solutions. The determined contact angle values are presented.

leading to an expectation of low polarity surfaces under equilibrium growth.[348] Hence, the different surface energies of CuSCN thin films may result from non-equilibrium processes yielding different surface orientations, affected by both the nature of Cu(I)-solvent molecule complexes in solutions and the kinetics of layer deposition. Further work will be needed to understand the degree to which the CuSCN surface orientation can be controlled and its long-term microstructural stability.

Next, PTB7 (1-Material Inc.) was dissolved in chlorobenzene (99.8 %, anhydrous, Sigma-Aldrich) at 20 mg ml^{-1}, and was spin-coated onto CuSCN interlayers (deposited from each of the six solvents) at 1000 rpm to investigate the influence of CuSCN surface energy on PTB7 crystallite orientations. For this purpose, grazing-incidence wide-angle X-ray scattering (GIWAXS) patterns were collected for all CuSCN / PTB7 samples. In

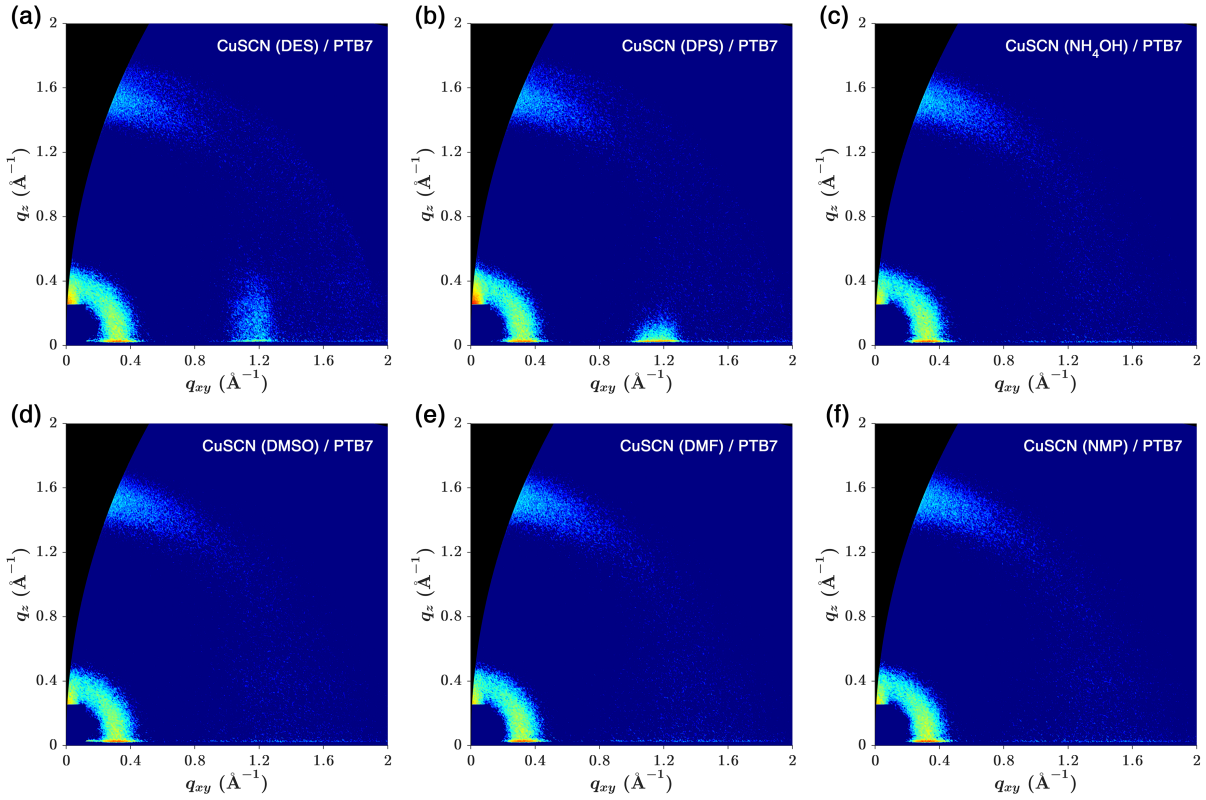

Figure 5.14 | GIWAXS Patterns of PTB7 Deposited on CuSCN Interlayers. CuSCN interlayers were spin-coated from (a) DES, (b) DPS, (c) NH_4OH, (d) DMSO, (e) DMF, and (f) NMP solutions. Note that peaks at $q_{xy} \approx 1.2\,\text{Å}^{-1}$ in (a,b) are from the CuSCN layer underneath.

Fig. 5.14, peaks at $q_{xy} \approx 0.38\,\text{Å}^{-1}$ and $q_z \approx 1.6\,\text{Å}^{-1}$ correspond to face-on orientated crystallites, while the peak at $q_z \approx 0.38\,\text{Å}^{-1}$ signals the presence of edge-on orientated.[349] Note that peaks at $q_{xy} \approx 1.2\,\text{Å}^{-1}$ in Fig. 5.14(a,b) are from the CuSCN layer underneath. In order to quantitatively compare the face-on content, we calculated the face-on relative ratio for each sample, defined as the intensity ratio of the $q_{xy} \approx 0.38\,\text{Å}^{-1}$ peak (face-on) to the $q_z \approx 0.38\,\text{Å}^{-1}$ peak (edge-on). These values are plotted in Fig. 5.12(a) as red dots, and a positive correlation between the PTB7 face-on content and the CuSCN interlayer surface energy can be decidedly drawn, in agreement with previous reports.[134,185,186] Therefore, use of NH_4OH, DMSO, DMF, or NMP as CuSCN solvent allows a higher fraction of face-on orientation for the PTB7 layer.

To test the influence of crystallite orientation on charge transport in diode structures, we employed the MIS-CELIV technique to characterise the hole mobility for PTB7

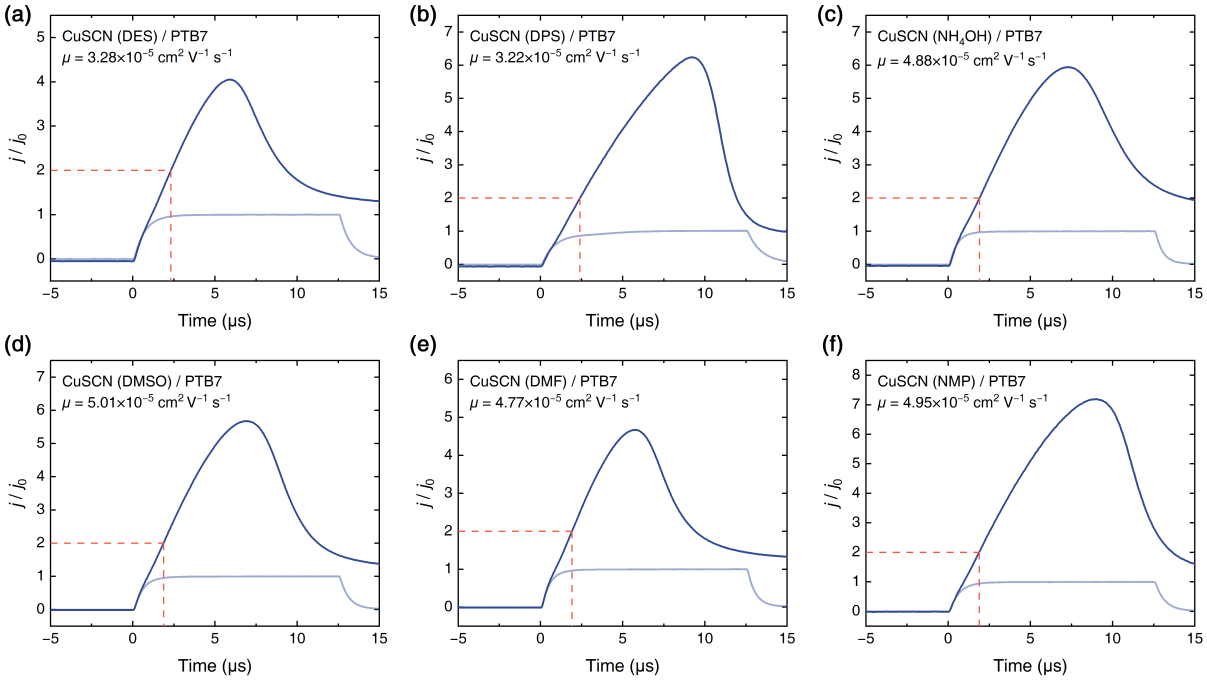

Figure 5.15 | Typical MIS-CELIV Transients for Hole Mobility Determination of PTB7 Deposited on CuSCN Interlayers. CuSCN interlayers were spin-coated from (a) DES, (b) DPS, (c) NH_4OH, (d) DMSO, (e) DMF, and (f) NMP solutions. Both current density transients with (blue) and without (light blue) charge injection are shown, with red dashed lines highlighting the time when $j = 2j_0$. The voltage increasing rate in this dataset was $800\,\mathrm{V\,ms^{-1}}$.

deposited on different CuSCN interlayers, with the device structure comprising ITO / CuSCN / PTB7 (100 nm) / MgF_2 (15 nm) / Al (100 nm). The PTB7 layer was spin-coated using the same parameters as for GIWAXS samples, and MgF_2 (99.99 %, Kurt J. Lesker) and Al (99.99 %, Kurt J. Lesker) were evaporated at 0.2 and $1\,\mathrm{Å\,s^{-1}}$, respectively. The typical current density transients are shown in Fig. 5.15, with which the MIS-CELIV mobility can be extracted (Eq. (3.9)). As illustrated in Fig. 5.12(a) by blue bars, which are obtained from more than 10 devices for each interlayer, the higher face-on orientation fraction for PTB7 on NH_4OH-, DMSO-, DMF-, and NMP-processed CuSCN interlayers leads to a higher hole mobility around $5 \times 10^{-5}\,\mathrm{cm^2\,V^{-1}\,s^{-1}}$, compared with $\sim 3 \times 10^{-5}\,\mathrm{cm^2\,V^{-1}\,s^{-1}}$ for DES- and DPS-processed CuSCN interlayers, i.e. an improvement by ~40 %.

These results confirm that the choice of CuSCN solvent can significantly affect the

charge transport properties of a p-type semicrystalline conjugated polymer overlayer via the resulting differences in surface energy and their influence on polymer crystallite orientation. NH_4OH, DMSO, DMF, and NMP are better choices than conventional DES and DPS to achieve improved diode-relevant, normal-to-plane mobility.

5.6 Energy Levels and Hole Injection

We next turn to the hole-injection properties of the differently processed CuSCN interlayers, which should primarily be dictated by their energy levels. To this end, air photoemission spectroscopy (APS) was used to measure the IPs of CuSCN thin films spin-coated on ITO substrates. The measured photoelectron yields and the determined IPs are shown in Fig. 5.16.

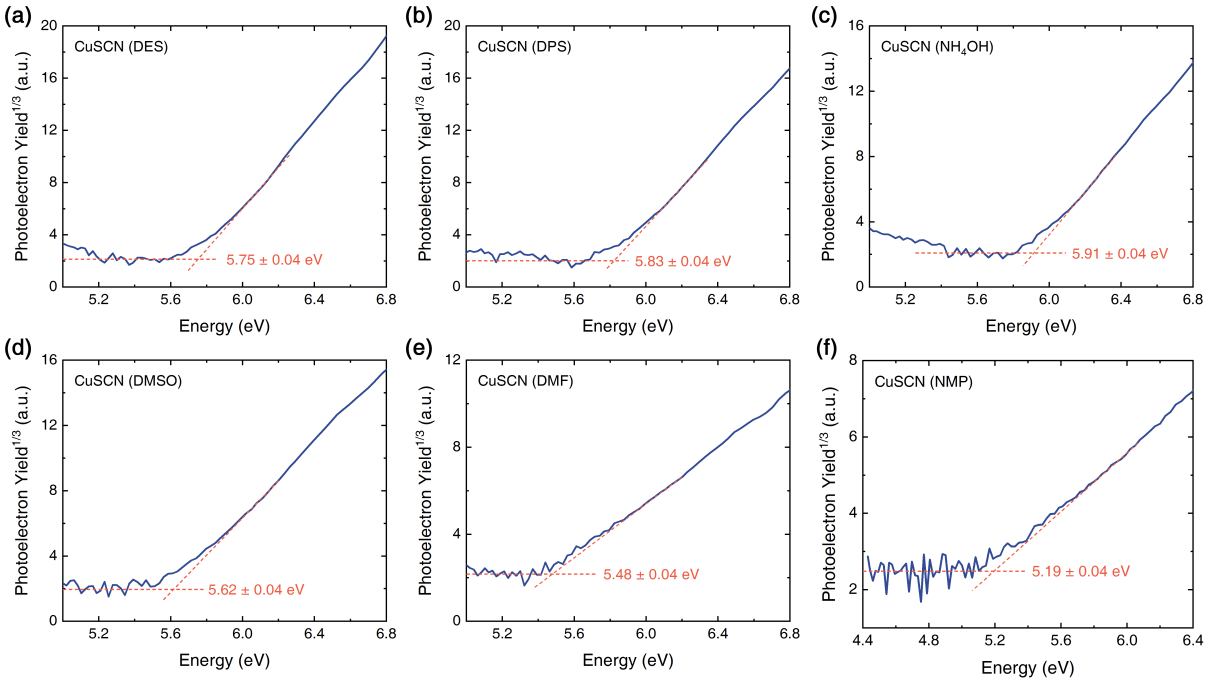

Figure 5.16 | APS Results and Extracted IPs of CuSCN Thin Films. Samples were spin-coated from (a) DES, (b) DPS, (c) NH_4OH, (d) DMSO, (e) DMF, and (f) NMP solutions. Solid blue curves show the experimental data, and dotted red lines denote the extraction of IPs.

In addition, the optical gaps (E_{opt}) of different CuSCN thin films spin-coated on fused silica substrates were extracted from their absorbance spectra via Tauc plots

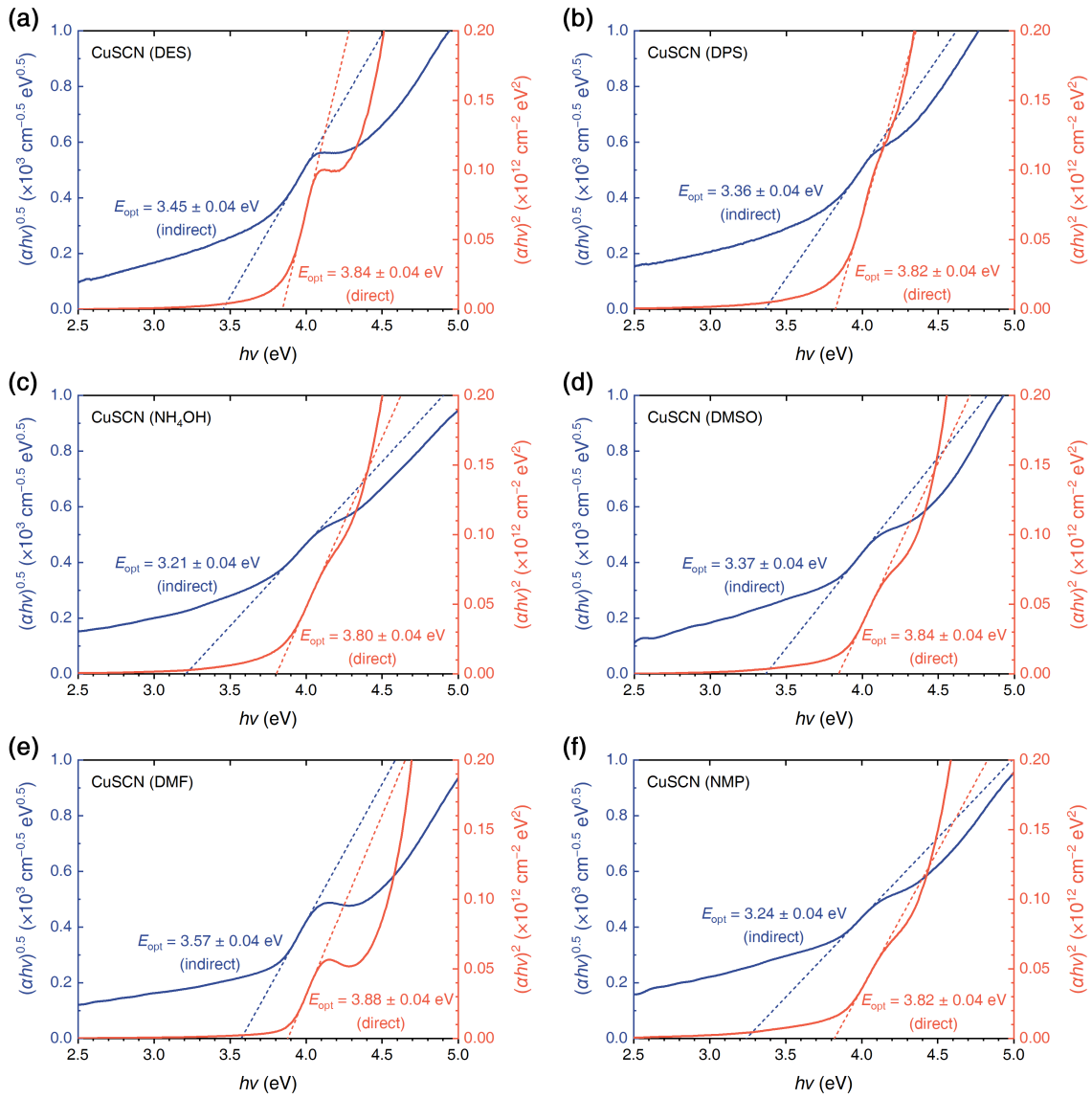

Figure 5.17 | Tauc Plots and Extracted Optical Gaps of CuSCN Thin Films. Samples were spin-coated from (a) DES, (b) DPS, (c) NH_4OH, (d) DMSO, (e) DMF, and (f) NMP solutions. Both $(\alpha h\nu)^{0.5}$ and $(\alpha h\nu)^2$ are calculated, corresponding to the expectation for indirect (blue) and direct (red) band gaps, respectively.

(Section 3.2.2). Figure 5.17 shows the Tauc analysis on all CuSCN samples assuming either a direct or an indirect band gap. We note that the nature of CuSCN band gap is still under debate,[315] and that is why we analyse the same dataset of CuSCN absorbance using both models. In the literature, although DFT calculations predict CuSCN band gap to be indirect,[314] most experimental values are around 3.8 eV, consistent with the calculated value of a direct band gap.[314,315,341] This discrepancy is supposed to be relevant to the

very small oscillator strength of the lowest indirect transition, as this process requires phonons to assist.[314] For our measurements, it can be clearly seen from Fig. 5.17 that the presumption of a direct band gap (red) is more reasonable, since for the indirect (blue), the characteristic parameter $(\alpha h\nu)^{0.5}$ does not cut off at the nominal "band gap". Also, the extracted direct band gap values are very consistent for different CuSCN samples, in contrast with the scattered values obtained from the indirect gap model. Nonetheless, these results are not unambiguous evidence for a direct band gap of CuSCN due to the $>0.5\,\text{eV}$ absorption tail below the determined direct gaps rather than an abrupt cut-off (Fig. 5.17), e.g. $\alpha \approx 2 \times 10^4\,\text{cm}^{-1}$ for the CuSCN-DES thin film at $h\nu = 3.5\,\text{eV}$. Possible reasons for this absorption feature include the weak indirect transitions at lower energies, non-crystallinity, polymorphism, or a combination of these factors.[314,315] Therefore, this topic still needs further elucidation, but what for sure is that the band gap, irrelevant to its nature, is wide enough ($\geqslant 3.80\,\text{eV}$) for CuSCN interlayers to absorb very little in the visible spectral range.

For inorganic semiconductors such as CuSCN, we can calculate the electron affinity (EA) by $\text{EA} \approx \text{IP} - E_{\text{opt}}$ (Section 3.2.3, assuming a direct band gap and insignificant excitonic effects), enabling us to establish a complete energy level diagram for the CuSCN thin films processed from different solvents, as shown in Fig. 5.18. Apart from the small EA ($\leqslant 2.00\,\text{eV}$) of all samples that is conducive to effective electron blocking, interestingly, IPs of CuSCN interlayers are significantly different and dependent on the solvents used, ranging from 5.19 eV for the NMP-processed thin film to 5.91 eV for the NH_4OH-processed. Previous DFT calculations indicated that the position of CuSCN valence band edge is mainly affected by the Cu 3d states, with a small contribution from S 3p hybridisation.[314] As shown in the XPS spectra of S 2p (Fig. 5.9) and Cu 2p (Fig. 5.10) core levels, six CuSCN thin films do differ in the chemical states of these two elements, resulting in their different outermost (3d for Cu ions and 3p for S) electron configurations and consequently, different IPs of CuSCN interlayers. However, the detailed mechanisms behind this may require further theoretical input to clarify.

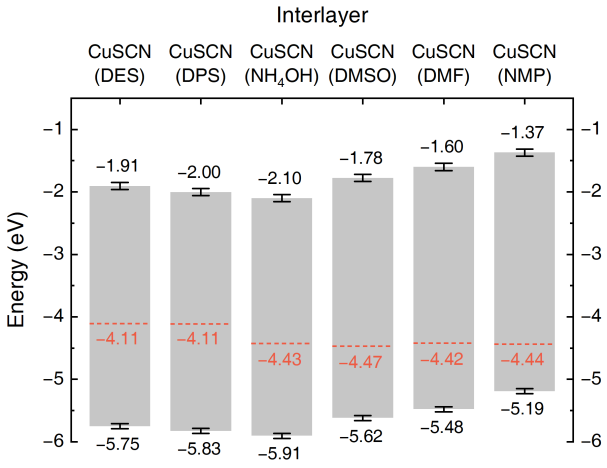

Figure 5.18 | Energy Level Diagram of CuSCN Interlayers. Red dashed lines represent the WFs measured by the Kelvin probe, the uncertainties for which are small and therefore not shown. The band gap (grey bars) is assumed to be direct.

Besides, the WFs for CuSCN thin films deposited from all six solvents were measured using the Kelvin probe, and the results are displayed in Fig. 5.18 by red dashed lines. The WF values of CuSCN interlayers processed from DES and DPS are 4.11 eV, whereas for the other four they are around 4.45 eV, indicating deeper Fermi levels than band gap centres for all samples. For DES- and DPS-processed, this can be understood from CuSCN being an intrinsic p-type semiconductor with a higher electron effective mass than hole.[314,315,320] For the other four, whose Fermi levels are much closer to their valence band edges, we attribute this, in addition to the intrinsic p-conductivity of CuSCN, to the extrinsic p-doping. As mentioned in Section 5.4 along with the XPS spectra of Cu 2p core levels (Fig. 5.10), the partial oxidation of Cu^{+} to Cu^{2+} can result in either Cu^{2+} acting as the p-dopants or the introduction of Cu vacancies in the CuSCN lattice. It has been demonstrated that the latter defect/nonstoichiometry can contribute to an increased hole concentration in CuSCN,[314,315,329] leading to a similar effect on the Fermi level to the p-doping. In all, we infer that it is the partial oxidation of Cu^{+} in NH_4OH-, DMSO-, DMF-, and NMP-processed CuSCN thin films that further deepens their Fermi levels.

Whilst IP values are a good indicator of the expected hole-injection properties of interlayers, other interfacial processes are known to play a role (Section 2.4.2.2) and may cause

deviation of hole-injection barriers from what can be predicted from the nominal energy level diagrams. To further compare the hole-injection properties of different CuSCN interlayers in real devices, we fabricated hole-only diodes using poly[*N*-9′-heptadecanyl-2,7-carbazole-*alt*-5,5-(4′,7′-di-2-thienyl-2′,1′,3′-benzothiadiazole)] (PCDTBT, Fig. 5.19(a)), a conjugated polymer with a suitable IP of 5.34 eV.[350] The device structure was ITO / CuSCN / PCDTBT / MoO_3 (10 nm) / Al (100 nm). PCDTBT (1-Material Inc.) was dissolved in chlorobenzene at a concentration of 8 mg ml^{-1}, and was spin-coated on top of ITO / CuSCN at 1000 rpm, resulting in ~85 nm active layers. The top MoO_3 (99.95 %, Testbourne) / Al composite electrode was evaporated at 0.2 and 1 Å s^{-1}, respectively, and was defined as the cathode of the device. Thus, the different hole injection properties of CuSCN interlayers can be reflected from the current density in the forward bias.

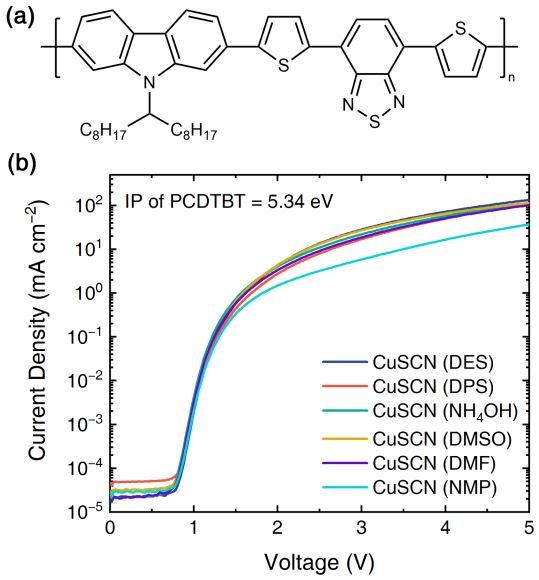

Figure 5.19 | (a) Chemical structure of PCDTBT. (b) Forward bias J–V characteristics for PCDTBT hole-only diodes using differently processed CuSCN interlayers, from which holes are injected into the PCDTBT layer.

In the absence of any complicating factors at the interface, from the deduced IP values, barrier-free hole injection is expected for all CuSCN interlayers into PCDTBT except for that processed from NMP (IP = 5.19 ± 0.04 eV, smaller than 5.34 eV of PCDTBT). The measured current density–voltage (J–V) characteristics (Fig. 5.19(b)) are fully consistent

with this expectation, with the curve for the CuSCN-NMP device showing a significantly lower current density at voltages above ~1.5 V. All of the other curves closely align.

To summarise this section, we have established a detailed picture of the variation in energy level structure for CuSCN interlayers processed from different solvents. The wide tuneability of CuSCN interlayer IP value from 5.19 to 5.91 eV opens an opportunity to minimise hole injection barriers for specific active materials by the careful selection of processing solvent.

5.7 Device Performance

5.7.1 Organic light-emitting diodes (OLEDs)

Having investigated the optical and electrical properties of CuSCN interlayers processed from different solvents, we now report on their performance in representative OLED, OPV and OFET devices. First, OLEDs using the commercially available phenylene–vinylene copolymer Super Yellow (SY, number-average molecular weight $M_n > 400\,000$, weight-average molecular weight $M_w > 1\,300\,000$, Sigma-Aldrich, Fig. 5.20(b)) as EMLs were fabricated. Comparison was made between PEDOT:PSS and a selection of CuSCN HILs/HTLs in the conventional bottom emission device structure: ITO / PEDOT:PSS or CuSCN / SY (~90 nm) / LiF (1 nm) / Al (100 nm) (Fig. 5.20(a)). The SY layer was spin-coated from the 5 mg ml^{-1} toluene (99.8 %, anhydrous, Sigma-Aldrich) solution at 1500 rpm, followed by thermal annealing at 80 °C for 10 min. The top cathode of LiF (99.99 %, Testbourne) and Al was evaporated at 0.2 and 1 Å s^{-1}, respectively. The nominal energy level diagram is shown in Fig. 5.20(c), with the data of SY sourced elsewhere.[351]

Two figures of merit, namely the luminance (at 6 V) and maximum external quantum efficiency (EQE) are reported in Fig. 5.20(d) for each of the devices. All SY OLEDs share a similar EQE of ~3.5 % but they differ in luminance, consistent with the difference in charge injection properties of different interlayers. In detail, the device using a CuSCN-DMSO interlayer exhibits the highest luminance at 6 V ($13\,585 \pm 1204$ cd m^{-2}), significantly

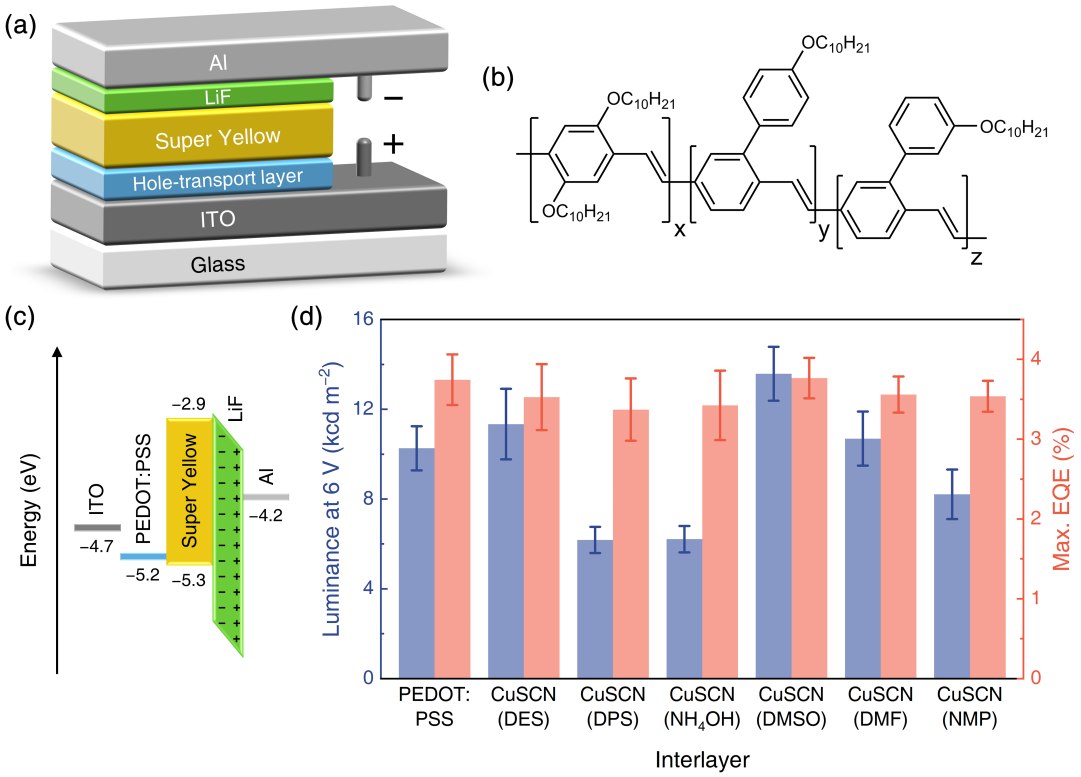

Figure 5.20 | Performance of SY Polymer OLEDs Using Different Interlayers. (a) Illustration of the device structure. (b) Chemical structure of SY. (c) Nominal device energy level diagram. For energy levels of CuSCN interlayers, see Fig. 5.18. (d) Luminance (at 6 V) and maximum EQE values of devices with different interlayers.

better than the reference device using PEDOT:PSS ($10\,264 \pm 981$ cd m^{-2}). In addition, when DES or DMF is used as the solvent, a similar/somewhat higher luminance to that for the PEDOT:PSS-based device can be achieved. Previous research showed that for phosphorescent OLEDs, replacing PEDOT:PSS with DES-processed CuSCN retained comparable performance.[177] Here we further demonstrate that by choosing a specific solvent, namely DMSO in this case, it is possible to fabricate CuSCN-containing polymer fluorescent OLEDs that notably outperform PEDOT:PSS-containing devices by ~32 % higher luminance (at 6 V).

5.7.2 Organic solar cells (OPVs)

Inspired by the favourable polymer OLED performance, we next fabricated BHJ OPVs using a blend of PTB7 and $PC_{71}BM$ (1-Material Inc., Fig. 5.21(b)) as the active material.

Again, comparison is made between CuSCN processed from different solvents and PEDOT:PSS, and the device structure is ITO / PEDOT:PSS or CuSCN / PTB7:$PC_{71}BM$ (~100 nm) / Ca (10 nm) / Al (100 nm) (Fig. 5.21(a)). The active materials, PTB7 (donor, D) and $PC_{71}BM$ (acceptor, A), were dissolved in chlorobenzene, with 3 vol% 1,8-diiodooctane (DIO, 98 %, Sigma-Aldrich) as the additive, at a total concentration of 25 mg ml^{-1} (D : A = 2 : 3 by weight). The solution was spin-coated at 1000 rpm, and the resulting active layer was annealed at 80 °C for 10 min. Finally, the top cathode comprising Ca (at 0.2 Å s^{-1}, 99 %, Kurt J. Lesker) and Al (at 1 Å s^{-1}) was evaporated. The device energy level diagram is presented in Fig. 5.21(c), and the active materials' EAs and IPs are from a previous report.[352]

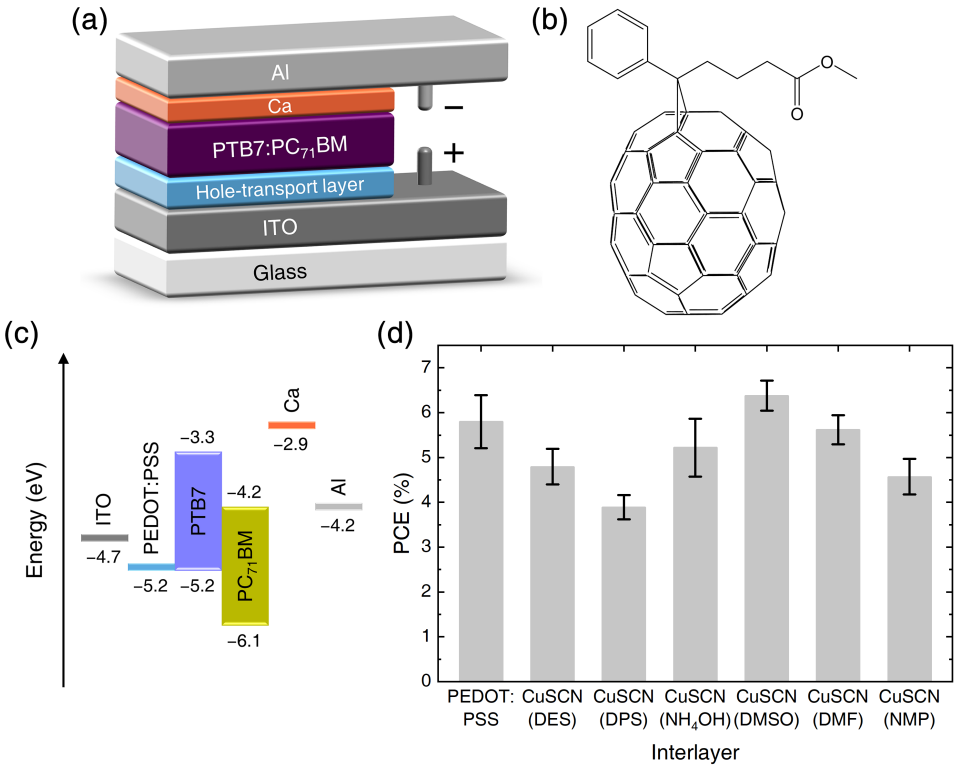

Figure 5.21 | Performance of PTB7:$PC_{71}BM$ OPVs Using Different Interlayers. (a) Illustration of the device structure. (b) Chemical structure of $PC_{71}BM$. (c) Nominal device energy level diagram. For energy levels of CuSCN interlayers, see Fig. 5.18. (d) The PCE of devices with different interlayers.

As shown in Fig. 5.21(d), a higher average power conversion efficiency (PCE) of ~6.4 %

is achieved for the device using a CuSCN-DMSO interlayer, compared with the reference PEDOT:PSS device (~5.8 %). Despite the overlapping of error bars not allowing us to unambiguously confirm the PCE enhancement arising from the CuSCN-DMSO interlayer, at least a higher average PCE with a narrower spread can be summarised for sure. Prior reports have also shown OPV efficiency improvement relative to PEDOT:PSS for CuSCN-DES[317,318] and -NH_4OH[322] interlayers when using different active materials. It will be interesting, in future, to explore the suitable combination of different active materials with different CuSCN solvent choices for even better overall performance.

5.7.3 Organic field-effect transistors (OFETs)

Lastly, OFETs were fabricated using the high-mobility conjugated polymer, poly[[2,5-bis-(2-octyldodecyl)-2,3,5,6-tetrahydro-3,6-dioxopyrrolo[3,4-*c*]pyrrole-1,4-diyl]-*alt*-[[2,2′-(2,5-thiophene)bis-thieno[3,2-*b*]thiophen]-5,5′-diyl]] (PDPPTTT, M_w = 75 000, polydispersity index n = 5.4, supplied courtesy of Dr. Sungho Nam, Fig. 5.22(b)). The devices were studied in top-gate bottom-contact configuration with CuSCN interlayers inserted between the electrodes (drain and source) and the polymer layer (Fig. 5.22(a)). In this case, comparison was referenced to uncoated Au electrodes. The source and drain (50 nm thickness Au, 99.99 %, Testbourne) were evaporated on glass substrates through shadow masks at 0.2 Å s^{-1}, leading to a channel length of 50 µm and width of 2 mm. After the deposition of CuSCN interlayers, PDPPTTT (~30 nm) were spin-coated on top from the 10 mg ml^{-1} 1,2-dichlorobenzene (99 %, anhydrous, Sigma-Aldrich) solution at 2000 rpm, followed by thermal annealing at 150 °C for 10 min. Next, poly(methyl methacrylate) (PMMA, M_w = 120 000, n = 2.2, Sigma-Aldrich) dielectric layers of ~350 nm were spin-coated from the 40 mg ml^{-1} *n*-butyl acetate (99.5 %, Sigma-Aldrich) solution at 1500 rpm and then baked at 60 °C for 30 min. The OFET fabrication was completed by evaporating Al gate electrodes (80 nm) at 1 Å s^{-1}. Figure 5.22(c) displays the energy level diagram, in which the data are extracted from previous papers.[353,354]

The hole mobility extracted from the linear regime (μ_{lin}) for all devices is shown

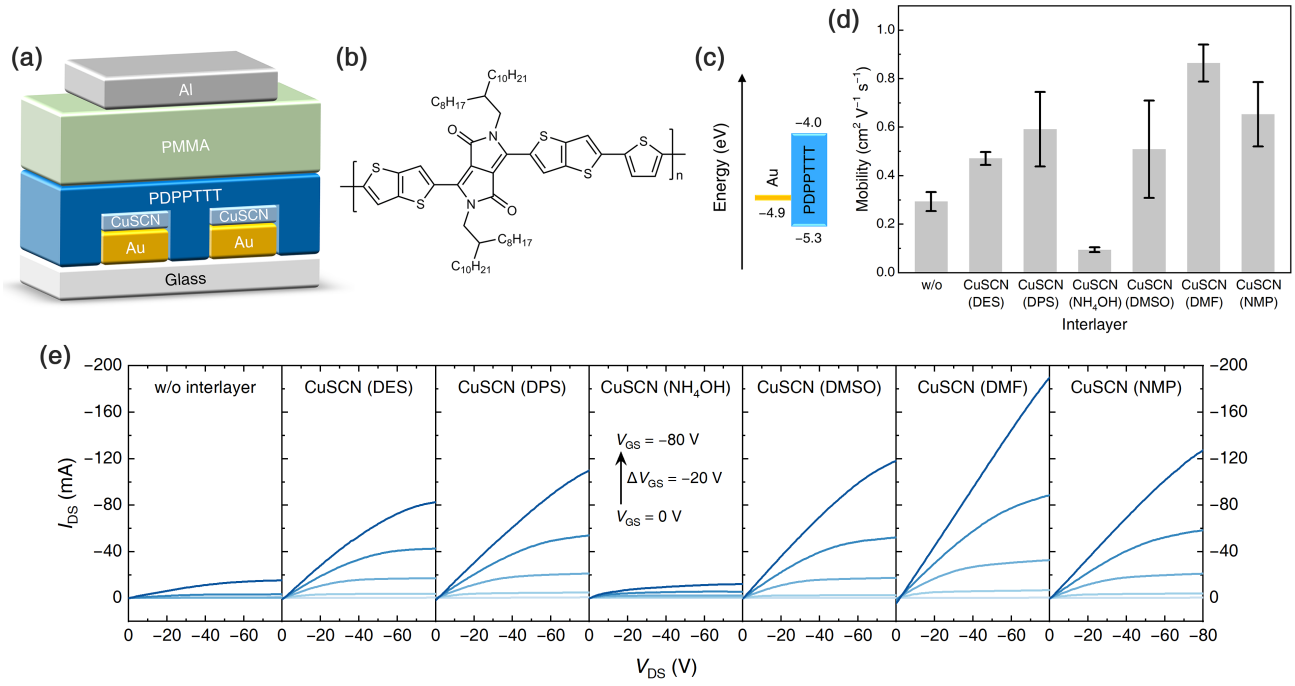

Figure 5.22 | Performance of PDPPTTT OFETs Using Different Interlayers. (a) Illustration of the device structure. (b) Chemical structure of PDPPTTT. (c) Nominal device energy level diagram. For energy levels of CuSCN interlayers, see Fig. 5.18. (d) Hole mobility (extracted from the linear regime) for PDPPTTT with different interlayers. (e) Output characteristics parametric in V_{GS} (from 0 to −80 V in −20 V steps).

in Fig. 5.22(d). The highest $\mu_{lin} = 0.86 \pm 0.07\,cm^2\,V^{-1}\,s^{-1}$ is achieved for devices using a CuSCN-DMF interlayer, some three times higher than that for the reference device with no interlayer ($0.29 \pm 0.04\,cm^2\,V^{-1}\,s^{-1}$). Five of the six solvents yield higher mobility than the reference device; CuSCN-NH_4OH is the exception. We note that CuSCN processed from NH_4OH has been used as the semiconducting layer, rather than the interlayer, in transistors, showing higher hole mobility than the DES-processed.[322] The output characteristics in Fig. 5.22(e) also clearly show the significant enhancement engendered by the CuSCN-DMF interlayer; the drain current I_{DS} at $V_{GS} = V_{DS} = -80$ V can reach ~190 mA, whilst it drops to ~20 mA when the interlayer is absent. The improved hole mobility and channel current are expected to be related to the better energy level match between the CuSCN-modified electrodes and PDPPTTT. Specifically, the IP of PDPPTTT was measured to be 5.3 eV (Fig. 5.22(c)),[354] and the CuSCN interlayer

processed from DMF has an IP (5.48 ± 0.04 eV) not only larger than but also closest to it (Fig. 5.18).

To summarise this section, we successfully demonstrated that by choosing an appropriate CuSCN solvent, representative polymer OLEDs, OPVs, and OFETs with CuSCN interlayers can perform better than reference devices either with PEDOT:PSS or without an interlayer. Besides, DMSO and DMF solvents are found to allow CuSCN interlayers to facilitate better device performance than for the conventional solvent choices of DES and DPS that are neither convenient to use nor eco-friendly. An additional comment we would like to make here is that it is not straightforward to explicitly attribute the improved device performance to one or more factors studied above, i.e. the surface roughness, polymorphism, chemical composition, surface energy, and energy levels, as their impacts on device performance are somewhat interwoven and difficult to decouple, e.g. the deduced influence of some may counteract others'. Despite that at this stage we cannot clearly recognise the predominant factors, our device tests do exemplify that there are novel options for CuSCN solvents other than the conventional DES and DPS that can lead to better device performance. It is these new possibilities that contribute to the significance of this comparative study.

5.8 Conclusions and Outlook

In this chapter, we report a comprehensive study on the properties and applications of CuSCN interlayers processed from six different solvents, namely DES, DPS, NH_4OH, DMSO, DMF, and NMP. In the case of DMSO, drop-cast thick films comprise a mixture of the α- and β-phase crystalline polymorphs whereas all other solvents yield films containing only the β-CuSCN. Thin films deposited by spin-coating show similar surface roughness, with R_{rms} values close to that of the underlying ITO-coated glass substrate (except the NMP-processed one which is ~30 % rougher), but their chemical characteristics differ. In samples processed from NH_4OH, DMSO, DMF, and NMP solutions, there is a noticeable oxidation of sulphur, yielding S−O bonds, and copper to Cu^{2+}, with an associated impact

on CuSCN electronic structure.

The solvent used to deposit CuSCN interlayers affects the hole injection and transport properties in two different ways. For one thing, the crystallite orientation of a semicrystalline conjugated polymer, PTB7, deposited on top of the CuSCN interlayers processed from the six solvents is influenced by their different surface energies. This leads to different PTB7 normal-to-plane hole mobility, with ~40 % higher values of ~$5 \times 10^{-5}\,\mathrm{cm^2\,V^{-1}\,s^{-1}}$ when NH_4OH, DMSO, DMF, or NMP is used as the solvent. The higher surface energies of CuSCN thin films processed therefrom (~$75\,\mathrm{mJ\,m^{-2}}$, compared with ~$60\,\mathrm{mJ\,m^{-2}}$ for DES- and DPS-processed) support a higher fraction of face-on orientated crystallites. For another, significantly different IP values ranging from 5.19 to 5.91 eV result for CuSCN interlayers processed from different solvents in the sequence NMP < DMF < DMSO < DES < DPS < NH_4OH, leading to different hole injection properties. This is confirmed by the J–V characteristics for hole-only diodes, demonstrating the possibility to minimise hole injection barriers by appropriate selection of CuSCN solvent to achieve a good match in IP values between CuSCN interlayers and active materials.

Finally, device tests show that in polymer OLEDs, OPVs, and OFETs, using CuSCN interlayers processed from suitable solvents can boost the performance compared with reference devices. In particular, for the devices studied in this work, the best performance is provided by DMSO and DMF, more benign solvents than the initially used DES and DPS. These results pave the way for a wider use of solution-processed CuSCN interlayers in a variety of OSC devices for both lab-scale research and large-area fabrication, and expand the selection range for hole-injection/transport materials, making CuSCN a more competitive substitute for PEDOT:PSS. Further research about the solvent-dependent electronic structure and crystallisation mechanisms of CuSCN films, as well as more examples of promoting OSC device performance using CuSCN interlayers processed from different solvents, will be helpful in better understanding this promising hole injection/ transport material.

Chapter 6

Solution-Processed Organic Schottky Diodes for High-Frequency Rectifiers

6.1 Introduction

Modern human society is developing towards a higher degree of automation and connectivity. Under such a scenario, physical objects around people are interconnected to achieve the Internet of Things (IoT), which allows them to "sense the environment, communicate with each other, and coordinate their behaviour over wireless connections".[355] Therefore, a prerequisite for IoT is the automatic identification of objects by, for instance, barcode labels. However, the small storage capacity of barcodes, as well as the inability to be re-programmed,[356] restricts their applications, thereby spawning the more powerful radio-frequency identification (RFID) system.

An RFID system uses electromagnetic waves in the RF range (125 kHz–5.8 GHz)[357] to transmit data wirelessly. Such a system comprises a tag (or transponder) attached to the object to be identified, and a reader (or interrogator) to generate the RF signal and receive the information from the tag.[356] The tag can be either passive or active depending on the source of power; the former is driven by the incoming RF signal, whereas the latter has its own energy supply, e.g. a battery or a photovoltaic module. Due to the lower cost and the smaller form factor, passive tags are growing in popularity.[358] A passive RFID tag has three main components: an antenna, a rectifier, and logic circuitry.[359] During operation, the tag is placed within the reader's interrogation zone, so the antenna can capture the alternating current (AC) signal from the reader, which is then rectified to the

direct current (DC) signal by the rectifier. The resultant DC voltage drives the transistors in logic circuitry, enabling the stored information to be relayed back to the reader.

Two crucial selection criteria for RFID tags are the operating frequency (f) and the detection range,[356] which generally are positively correlated. At 125 kHz and 134 kHz, the tag works in the low-frequency (LF) regime with a typical reading range of ~30 cm,[357] and can be used in animal tagging and access control.[359] High-frequency (HF) RFID tags operate at 13.56 MHz, and the detection range can be extended to ~1 m,[357] suitable for industrial automation and near-field communication (NFC) such as contactless payment cards.[359] The ultrahigh frequency (UHF) of 865 MHz (within Europe) or 915 MHz (outside Europe)[356] allows an even longer reading distance of ~10 m for tracking and logistics purposes.[357] Finally, the microwave regime (f = 2.45 GHz or 5.8 GHz) can cover the largest distance (> 10 m),[357] but microwave tags are more expensive because of the low demand.[359] Thus it is not surprising to see from recent statistics that the HF (13.56 MHz) is the most popular frequency band, with an increasing tendency for UHF tags to dominate the market in the near future due to their longer detection distances.[359]

The working frequency of an RFID tag largely hinges on the capability of the rectifier to convert the AC signal to the DC, leading the rectifier to be the key component of RFID tags. Therefore, we shall primarily discuss the rectifier below. The rectifier circuit can be half-wave, double-half-wave, or full-wave,[360] and the simplest half-wave rectifier is composed of a rectifying device (usually a diode D), a smoothing capacitor C, and a load resistor R,[361] as Fig. 6.1(a) illustrates. When the diode is in the forward bias, charges are allowed to pass through and can then be stored in the capacitor or consumed by the load. In the reverse bias, the diode blocks the current, so the capacitor discharges to try to maintain a constant DC voltage across the resistor. As long as the current from the next forward bias can charge the capacitor fast enough before significant discharge occurs, stable DC output without noticeable ripples results.[359] The performance of a rectifier is usually evaluated by two figures of merit, the output voltage V_o at low frequencies (under a particular AC input voltage V_i) and the 3-dB frequency f_{3dB}, at which the output voltage

drops to half the V_o,[362] corresponding to a voltage gain of −3 dB. These two proxies can be obtained from the rectifier's V_o–f characteristics, exemplified in Fig. 6.1(b); a V_o of 6.02 V and an f_{3dB} of 1.24 GHz can be extracted for this rectifier.[182] It is evident that an outstanding rectifier features a large V_o (under a particular V_i) and a high f_{3dB}, so the voltage loss is small and the device has the potential for HF/UHF applications.

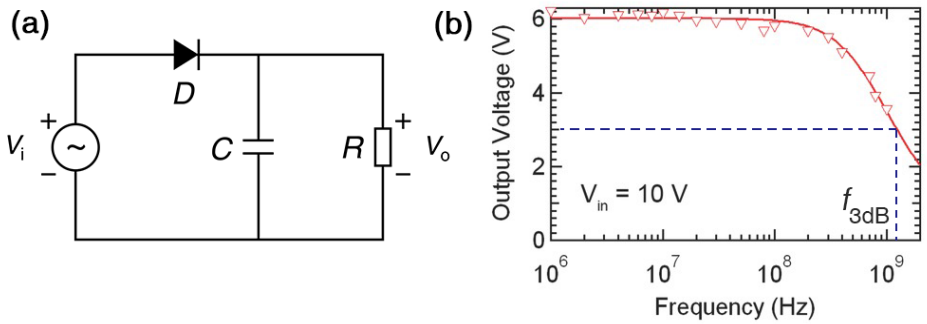

Figure 6.1 | (a) Schematic diagram of the simplest half-wave rectifier. (b) Representative V_o–f characteristics for a half-wave rectifier (red triangles), with dashed blue lines denoting the determination of f_{3dB}. The rectifier comprises a 10 nF smoothing capacitor, a 1 MΩ load resistor, and a pentacene-based organic Schottky diode. The amplitude of the input sinusoidal AC signal is 10 V. Adapted with permission.[182] Copyright 2016, Wiley.

Apart from the frequency-dependent performance, the cost and mechanical properties are two practical considerations in appraising the rectifier. For one thing, achieving the IoT requires a huge number of RFID tags to be affixed to every physical object, which can only be realistic if high-throughput manufacturing can substantially reduce the cost. This is exactly the strength of solution-processing techniques such as roll-to-roll printing.[363] For another, flexible tags are preferable due to the reduced possibility of mechanical failure under various usage scenarios. Though Si-based flexible electronics can be achieved by, for example, decreasing the Si layer thickness,[359,364] the intrinsically bendable and stretchable OSCs offer us more feasibility. In all, solution-processed organic rectifiers are a promising component for the low-cost, mechanically flexible HF/UHF RFID tags.

In this chapter, we investigate solution-processed rectifiers based on organic Schottky diodes (OSDs). The reasoning behind using OSDs as the rectifying device is given in

Section 6.2 by comparing OSDs with organic heterojunction diodes (OHDs) and organic field-effect transistors (OFETs) operating in the transdiode mode. Next, numerical simulation of the rectifier's performance is carried out in Section 6.3 on the basis of an improved device model which was originally proposed by Steudel et al.[365] The simulation results then guide us through the design, fabrication, and optimisation of solution-processed OSD-based rectifiers, and three types of devices are presented and discussed in Sections 6.4, 6.5, and 6.6, among which the best can exhibit $V_o = 4.00\,V$ (under a sinusoidal AC input whose amplitude $V_m = 5.00\,V$) and $f_{3dB} = 243\,MHz$ (estimated by simulation). Our results demonstrate the potential of achieving UHF RFID tags using solution-processed OSD-based rectifiers, widening the application range of OSCs beyond OLEDs, OPVs, and OFETs to the RFID field, a market forecast to be worth $10.7 billion in 2021 under the impact of COVID-19 and $17.4 billion by 2026.[366]

6.2 Comparison of Organic Rectifying Devices

In this section, we shall introduce three kinds of organic rectifying devices that can be used in rectifiers, namely OHDs, OFETs in the transdiode mode, and OSDs, and discuss their respective advantages and disadvantages for HF applications. Representative literature and recent progress are summarised as well.

6.2.1 Organic heterojunction diodes (OHDs)

The most common rectifying device is the Si-based pn-junction diode. Its asymmetric conductance comes from the voltage-dependent built-in potential barrier, which decreases in the forward bias so the large, majority-carrier diffusion current dominates, and increases in the reverse bias so the small, minority-carrier drift current takes over.[47] For organic diodes, the rectifying properties can be achieved by using type-II heterojunctions, where the transport gap of two components overlaps but neither is contained within the other. The n- and p-type characters may rely on doping with proper dopants, similar to the case of Si; for those undoped, their energy levels and the ability to transport electrons

and holes are key factors. In the latter category, both metal–OSC contacts in OHDs are Ohmic to ensure efficient charge injection in the forward bias, but in the reverse bias large injection barriers exist, leading to very different magnitudes of current density, i.e. the rectifying properties.

The main advantage of OHDs is the small reverse current density,[362] resulting in a high rectification ratio (RR), an evaluation of the rectifying properties defined as the current density ratio at the same absolute voltage between the forward and reverse biases. Another bonus for doped OHDs is that the current density can be controlled by adjusting the doping concentration, and a high concentration additionally allows charge carriers to tunnel through the thin depletion region, so quasi-Ohmic metal–OSC contacts can form irrespective to the metal's WF.[362] However, a drawback that can downgrade the HF performance of OHDs is the junction-capacitance-related reverse recovery time, t_{rr}, usually in the microsecond scale.[362] In detail, in the forward bias, some charges are stored at the junction interface and have to be discharged when the OHD is switched to the reverse bias.[362] This means that at the beginning t_{rr} time of the reverse bias, considerably large current can still pass the diode. If the frequency $f > 1/t_{rr}$, then the OHD does not have an off-state anymore and fails in rectifying the AC input, more like a capacitor. In addition, from the perspective of device fabrication, a solution-processed OHD with the planar heterojunction structure requires the active material deposited first to be orthogonal to the other's solvent, which can hardly be achieved in that most soluble OSCs share similar solvents. Admittedly, the BHJ-type device does not have such fabrication issues, but its interpenetrating microstructure is unfavourable to charge transport. Previous results have shown that both hole and electron mobilities for BHJ diodes are lower than those for unipolar diodes using the constituent active materials of the BHJ.[210] The reduced mobility can lower the forward current density, thereby decreasing the RR.

Due to these disadvantages, up to now there are few reports on OHD-based rectifiers, and their performance is usually mediocre. For instance, the rectifier with a ZnO / poly(3,3‴-didodecylquater-thiophene) (PQT-12) inorganic–organic hybrid pn-

heterojunction diode exhibited an f_{3dB} of ~2 MHz,[367] and with a *N*,*N*′-bis(3-methylphenyl)-*N*,*N*′-diphenylbenzidine (TPD) / C_{60} OHD gave a similar f_{3dB} of ~2.5 MHz.[368] However, it has been shown that doped OHDs can lead to better performance, e.g. $f_{3dB} \approx$ 60 MHz for a rectifier containing a p-doped pentacene / n-doped C_{60} heterojunction with an undoped pentacene interlayer.[369] Recently, a molecular diode with a fluorinated cobalt phthalocyanine (F_{16}CoPc) / copper phthalocyanine (CuPc) nano-heterojunction enabled the rectifier to operate at 10 MHz, but its working principles are very different from the common OHDs.[370]

6.2.2 Organic field-effect transistors (OFETs) in the transdiode mode

OFETs can be employed as rectifying devices under the transdiode mode, where the drain and gate are shorted, leading the drain–source voltage V_{DS} to equal the gate–source voltage V_{GS}.[359] Thus in the "forward bias", $V_{DS} = V_{GS} > V_{GS} - V_{Th}$, so the OFET works in the saturation regime with the drain–source current I_{DS} increasing quadratically with $V_{GS} - V_{Th}$.[153] In the "reverse bias", the direction of V_{GS} changes, so few charge carriers can be injected from the source and then transported in the channel. The different magnitudes of I_{DS} in the forward and reverse biases render OFETs in the transdiode mode the rectifying properties.

When talking about OFET-based rectifiers, people usually adopt the transition frequency f_T as the analogue to f_{3dB}. It is defined as the frequency at which the current gain is unity, i.e. $I_{DS} / I_{GS} = 1$.[359] Theoretical analysis has found that two critical requirements for reaching a high f_T are the low contact resistance R_c and the short channel length L,[371] which are impediments for OFET-based rectifiers to operate at high frequencies. On the one hand, the contact resistance, caused by the non-idealities at the source– and the drain–OSC interfaces, is widely observed in OFETs but hard to control under a reasonably small value, because R_c is affected by a number of interdependent parameters such as the injection barrier, mobility, channel length, interface, and device configuration.[372] On the other hand, reducing L to the sub-μm scale remains challenging.

The usual way to define L is by evaporating electrodes with a shadow mask, on which creating a pattern with such small dimensions is demanding.

The majority of OFETs used in rectifiers are vacuum-deposited. For example, a pentacene-based OFET enabled the rectifier to operate at 13.56 MHz,[373] and using 2,9-diphenyl-dinaphtho[2,3-*b*:2′,3′-*f*]thieno[3,2-*b*]thiophene (DPh-DNTT) as the active material can achieve an f_T of 21 MHz.[374] Solution-processed devices were also reported, though usually with compromised performance, e.g. f_T = 10.4 MHz for a poly[[*N*,*N*′-bis(2-octyldodecyl)-naphthalene-1,4,5,8-bis(dicarboximide)-2,6-diyl]-*alt*-5,5′-(2,2′-bithiophene)] (N2200) OFET rectifier.[375] Very recently, another solution-processed N2200 OFET rectifier exhibited a high f_T of 160 MHz, but it is noteworthy that the applied voltage was also much higher than normal (40 V),[376] precluding its application in RFID tags. It can thus be concluded that nowadays most OFET-based rectifiers can only work in the HF regime. Notwithstanding, they still draw some attention since their manufacturing is compatible with logic circuitry in RFID tags, allowing both to share the same production line.[359]

6.2.3 Organic Schottky diodes (OSDs)

In contrast to OHDs, OSDs are unipolar devices with the active layer sandwiched between two electrodes. The different nature of two metal–OSC contacts underlies the rectifying properties of OSDs. Specifically, one contact is Ohmic, and the electrode's WF matches the active material's EA (or IP) for electron (or hole) injection. Thus in the forward bias, electrons (or holes) can be readily injected with a very small barrier (usually < 0.3 eV),[114] leading to large forward current density. The other contact, however, is a Schottky contact, effective in blocking charge injection. Ideally, the electrode's WF is close to the active material's transport gap centre, so in the reverse bias, a limited number of electrons (or holes) can overcome the injection barrier, resulting in small reverse current density.

The main advantage of Schottky diodes is that they are particularly qualified to operate at high frequencies. Unlike OHDs, OSDs do not have a "junction" structure that

can store charge carriers in the forward bias, so their switching speed is not restricted by any "reverse recovery time". Consequently, OSDs can cease the conduction in the reverse bias way faster than OHDs, contributing to their superior rectifying performance in the HF/UHF regime. The downside of OSDs, unfortunately, is their relatively large reverse current density, as at high reverse voltages the electric field can assist charge carriers to overcome the injection barrier. Such leakage current is not only detrimental to the RR, but can also cause the accumulation of heat that threatens the device stability.

Owing to their high working frequencies, OSD-based rectifiers received more attention relative to the OHD- and OFET-based. In the seminal paper about organic rectifiers, Steudel et al. fabricated a 50 MHz rectifier using a vacuum-deposited pentacene OSD.[365] The full potential of pentacene was then exploited by Kang et al., who reported a pentacene-OSD-based rectifier with $f_{3dB} = 1.24$ GHz, thanks to the well-controlled molecular orientation.[182] Besides pentacene, other evaporated OSCs were also investigated, such as C_{60}, with which the rectifier's f_{3dB} can reach 700 MHz,[377] and very recently, rubrene, which enabled the rectifier to work in the gigahertz regime with considerably lower voltage loss than the pentacene-based device.[378]

Compared with the high performance of vacuum-deposited OSD rectifiers, those processed from solutions lag behind. For example, the one with P3HT only showed an f_{3dB} of 1.8 MHz,[379] and with poly(triarylamine) (PTAA) can operate at 13.56 MHz.[380] Recently, an N2200-based OSD rectifier achieved an f_{3dB} of >25 MHz,[381] and using an indacenodithiophene–benzothiadiazole copolymer, C_{16}IDT-BT, can further improve this value to >68 MHz.[382] Additionally, an exceptionally high f_{3dB} of ~400 MHz was attained using solution-processed C_{60} OSD,[383] but it should be mentioned that the device was in an unusual planar configuration, where the deposition of two asymmetric electrodes separated by a ~20 nm gap involved complicated nanofabrication.

In summary, OSDs are suitable for organic HF/UHF RFID tags, but it is still tough to achieve cost-effective, solution-processed OSDs with outstanding frequency response. These facts motivate us to investigate HF/UHF solution-processed OSD-based rectifiers,

and a good starting point is to find the factors that limit their performance.

6.3 Performance Simulation of Organic-Schottky-Diode-Based Rectifiers

A viable way to understand how different factors affect the performance of OSD-based rectifiers is by simulating the V_o–f characteristics, and the results can in turn provide us with guidance on optimising the device sensibly. In this section, we shall first briefly review the device model proposed by Steudel et al.,[365] emphasising its basic ideas and drawbacks. Next, an improved model is introduced, based on which numerical simulation was performed and factors that can influence OSD-based rectifiers' performance are recognised and discussed. Finally, strategies for high-performance OSD-based rectifiers are summarised.

6.3.1 Steudel's model

Steudel's model correlates the maximum working frequency f of the rectifier with the OSC's mobility μ, the active layer thickness d, the output DC voltage V_o, the input sinusoidal AC voltage $V_i = V_m \sin 2\pi ft = V_m \sin \omega t$, and a transition voltage V_T, above which the current in OSDs shows trap-free SCLC characteristics. It assumes that[365]

1. the leakage current density in the reverse bias $J_r = 0$;
2. the charging time of the capacitor is negligible;
3. the diode active area A can be arbitrarily chosen without any fabrication issue;
4. the output DC voltage V_o is stable without any ripple.

The derivation of f is enabled by considering that in one period $T = 2\pi/\omega$, the charge consumed by the load R has to be equal to the charge passing through the diode in its forward bias:

$$\frac{V_o}{R} \cdot \frac{2\pi}{\omega} = \int_{t_a}^{t_b} I_f \, dt \tag{6.1}$$

Here the lower and upper limits of the integral, t_a and t_b, defines the time range within

which the diode is in the trap-free SCLC regime with the current I_f. The left side of this equation can be further simplified by paraphrasing the fourth assumption mentioned above; the circuit's RC constant should be way larger than the period T, and the capacitance of the diode should be much smaller than that of the smoothing capacitor C:

$$RC \gg \frac{2\pi}{\omega} \Longrightarrow RC = N_1 \frac{2\pi}{\omega} \tag{6.2}$$

$$C \gg \frac{\varepsilon_0 \varepsilon_\mathrm{r} A}{d} \Longrightarrow C = N_2 \frac{\varepsilon_0 \varepsilon_\mathrm{r} A}{d} \tag{6.3}$$

Here N_1 and N_2 are very large numerical factors; ε_0 and ε_r are the vacuum and the OSC's relative permittivities, respectively. Following Steudel's derivation and equating N_1 with N_2, we can obtain the expression of R, with which Eq. (6.1) can be rewritten as:

$$\frac{V_\mathrm{o} \varepsilon_0 \varepsilon_\mathrm{r} A}{d} = \int_{t_\mathrm{a}}^{t_\mathrm{b}} I_\mathrm{f} \, \mathrm{d}t \tag{6.4}$$

For the right side of this equation, the time-dependent I_f can be described by the Mott–Gurney law (Eq. (2.9)), with the voltage across the diode $V_\mathrm{D} = V_\mathrm{m} \sin \omega t - V_\mathrm{o}$. This implies that below V_T, I_f is too small to be considered. The limits of integration, t_a and t_b, are given by (Fig. 6.2):

$$t_\mathrm{a} = \frac{1}{\omega} \arcsin \frac{V_\mathrm{o} + V_\mathrm{T}}{V_\mathrm{m}} \qquad t_\mathrm{b} = \frac{1}{\omega} \left(\pi - \arcsin \frac{V_\mathrm{o} + V_\mathrm{T}}{V_\mathrm{m}} \right) \tag{6.5}$$

Finally, by combining Eqs. (2.9), (6.4), and (6.5), we can derive the angular frequency ω, so f can be expressed as:[365]

$$\begin{aligned} f &= \frac{\omega}{2\pi} \\ &= \frac{9\mu}{16\pi V_\mathrm{o} d^2} \left((V_\mathrm{m}^2 + 2V_\mathrm{o}^2) \arccos \frac{V_\mathrm{o} + V_\mathrm{T}}{V_\mathrm{m}} + (V_\mathrm{T} - 3V_\mathrm{o}) \sqrt{V_\mathrm{m}^2 - (V_\mathrm{o} + V_\mathrm{T})^2} \right) \end{aligned} \tag{6.6}$$

Steudel's model has been successfully employed in several papers[182,365,382] to predict

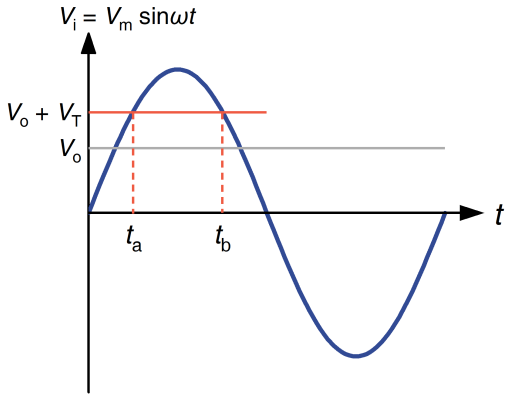

Figure 6.2 | Illustration of Limits of Integration in Steudel's Model. When the voltage across the diode is higher than the transition voltage V_T, the diode is in the trap-free SCLC regime, and the input voltage should be higher than $V_o + V_T$ since the output voltage is always V_o. Thus the time when $V_i = V_o + V_T$ defines t_a and t_b, within which the diode is in the trap-free SCLC regime.

and/or simulate the rectifier's performance due to its higher accuracy compared with simply extracting the maximum frequency from the charge transit time in the active layer, which results in a time-of-flight-type expression.[365] However, drawbacks of this model include (i) its negligence in the reverse leakage current density J_r, which is usually too large to be omitted for a Schottky diode; and (ii) its oversimplified approach to describe the forward bias current using the trap-free SCLC equation, since the existence of trap states is the rule rather than the exception in real OSC devices (Section 2.4.3.4). In the following subsection, we shall improve Steudel's model by incorporating these two considerations into it. In addition, some other models are available to predict the frequency response of OSD-based rectifiers, e.g. the time-dependent drift–diffusion analysis coupled with the Poisson equation, and the equivalent circuit method with a time-dependent conductance.[384] However, the former is relatively time-consuming due to the calculation complexity, especially at high frequencies (as a whole set of partial differential equations need to be solved every Δt time, and Δt must be much smaller than the period of the AC input), and the latter can provide very limited information on device optimisation due to its phenomenological nature. Thus Steudel's model, despite its shortcomings, is still one of the best choices.

6.3.2 The improved model

As mentioned above, the reverse leakage current density J_r and the trap states are additionally included in the improved model. For J_r, inorganic semiconductor physics show that in Schottky diodes, it can be approximated to a saturated current density,[47] and measured J–V characteristics for OSDs support this treatment.[182,381] Admittedly, a more precise description of J_r is possible, but here we primarily care about the charge wasted by the diode in the reverse bias, so assuming a constant J_r is acceptable and avoids over-parameterisation. Concerning traps, we adopt an exponentially distributed density of trap states (Eq. (2.27)) that is suitable for OSCs (Section 2.4.3.4), with the total trap density N_t and the trap depth parameter m being variables. As introduced in Section 2.4.3.4, m is the mean trap depth divided by the unit energy kT, and $m+1$ is the exponent of voltage in the trap-controlled SCLC expression (Eq. (2.28)). The J–V characteristics in the forward bias are consequently separated by two critical voltages, the transition voltage V_T and the trap-controlled voltage V_TC (Eq. (2.29)). When $V_\mathrm{T} < V_\mathrm{D} < V_\mathrm{TC}$, the diode current density follows the trap-controlled SCLC (J_TC, Eq. (2.28)), whereas when $V_\mathrm{D} > V_\mathrm{TC}$ the trap-free SCLC results (J_TF, Eq. (2.9)). Note that below V_T, the applied voltage counteracts the built-in voltage V_bi (Section 2.4.2.1) and assists charge carriers to overcome the injection barrier φ_B (Section 2.4.2.2), so the resultant injection-limited current density is negligible, as Steudel's model also implies.

The improved model relies on the relationship that within a period $t \in [t_1,\ t_1 + T]$, the charge consumed per unit area by the load R and by the diode in its reverse bias equals the charge per unit area passing through the diode in its forward bias. Similar to Eq. (6.4), this can be expressed as (Fig. 6.3):

$$\frac{V_\mathrm{o}\varepsilon_0\varepsilon_\mathrm{r}}{d} + \int_{t_1'}^{t_1+T} J_\mathrm{r}\,\mathrm{d}t = \int_{t_2}^{t_3} J_\mathrm{TC}(t)\,\mathrm{d}t + \int_{t_3}^{t_3'} J_\mathrm{TF}(t)\,\mathrm{d}t + \int_{t_3'}^{t_2'} J_\mathrm{TC}(t)\,\mathrm{d}t \tag{6.7}$$

The relevant limits of integration are (Fig. 6.3):

$$t_1 = \frac{1}{\omega}\arcsin\frac{V_\mathrm{o}}{V_\mathrm{m}} \qquad t_1{}' = \frac{1}{\omega}\left(\pi - \arcsin\frac{V_\mathrm{o}}{V_\mathrm{m}}\right) \tag{6.8}$$

$$t_2 = \frac{1}{\omega}\arcsin\frac{V_\mathrm{o}+V_\mathrm{T}}{V_\mathrm{m}} \qquad t_2{}' = \frac{1}{\omega}\left(\pi - \arcsin\frac{V_\mathrm{o}+V_\mathrm{T}}{V_\mathrm{m}}\right) \tag{6.9}$$

$$t_3 = \frac{1}{\omega}\arcsin\frac{V_\mathrm{o}+V_\mathrm{TC}}{V_\mathrm{m}} \qquad t_3{}' = \frac{1}{\omega}\left(\pi - \arcsin\frac{V_\mathrm{o}+V_\mathrm{TC}}{V_\mathrm{m}}\right) \tag{6.10}$$

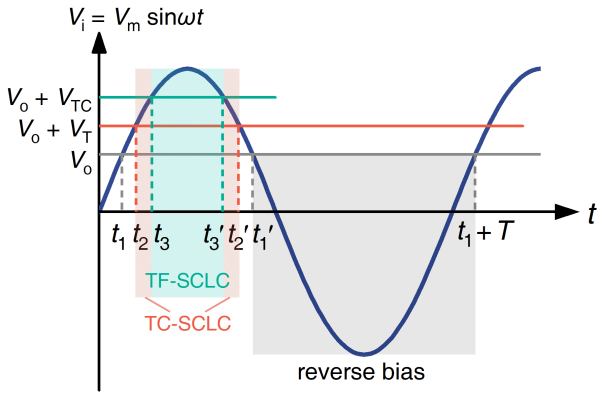

Figure 6.3 | Illustration of Limits of Integration in the Improved Model. When the voltage across the diode V_D is higher than the transition voltage V_T but smaller than the trap-controlled voltage V_TC, the diode is in the trap-controlled SCLC regime (red). When $V_\mathrm{D} > V_\mathrm{TC}$, the diode is in the trap-free SCLC regime (green). When $V_\mathrm{D} < 0$, that is, the input voltage is smaller than V_o, the diode is in the reverse bias (grey).

Therefore, $f = \omega/2\pi$ can be extracted using Eqs. (2.9), (2.28), (2.29), (6.7), (6.8), (6.9), and (6.10). Although the result cannot be given analytically, numerical simulation allows us to find out how different factors affect the rectifier's V_o–f characteristics intuitively, as shown in the next subsection. The simulation was completed using a MATLAB program written by the author, and the code can be found on the GitHub repository.[221]

6.3.3 Simulation results

In the improved model, the maximum frequency $f = f(\mu,\ d,\ V_\mathrm{T},\ J_\mathrm{r},\ N_\mathrm{t},\ m,\ V_\mathrm{m},\ V_\mathrm{o})$. Since the V_o–f plot is commonly used to characterise the rectifier's performance, we shall

discuss the remaining seven factors (i.e. all but V_o) successively by changing one at a time within a reasonably wide range while keeping the others at their default values: $\mu = 10^{-4}\,\mathrm{cm^2\,V^{-1}\,s^{-1}}$, $d = 100\,\mathrm{nm}$, $V_T = 0.5\,\mathrm{V}$, $J_r = 10^{-4}\,\mathrm{A\,cm^{-2}}$, $N_t = 5 \times 10^{23}\,\mathrm{m^{-3}}$,[385] $m = 4$, $V_m = 5\,\mathrm{V}$. Besides, ε_r is set to be 3.5,[13] and the total density of transport states N is chosen to be $5 \times 10^{26}\,\mathrm{m^{-3}}$,[149,386] both of which are typical values in the literature.

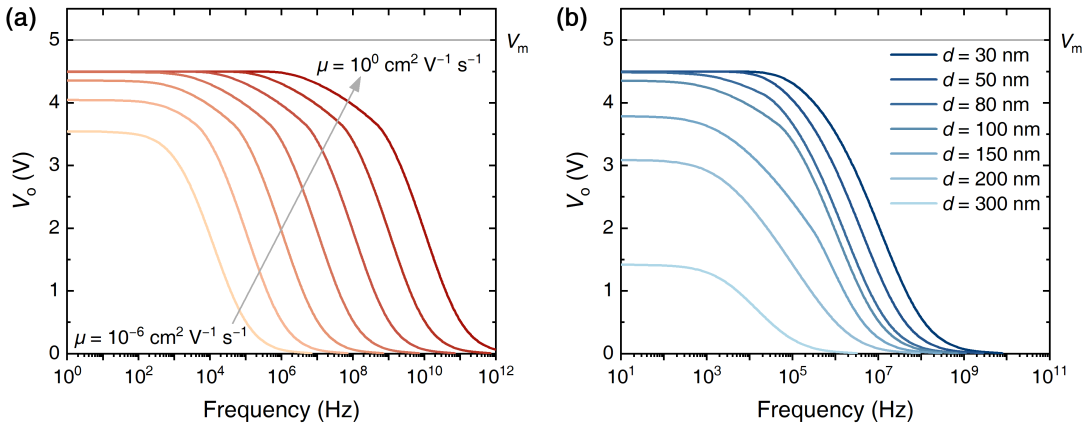

Figure 6.4 | Simulation of V_o–f Characteristics with Different (a) Mobility μ and (b) Active Layer Thickness d. The mobility changes from 10^{-6} to $10^0\,\mathrm{cm^2\,V^{-1}\,s^{-1}}$, and the thickness from 30 to 300 nm.

Figure 6.4(a) shows how mobility μ affects the V_o–f characteristics. It can be seen that when the mobility increases by one order of magnitude, the frequency will rise by a similar scale. In order to achieve UHF rectifiers whose f_{3dB} is ~1 GHz, the required mobility is $\sim 10^{-1}\,\mathrm{cm^2\,V^{-1}\,s^{-1}}$, in excellent agreement with previous experimental results.[182] For common mobility of $\sim 10^{-4}\,\mathrm{cm^2\,V^{-1}\,s^{-1}}$ for solution-processed OSCs, the corresponding f_{3dB} is around 1 MHz, even below the HF regime (13.56 MHz). At very low mobility of $\sim 10^{-6}\,\mathrm{cm^2\,V^{-1}\,s^{-1}}$, which is not rare for OSCs (e.g. 90F8:10BT, see Table 4.3), not only f_{3dB} decreases to ~10 kHz that precludes most practical applications, but V_o is also adversely affected, dropping from 4.5 V to about 3.5 V. These results confirm the vital role of high mobility in achieving HF/UHF rectifiers.

The effect of different active layer thickness is presented in Fig. 6.4(b), and both f_{3dB} and V_o increase with reduced thickness. Compared with the "default" device with

a 100 nm active layer, a three times thinner layer of ~30 nm can boost the f_{3dB} by an order of magnitude from ~1 MHz to ~10 MHz, whilst a three times thicker layer of 300 nm drastically weakens the f_{3dB} and V_o to ~10 kHz and ~1.4 V, respectively. Therefore, use thin active layers is a simple but effective way to enhance the rectifier's performance, and at the same time, less material is needed so some fabrication cost can be saved.

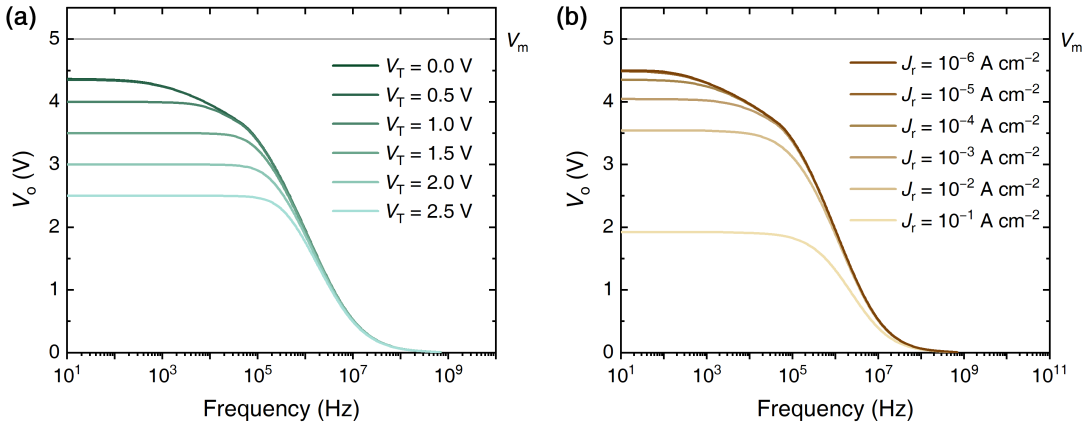

Figure 6.5 | Simulation of V_o–f Characteristics with Different (a) Transition Voltages V_T and (b) Reverse Leakage Current Density J_r. The transition voltage changes from 0 to 2.5 V, and the reverse leakage current density from 10^{-6} to 10^{-1} A cm^{-2}. Note that for $V_T = 0$ and 0.5 V, and for $J_r = 10^{-6}$ and 10^{-5} A cm^{-2}, their V_o–f curves are not distinguishable.

As Fig. 6.5 illustrates, the transition voltage V_T and the reverse leakage current density J_r primarily influence the V_o while the shape and position of V_o–f curves remain unchanged, except when J_r is as high as 10^{-1} A cm^{-2} the curve slightly shifts to the low-frequency regime. Both a lower V_T and a smaller J_r can lead to a higher V_o, though f_{3dB}, by definition, becomes smaller—this should not be understood as worse performance since the only reason is the improved V_o, and the rectifier's response at high frequencies is not affected. It is also noteworthy that below some threshold, i.e. ~0.5 V for V_T and ~10^{-5} A cm^{-2} for J_r, the resultant V_o will saturate and not rise further. This may be understood from the very small forward current density at $V < 0.5$ V and reverse current density when $J_r < 10^{-5}$ A cm^{-2} being insignificant to the total charge passing through the diode in one period.

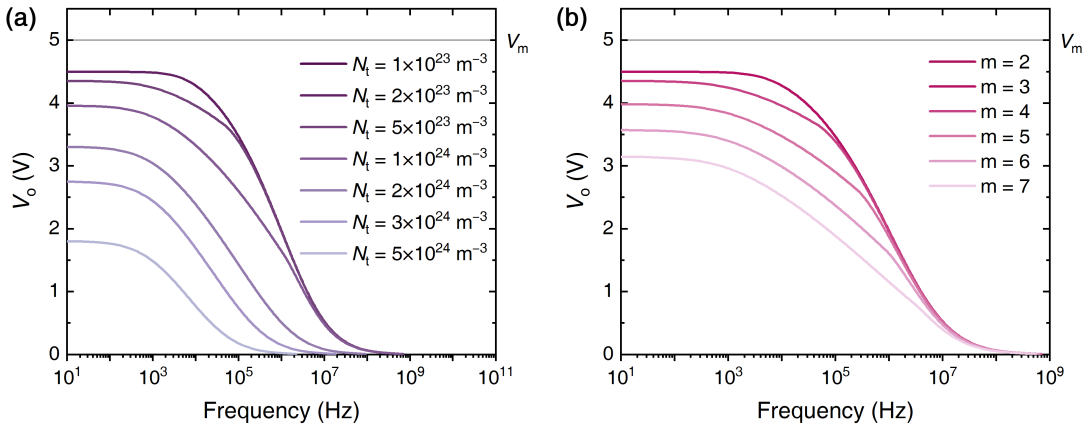

Figure 6.6 | Simulation of V_o–f Characteristics with Different (a) Total Trap Density N_t and (b) Trap Depth Parameters m. The total trap density changes from 1×10^{23} to $5 \times 10^{24}\,\mathrm{m}^{-3}$, and the trap depth parameter from 2 to 7. Note that for $N_t = 1 \times 10^{23}$ and $2 \times 10^{23}\,\mathrm{m}^{-3}$, and for $m = 2$ and 3, their V_o–f curves are not distinguishable.

The trap effect on the rectifier's performance is shown in Fig. 6.6. With higher trap density N_t and more deep traps (i.e. bigger m), both V_o and f_{3dB} become inferior. This is somewhat expected due to trap states being detrimental to charge transport and deep traps likely to capture charge carriers permanently (Section 2.4.3.4). Although traps are inevitable in OSCs, their concentration has to surpass some limit to enable observable impact on the V_o–f characteristics. Considering the total density of transport states $N = 5 \times 10^{26}\,\mathrm{m}^{-3}$ used in our simulation, we can infer that the result of undistinguishable V_o–f curves at $N_t < 2 \times 10^{23}\,\mathrm{m}^{-3}$ corresponds to a trap concentration of 0.04 %. That is to say, if we can somehow control the trap density below this threshold, then traps become irrelevant to the rectifier's performance. Similarly, when $m < 3$, i.e. the mean depth of exponentially distributed traps is smaller than $3kT$, these relatively shallow traps have no significant impact on the resulting V_o–f characteristics.

Figure 6.7(a) demonstrates that a larger amplitude V_m of the input sinusoidal AC signal is conducive to V_o (normalised by V_m) and f_{3dB}. This is probably because a high V_m allows the diode to stay in the trap-free SCLC regime longer with higher current density in the forward bias, so more charges are stored in the capacitor and are available to be discharged in the reverse bias. We argue that increasing V_m should not be regarded

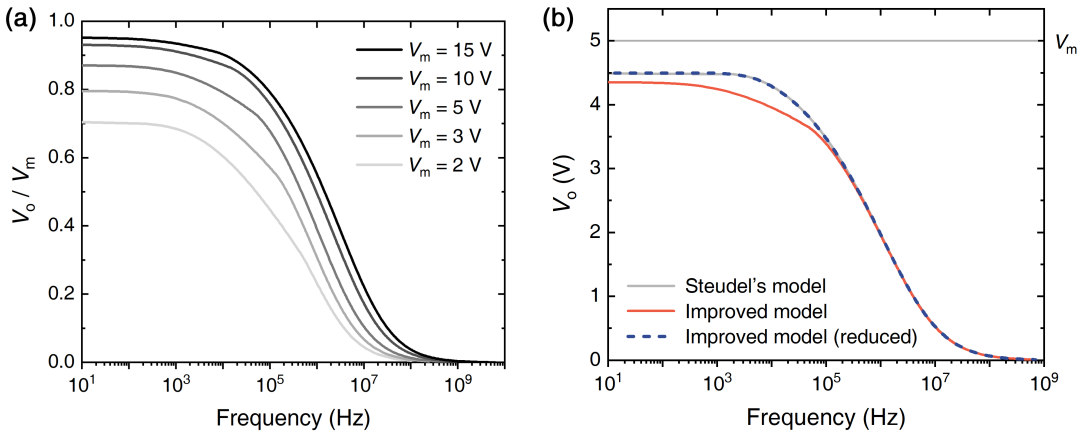

Figure 6.7 | Simulation of V_o–f Characteristics with Different Amplitudes V_m of the Input AC Signal and the Comparison between Steudel's and the Improved Model. (a) Simulated V_o–f characteristics with the amplitude varying from 2 to 15 V. The output voltage V_o is normalised by V_m. (b) Comparison between Steudel's (grey) and the improved model (red). The blue dashed curve shows that with properly chosen parameters, the improved model reduces to Steudel's.

as a device optimisation strategy since it has nothing to do with the device itself. Besides, from the application perspective, a smaller V_m may be even better due to the reduced driving power of RFID tags. In the experiments below, we set the V_m to a relatively small value of 5.00 V to ensure the good comparability and practical significance of our results, as many commercial RFID readers use a 5 V signal to send data.[356]

A parameter that does not explicitly present in our model but deserves consideration is the active area A. In the literature, A was usually controlled within the sub-mm^2 range,[182,365,378,381,382] and the reasons are at least threefold. First, the derivation of Steudel's model is premised on a very small diode capacitance relative to the smoothing capacitor (Eq. (6.3)), thus a tiny area is preferred to minimise the output voltage ripple. Second, the heat generated during device operation can be dissipated more readily for tiny devices.[182] Third and more importantly, the number of structural defects, such as pinholes and external contaminants accidentally introduced into the device during fabrication, can be significantly reduced if a tiny area is used. In our devices, the active area is $100 \times 100\,\mu m^2$ as defined by the overlapping of the top and bottom electrodes.

Finally, in Fig. 6.7(b) we compare our improved model (red) with Strudel's original one (grey) by generating V_o–f characteristics using the same parameters (i.e. those default values). It can be seen that in the high-frequency regime, two models can give identical V_o–f dependences, whereas at low frequencies, our model predicts a much smaller V_o. Previous reports on pentacene-OSD-based rectifiers found that the experimental data could fit Steudel's model well at $f > 10^8$ Hz but a large discrepancy (~1 V in V_o) was observed below this frequency, with measured V_o being smaller.[182] This implies that Steudel's model tends to overestimate the V_o in the low-frequency regime, and is thus supportive to the more stringent and realistic nature of our approach. Furthermore, if we lower J_r, N_t, and m, three new-introduced parameters, below their respective threshold values obtained from the simulation above, i.e. when they are not in effect, then our model (blue dashed curve in Fig. 6.7(b)) successfully reduces to Steudel's. This consistency increases our confidence in using the improved model to investigate the rectifier's performance.

6.3.4 Strategies for high-performance rectifiers

The simulation results show us how a rectifier's performance is affected by a number of factors, and accordingly, strategies for high-performance OSD-based rectifiers with large V_o and high f_{3dB} can be summarised. First and foremost, the solution-processed active material has to exhibit high out-of-plane mobility in the low-charge-carrier-density regime, in contrast to the situation in OFETs where $\mu > 10^1$ cm^2 V^{-1} s^{-1} has been reported.[52,53] It now still remains challenging for solution-processed OSCs to achieve $\mu > 10^{-2}$ cm^2 V^{-1} s^{-1} in diode structures, and the main reason lies in the difficulty of controlling well-ordered microstructure that can facilitate interchain charge transport and reduce the number of traps. Although some solutions to this problem have been proposed, e.g. using highly ordered discotic liquid crystals as the active material,[387] connecting crystalline regions over the amorphous by tie chains,[136] and designing new OSC materials with higher crystallinity and face-on anisotropy[388] and lower degree of structural disorder,[389] the

unsatisfied mobility is still a limiting factor for not only OSD-based rectifiers, but also other applications such as electrically pumped organic lasers.[390]

Second, device structure design and interface engineering[362] are crucial to decrease both V_T and J_r. In other words, the injection contact should be Ohmic or quasi-Ohmic, and the blocking contact should have a sufficiently large Schottky barrier. To fulfil these requirements, one may refer to the energy level diagram, but the poor predictability of interfacial processes (Section 2.4.2.2) can reduce its reliability. Additionally, sometimes we need to consider the forward and reverse biases jointly and reach a compromise. For example, decreasing J_r by inserting a charge-blocking layer may result in reduced forward current density because of the increased series resistance, and by a large energy level offset between the active material and the blocking electrode can adversely increase V_{bi} and consequently V_T. In all, the complexity of energy level alignment in real devices makes the J–V characteristics the ultimate basis for device optimisation. In the ideal case, the forward current density is as high as possible and the device enters the SCLC regime at a very low V_T, and in the reverse bias J_r is suppressed to minimal, leading to exceptional rectifying properties with a large RR. The energy level diagram, on the other hand, is only a fair starting point for device structure design and interface engineering.[362]

Third, the trap concentration should be controlled below the threshold of ~0.04 % with the mean trap depth smaller than ~$3kT$. Recent studies have shown that the trap density can be lowered by diluting the OSC with large-transport-gap polymers,[391] introducing molecular or solvent additives,[392–394] and thermal annealing.[395] It is therefore possible to alleviate or even eliminate the adverse trap effect on the rectifier's performance.

Finally, two simple but very effective strategies for OSD-based rectifier optimisation are reducing the active layer thickness d and the active area A, as long as there is no fabrication issue, e.g. local shorts caused by the very thin active layer failing to cover the bottom electrode uniformly. In the following three sections, OSD-based rectifiers using three different active materials will be presented, with their performance optimisation according to strategies summarised here.

6.4 The Benchmark: PTB7-Based Rectifiers

We first choose PTB7 (Fig. 5.12(b)) as the active material due to its favourable face-on crystallite orientation (Fig. 5.14) for vertical charge transport. Figure 6.8(a) illustrates the device structure, with PEDOT:PSS or CuSCN processed from DMSO being the HTL. The nominal energy level diagram is shown in Fig. 6.8(b); data of ITO,[269] PEDOT:PSS,[270] PTB7,[352] and Al[396] are extracted from previous publications. The device fabrication details are the same as mentioned in Section 5.5. For the frequency-dependent rectification measurement, an Agilent 33600A signal generator provided the input sinusoidal signal with $V_{\mathrm{m}} = 5.00\,\mathrm{V}$, and a Tektronix TDS 2024B oscilloscope detected and saved the rectified signal. A smoothing capacitor of 22 nF and a load resistor of 1 MΩ were soldered on a stripboard and connected parallel to the oscilloscope (Fig. 6.9(a)). The corresponding RC constant was 22 ms, significantly larger than the period of the AC signal when $f > 1\,\mathrm{kHz}$ (Eq. (6.2)). Besides, the capacitance of our diodes is estimated to be 3.9 pF for an active area of $100 \times 100\,\mu\mathrm{m}^2$ (using $d = 80\,\mathrm{nm}$ and $\varepsilon_{\mathrm{r}} = 3.5$), so Eq. (6.3) is also satisfied in order to minimise the output voltage ripple.[182,365] All components were connected by Bayonet Neill–Concelman (BNC) and Sub Miniature version A (SMA) cables, and all frequency-dependent measurements throughout this chapter were completed on this setup in air. Note that due to the limitation of our signal generator, only the response at $f < 20\,\mathrm{MHz}$ can be measured, which was verified by a commercial Si Schottky diode. Figure 6.9 shows the schematic diagram and photographs of this setup.

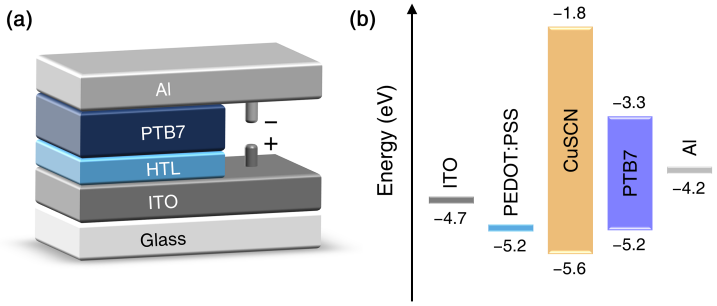

Figure 6.8 | (a) Schematic device structure and (b) nominal energy level diagram of PTB7-based OSDs.

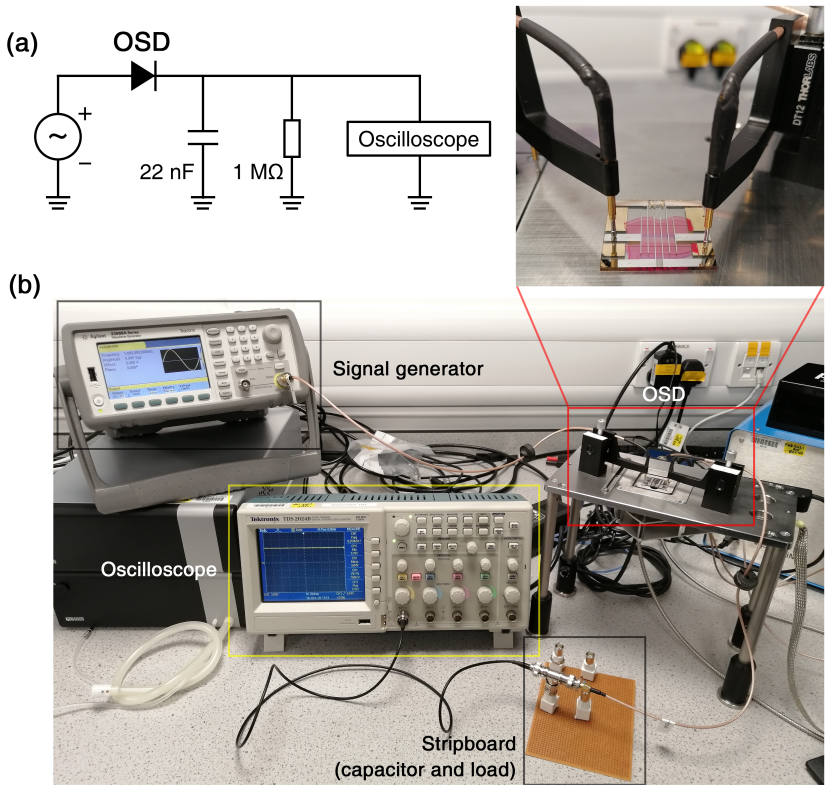

Figure 6.9 | (a) Schematic diagram and (b) photographs of the setup for frequency-dependent measurements. Enlarged is an OSD device with electric connections via flexible probes.

The J–V characteristics for PTB7-based OSDs are shown in Fig. 6.10(a). In the forward bias, the two devices with different HTLs can achieve similar current density at $V > 3\,\mathrm{V}$, and the SCLC-mobility is extracted to be $2.5 \times 10^{-5}\,\mathrm{cm^2\,V^{-1}\,s^{-1}}$ (Eq. (2.9)). The device using CuSCN (DMSO) interlayer exhibits a smaller V_T of ~0.8 V than that of the PEDOT:PSS device (~1.2 V), suggesting a more Ohmic nature of the CuSCN (DMSO)–PTB7 contact despite that the nominal energy level diagram (Fig. 6.8(b)) predicts both devices to be injection-barrier-free. A more appreciable difference is in the reverse bias; the CuSCN (DMSO) interlayer effectively reduces the J_r to $\sim 10^{-5}\,\mathrm{A\,cm^{-2}}$ thanks to its large band gap that can block the electron injection from the ITO electrode. In comparison, the poor electron-blocking properties of PEDOT:PSS result in J_r being two orders of magnitude higher.

The superior J–V characteristics for the PTB7-based OSD with CuSCN (DMSO) interlayer to PEDOT:PSS lead the former to show better performance in rectifiers

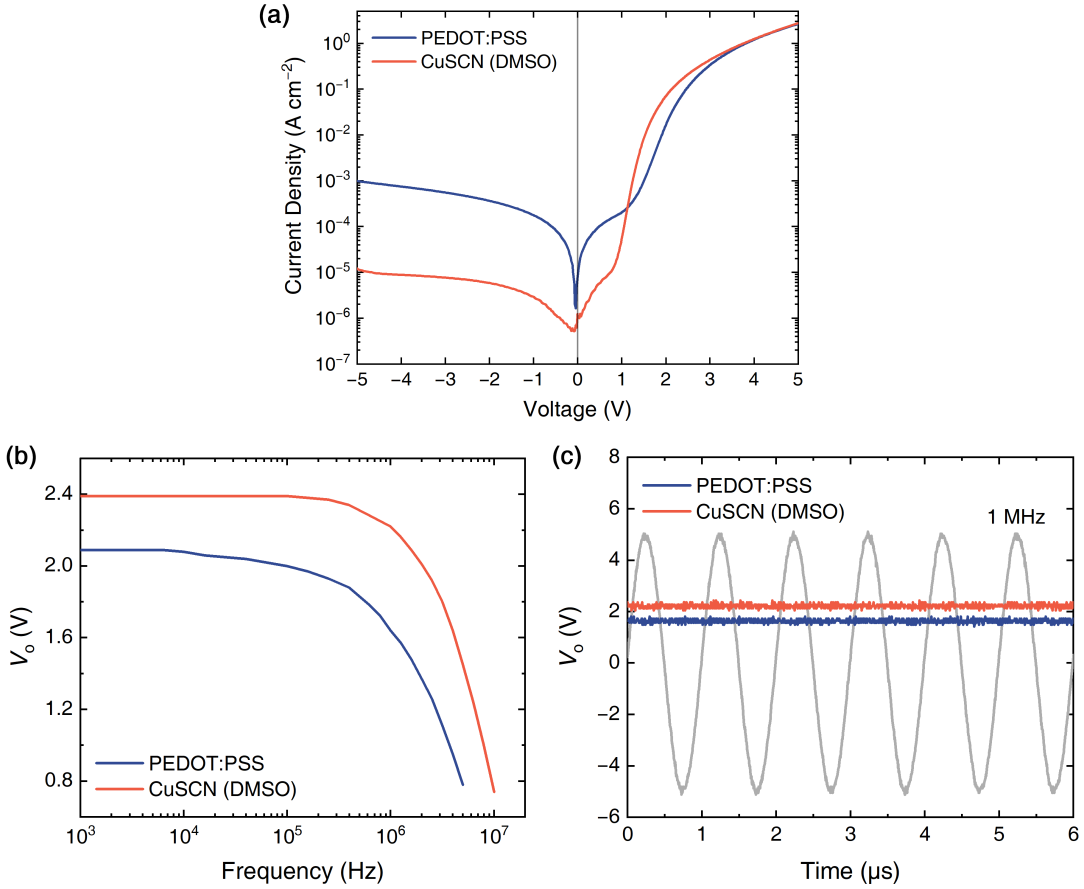

Figure 6.10 | Performance of PTB7-Based Rectifiers. (a) J–V characteristics for diodes with different HTLs. (b) V_o–f characteristics for rectifiers. (c) Time-dependent V_o at $f = 1\,\text{MHz}$, suggesting stable DC output. Devices using PEDOT:PSS and CuSCN (DMSO) HTLs are shown by blue and red curves, respectively.

(Fig. 6.10(b)). At low frequencies, the V_o reaches 2.39 V, which is 0.30 V higher than that for the device with PEDOT:PSS. Similar improvements are also observed in f_{3dB}, i.e. ~6.5 MHz vs ~3.5 MHz. Moreover, the output DC signal of both rectifiers are stable below their f_{3dB} at 1 MHz (Fig. 6.10(c)), indicating the success of PTB7-based OSD rectifiers.

In summary, these results clearly manifest the significance of choosing proper interlayers. As already demonstrated in Chapter 5, the advantages of CuSCN over PEDOT:PSS as the HTL bring the resultant rectifiers remarkable performance improvements. However, PTB7 was not specially designed for high-mobility purposes, and here its SCLC-mobility is lower than $10^{-4}\,\text{cm}^2\,\text{V}^{-1}\,\text{s}^{-1}$, a value representative of the majority

of conjugated polymers. Therefore, even though the interlayer has been optimised, V_o is still smaller than $0.5\,V_m$, and f_{3dB} is below the 13.56 MHz boundary for HF applications. This performance can thus be accepted as a benchmark for a number of solution-processed OSD-based rectifiers, and surpassing it largely relies on using high-mobility materials.

6.5 Electron-Only Fullerene-Mixture-Based Rectifiers

Fullerenes such as C_{60} and C_{70} are attractive OSCs due to their high electron mobility. Besides, differing from conjugated polymers with strong anisotropy, fullerene molecules are in (quasi-)spherical shape, so it is possible for fullerene-based diodes to achieve comparable mobility with OFETs, e.g. $\mu_e = 0.42$ and $2.5\,cm^2\,V^{-1}\,s^{-1}$ for C_{60}-based diodes[377] and OFETs,[397] respectively. However, pristine C_{60} or C_{70} has limited solubility in common solvents,[398] and the quality of solution-processed fullerene thin films usually suffers from the rapid crystallisation, leading to rough surfaces and high density of grain boundaries as traps.[399] Recently, it was found that co-dissolving the same amount of C_{60} and C_{70} in 1,2-dichlorobenzene (*o*-DCB) could result in a high solubility of $>50\,mg\,ml^{-1}$ due to the increased configurational entropy of the mixture, and the spin-coated films were amorphous.[400] Therefore, we use C_{60}:C_{70} mixture as the active material in OSD-based rectifiers to see if its high mobility can boost the device performance.

C_{60} (99.5 %, Lumtec, Fig. 6.12(b)) and C_{70} (99 %, Lumtec, Fig. 6.12(b)) were dissolved in *o*-DCB (99 % anhydrous, Sigma-Aldrich) at a total concentration of $40\,mg\,ml^{-1}$ (weight ratio = 1 : 1). Despite the ease of dissolving, the film obtained by spin-coating the solution at 1000 rpm was not continuous (Fig. 6.11(a)). This is possibly because the low solution viscosity makes it very easy to be spun off before the substrate is wet uniformly. Previous researchers have added some binders into the fullerene-mixture solution to improve the processability by increasing the solution viscosity and improving the adhesion between the film and the substrate. For example, ultrahigh-molecular-weight polystyrene (number-average molecular weight $M_n > 3 \times 10^{10}$) was used as the additive to promote the formation of a uniform fullerene-mixture thin film.[400] Given the great

difficulty in synthesising and acquiring the polystyrene with such high molecular weight, here we added another n-type conjugated polymer, N2200 (M_n = 29 700, polydispersity index n = 2.1, Flexterra, Fig. 6.12(b)), into the C_{60}:C_{70} solution as the binder. As Fig. 6.11(b) shows, N2200 at a low concentration of 1 mg ml^{-1} can significantly improve the thin-film quality and avoid dewetting. Thus, the blend of C_{60}:C_{70}:N2200 (CCN) is used as the active material in this study in lieu of the fullerene mixture.

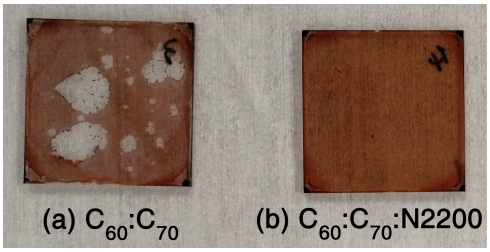

Figure 6.11 | Photographs of (a) C_{60}:C_{70} and (b) C_{60}:C_{70}:N2200 (CCN) Thin Films on Glass. A small amount of N2200 (1 mg ml^{-1}) can significantly improve the thin-film quality. The substrate size is 25 × 25 mm^2.

We start the CCN-based OSD fabrication (Fig. 6.12(a)) by following the device structure proposed by Im et al.[377] who used vacuum-deposited C_{60} as the active material in OSDs. A 100 nm Ag (99.99 %, Kurt J. Lesker) bottom electrode, as the replacement for ITO to further reduce the series resistance and the voltage loss, was evaporated at 1 Å s^{-1} on soda–lime glass (Lumtec), on which a 20 nm MoO_3 (99.95 %, Testbourne) electron-blocking layer (EBL) was subsequently evaporated at 0.2 Å s^{-1}. As a well-known hole injection material, MoO_3 can form strong interface dipoles with layers below and above,[401] so its local vacuum level is shifted to equilibrate its WF (6.9 eV)[401] with the electrode's, e.g. 4.4 eV for Ag (Fig. 6.12(c)).[353] This typically causes the match between its deep conduction band edge (CBE) at 6.7 eV[401] with the HOMO of OSCs, so hole injection can be facilitated through the electron extraction from the OSC's HOMO to MoO_3's CBE,[401] very different from the common HOMO (or valence band edge)-to-HOMO hole injection mechanism. Considering many HTLs can also be applied as EBLs, here we sought to use MoO_3 to block the electrons injected from Ag in the reverse bias. On top of the

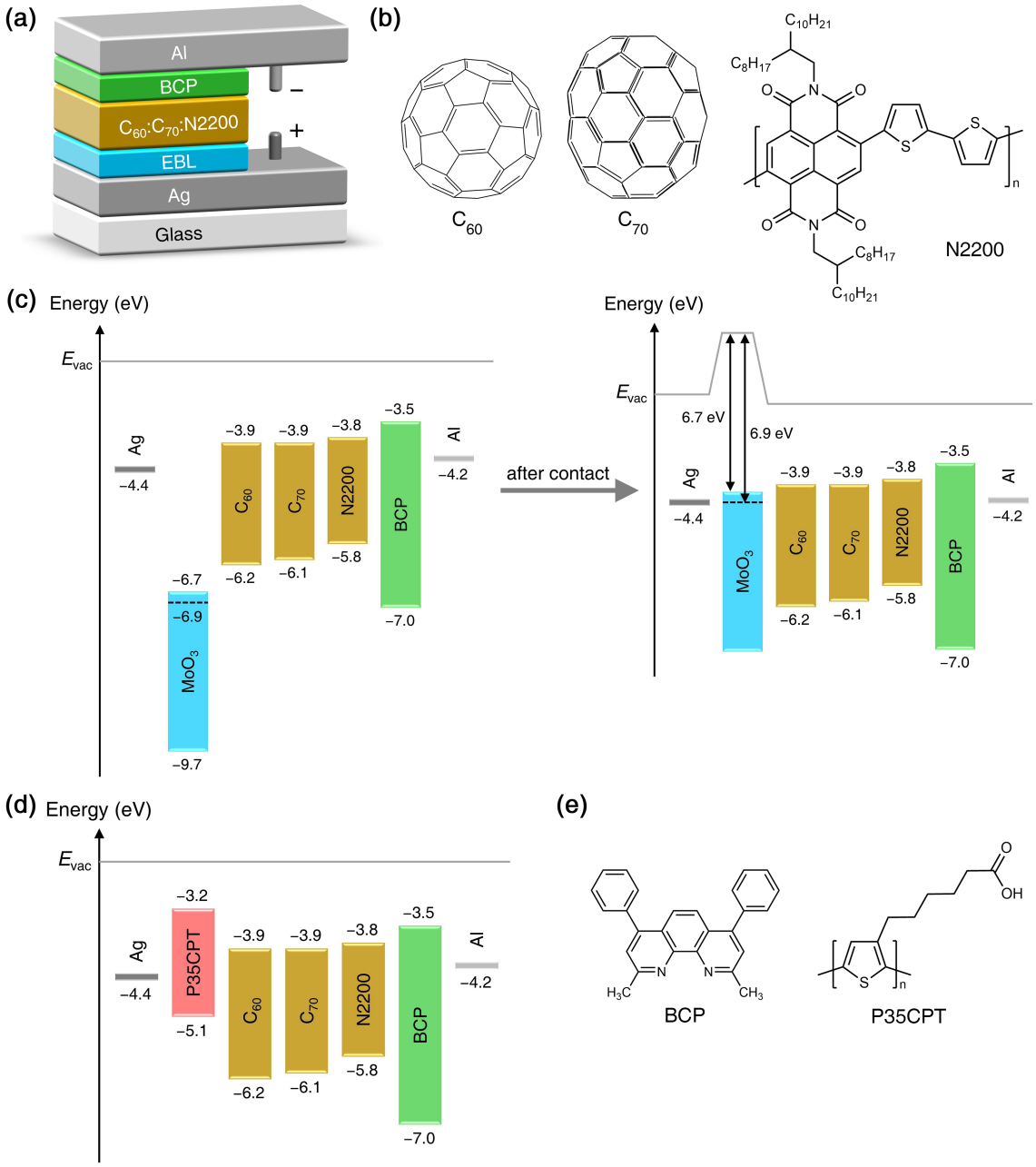

Figure 6.12 | (a) Schematic device structure of CCN-based OSDs. (b) Chemical structures of active materials. (c) Nominal energy level diagram of the MoO_3-containing device before (left) and after (right) the layers are connected. The WFs of Ag and MoO_3 align after device fabrication, and the interface dipole of MoO_3 leads to the shift of its local vacuum level. (d) Nominal energy level diagram of the P35CPT-containing device. (e) Chemical structures of interlayer materials.

Ag / MoO_3 bilayer anode, the CCN solution was spin-coated at 1000 rpm followed by thermal annealing at 150 °C for 10 min, giving us a ~90 nm active layer. We note that

in the energy level diagrams (Fig. 6.12(c–d)), the energy gap of C_{60} and C_{70} are different from the values normally found in papers about fullerene-based OPVs.[402] This is because in OPVs the optical gap E_{opt} matters, whereas in rectifying diodes we care about the transport gap E_g. It is well documented that these two gaps are different for fullerenes, i.e. $E_{opt}(C_{60}) = 1.5$–$2.0\,eV$ vs $E_g(C_{60}) = 2.3 \pm 0.1\,eV$,[403] and $E_{opt}(C_{70}) \approx 1.9\,eV$ vs $E_g(C_{70}) \approx 2.2\,eV$.[404] Above the active layer, a bathocuproine (BCP, 99.99 %, Sigma-Aldrich, Fig. 6.12(e)) ETL was spin-coated from $0.5\,mg\,ml^{-1}$ ethanol (99 %, Fisher Chemical) solution at 3000 rpm, and its energy levels are sourced elsewhere.[176] The device fabrication was finished by evaporating a 100 nm Al (99.99 %, Kurt J. Lesker) top electrode at $1\,Å\,s^{-1}$.

Figure 6.13(a) shows the J–V characteristics for CCN OSDs with the MoO_3 EBL (in blue). Although in the forward bias, the current density is very high (~$50\,A\,cm^{-2}$ at 5 V), leading to an SCLC-mobility of $5.1 \times 10^{-3}\,cm^2\,V^{-1}\,s^{-1}$, i.e. over two orders of magnitude higher than that for PTB7, in the reverse bias J_r is also large and approaches ~$1\,A\,cm^{-2}$ at −5 V. This suggests that MoO_3 cannot effectively block the leakage current, so another EBL is required. We tried using PEDOT:PSS (~30 nm) and CuSCN (~10 nm), however in CCN OSDs they only ended up with significantly dropped forward current density. Other solution-processable EBLs, such as poly(9,9-dioctylfluorene-*alt*-*N*-(4-*sec*-butylphenyl)diphenyl-amine) (TFB) and poly[bis(4-phenyl)(2,4,6-trimethylphenyl)amine] (PTAA), are not applicable as well due to their high solubility in the solvent of CCN, i.e. *o*-DCB. A prospective candidate we found is poly[3-(5-carboxypentyl)thiophene-2,5-diyl] (P35CPT, Fig. 6.12(e)), which is a derivative of P3HT but insoluble in chlorinated solvents because of the introduction of carboxyl end groups.[405] We dissolved P35CPT (supplied courtesy of Dr. Sungho Nam) in *N*,*N*-dimethylformamide (DMF, 99.8 % anhydrous, Sigma-Aldrich) at a concentration of $2\,mg\,ml^{-1}$, and the solution was heated at 80 °C overnight and filtered through 0.45 µm polytetrafluoroethylene (PTFE) filters before use. The ~5 nm P35CPT interlayer was deposited onto the Ag electrode by spin-coating the solution at 3000 rpm and then thermal annealing at 80 °C for 10 min in glovebox. With the P35CPT

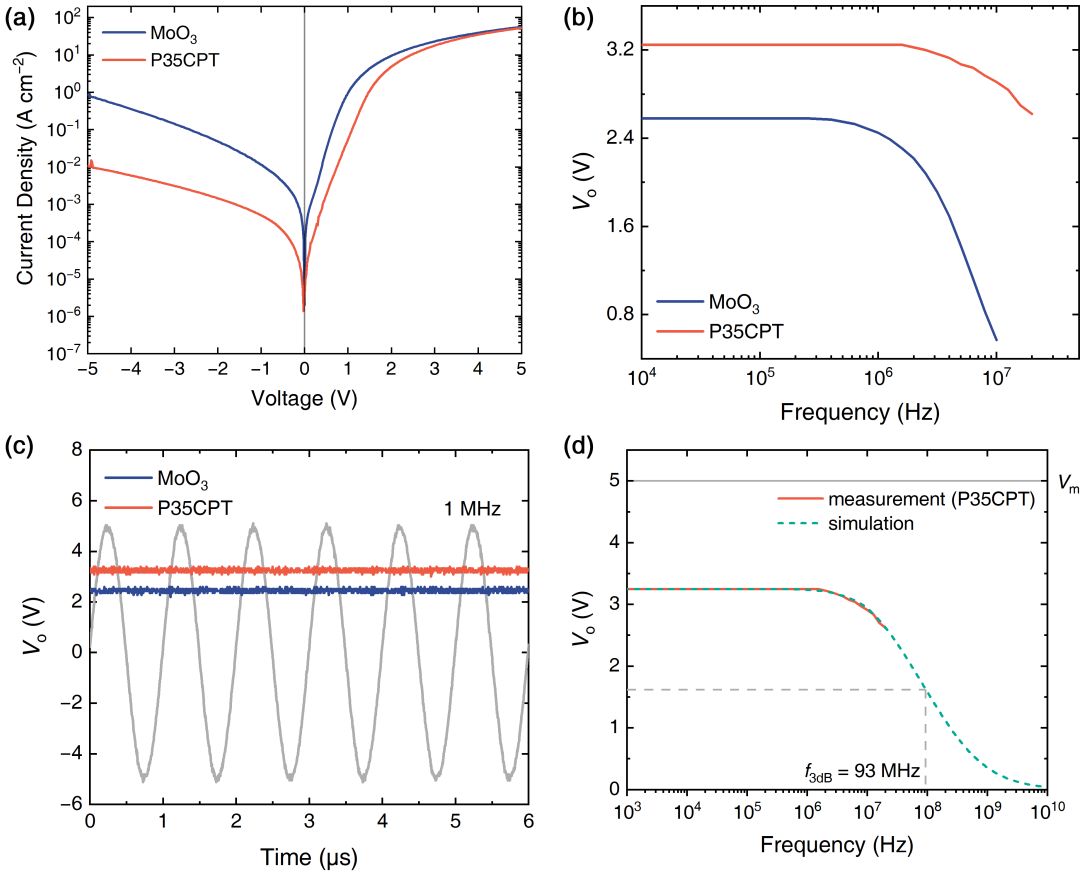

Figure 6.13 | Performance of CCN-Based Rectifiers. (a) J–V characteristics for diodes with different EBLs. (b) V_o–f characteristics for rectifiers. (c) Time-dependent V_o at $f = 1\,\mathrm{MHz}$, suggesting stable DC output. (d) Prediction of the f_{3dB} for the CCN-based rectifier with the P35CPT EBL using the improved model. From the simulation, f_{3dB} is estimated to be 93 MHz. Devices using MoO_3 and P35CPT EBLs are shown by blue and red curves, respectively, and the simulation results are denoted by dashed green curve.

EBL, the forward current density and the mobility for CCN OSDs remain their high values, and at the same time J_r substantially decreases by two orders of magnitude to $\sim 10^{-2}\,\mathrm{A\,cm^{-2}}$ at $-5\,\mathrm{V}$ (Fig. 6.13(a), red). The difference between MoO_3 and P35CPT in electron-blocking properties can be explained by their energy levels (Fig. 6.12(c–d)). The unique electronic structure of MoO_3 results in the LUMO of fullerenes matching the states within MoO_3's conduction band, whereas for P35CPT the corresponding energy level is around the middle of its transport gap.[405]

As can be predicted from the J–V characteristics, the CCN rectifier with the P35CPT EBL outperforms its counterpart with MoO_3 (Fig. 6.13(b)). The former exhibits a high

V_o of 3.25 V, and for the latter V_o = 2.58 V, $f_{3dB} \approx$ 6.0 MHz; both have a stable DC output at 1 MHz (Fig. 6.13(c)). Restricted by the frequency our signal generator can provide, we cannot directly measure the f_{3dB} of the P35CPT-containing rectifier, but an estimation is possible thanks to our improved model. We carried out simulation using experimentally derived parameters, i.e. $\mu = 5.1 \times 10^{-3}\,\mathrm{cm^2\,V^{-1}\,s^{-1}}$, $d = 90\,\mathrm{nm}$, $V_T = 1.7\,\mathrm{V}$, $J_r = 5 \times 10^{-3}\,\mathrm{A\,cm^{-2}}$, and $m = 5$, as well as the default trap density $N_t = 5 \times 10^{23}\,\mathrm{m^{-3}}$. An excellent agreement between the measured and simulated results is achieved (Fig. 6.13(d)), giving us an f_{3dB} of 93 MHz, higher than the 13.56 MHz threshold. Therefore, solution-processed CCN-based OSD rectifiers are capable of working in the HF regime.

To summarise, solution-processed HF organic rectifiers are enabled by the combination of high-mobility OSCs (fullerenes) and proper interface engineering (the P35CPT EBL). However, the SCLC-mobility for spin-coated fullerenes is still at least one order of magnitude inferior to that for evaporated ($\sim$0.42 $\mathrm{cm^2\,V^{-1}\,s^{-1}}$),[377] suggesting the thin-film microstructure, processing conditions, and the binder can still be further optimised. Also, the leakage current density $J_r \approx 5 \times 10^{-3}\,\mathrm{A\,cm^{-2}}$ is still much higher than expected (cf. $\sim 10^{-5}\,\mathrm{A\,cm^{-2}}$ for PTB7 OSDs using CuSCN interlayers processed from DMSO), and experiment results confirmed that further increasing the thickness of P35CPT EBLs only led to simultaneously decreased forward and reverse bias current density, which has no contribution to the rectifying properties. These results inspire us to stick to high-mobility materials, but with more careful interlayer optimisation.

6.6 Hole-Only TIF-BT-Based Rectifiers

Apart from fullerenes, another high-mobility OSC material recently synthesised is TIF-BT (Fig. 6.14(c)), a dithiopheneindenofluorene–benzothiadiazole alternating copolymer. In OFETs, its hole mobility can reach as high as 2.8 $\mathrm{cm^2\,V^{-1}\,s^{-1}}$.[406] Unlike conventional high-mobility conjugated polymers for OFETs, which are usually characterised by high crystallinity with predominately edge-on orientated crystallites[407] or strong chain

alignment parallel to the channel length direction,[169] TIF-BT exhibits much weaker semicrystalline order without any noticeable assembly behaviour.[406,408] Features of this material that can facilitate its charge transport includes (i) the high backbone rigidity and planarity, leading to more delocalised π-orbitals for intrachain charge transport and a relatively low degree of energetic disorder;[406,408,409] (ii) the diluted alkyl side chain density thanks to the linearly extended TIF unit, promoting interchain charge transfer;[406,409] and (iii) the large IP of 5.7 eV,[406] meaning that there is a reduced susceptibility for TIF-BT to be accidentally doped during processing, contributing to lower trap density and higher environmental stability.[409] Recently, it was found that the key of its high mobility probably lies in the great density of close-crossing points between adjacent chains that can enhance interchain electronic coupling.[408,410] We note that all these benefits to charge transport are not specific to OFETs, encouraging us to employ TIF-BT as the high-mobility active material in OSD-based rectifiers.

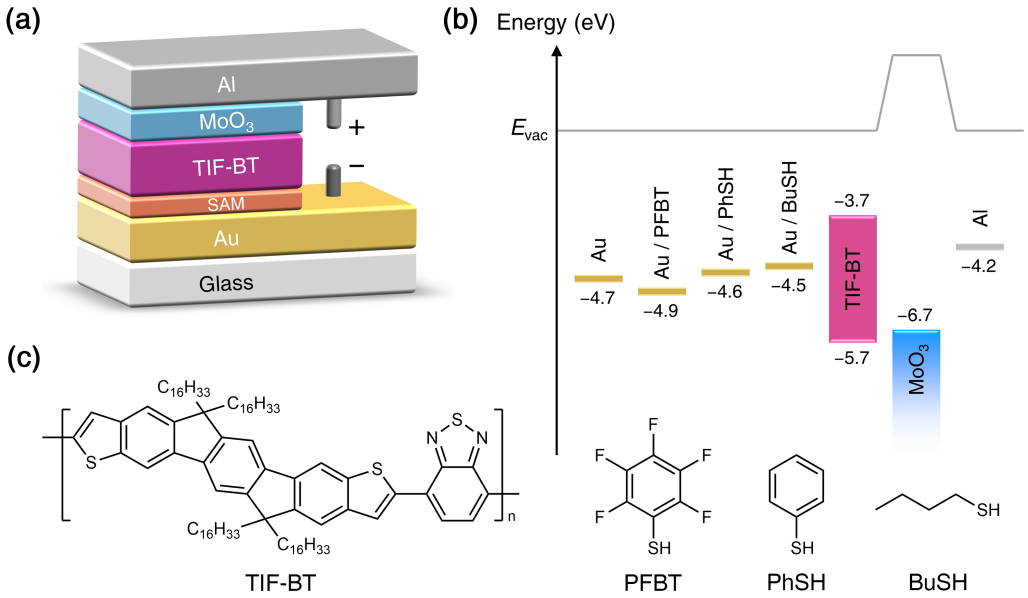

Figure 6.14 | (a) Schematic device structure, (b) nominal energy level diagram, and (c) materials' chemical structures of TIF-BT-based OSDs.

The device structure of TIF-BT OSDs is illustrated in Fig. 6.14(a). The bottom electrode of 60 nm Au (99.99 %, Testbourne) was evaporated on soda–lime glass at

0.5 Å s^{-1}, with a 3 nm Cr (plated on W rods, Kurt J. Lesker, evaporated at 0.2 Å s^{-1}) layer in between (not shown in Fig. 6.14(a)) to promote the adhesion. Au usually functions as the hole-injection electrode due to its relatively high WF. However, the strong push-back effect (Section 2.4.2.2) leads to an effective WF of 4.7 eV, as measured by the Kelvin probe, which is in exactly the middle of TIF-BT's transport gap (Fig. 6.14(b)).[406] Since Au has been successfully employed as the hole-blocking electrode in OSDs,[382] here we also use the bottom electrode as the cathode of the hole-only device. Some self-assembled monolayer (SAM) molecules are chosen to further modify the Au–TIF-BT interface, including 2,3,4,5,6-pentafluorothiophenol (PFBT, 97 %, Sigma-Aldrich), thiophenol (PhSH, 99 %, Sigma-Aldrich), and 1-butanethiol (BuSH, 99 %, Sigma-Aldrich) (Fig. 6.14(c)). The thiol groups (−SH) in these molecules have strong affinities to the Au surface,[179] and their molecular dipole moment can regulate the WF of Au, revealed by Kelvin probe measurement results and shown in Fig. 6.14(b). The SAM was deposited via dipping the Au electrode into the SAM-material–toluene solution (10 mM) for 30 min, followed by rinsing the sample with pure toluene (99.8 % anhydrous, Sigma-Aldrich) three times and vacuum drying for another 30 min. Then TIF-BT (supplied courtesy of Dr. Sungho Nam and Prof. Iain McCulloch) was spin-coated from 10 mg ml^{-1} chlorobenzene (99.8 % anhydrous, Sigma-Aldrich) solution at 1500 rpm, resulting in ~90 nm active layers. The device fabrication was completed by evaporating the MoO_3 (10 nm) / Al (100 nm) bilayer anode at 0.2 and 1 Å s^{-1}, respectively.

The J–V characteristics for TIF-BT-based OSDs are shown in Fig. 6.15(a). In the reverse bias, the device with the Au / PFBT cathode leaks the largest J_r, in line with its smallest Schottky barrier for hole blocking (Fig. 6.14(b)). The PFBT SAM has previously been used to increase the WF of Au and improve the hole injection in the forward bias of pentacene OSDs,[182] but here it performs worse than bare Au since now Au is the hole-blocking electrode. Removing all substituted fluorine atoms in PFBT leaves PhSH, and the direction of molecular dipole moment changes as the electronegativity of sulphur is between fluorine and carbon. Thus the PhSH SAM slightly decreases the WF of Au from

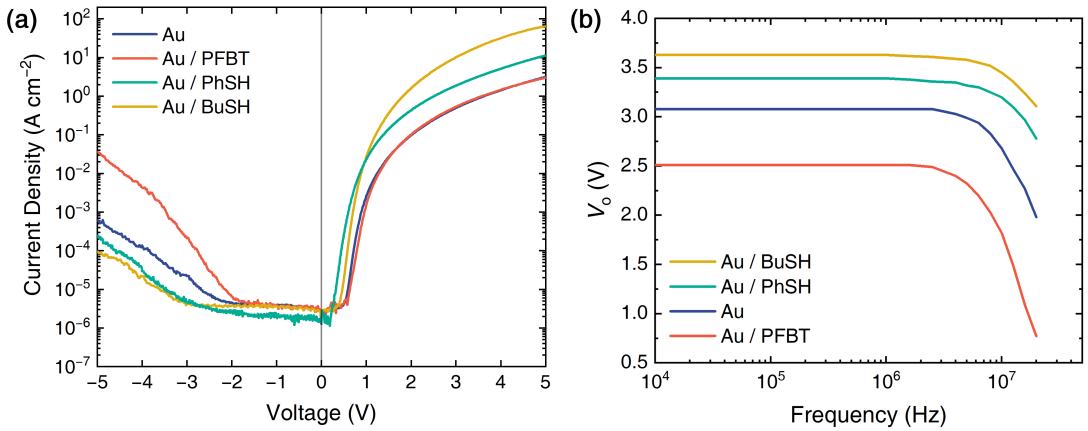

Figure 6.15 | Performance of TIF-BT-Based Rectifiers. (a) J–V characteristics for diodes with different SAMs. (b) V_o–f characteristics for rectifiers. Devices using Au (blue), Au / PFBT (red), Au / PhSH (green), and Au / BuSH (brown) cathodes are shown.

4.7 to 4.6 eV (Fig. 6.14(b)), and the consequently enlarged Schottky barrier blocks the leakage current more effectively than the unmodified Au (Fig. 6.15(a)). The alkyl thiol BuSH has a similar reduction effect to the WF of Au, but to a larger extent. The resultant $J_r \approx 10^{-5}$ A cm^{-2} is also close to that in the device with the Au / PhSH cathode, and is one order of magnitude lower than in the device with bare Au (Fig. 6.15(a)).

In the forward bias, devices with Au and Au / PFBT electrodes exhibit very similar J–V dependences (Fig. 6.15(a)). In contrast, the inclusion of non-fluorinated SAMs considerably increases the current density, especially for BuSH; at 5 V, the current density approaches 10^2 A cm^{-2}, corresponding to an SCLC-mobility of 4.1×10^{-3} cm^2 V^{-1} s^{-1}, comparable with CCN (5.1×10^{-3} cm^2 V^{-1} s^{-1}) in the preceding section. It is surprising to observe that SAMs have an impact on the forward bias, as their main function is assumed to be WF and Schottky barrier height tuning. Considering the mobility is also associated with the active material's crystallite orientation, which can be regulated by the layer underneath, e.g. the study on CuSCN / PTB7 in Section 5.5, we collected GIWAXS patterns of TIF-BT deposited on different electrodes (Fig. 6.16). However, results from these samples, including the in-plane and out-of-plane scattering intensity distribution, the position of peaks (i.e. the crystallite interplanar spacing), and the width of peaks (i.e. the mean size of crystallites) are not distinguishable. At the moment it is not clear

why such evident improvements in the forward current density can occur when PhSH and BuSH are used. We speculate that different end groups of SAM molecules may interact with TIF-BT in different ways, leading to varied density of close-crossing points, which are critical to TIF-BT's mobility[408,410] but can hardly be detected by GIWAXS. Verification of this hypothesis remains outstanding, and may be achieved in the future using the method proposed by Thomas et al,[410] i.e. extracting the radiative decay rate of intrachain charge transfer states residing in proximity of close-contact points from a combination of SSPL, TRPL, and transient absorption spectroscopy results.

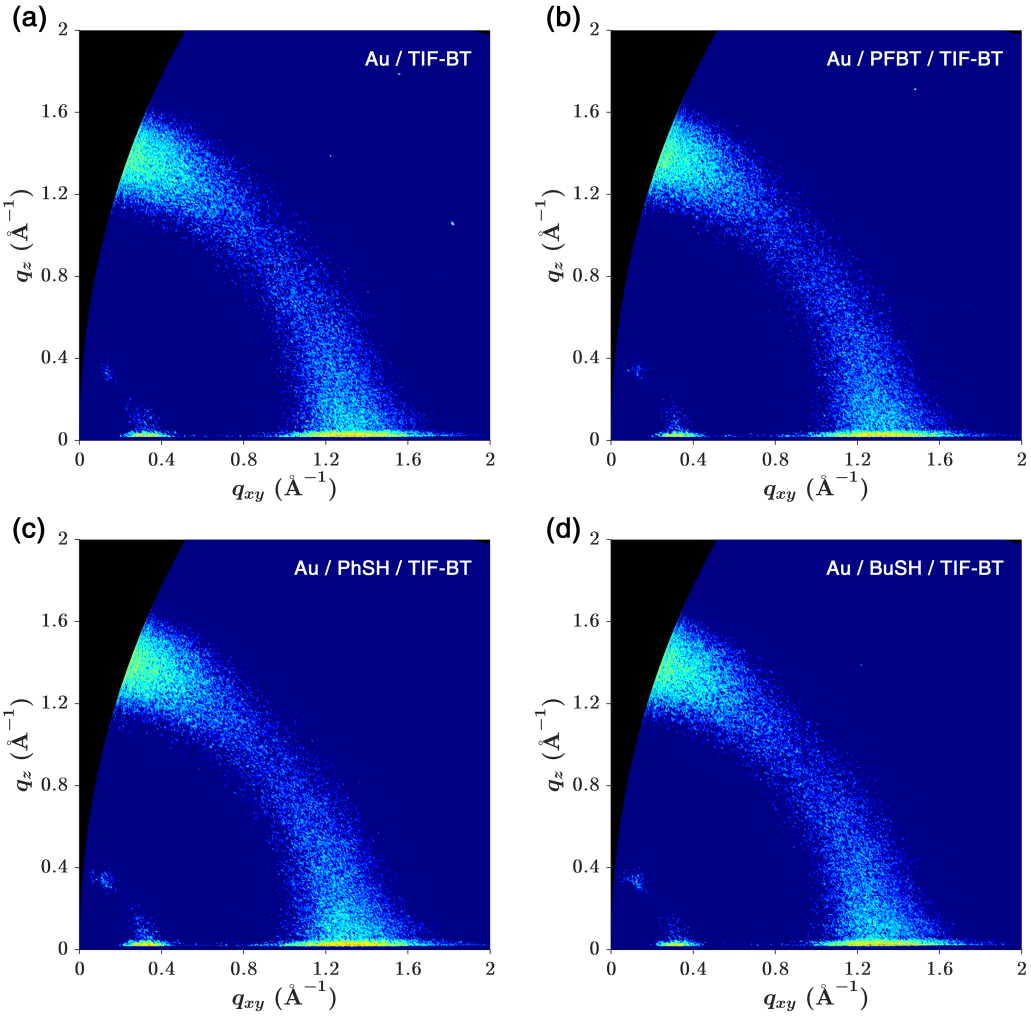

Figure 6.16 | GIWAXS Patterns of TIF-BT Deposited on Different Electrodes. (a) On bare Au; (b) on Au / PFBT; (c) on Au / PhSH; (d) on Au / BuSH.

Since the OSD with the Au / BuSH bottom electrode combines high mobility with

low leakage current density, the corresponding rectifier shows the best performance with a V_o reaching 3.63 V (Fig. 6.15(b)). In comparison, the V_o is 3.08 V for the device with unmodified Au electrode, and using the favourable PhSH and the unfavourable PFBT can change this value to 3.39 V and 2.51 V, respectively (Fig. 6.15(b)).

Finally, as discussed in Section 6.3.4, the rectifier can be further optimised by a simple method, i.e. reducing the active layer thickness d. To demonstrate its effectiveness, we fabricated rectifiers with the Au / BuSH electrode but with different TIF-BT thickness, i.e. 115, 60, and 40 nm; the device mentioned in the last two paragraphs with $d = 90$ nm is also included for comparison. As shown in Fig. 6.17(a), V_o monotonically increases with decreasing d. The highest V_o of 4.00 V ($= 0.8V_m$) is attained when $d = 40$ nm without any fabrication issues. This rectifier can successfully rectify the AC signal at 13.56 MHz (threshold of the HF regime, Fig. 6.17(b) upper) and 20 MHz (the upper limit of our signal generator, Fig. 6.17(b) lower). We also use our improved model to simulate this rectifier's performance and predict its f_{3dB}. With experiment-based parameters of $\mu = 4.1 \times 10^{-3}\,\mathrm{cm^2\,V^{-1}\,s^{-1}}$, $d = 40$ nm, $V_T = 1.0$ V, $J_r = 5 \times 10^{-5}\,\mathrm{A\,cm^{-2}}$, and $m = 4$, as well as the default trap density $N_t = 5 \times 10^{23}\,\mathrm{m^{-3}}$, the simulation results match the measured data exceptionally well, and an f_{3dB} of 243 MHz can be acquired (Fig. 6.17(c)). Although this value is awaiting experimental substantiation, it is among the highest f_{3dB} the solution-processed OSD-based rectifiers can achieve nowadays.[381–383] We also compare the measured and simulated V_o–f characteristics for all devices with different thickness (Fig. 6.17(d)). The dashed simulation curves are in reasonable agreement with those solid from experiments, indicating the appropriateness of our improved model to describe the rectifier's performance. However, there is a noticeable deviation for the 90 nm device. Considering that the deviation becomes smaller both above and below this thickness, we do not suspect that there is a systematic error in our model regarding the thickness. Rather, accidental factors in experiments that can vary from batch to batch (e.g. the solution quality and the fluctuated electrode evaporation rate) might be the case, since the 90 nm device was not fabricated in the same batch with the others (but originally for

the study on the effect of SAMs) due to the very limited material availability.

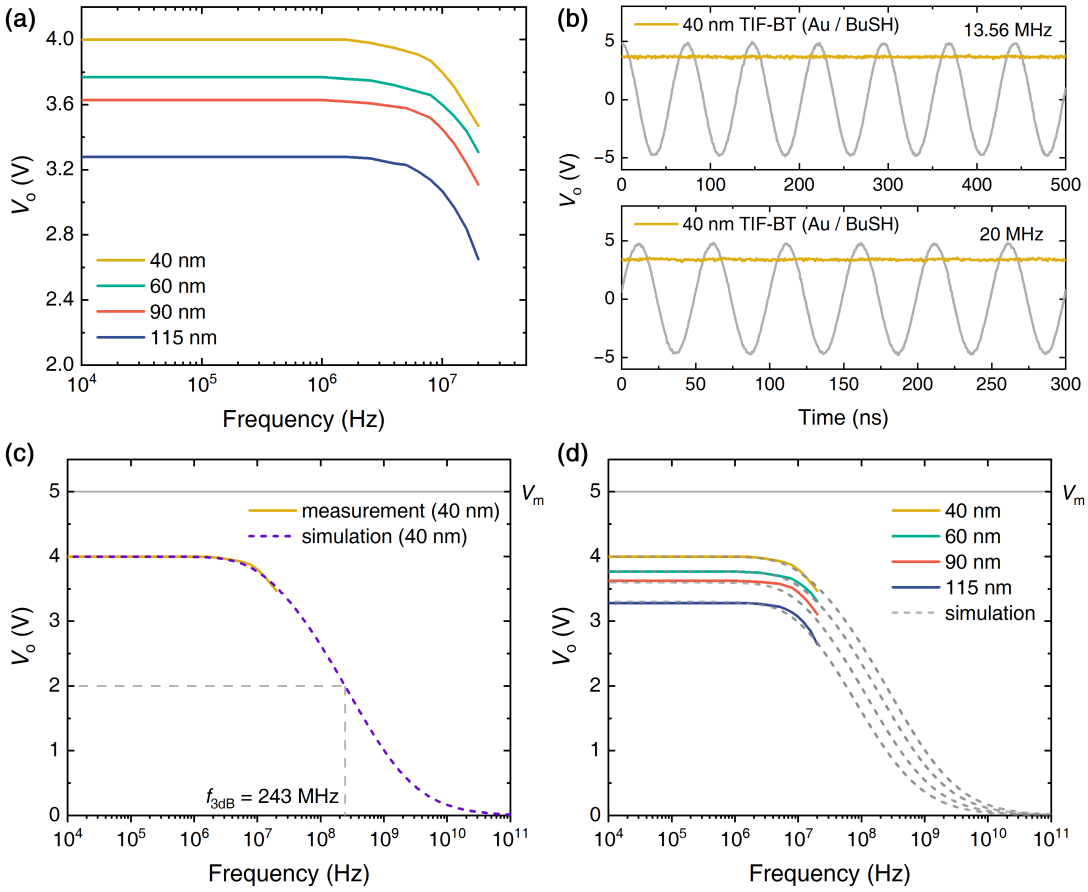

Figure 6.17 | Thickness Optimisation of TIF-BT-Based Rectifiers Using the Au / BuSH Bottom Electrode. (a) V_o–f curves for rectifiers with different active layer thickness. (b) Time-dependent V_o at f = 13.56 MHz (upper) and 20 MHz (lower). (c) For the champion device (d = 40 nm), prediction of its f_{3dB} using the improved model. A high value of 243 MHz is estimated from the simulation. (d) Comparison of the measured and simulated V_o–f characteristics for all devices. Experimental data for d = 115 nm (blue), 90 nm (red), 60 nm (green), and 40 nm (brown) devices are shown by solid curves, and those from simulation are denoted by dashed curves.

To sum up, the TIF-BT-based OSD enables a high-performance rectifier with V_o = 4.00 V (at V_m = 5.00 V) and f_{3dB} = 243 MHz, thanks to the properly chosen SAM and the thin active layer. Despite this frequency being only ~30 % of the UHF threshold (865 MHz), we are optimistic about realising the solution-processed OSD-based UHF rectifier in the near future, given the ongoing development of high-mobility OSC materials and the abundance of device optimisation strategies.

6.7 Conclusions and Outlook

In conclusion, investigations of solution-processed OSD-based rectifiers for RFID applications are carried out in this chapter. Having recognised the superiority of OSDs over OHDs and OFETs in the transdiode mode, we establish an improved model to describe the frequency response of OSD-based rectifiers, elucidating how the mobility, active layer thickness, transition voltage, leakage current density, trap density and depth, and amplitude of the input signal affect the rectifier's performance. The mobility is found to be the most critical parameter that has a great impact on $f_{3\mathrm{dB}}$: once μ increases by one order of magnitude, $f_{3\mathrm{dB}}$ rises by a similar scale. The active layer thickness can influence both V_{o} and $f_{3\mathrm{dB}}$, and thinner layers are conducive to both. The transition voltage and the reverse leakage current density mainly affect the rectifier's performance in the low-frequency regime; reducing either of them can lead to a higher V_{o}. The trap concentration and depth are also relevant, but their detrimental effects on V_{o} and $f_{3\mathrm{dB}}$ are only pronounced after surpassing some thresholds, i.e. 0.04 % for the former and $3kT$ for the latter. Finally, higher amplitudes of the input AC signal, a device-independent parameter, can result in higher normalised V_{o}, and a small device active area is helpful in minimising the output voltage ripple, dissipating heat, and reducing structural defects in the active layer.

Guided by our simulation results, we fabricate OSDs using PTB7, CCN, and TIF-BT, respectively, and optimise the resultant rectifiers. The best performance we obtained is from the TIF-BT device, which can exhibit a V_{o} of 4.00 V (at $V_{\mathrm{m}} = 5.00$ V) and an $f_{3\mathrm{dB}}$ of 243 MHz (estimated by simulation), enabling stable and efficient DC output at 13.56 MHz (the HF regime). This $f_{3\mathrm{dB}}$ is at the same order of magnitude as UHF, and is among the highest values the solution-processed OSD-based rectifier can achieve currently. Moreover, from the examples of PTB7-, CCN-, and TIF-BT-based rectifiers, where an improvement of $f_{3\mathrm{dB}}$ from below HF, to above HF, and finally towards UHF is presented, our methodology for boosting the organic rectifier's performance, i.e. (i) choosing high-

mobility materials, (ii) interface engineering, and (iii) thickness adjustment, is proved to be effective. These strategies are summarised from the simulation results using our improved model, whose correctness is verified by the agreement with experimental data.

Our work demonstrates that solution-processed OSD-based rectifiers are promising for HF/UHF applications. Further investigations of developing and using other high-mobility OSC materials, better control of trap density and depth, and exploring all-printed and/or flexible OSD-based rectifiers are entailed to improve the competitiveness of organic rectifiers against their Si counterparts in RFID tags.

Chapter 7

Conclusions and Outlook

7.1 Conclusions

Concerning strategies for high-performance OSC devices, we present three examples in this thesis to demonstrate the effectiveness of controlling the microstructure of conjugated polymers and selecting proper interlayers, as well as device optimisation for emerging applications. In Chapter 4, the chain conformation of a fluorene–benzothiadiazole copolymer, 90F8:10BT, is regulated so that the planar-zigzag β-phase chain segments are generated. We show that at a fraction of ~5 %, this particular microstructure can affect multiple properties of 90F8:10BT, including the appearance of the characteristic ~430 nm peak in absorption spectra, the slightly decreased exciton lifetime (from 2.502 to 2.286 ns), the increased hole mobility (from 2.16×10^{-7} to $4.71 \times 10^{-7}\,\mathrm{cm^2\,V^{-1}\,s^{-1}}$ measured by MIS-CELIV and from 1.48×10^{-6} to $5.59 \times 10^{-6}\,\mathrm{cm^2\,V^{-1}\,s^{-1}}$ measured by $-\Delta B$ method), the reduced hole injection barrier (the SCLC-transition voltage from 1.07 to 0.39 V, and the peak voltage from 4.2 to 3.7 V in C–V measurements), and fewer trap states (faster EL drop-off after turning the voltage pulse off in TREL measurements), while the PL spectra, PLQE, electron injection barrier, and electron mobility are barely changed. The resulting β-phase LEDs exhibit higher luminance (5940 vs 4750 $\mathrm{cd\,m^{-2}}$), efficiencies (EQE: 1.91 % vs 1.19 %, η_L: 6.18 vs 4.10 $\mathrm{cd\,A^{-1}}$, η_LP: 3.69 vs 2.22 $\mathrm{lm\,W^{-1}}$), and operational stability ($\mathrm{LT_{90}}$: >20 h vs 10.4 h) compared with reference devices using unmodified glassy 90F8:10BT as the EML. The significance of this study lies not only in the generalisation of previously reported β-phase in the homopolymer PFO to F8-

based copolymers, but also in the successful implementation of conformational control for polymer LED optimisation, an intervention level that lies between chemical modification and device engineering.

In Chapter 5, CuSCN hole injection/transport material is investigated, emphasising the solvent effect on the resulting interlayers. We systematically compare the properties of CuSCN processed from six different solvents, namely DES, DPS, NH_4OH, DMSO, DMF, and NMP. Their solutions show different colours depending on the nature of copper–solvent-molecule complexes, and the spin-coated thins films exhibit similar roughness to the ITO substrate ($R_{rms} \approx 3\,nm$), except the one processed from NMP with ~30 % higher R_{rms} values. The polymorph of drop-cast thick films are characterised by Raman and FTIR spectroscopy as well as XRD. All techniques confirm the existence of the thermodynamically most stable β-phase, yet the sample processed from DMSO additionally contains the meta-stable α-phase. The chemical composition and bonding of different CuSCN thin films are investigated by XPS, and the most noticeable feature is that in samples processed from NH_4OH, DMSO, DMF, and NMP, more S and Cu atoms are oxidised compared with those processed from DES and DPS. Moreover, two important features of CuSCN interlayers that have impacts on hole injection and transport properties, the surface energy and the ionisation potential, are discussed in detail. For the former, using NH_4OH, DMSO, DMF, and NMP as the solvent, in comparison with DES and DPS, can increase the surface energy of CuSCN thin films from about $60\,mJ\,m^{-2}$ to about $75\,mJ\,m^{-2}$, leading to more face-on orientated crystallites in the PTB7 layer deposited on top, so the hole mobility for PTB7 in diode structures rises from ~3×10^{-5} to ~$5 \times 10^{-5}\,cm^2\,V^{-1}\,s^{-1}$ (measured by MIS-CELIV). For the latter, IPs of different CuSCN interlayers vary significantly from 5.19 to 5.91 eV across the sequence NMP < DMF < DMSO < DES < DPS < NH_4OH, and such differences are comfirmed by J–V characteristics for hole-only diodes. Finally, examples of using CuSCN interlayers in selected OLEDs, OPVs, and OFETs additionally demonstrate the significance of

choosing appropriate solvents, with DMSO and DMF, two more benign solvents than the conventional DES and DPS, offering the devices investigated in this chapter the best performance. This study expands the selection range of CuSCN solvents to two novel, so-far unexplored chemicals (DMF and NMP), and the side-by-side comparison of these solvents enables a better understanding of CuSCN as highly efficient hole injection/transport interlayers in favour of boosting OSC device performance.

In Chapter 6, an emerging application of OSCs, solution-processed OSD-based rectifiers for RFID tags, is presented. We first compare three different organic rectifying devices, namely OHDs, OFETs in the transdiode mode, and OSDs. For HF applications, OHDs are not especially suitable due to its non-negligible reverse recovery time, and OFETs are restricted by their relatively large contact resistance and channel length, hence OSDs are superior. Considering previous research about OSD-based rectifiers mainly focussed on experiment-based device optimisation, we then construct an improved theoretical model to describe the rectifier's V_o–f characteristics. Compared with the original model, our improved approach additionally takes the leakage current density in the reverse bias and the trap density and depth into account. A number of factors are thus recognised to be relevant to the rectifier's frequency response (as shown by numerical simulation results), among which the crucial one is the active material's mobility; each time the mobility rises/drops by one order of magnitude, the rectifier's f_{3dB} changes by a similar scale. These results equip us with a methodology for improving the performance of solution-processed OSD-based rectifiers. Following the steps of (i) choosing high-mobility OSC materials, (ii) engineering the interface, and (iii) adjusting the active layer thickness, we successively fabricate rectifiers that can operate below HF (PTB7-based, 6.5 MHz), above HF (fullerene-mixture-based, 93 MHz), and towards UHF (TIF-BT-based, 243 MHz). These inspiring achievements not only raise our confidence in realising solution-processed OSD-based UHF rectifiers, but also exemplify how theoretical and experimental studies can work synergistically towards high-performance OSC devices.

7.2 Outlook

Undoubtedly, there remain some opportunities to deepen and/or broaden the research presented in this thesis. For the 90F8:10BT copolymer, the detailed mechanisms of its conformation-dependent charge transport, trap formation and distribution, and chemical- and photo-degradation are worth more investigations. Regarding the β-phase, recently it has been successfully generated in a PFO-derivative, poly[4-(octyloxy)-9,9-diphenylfluoren-2,7-diyl]-*co*-[5-(octyloxy)-9,9-diphenylfluoren-2,7-diyl] (PODPF), by the convenient thermal annealing method.[411] It is thus interesting to explore what characteristics of PODPF allow the adoption of the β-phase by such simple treatment, and if these features can be reproduced in novel PFO-based optoelectronic conjugated polymers to simplify the generation of the β-phase. Under a broader context, generalising the benefits of the β-phase, or other particular conformations, to more conjugated polymer families (beyond the PFO) and more OSC devices (beyond OLEDs) can result in new perspectives on material property control and device optimisation.

With respect to CuSCN, it is worthwhile to investigate its solvent-dependent electronic structures and crystallisation routes with the help of computational chemistry, e.g. *ab initio* methods for the former and molecular dynamics for the latter. Besides, more examples of using CuSCN interlayers processed from different solvents in OSC devices, or even perovskite devices, can be useful to widen the applicability range of CuSCN and deepen our understanding of which active materials can work well with CuSCN interlayers and why. Furthermore, finding new solvents for CuSCN is still necessary, as the two that we proved to be advantageous to selected OSC device performance in Section 5.7, DMSO and DMF, require relatively harsh dissolving conditions (heating at 120 °C over 24 h with vigorous stirring), and the solubility of CuSCN in DMF is not high enough (Table 5.1). An ideal solvent should combine mild dissolving conditions (cf. DMSO, DMF, and NMP), reasonably high solubility (cf. DMF and NMP), low toxicity and odour (cf. DES and DPS), a suitable boiling point for its easy removal during spin-coating (cf. DMSO and NMP),

and the ability to form high-quality films together. We note that Pearson's Hard and Soft Acids and Bases theory can provide us with some constructive guidance. For example, a recent study demonstrated that "softer" solvents, achieved by replacing oxygen atoms with sulphur, can interact stronger with Pb^{2+},[412] a soft acid similar to Cu^{+} and underlying the popular perovskite materials. This encouraged us to try sulphur-substituted-DMF and -NMP, namely *N*,*N*-dimethylthioformamide (DMTF) and 1-methylpyrrolidine-2-thione (NMPT), respectively. Preliminary dissolving experiments confirmed the high solubility of CuSCN in both ($> 20\,\mathrm{mg\,ml^{-1}}$) by simply stirring the solution at room temperature for several minutes. Even better is that they have relatively low boiling points, especially for DMTF (60 °C), which is also categorised as a non-hazardous material.[413] These results motivated us to continue studying the DMTF- and NMPT-processed CuSCN interlayers in the future. We also found that adding some thiocyanate salts, e.g. LiSCN and KSCN, into the CuSCN-DMF solution at a low concentration of $1\,\mathrm{mg\,ml^{-1}}$ can substantially improve the solubility without significantly affecting the device performance, which opens another possibility to resolve the solvent issue. On the other hand, we list here some unsuccessful solvents for CuSCN (due to the insufficient solubility even at elevated temperatures) that we have already tried as a service to the community: common aromatic solvents (chlorobenzene, dichlorobenzene, toluene, xylene, and mesitylene), common alcohols (methanol, ethanol, and isopropanol), acetone, diethyl ether, chloroform, tetrahydrofuran (THF), acetonitrile, butyronitrile, and *N*,*N*-dimethylacetamide (DMAc).

Finally, the TIF-BT-based rectifier still has plenty of room to be optimised, e.g. employing other SAMs, controlling the trap density and depth to be smaller than the threshold values (i.e. $N_t/N < 0.04\,\%$ and $m < 3$, see Section 6.3.4), and applying suitable post-treatment. In addition, the underlying principles of the high mobility for TIF-BT, as well as the reason why certain SAMs can significantly improve its mobility, deserve more theoretical and experimental research. As to OSD-based rectifiers, they are likely to develop towards reduced fabrication cost, better mechanical properties, and higher working frequencies. The first two largely rely on the upcoming studies on all-

printed and flexible organic rectifiers (e.g. roll-to-roll printing on plastic substrates), and the last one, as discussed in Section 6.3, primarily requires high-mobility OSCs, e.g. $\mu \approx 10^{-1}\,\mathrm{cm^2\,V^{-1}\,s^{-1}}$ for UHF applications (Fig. 6.4(a)). This can definitely be achieved by synthesising new materials, but those seemingly obsolete should not be simply discarded. For instance, it is surprising to see that P3HT can exhibit an out-of-plane hole mobility of $2.6\,\mathrm{cm^2\,V^{-1}\,s^{-1}}$ after being nanoimprinted,[414] and a solution-processable phthalocyanine derivative can reach an SCLC-mobility of $0.12\,\mathrm{cm^2\,V^{-1}\,s^{-1}}$ when spin-coated from a mixed solvent.[415] Our closing remarks convey such an opinion that realising high mobility, or other desired material properties or device performance, does not necessarily entail completely new materials or techniques; old ones with underestimated potential may be awaiting our greater exploitation.

Bibliography

1. Wade, L. G. *Organic Chemistry* 8th edn. (Pearson, NY, USA, 2013) (p. 1).
2. Baekeland, L. *US Patent* 942699A (1907) (p. 1).
3. Staudinger, H. *Ber. dtsch. Chem. Ges. A/B* **53,** 1073–1085 (1920) (p. 1).
4. Rudin, A. & Choi, P. *The Elements of Polymer Science and Engineering* 3rd edn. (Academic Press, MA, USA, 2013) (pp. 2, 62).
5. Köhler, A. & Bässler, H. *Electronic Processes in Organic Semiconductors* (Wiley-VCH, Weinheim, Germany, 2015) (pp. 2, 3, 4, 13, 15, 17, 19, 21, 22, 24, 26, 30, 32, 34, 35, 37, 44, 45, 46, 47, 48, 56, 58, 61, 68, 72, 73, 75, 77, 89, 92, 93, 103, 107, 112).
6. Abbasi, E. *et al. Nanoscale Res. Lett.* **9,** 247. doi:10.1186/1556-276x-9-247 (2014) (p. 2).
7. Akamatu, H., Inokuchi, H. & Matsunaga, Y. *Nature* **173,** 168–169. doi:10.1038/173168a0 (1954) (p. 2).
8. McNeill, R., Siudak, R., Wardlaw, J. H. & Weiss, D. E. *Aust. J. Chem.* **16,** 1056–1075. doi:10.1071/ch9631056 (1963) (p. 2).
9. Bolto, B. A. & Weiss, D. E. *Aust. J. Chem.* **16,** 1076–1089. doi:10.1071/ch9631076 (1963) (p. 2).
10. Bolto, B. A., McNeill, R. & Weiss, D. E. *Aust. J. Chem.* **16,** 1090–1103. doi:10.1071/ch9631090 (1963) (p. 2).
11. Shirakawa, H., Louis, E. J., MacDiarmid, A. G., Chiang, C. K. & Heeger, A. J. *J. Chem. Soc., Chem. Commun.,* 578–580. doi:10.1039/c39770000578 (1977) (p. 2).
12. Kittel, C. *Introduction to Solid State Physics* 8th edn. (John Wiley & Sons, NJ, USA, 2005) (pp. 3, 46, 67, 68).
13. Brebels, J., Manca, J. V., Lutsen, L., Vanderzande, D. & Maes, W. *J. Mater. Chem. A* **5,** 24037–24050. doi:10.1039/c7ta06808e (2017) (pp. 4, 34, 170).
14. El-Nahass, M. M., Zeyada, H. M., Aziz, M. S. & El-Ghamaz, N. A. *Opt. Mater.* **27,** 491–498. doi:10.1016/j.optmat.2004.04.010 (2004) (p. 4).
15. Alvarado, S., Seidler, P., Lidzey, D. & Bradley, D. *Phys. Rev. Lett.* **81,** 1082–1085. doi:10.1103/physrevlett.81.1082 (1998) (p. 4).
16. Meredith, P., Li, W. & Armin, A. *Adv. Energy Mater.* **10,** 2001788. doi:10.1002/aenm.202001788 (2020) (pp. 5, 8).

17. Bradley, D. D. C. *J. Phys. D Appl. Phys.* **20,** 1389–1410. doi:10.1088/0022-3727/20/11/007 (1987) (p. 5).
18. Destriau, G. *J. Chim. Phys.* **33,** 587–625. doi:10.1051/jcp/1936330587 (1936) (p. 6).
19. Pope, M., Kallmann, H. P. & Magnante, P. *J. Chem. Phys.* **38,** 2042–2043. doi:10.1063/1.1733929 (1963) (p. 6).
20. Tang, C. W. & VanSlyke, S. A. *Appl. Phys. Lett.* **51,** 913–915. doi:10.1063/1.98799 (1987) (p. 6).
21. Burroughes, J. H. *et al. Nature* **347,** 539–541. doi:10.1038/347539a0 (1990) (pp. 6, 95).
22. Hong, G. *et al. Adv. Mater.* **33,** 2005630. doi:10.1002/adma.202005630 (2021) (pp. 6, 7).
23. Song, J. *et al. Nat. Commun.* **9,** 3207. doi:10.1038/s41467-018-05671-x (2018) (p. 6).
24. Hosoumi, S. *et al. SID Symp. Dig. Tech. Pap.* **48,** 13–16. doi:10.1002/sdtp.11562 (2017) (p. 6).
25. Huang, Y., Hsiang, E.-L., Deng, M.-Y. & Wu, S.-T. *Light Sci. Appl.* **9,** 105. doi:10.1038/s41377-020-0341-9 (2020) (p. 7).
26. Kotadiya, N. B., Blom, P. W. M. & Wetzelaer, G.-J. A. H. *Nat. Photonics* **13,** 765–769. doi:10.1038/s41566-019-0488-1 (2019) (p. 7).
27. Noda, K., Komatsu, T., Fukuda, T. & Goto, M. *SID Symp. Dig. Tech. Pap.* **51,** 587–590. doi:10.1002/sdtp.13936 (2020) (p. 7).
28. Forrest, S. R. *Nanophotonics* **10,** 31–40. doi:10.1515/nanoph-2020-0322 (2020) (pp. 7, 9, 10).
29. Chapin, D. M., Fuller, C. S. & Pearson, G. L. *J. Appl. Phys.* **25,** 676–677. doi:10.1063/1.1721711 (1954) (p. 8).
30. Green, M. A. *et al. Prog. Photovolt. Res. Appl.* **29,** 657–667. doi:10.1002/pip.3444 (2021) (p. 8).
31. Kallmann, H. & Pope, M. *J. Chem. Phys.* **30,** 585–586. doi:10.1063/1.1729992 (1959) (p. 8).
32. Tang, C. W., Marchetti, A. P. & Young, R. H. *US Patent* 4125414A (1978) (p. 8).
33. Tang, C. W. *US Patent* 4164431A (1979) (p. 8).
34. Tang, C. W. *Appl. Phys. Lett.* **48,** 183–185. doi:10.1063/1.96937 (1986) (p. 8).
35. Hiramoto, M., Fujiwara, H. & Yokoyama, M. *Appl. Phys. Lett.* **58,** 1062–1064. doi:10.1063/1.104423 (1991) (p. 8).
36. Yu, G., Gao, J., Hummelen, J. C., Wudl, F. & Heeger, A. J. *Science* **270,** 1789–1791. doi:10.1126/science.270.5243.1789 (1995) (p. 8).

37. Halls, J. J. M. *et al. Nature* **376,** 498–500. doi:10.1038/376498a0 (1995) (p. 8).
38. Shaheen, S. E. *et al. Appl. Phys. Lett.* **78,** 841–843. doi:10.1063/1.1345834 (2001) (p. 8).
39. Tong, Y. *et al. Sci. China Chem.* **63,** 758–765. doi:10.1007/s11426-020-9726-0 (2020) (p. 8).
40. Liang, Y. *et al. J. Am. Chem. Soc.* **131,** 56–57. doi:10.1021/ja808373p (2009) (p. 8).
41. Zhao, J. *et al. Nat. Energy* **1,** 15027. doi:10.1038/nenergy.2015.27 (2016) (p. 8).
42. Liu, Q. *et al. Sci. Bull.* **65,** 272–275. doi:10.1016/j.scib.2020.01.001 (2020) (p. 8).
43. Zhang, M. *et al. Nat. Commun.* **12,** 309. doi:10.1038/s41467-020-20580-8 (2021) (p. 8).
44. National Renewable Energy Laboratory (NREL). *Best Research-Cell Efficiency Chart* https://www.nrel.gov/pv/cell-efficiency.html (2021-08-24) (p. 9).
45. Gambhir, A., Sandwell, P. & Nelson, J. *Sol. Energy Mater. Sol. Cells* **156,** 49–58. doi:10.1016/j.solmat.2016.05.056 (2016) (p. 9).
46. Riede, M., Spoltore, D. & Leo, K. *Adv. Energy Mater.* **11,** 2002653. doi:10.1002/aenm.202002653 (2020) (p. 9).
47. Neamen, D. A. *Semiconductor Physics and Devices: Basic Principles* 4th edn. (McGraw-Hill, NY, USA, 2012) (pp. 9, 44, 160, 168).
48. Kahng, D. *IEEE Trans. Electron Devices* **23,** 655–657. doi:10.1109/t-ed.1976.18468 (1976) (p. 9).
49. Horowitz, G. *Adv. Mater.* **10,** 365–377. doi:10.1002/(sici)1521-4095(199803)10:5<365::aid-adma365>3.0.co;2-u (1998) (p. 10).
50. Klauk, H. *Chem. Soc. Rev.* **39,** 2643–2666. doi:10.1039/b909902f (2010) (p. 10).
51. Tsumura, A., Koezuka, H. & Ando, T. *Appl. Phys. Lett.* **49,** 1210–1212. doi:10.1063/1.97417 (1986) (p. 10).
52. Paterson, A. F. *et al. Adv. Mater.* **30,** 1801079. doi:10.1002/adma.201801079 (2018) (pp. 10, 53, 93, 94, 174).
53. Paterson, A. F. *et al. Adv. Mater.* **31,** 1900871. doi:10.1002/adma.201900871 (2019) (pp. 10, 53, 174).
54. Wu, M., Pangal, K., Sturm, J. C. & Wagner, S. *Appl. Phys. Lett.* **75,** 2244–2246. doi:10.1063/1.124978 (1999) (p. 10).
55. Bittle, E. G., Basham, J. I., Jackson, T. N., Jurchescu, O. D. & Gundlach, D. J. *Nat. Commun.* **7,** 10908. doi:10.1038/ncomms10908 (2016) (pp. 10, 94).
56. Choi, H. H., Cho, K., Frisbie, C. D., Sirringhaus, H. & Podzorov, V. *Nat. Mater.* **17,** 2–7. doi:10.1038/nmat5035 (2018) (pp. 10, 94).

57. Yang, J., Zhao, Z., Wang, S., Guo, Y. & Liu, Y. *Chem* **4,** 2748–2785. doi:10.1016/j.chempr.2018.08.005 (2018) (p. 11).
58. Yuvaraja, S. *et al. Chem. Soc. Rev.* **49,** 3423–3460. doi:10.1039/c9cs00811j (2020) (p. 11).
59. Atkins, P. & Jones, L. *Chemical Principles: The Quest for Insight* 5th edn. (W. H. Freeman and Company, NY, USA, 2010) (pp. 13, 17).
60. Atkins, P., de Paula, J. & Keeler, J. *Atkins' Physical Chemistry* 11th edn. (Oxford University Press, 2018) (pp. 15, 16, 17, 23, 24, 26).
61. Atkins, P. & Friedman, R. *Molecular Quantum Mechanics* 5th edn. (Oxford University Press, NY, USA, 2010) (pp. 15, 16, 19, 20, 22, 29).
62. Jablonski, A. *Nature* **131,** 839–840. doi:10.1038/131839b0 (1933) (p. 21).
63. Brédas, J.-L. *Mater. Horiz.* **1,** 17–19. doi:10.1039/c3mh00098b (2014) (pp. 22, 29, 31, 68).
64. Nakata, M. & Shimazaki, T. *J. Chem. Inf. Model.* **57,** 1300–1308. doi:10.1021/acs.jcim.7b00083 (2017) (p. 22).
65. Fermi, E. *Nuclear Physics* (University of Chicago Press, IL, USA, 1950) (p. 22).
66. Sandee, A. J. *et al. J. Am. Chem. Soc.* **126,** 7041–7048. doi:10.1021/ja039445o (2004) (p. 24).
67. Beljonne, D. *et al. Proc. Natl. Acad. Sci. U.S.A.* **99,** 10982–10987. doi:10.1073/pnas.172390999 (2002) (p. 24).
68. Rossi, G., Chance, R. R. & Silbey, R. *J. Chem. Phys.* **90,** 7594–7601. doi:10.1063/1.456193 (1989) (p. 24).
69. Hilborn, R. C. *Am. J. Phys.* **50,** 982–986. doi:10.1119/1.12937 (1982) (p. 24).
70. Franck, J. & Dymond, E. G. *Trans. Faraday Soc.* **21,** 536–542. doi:10.1039/tf9262100536 (1926) (p. 24).
71. Condon, E. U. *Phys. Rev.* **32,** 858–872. doi:10.1103/physrev.32.858 (1928) (p. 24).
72. Adachi, C. *Jpn. J. Appl. Phys.* **53,** 060101. doi:10.7567/jjap.53.060101 (2014) (p. 27).
73. Cahen, D. & Kahn, A. *Adv. Mater.* **15,** 271–277. doi:10.1002/adma.200390065 (2003) (p. 28).
74. Kahn, A. *Mater. Horiz.* **3,** 7–10. doi:10.1039/c5mh00160a (2016) (pp. 28, 29, 41, 68).
75. *IUPAC Compendium of Chemical Terminology (the "Gold Book")* 2nd edn. (International Union of Pure and Applied Chemistry, NC, USA, 2019) (pp. 28, 32).
76. Koopmans, T. *Physica* **1,** 104–113. doi:10.1016/s0031-8914(34)90011-2 (1934) (p. 29).

77. Ranasinghe, D. S., Margraf, J. T., Perera, A. & Bartlett, R. J. *J. Chem. Phys.* **150,** 074108. doi:10.1063/1.5084728 (2019) (p. 29).
78. Fang, H.-H. *et al. Laser Photonics Rev.* **8,** 687–715. doi:10.1002/lpor.201300222 (2014) (p. 30).
79. Paterson, A. F. *et al. Adv. Mater.* **28,** 7791–7798. doi:10.1002/adma.201601075 (2016) (p. 30).
80. Noriega, R. *et al. Nat. Mater.* **12,** 1038–1044. doi:10.1038/nmat3722 (2013) (p. 30).
81. Müller, C. *et al. Adv. Funct. Mater.* **23,** 2368–2377. doi:10.1002/adfm.201202983 (2013) (p. 30).
82. Campbell, A. J. *et al. Adv. Funct. Mater.* **26,** 3720–3729. doi:10.1002/adfm.201504722 (2016) (pp. 30, 53, 110).
83. Amirav, A., Even, U. & Jortner, J. *Chem. Phys. Lett.* **72,** 16–20. doi:10.1016/0009-2614(80)80231-4 (1980) (pp. 31, 33).
84. Hesse, R., Hofberger, W. & Bässler, H. *Chem. Phys.* **49,** 201–211. doi:10.1016/0301-0104(80)85257-8 (1980) (pp. 31, 33).
85. Yoshida, H., Yamada, K., Tsutsumi, J. & Sato, N. *Phys. Rev. B* **92,** 075145. doi:10.1103/physrevb.92.075145 (2015) (p. 31).
86. Huang, W., Mi, B. & Gao, Z. *Youji Dianzixue [Organic Electronics]* (Science Press, Beijing, China, 2011) (pp. 31, 35, 36, 37, 46, 55, 56, 57, 59, 60, 61).
87. Liang, W. Y. *Phys. Educ.* **5,** 226–228. doi:10.1088/0031-9120/5/4/003 (1970) (pp. 33, 35).
88. Frenkel, J. *Phys. Rev.* **37,** 17–44. doi:10.1103/physrev.37.17 (1931) (p. 33).
89. Frenkel, J. *Phys. Rev.* **37,** 1276–1294. doi:10.1103/physrev.37.1276 (1931) (p. 33).
90. Wannier, G. H. *Phys. Rev.* **52,** 191–197. doi:10.1103/physrev.52.191 (1937) (p. 33).
91. Pope, M., Burgos, J. & Giachino, J. *J. Chem. Phys.* **43,** 3367–3371. doi:10.1063/1.1726399 (1965) (p. 33).
92. Pope, M. & Swenberg, C. E. *Electronic Processes in Organic Crystals and Polymers* 2nd edn. (Oxford University Press, NY, USA, 1999) (pp. 33, 37, 46, 48).
93. Köhler, A. & Wilson, J. *Org. Electron.* **4,** 179–189. doi:10.1016/j.orgel.2003.08.011 (2003) (p. 35).
94. Dhoot, A. S. & Greenham, N. C. *Adv. Mater.* **14,** 1834–1837. doi:10.1002/adma.200290013 (2002) (p. 35).
95. Dhoot, A. S., Ginger, D. S., Beljonne, D., Shuai, Z. & Greenham, N. C. *Chem. Phys. Lett.* **360,** 195–201. doi:10.1016/s0009-2614(02)00840-0 (2002) (p. 35).

96. Köhler, A. & Bässler, H. *Mater. Sci. Eng. R Rep.* **66,** 71–109. doi:10.1016/j.mser.2009.09.001 (2009) (p. 35).
97. Wallikewitz, B. H., Kabra, D., Gélinas, S. & Friend, R. H. *Phys. Rev. B* **85,** 045209. doi:10.1103/physrevb.85.045209 (2012) (p. 35).
98. Förster, T. *Ann. Phys. (Leipzig)* **437,** 55–75. doi:10.1002/andp.19484370105 (1948) (p. 35).
99. Dexter, D. L. *J. Chem. Phys.* **21,** 836–850. doi:10.1063/1.1699044 (1953) (p. 35).
100. Ostroverkhova, O. *Chem. Rev.* **116,** 13279–13412. doi:10.1021/acs.chemrev.6b00127 (2016) (pp. 35, 36).
101. Zhao, C. & Duan, L. *J. Mater. Chem. C* **8,** 803–820. doi:10.1039/c9tc05373e (2020) (pp. 37, 119).
102. Walzer, K., Maennig, B., Pfeiffer, M. & Leo, K. *Chem. Rev.* **107,** 1233–1271. doi:10.1021/cr050156n (2007) (p. 38).
103. Lüssem, B., Riede, M. & Leo, K. *Phys. Status Solidi A* **210,** 9–43. doi:10.1002/pssa.201228310 (2013) (p. 38).
104. Mott, N. F. & Gurney, R. W. *Electronic Processes in Ionic Crystals* (Oxford University Press, NY, USA, 1940) (p. 38).
105. Child, C. D. *Phys. Rev. (Series I)* **32,** 492–511. doi:10.1103/physrevseriesi.32.492 (1911) (p. 38).
106. Braun, S., Salaneck, W. R. & Fahlman, M. *Adv. Mater.* **21,** 1450–1472. doi:10.1002/adma.200802893 (2009) (pp. 41, 42, 43).
107. Fahlman, M. *et al. Nat. Rev. Mater.* **4,** 627–650. doi:10.1038/s41578-019-0127-y (2019) (pp. 41, 42, 123).
108. Kahn, A., Koch, N. & Gao, W. *J. Polym. Sci. B Polym. Phys.* **41,** 2529–2548. doi:10.1002/polb.10642 (2003) (p. 41).
109. Heimel, G., Romaner, L., Zojer, E. & Brédas, J.-L. *Acc. Chem. Res.* **41,** 721–729. doi:10.1021/ar700284q (2008) (p. 42).
110. Van Reenen, S., Kouijzer, S., Janssen, R. A. J., Wienk, M. M. & Kemerink, M. *Adv. Mater. Interfaces* **1,** 1400189. doi:10.1002/admi.201400189 (2014) (p. 42).
111. Bao, Q., Liu, X., Braun, S., Gao, F. & Fahlman, M. *Adv. Mater. Interfaces* **2,** 1400403. doi:10.1002/admi.201400403 (2015) (p. 42).
112. Zojer, E., Taucher, T. C. & Hofmann, O. T. *Adv. Mater. Interfaces* **6,** 1900581. doi:10.1002/admi.201900581 (2019) (pp. 42, 43, 44).
113. Paasch, G., Peisert, H., Knupfer, M., Fink, J. & Scheinert, S. *J. Appl. Phys.* **93,** 6084–6089. doi:10.1063/1.1562731 (2003) (p. 42).
114. Davids, P. S., Campbell, I. H. & Smith, D. L. *J. Appl. Phys.* **82,** 6319–6325. doi:10.1063/1.366522 (1997) (pp. 44, 163).

115. Fowler, R. H. & Nordheim, L. *Proc. Royal Soc. A* **119,** 173–181. doi:10.1098/rspa.1928.0091 (1928) (pp. 44, 45).
116. Simmons, J. G. *Phys. Rev. Lett.* **15,** 967–968. doi:10.1103/physrevlett.15.967 (1965) (p. 44).
117. Chiguvare, Z., Parisi, J. & Dyakonov, V. *J. Appl. Phys.* **94,** 2440–2448. doi:10.1063/1.1588358 (2003) (pp. 44, 45).
118. Crowell, C. R. *Solid-State Electron.* **8,** 395–399. doi:10.1016/0038-1101(65)90116-4 (1965) (p. 44).
119. Wolf, U., Arkhipov, V. I. & Bässler, H. *Phys. Rev. B* **59,** 7507–7513. doi:10.1103/physrevb.59.7507 (1999) (p. 45).
120. Arkhipov, V. I., Wolf, U. & Bässler, H. *Phys. Rev. B* **59,** 7514–7520. doi:10.1103/physrevb.59.7514 (1999) (p. 45).
121. Mousty, F., Ostoja, P. & Passari, L. *J. Appl. Phys.* **45,** 4576–4580. doi:10.1063/1.1663091 (1974) (p. 46).
122. Warta, W. & Karl, N. *Phys. Rev. B* **32,** 1172–1182. doi:10.1103/physrevb.32.1172 (1985) (p. 46).
123. Austin, I. G. & Mott, N. F. *Adv. Phys.* **18,** 41–102. doi:10.1080/00018736900101267 (1969) (p. 47).
124. Holstein, T. *Ann. Phys.* **8,** 325–342. doi:10.1016/0003-4916(59)90002-8 (1959) (p. 47).
125. Holstein, T. *Ann. Phys.* **8,** 343–389. doi:10.1016/0003-4916(59)90003-x (1959) (p. 47).
126. Coropceanu, V. *et al. Chem. Rev.* **107,** 926–952. doi:10.1021/cr050140x (2007) (pp. 47, 48, 52, 53).
127. Tessler, N., Preezant, Y., Rappaport, N. & Roichman, Y. *Adv. Mater.* **21,** 2741–2761. doi:10.1002/adma.200803541 (2009) (p. 48).
128. Bässler, H. *Phys. Status Solidi B* **175,** 15–56. doi:10.1002/pssb.2221750102 (1993) (pp. 48, 49).
129. Miller, A. & Abrahams, E. *Phys. Rev.* **120,** 745–755. doi:10.1103/physrev.120.745 (1960) (p. 48).
130. Novikov, S. V., Dunlap, D. H., Kenkre, V. M., Parris, P. E. & Vannikov, A. V. *Phys. Rev. Lett.* **81,** 4472–4475. doi:10.1103/physrevlett.81.4472 (1998) (p. 49).
131. Parris, P. E., Kenkre, V. M. & Dunlap, D. H. *Phys. Rev. Lett.* **87,** 126601. doi:10.1103/physrevlett.87.126601 (2001) (p. 49).
132. Fishchuk, I. I. *et al. Phys. Rev. B* **88,** 125202. doi:10.1103/physrevb.88.125202 (2013) (p. 49).

133. Baker, J. L. *et al. Langmuir* **26,** 9146–9151. doi:10.1021/la904840q (2010) (pp. 50, 84).
134. Osaka, I. & Takimiya, K. *Polymer* **59,** A1–A15. doi:10.1016/j.polymer.2014.12.066 (2015) (pp. 50, 51, 64, 140, 143).
135. Fratini, S., Nikolka, M., Salleo, A., Schweicher, G. & Sirringhaus, H. *Nat. Mater.* **19,** 491–502. doi:10.1038/s41563-020-0647-2 (2020) (p. 51).
136. Gu, K. *et al. ACS Macro Lett.* **7,** 1333–1338. doi:10.1021/acsmacrolett.8b00626 (2018) (pp. 51, 174).
137. Veres, J., Ogier, S. D., Leeming, S. W., Cupertino, D. C. & Khaffaf, S. M. *Adv. Funct. Mater.* **13,** 199–204. doi:10.1002/adfm.200390030 (2003) (p. 52).
138. Gill, W. D. *J. Appl. Phys.* **43,** 5033–5040. doi:10.1063/1.1661065 (1972) (p. 52).
139. Mozer, A. J. *et al. Phys. Rev. B* **71,** 035214. doi:10.1103/physrevb.71.035214 (2005) (p. 52).
140. Tanase, C., Meijer, E. J., Blom, P. W. M. & de Leeuw, D. M. *Phys. Rev. Lett.* **91,** 216601. doi:10.1103/physrevlett.91.216601 (2003) (pp. 52, 110).
141. Craciun, N. I., Wildeman, J. & Blom, P. W. M. *Phys. Rev. Lett.* **100,** 056601. doi:10.1103/physrevlett.100.056601 (2008) (p. 53).
142. Haneef, H. F., Zeidell, A. M. & Jurchescu, O. D. *J. Mater. Chem. C* **8,** 759–787. doi:10.1039/c9tc05695e (2020) (p. 53).
143. Rose, A. *Phys. Rev.* **97,** 1538–1544. doi:10.1103/physrev.97.1538 (1955) (p. 54).
144. Podzorov, V., Sysoev, S. E., Loginova, E., Pudalov, V. M. & Gershenson, M. E. *Appl. Phys. Lett.* **83,** 3504–3506. doi:10.1063/1.1622799 (2003) (p. 55).
145. Jurchescu, O. D., Baas, J. & Palstra, T. T. M. *Appl. Phys. Lett.* **84,** 3061–3063. doi:10.1063/1.1704874 (2004) (p. 55).
146. Mark, P. & Helfrich, W. *J. Appl. Phys.* **33,** 205–215. doi:10.1063/1.1728487 (1962) (p. 55).
147. Nešpůrek, S. & Silinsh, E. A. *Phys. Status Solidi A* **34,** 747–759. doi:10.1002/pssa.2210340240 (1976) (p. 55).
148. Nešpůrek, S. & Sworakowski, J. *Int. J. Radiat. Appl. Instrum. C Radiat. Phys. Chem.* **36,** 3–12. doi:10.1016/1359-0197(90)90156-c (1990) (p. 55).
149. Steiger, J., Schmechel, R. & von Seggern, H. *Synth. Met.* **129,** 1–7. doi:10.1016/s0379-6779(02)00012-7 (2002) (pp. 55, 170).
150. Vandewal, K. *Annu. Rev. Phys. Chem.* **67,** 113–133. doi:10.1146/annurev-physchem-040215-112144 (2016) (p. 58).
151. Peumans, P. & Forrest, S. R. *Chem. Phys. Lett.* **398,** 27–31. doi:10.1016/j.cplett.2004.09.030 (2004) (p. 59).

152. Zaumseil, J. & Sirringhaus, H. *Chem. Rev.* **107,** 1296–1323. doi:10.1021/cr0501543 (2007) (pp. 60, 94).
153. Lamport, Z. A., Haneef, H. F., Anand, S., Waldrip, M. & Jurchescu, O. D. *J. Appl. Phys.* **124,** 071101. doi:10.1063/1.5042255 (2018) (pp. 61, 162).
154. Baer, E., Hiltner, A. & Keith, H. D. *Science* **235,** 1015–1022. doi:10.1126/science.3823866 (1987) (p. 61).
155. Lakes, R. *Nature* **361,** 511–515. doi:10.1038/361511a0 (1993) (p. 61).
156. Ma, R. *et al. Sci. China Chem.* **63,** 325–330. doi:10.1007/s11426-019-9669-3 (2020) (p. 62).
157. Mauer, R., Kastler, M. & Laquai, F. *Adv. Funct. Mater.* **20,** 2085–2092. doi:10.1002/adfm.201000320 (2010) (p. 62).
158. Bronstein, H., Nielsen, C. B., Schroeder, B. C. & McCulloch, I. *Nat. Rev. Chem.* **4,** 66–77. doi:10.1038/s41570-019-0152-9 (2020) (p. 62).
159. Bradley, D. D. C. *et al. Proc. SPIE* **3145,** 254–259. doi:10.1117/12.295530 (1997) (pp. 62, 95, 96, 99, 101).
160. Cadby, A. J. *et al. Phys. Rev. B* **62,** 15604–15609. doi:10.1103/physrevb.62.15604 (2000) (pp. 62, 96, 97, 114).
161. Perevedentsev, A., Chander, N., Kim, J.-S. & Bradley, D. D. C. *J. Polym. Sci. B Polym. Phys.* **54,** 1995–2006. doi:10.1002/polb.24106 (2016) (pp. 62, 96, 97, 99, 101, 102).
162. Lu, H.-H., Liu, C.-Y., Chang, C.-H. & Chen, S.-A. *Adv. Mater.* **19,** 2574–2579. doi:10.1002/adma.200602632 (2007) (pp. 62, 96, 97, 109).
163. Perevedentsev, A. *et al. Nat. Commun.* **6,** 5977. doi:10.1038/ncomms6977 (2015) (pp. 62, 96, 97).
164. Le Roux, F. & Bradley, D. D. C. *Phys. Rev. B* **98,** 195306. doi:10.1103/physrevb.98.195306 (2018) (pp. 62, 95, 97).
165. Rivnay, J. *et al. Adv. Mater.* **22,** 4359–4363. doi:10.1002/adma.201001202 (2010) (p. 63).
166. Yan, H. *et al. Nature* **457,** 679–686. doi:10.1038/nature07727 (2009) (p. 63).
167. Schuettfort, T., Thomsen, L. & McNeill, C. R. *J. Am. Chem. Soc.* **135,** 1092–1101. doi:10.1021/ja310240q (2013) (p. 63).
168. Yuan, Y. *et al. Nat. Commun.* **5,** 3005. doi:10.1038/ncomms4005 (2014) (p. 63).
169. Luo, C. *et al. Nano Lett.* **14,** 2764–2771. doi:10.1021/nl500758w (2014) (pp. 63, 185).
170. Grell, M., Bradley, D. D. C., Inbasekaran, M. & Woo, E. P. *Adv. Mater.* **9,** 798–802. doi:10.1002/adma.19970091006 (1997) (pp. 63, 95).

171. Sakamoto, K. *et al. J. Appl. Phys.* **107,** 113108. doi:10.1063/1.3445774 (2010) (p. 63).
172. Jiao, X., Ye, L. & Ade, H. *Adv. Energy Mater.* **7,** 1700084. doi:10.1002/aenm.201700084 (2017) (p. 63).
173. Ye, L. *et al. Nat. Mater.* **17,** 253–260. doi:10.1038/s41563-017-0005-1 (2018) (p. 63).
174. Kim, J.-S., Friend, R. H., Grizzi, I. & Burroughes, J. H. *Appl. Phys. Lett.* **87,** 023506. doi:10.1063/1.1992658 (2005) (pp. 64, 104).
175. Suh, M. *et al. ACS Appl. Mater. Interfaces* **7,** 26566–26571. doi:10.1021/acsami.5b07862 (2015) (p. 64).
176. Patil, B. R. *et al. Sci. Rep.* **8,** 12608. doi:10.1038/s41598-018-30826-7 (2018) (pp. 64, 182).
177. Perumal, A. *et al. Adv. Mater.* **27,** 93–100. doi:10.1002/adma.201403914 (2015) (pp. 64, 125, 129, 151).
178. Casalini, S., Bortolotti, C. A., Leonardi, F. & Biscarini, F. *Chem. Soc. Rev.* **46,** 40–71. doi:10.1039/c6cs00509h (2017) (p. 64).
179. Vericat, C. *et al. RSC Adv.* **4,** 27730–27754. doi:10.1039/c4ra04659e (2014) (pp. 64, 186).
180. Paniagua, S. A. *et al. Chem. Rev.* **116,** 7117–7158. doi:10.1021/acs.chemrev.6b00061 (2016) (p. 64).
181. Stoliar, P. *et al. J. Am. Chem. Soc* **129,** 6477–6484. doi:10.1021/ja069235m (2007) (p. 64).
182. Kang, C.-m. *et al. Adv. Electron. Mater.* **2,** 1500282. doi:10.1002/aelm.201500282 (2016) (pp. 64, 159, 164, 166, 168, 170, 173, 174, 176, 186).
183. Liu, G., Kerr, J. B. & Johnson, S. *Synth. Met.* **144,** 1–6. doi:10.1016/j.synthmet.2004.01.011 (2004) (p. 64).
184. Voigt, M. M. *et al. Sol. Energy Mater. Sol. Cells* **95,** 731–734. doi:10.1016/j.solmat.2010.10.013 (2011) (p. 64).
185. Umeda, T., Kumaki, D. & Tokito, S. *J. Appl. Phys.* **105,** 024516. doi:10.1063/1.3072669 (2009) (pp. 64, 140, 143).
186. Zhang, X. *et al. J. Am. Chem. Soc.* **133,** 15073–15084. doi:10.1021/ja204515s (2011) (pp. 64, 140, 143).
187. Wang, J. *et al. Adv. Mater.* **31,** 1806921. doi:10.1002/adma.201806921 (2019) (p. 64).
188. Fowler, R. H. *Phys. Rev.* **38,** 45–56. doi:10.1103/physrev.38.45 (1931) (p. 67).
189. Peng, Y. *et al. Appl. Phys. Lett.* **106,** 243302. doi:10.1063/1.4922758 (2015) (p. 67).

190. Liao, L. S. *et al. Appl. Phys. Lett.* **76,** 3582–3584. doi:10.1063/1.126713 (2000) (p. 67).
191. Deibel, C. *et al. Phys. Rev. B* **81,** 085202. doi:10.1103/physrevb.81.085202 (2010) (pp. 67, 68).
192. Tauc, J., Grigorovici, R. & Vancu, A. *Phys. Status Solidi B* **15,** 627–637. doi:10.1002/pssb.19660150224 (1966) (p. 67).
193. Wu, S., Cheng, L. & Wang, Q. *Mater. Res. Express* **4,** 085017. doi:10.1088/2053-1591/aa81da (2017) (p. 68).
194. Pattanasattayavong, P. *Solution-Processable Hole-Transporting Inorganic Semiconductors for Electronic Applications* PhD thesis (Imperial College London, London, UK, 2014) (pp. 68, 139).
195. Melitz, W., Shen, J., Kummel, A. C. & Lee, S. *Surf. Sci. Rep.* **66,** 1–27. doi:10.1016/j.surfrep.2010.10.001 (2011) (p. 68).
196. Bass, M. *Handbook of Optics: Vol. II. Design, Fabrication, and Testing; Sources and Detectors; Radiometry and Photometry* 3rd edn. (McGraw-Hill, NY, USA, 2010) (pp. 69, 70, 89, 90, 91).
197. Stenzel, O. *The Physics of Thin Film Optical Spectra: An Introduction* 2nd edn. (Springer, Cham, Switzerland, 2016) (p. 70).
198. Goebel, D. G. *Appl. Opt.* **6,** 125–128. doi:10.1364/ao.6.000125 (1967) (p. 71).
199. De Mello, J. C., Wittmann, H. F. & Friend, R. H. *Adv. Mater.* **9,** 230–232. doi:10.1002/adma.19970090308 (1997) (pp. 73, 74).
200. Hamilton, I. *et al. ACS Appl. Mater. Interfaces* **10,** 11070–11082. doi:10.1021/acsami.8b00243 (2018) (pp. 74, 97, 104, 106, 110, 114).
201. Kokil, A., Yang, K. & Kumar, J. *J. Polym. Sci. B Polym. Phys.* **50,** 1130–1144. doi:10.1002/polb.23103 (2012) (pp. 75, 77).
202. Röhr, J. A., Moia, D., Haque, S. A., Kirchartz, T. & Nelson, J. *J. Phys. Condens. Matter* **30,** 105901. doi:10.1088/1361-648x/aaabad (2018) (p. 76).
203. Kotadiya, N. B. *et al. Nat. Mater.* **17,** 329–334. doi:10.1038/s41563-018-0022-8 (2018) (pp. 76, 124).
204. Blakesley, J. C. *et al. Org. Electron.* **15,** 1263–1272. doi:10.1016/j.orgel.2014.02.008 (2014) (p. 76).
205. Weiß, O. J., Krause, R. K. & Hunze, A. *J. Appl. Phys.* **103,** 043709. doi:10.1063/1.2841362 (2008) (pp. 76, 112).
206. Cunningham, P. D. & Hayden, L. M. *J. Phys. Chem. C* **112,** 7928–7935. doi:10.1021/jp711827g (2008) (p. 76).
207. Juška, G., Arlauskas, K., Viliūnas, M. & Kočka, J. *Phys. Rev. Lett.* **84,** 4946–4949. doi:10.1103/physrevlett.84.4946 (2000) (p. 77).

208. Tiwari, S. & Greenham, N. C. *Opt. Quant. Electron.* **41,** 69–89. doi:10.1007/s11082-009-9323-0 (2009) (p. 77).
209. Juška, G., Nekrašas, N. & Genevičius, K. *J. Non-Cryst. Solids* **358,** 748–750. doi:10.1016/j.jnoncrysol.2011.12.016 (2012) (p. 77).
210. Armin, A. *et al. Adv. Energy Mater.* **4,** 1300954. doi:10.1002/aenm.201300954 (2014) (pp. 77, 161).
211. Martens, H. C. F., Brom, H. B. & Blom, P. W. M. *Phys. Rev. B* **60,** R8489–R8492. doi:10.1103/physrevb.60.r8489 (1999) (pp. 78, 111).
212. Okachi, T., Nagase, T., Kobayashi, T. & Naito, H. *Thin Solid Films* **517,** 1331–1334. doi:10.1016/j.tsf.2008.09.020 (2008) (p. 78).
213. Martens, H. C. F., Huiberts, J. N. & Blom, P. W. M. *Appl. Phys. Lett.* **77,** 1852–1854. doi:10.1063/1.1311599 (2000) (pp. 78, 111).
214. Budzisz, P., Signerski, R. & Jarosz, G. *Chem. Phys.* **456,** 61–64. doi:10.1016/j.chemphys.2015.02.014 (2015) (p. 79).
215. Reifenberger, R. *Fundamentals of Atomic Force Microscopy: Part I: Foundations* (World Scientific Publishing, MA, USA, 2016) (p. 80).
216. Nečas, D. & Klapetek, P. *Cent. Eur. J. Phys.* **10,** 181–188. doi:10.2478/s11534-011-0096-2 (2012) (p. 80).
217. Bragg, W. H. & Bragg, W. L. *Proc. Royal Soc. A* **88,** 428–438. doi:10.1098/rspa.1913.0040 (1913) (p. 82).
218. Kim, D. H. *et al. Adv. Mater.* **18,** 719–723. doi:10.1002/adma.200502442 (2006) (p. 83).
219. Widjonarko, N. *Coatings* **6,** 54. doi:10.3390/coatings6040054 (2016) (p. 83).
220. Hexemer, A. & Müller-Buschbaum, P. *IUCrJ* **2,** 106–125. doi:10.1107/s2052252514024178 (2015) (p. 84).
221. Wang, B. *MATLAB programs for GIWAXS data analysis and OSD-based rectifier performance simulation* https://github.com/bj-wang/DPhil-thesis/tree/main/Supplementary-files (2021-06-06) (pp. 85, 169).
222. Van der Heide, P. *X-ray Photoelectron Spectroscopy: An Introduction to Principles and Practices* (John Wiley & Sons, NJ, USA, 2012) (pp. 85, 86).
223. Shirley, D. A. *Phys. Rev. B* **5,** 4709–4714. doi:10.1103/physrevb.5.4709 (1972) (p. 87).
224. Shard, A. G. *J. Vac. Sci. Technol. A* **38,** 041201. doi:10.1116/1.5141395 (2020) (p. 87).
225. Van Oss, C. J. *Interfacial Forces in Aqueous Media* 2nd edn. (CRC Press, FL, USA, 2006) (pp. 87, 88).

226. Schrader, M. E. *Langmuir* **11,** 3585–3589. doi:10.1021/la00009a049 (1995) (p. 87).
227. Fowkes, F. M. *Ind. Eng. Chem.* **56,** 40–52. doi:10.1021/ie50660a008 (1964) (p. 87).
228. Kiessig, H. *Ann. Phys. (Leipzig)* **402,** 769–788. doi:10.1002/andp.19314020702 (1931) (p. 89).
229. Brower, D. T., Revay, R. E. & Huang, T. C. *Powder Diffr.* **11,** 114–116. doi:10.1017/s0885715600009076 (1996) (p. 89).
230. Tompkins, H. G. & Hilfiker, J. N. *Spectroscopic Ellipsometry: Practical Application to Thin Film Characterization* (Momentum Press, NY, USA, 2016) (p. 89).
231. Forrest, S. R., Bradley, D. D. C. & Thompson, M. E. *Adv. Mater.* **15,** 1043–1048. doi:10.1002/adma.200302151 (2003) (p. 91).
232. Zhang, Y., Ye, L. & Hou, J. *Small Methods* **1,** 1700159. doi:10.1002/smtd.201700159 (2017) (pp. 92, 93).
233. National Renewable Energy Laboratory (NREL). *Reference Air Mass 1.5 Spectra* https://www.nrel.gov/grid/solar-resource/spectra-am1.5.html (2021-08-24) (p. 92).
234. Snaith, H. J. *Energy Environ. Sci.* **5,** 6513–6520. doi:10.1039/c2ee03429h (2012) (p. 93).
235. Shrotriya, V. *et al. Adv. Funct. Mater.* **16,** 2016–2023. doi:10.1002/adfm.200600489 (2006) (p. 93).
236. Perevedentsev, A., Stavrinou, P. N., Smith, P. & Bradley, D. D. C. *J. Polym. Sci. B Polym. Phys.* **53,** 1492–1506. doi:10.1002/polb.23797 (2015) (p. 95).
237. Grell, M. *et al. Acta Polym.* **49,** 439–444. doi:10.1002/(sici)1521-4044(199808)49:8<439::aid-apol439>3.0.co;2-a (1998) (pp. 95, 96, 97).
238. Ariu, M. *et al. J. Phys. Condens. Matter* **14,** 9975–9986. doi:10.1088/0953-8984/14/42/310 (2002) (pp. 95, 97, 102, 114).
239. Redecker, M., Bradley, D. D. C., Inbasekaran, M. & Woo, E. P. *Appl. Phys. Lett.* **74,** 1400–1402. doi:10.1063/1.123563 (1999) (p. 95).
240. Whitehead, K. S., Grell, M., Bradley, D. D. C., Jandke, M. & Strohriegl, P. *Appl. Phys. Lett.* **76,** 2946–2948. doi:10.1063/1.126525 (2000) (p. 95).
241. Stavrinou, P. N., Ryu, G., Campoy-Quiles, M. & Bradley, D. D. C. *J. Phys. Condens. Matter* **19,** 466107. doi:10.1088/0953-8984/19/46/466107 (2007) (pp. 95, 97).
242. Le Roux, F., Taylor, R. A. & Bradley, D. D. C. *ACS Photonics* **7,** 746–758. doi:10.1021/acsphotonics.9b01596 (2020) (p. 95).

243. Grice, A. W. *et al. Appl. Phys. Lett.* **73,** 629–631. doi:10.1063/1.121878 (1998) (p. 95).
244. Neher, D. *Macromol. Rapid Commun.* **22,** 1365–1385. doi:10.1002/1521-3927(20011101)22:17<1365::aid-marc1365>3.0.co;2-b (2001) (p. 95).
245. Chunwaschirasiri, W., Tanto, B., Huber, D. L. & Winokur, M. J. *Phys. Rev. Lett.* **94,** 107402. doi:10.1103/physrevlett.94.107402 (2005) (p. 96).
246. Khan, A. L. T., Sreearunothai, P., Herz, L. M., Banach, M. J. & Köhler, A. *Phys. Rev. B* **69,** 085201. doi:10.1103/physrevb.69.085201 (2004) (pp. 96, 97, 99).
247. Peet, J., Brocker, E., Xu, Y. & Bazan, G. C. *Adv. Mater.* **20,** 1882–1885. doi:10.1002/adma.200702515 (2008) (p. 96).
248. Zhang, Q. *et al. Molecules* **22,** 315. doi:10.3390/molecules22020315 (2017) (p. 96).
249. Worsfold, O. *et al. Mater. Sci. Eng. C* **23,** 541–544. doi:10.1016/s0928-4931(03)00029-8 (2003) (p. 96).
250. Ryu, G., Stavrinou, P. N. & Bradley, D. D. C. *Adv. Funct. Mater.* **19,** 3237–3242. doi:10.1002/adfm.200900788 (2009) (pp. 96, 97).
251. Grell, M., Bradley, D. D. C., Ungar, G., Hill, J. & Whitehead, K. S. *Macromolecules* **32,** 5810–5817. doi:10.1021/ma990741o (1999) (pp. 97, 101).
252. Ariu, M. *et al. Phys. Rev. B* **67,** 195333. doi:10.1103/physrevb.67.195333 (2003) (pp. 97, 114).
253. Cheetham, N. J. *et al. Chem. Mater.* **31,** 6787–6797. doi:10.1021/acs.chemmater.9b01256 (2019) (p. 97).
254. Bright, D. W., Dias, F. B., Galbrecht, F., Scherf, U. & Monkman, A. P. *Adv. Funct. Mater.* **19,** 67–73. doi:10.1002/adfm.200800313 (2009) (p. 97).
255. Bright, D. W., Moss, K. C., Kamtekar, K. T., Bryce, M. R. & Monkman, A. P. *Macromol. Rapid Commun.* **32,** 983–987. doi:10.1002/marc.201100221 (2011) (p. 97).
256. Kuehne, A. J. C., Mackintosh, A. R. & Pethrick, R. A. *Polymer* **52,** 5538–5542. doi:10.1016/j.polymer.2011.09.044 (2011) (p. 97).
257. Wilkinson, C. I. *et al. Appl. Phys. Lett.* **79,** 171–173. doi:10.1063/1.1383799 (2001) (p. 98).
258. Belton, C. R. *et al. Adv. Funct. Mater.* **23,** 2792–2804. doi:10.1002/adfm.201202644 (2013) (pp. 98, 101).
259. Karl, M. *et al. Nat. Commun.* **9,** 1525. doi:10.1038/s41467-018-03874-w (2018) (p. 98).
260. Amarasinghe, D., Ruseckas, A., Vasdekis, A. E., Turnbull, G. A. & Samuel, I. D. W. *Adv. Mater.* **21,** 107–110. doi:10.1002/adma.200801930 (2009) (p. 98).

261. Demir, N., Oner, I., Varlikli, C., Ozsoy, C. & Zafer, C. *Thin Solid Films* **589,** 153–160. doi:10.1016/j.tsf.2015.05.006 (2015) (pp. 98, 104).
262. Wang, B., Ye, H., Riede, M. & Bradley, D. D. C. *ACS Appl. Mater. Interfaces* **13,** 2919–2931. doi:10.1021/acsami.0c18490 (2021) (p. 98).
263. Eggimann, H. J., Le Roux, F. & Herz, L. M. *J. Phys. Chem. Lett.* **10,** 1729–1736. doi:10.1021/acs.jpclett.9b00483 (2019) (p. 99).
264. Huang, L. *et al. J. Phys. Chem. C* **116,** 7993–7999. doi:10.1021/jp301102t (2012) (p. 99).
265. Chappell, J. *et al. Nat. Mater.* **2,** 616–621. doi:10.1038/nmat959 (2003) (p. 101).
266. Xia, R., Stavrinou, P. N., Bradley, D. D. C. & Kim, Y. *J. Appl. Phys.* **111,** 123107. doi:10.1063/1.4730041 (2012) (p. 101).
267. Winfield, J. M. *et al. J. Chem. Phys.* **131,** 035104. doi:10.1063/1.3177327 (2009) (pp. 101, 102, 112, 115).
268. Xia, R., Heliotis, G., Hou, Y. & Bradley, D. D. C. *Org. Electron.* **4,** 165–177. doi:10.1016/j.orgel.2003.08.009 (2003) (p. 102).
269. Sugiyama, K., Ishii, H., Ouchi, Y. & Seki, K. *J. Appl. Phys.* **87,** 295–298. doi:10.1063/1.371859 (2000) (pp. 104, 124, 176).
270. Koch, N., Vollmer, A. & Elschner, A. *Appl. Phys. Lett.* **90,** 043512. doi:10.1063/1.2435350 (2007) (pp. 104, 124, 176).
271. Shaheen, S. E. *et al. J. Appl. Phys.* **84,** 2324–2327. doi:10.1063/1.368299 (1998) (pp. 104, 114).
272. Yi, G. R., Kim, H. S., Jeong, K. W. & Kim, C. K. *Mol. Cryst. Liq. Cryst.* **651,** 99–107. doi:10.1080/09273948.2017.1338904 (2017) (pp. 104, 116).
273. Arredondo, B. *et al. Solid-State Electron.* **61,** 46–52. doi:10.1016/j.sse.2011.02.004 (2011) (p. 106).
274. Sun, Y., Seo, J. H., Takacs, C. J., Seifter, J. & Heeger, A. J. *Adv. Mater.* **23,** 1679–1683. doi:10.1002/adma.201004301 (2011) (p. 108).
275. Bai, Z. *et al. J. Phys. Chem. C* **120,** 27820–27828. doi:10.1021/acs.jpcc.6b08941 (2016) (p. 109).
276. Campbell, A. J., Bradley, D. D. C. & Antoniadis, H. *Appl. Phys. Lett.* **79,** 2133–2135. doi:10.1063/1.1406143 (2001) (p. 110).
277. Poplavskyy, D., Nelson, J. & Bradley, D. D. C. *Appl. Phys. Lett.* **83,** 707–709. doi:10.1063/1.1596722 (2003) (pp. 110, 124).
278. Sandberg, O. J. *et al. Appl. Phys. Lett.* **110,** 153504. doi:10.1063/1.4980101 (2017) (p. 111).
279. Tsang, S. W., So, S. K. & Xu, J. B. *J. Appl. Phys.* **99,** 013706. doi:10.1063/1.2158494 (2006) (p. 111).

280. Campbell, A. J., Bradley, D. D. C. & Lidzey, D. G. *J. Appl. Phys.* **82,** 6326–6342. doi:10.1063/1.366523 (1997) (pp. 113, 114).
281. Cornil, J. *et al. J. Chem. Phys.* **118,** 6615–6623. doi:10.1063/1.1561054 (2003) (pp. 114, 115).
282. Foster, S. *On the Influence of Physical and Chemical Structure on Charge Transport in Disordered Semiconducting Materials and Devices* PhD thesis (Imperial College London, London, UK, 2013) (p. 114).
283. O'Carroll, D. *et al. Adv. Mater.* **20,** 42–48. doi:10.1002/adma.200701539 (2008) (p. 114).
284. Van Mensfoort, S. L. M. & Coehoorn, R. *Phys. Rev. Lett.* **100,** 086802. doi:10.1103/physrevlett.100.086802 (2008) (p. 115).
285. C, A., Szymański, M. Z., Łuszczyńska, B. & Ulański, J. *Sci. Rep.* **9,** 8493. doi:10.1038/s41598-019-44824-w (2019) (p. 117).
286. Giebeler, C., Whitelegg, S. A., Lidzey, D. G., Lane, P. A. & Bradley, D. D. C. *Appl. Phys. Lett.* **75,** 2144–2146. doi:10.1063/1.124944 (1999) (p. 118).
287. Kawano, K. *et al. Sol. Energy Mater. Sol. Cells* **90,** 3520–3530. doi:10.1016/j.solmat.2006.06.041 (2006) (p. 118).
288. Donley, C. L. *et al. J. Am. Chem. Soc.* **127,** 12890–12899. doi:10.1021/ja051891j (2005) (p. 119).
289. Sims, M. *et al. Adv. Funct. Mater.* **14,** 765–781. doi:10.1002/adfm.200305149 (2004) (p. 120).
290. Ma, H., Yip, H.-L., Huang, F. & Jen, A. K.-Y. *Adv. Funct. Mater.* **20,** 1371–1388. doi:10.1002/adfm.200902236 (2010) (p. 123).
291. Chueh, C.-C., Li, C.-Z. & Jen, A. K.-Y. *Energy Environ. Sci.* **8,** 1160–1189. doi:10.1039/c4ee03824j (2015) (p. 123).
292. Jin, R. *et al. Phys. Chem. Chem. Phys.* **11,** 3455–3462. doi:10.1039/b819200f (2009) (p. 123).
293. Yang, H., Zhao, Y., Hou, J. & Liu, S. *Microelectron. J.* **37,** 1271–1275. doi:10.1016/j.mejo.2006.07.026 (2006) (p. 123).
294. Bao, Q., Braun, S., Wang, C., Liu, X. & Fahlman, M. *Adv. Mater. Interfaces* **6,** 1800897. doi:10.1002/admi.201800897 (2019) (p. 123).
295. Zhou, Y. *et al. Science* **336,** 327–332. doi:10.1126/science.1218829 (2012) (p. 124).
296. Duan, C., Zhang, K., Zhong, C., Huang, F. & Cao, Y. *Chem. Soc. Rev.* **42,** 9071–9104. doi:10.1039/c3cs60200a (2013) (p. 124).
297. Liang, Z., Zhang, Q., Jiang, L. & Cao, G. *Energy Environ. Sci.* **8,** 3442–3476. doi:10.1039/c5ee02510a (2015) (p. 124).

298. Nam, S. *et al. Nat. Commun.* **6,** 8929. doi:10.1038/ncomms9929 (2015) (p. 124).
299. Jiang, Y., Liu, T. & Zhou, Y. *Adv. Funct. Mater.* **30,** 2006213. doi:10.1002/adfm.202006213 (2020) (p. 124).
300. Meyer, J. *et al. Adv. Mater.* **24,** 5408–5427. doi:10.1002/adma.201201630 (2012) (pp. 124, 125).
301. Shi, H., Liu, C., Jiang, Q. & Xu, J. *Adv. Electron. Mater.* **1,** 1500017. doi:10.1002/aelm.201500017 (2015) (p. 124).
302. De Jong, M. P., van IJzendoorn, L. J. & de Voigt, M. J. A. *Appl. Phys. Lett.* **77,** 2255–2257. doi:10.1063/1.1315344 (2000) (p. 124).
303. Garcia, A. *et al. Adv. Mater.* **24,** 5368–5373. doi:10.1002/adma.201200963 (2012) (p. 124).
304. Alemu, D., Wei, H.-Y., Ho, K.-C. & Chu, C.-W. *Energy Environ. Sci.* **5,** 9662–9671. doi:10.1039/c2ee22595f (2012) (p. 124).
305. Ratcliff, E. L., Zacher, B. & Armstrong, N. R. *J. Phys. Chem. Lett.* **2,** 1337–1350. doi:10.1021/jz2002259 (2011) (p. 124).
306. Lane, P. A., Brewer, P. J., Huang, J., Bradley, D. D. C. & deMello, J. C. *Phys. Rev. B* **74,** 125320. doi:10.1103/physrevb.74.125320 (2006) (p. 124).
307. Huang, J. *et al. Adv. Funct. Mater.* **15,** 290–296. doi:10.1002/adfm.200400073 (2005) (p. 124).
308. Greiner, M. T., Chai, L., Helander, M. G., Tang, W.-M. & Lu, Z.-H. *Adv. Funct. Mater.* **22,** 4557–4568. doi:10.1002/adfm.201200615 (2012) (p. 124).
309. Wang, F., Tan, Z. & Li, Y. *Energy Environ. Sci.* **8,** 1059–1091. doi:10.1039/c4ee03802a (2015) (p. 125).
310. Pasquarelli, R. M., Ginley, D. S. & O'Hayre, R. *Chem. Soc. Rev.* **40,** 5406–5441. doi:10.1039/c1cs15065k (2011) (p. 125).
311. Ohisa, S., Kagami, S., Pu, Y.-J., Chiba, T. & Kido, J. *ACS Appl. Mater. Interfaces* **8,** 20946–20954. doi:10.1021/acsami.6b06723 (2016) (p. 125).
312. Ratcliff, E. L. *et al. Chem. Mater.* **23,** 4988–5000. doi:10.1021/cm202296p (2011) (p. 125).
313. Kumara, G. R. R. A. *et al. Sol. Energy Mater. Sol. Cells* **69,** 195–199. doi:10.1016/s0927-0248(01)00027-7 (2001) (pp. 125, 128).
314. Jaffe, J. E. *et al. J. Phys. Chem. C* **114,** 9111–9117. doi:10.1021/jp101586q (2010) (pp. 125, 131, 135, 137, 138, 146, 147, 148).
315. Pattanasattayavong, P., Promarak, V. & Anthopoulos, T. D. *Adv. Electron. Mater.* **3,** 1600378. doi:10.1002/aelm.201600378 (2017) (pp. 125, 146, 147, 148).
316. Wijeyasinghe, N. & Anthopoulos, T. D. *Semicond. Sci. Technol.* **30,** 104002. doi:10.1088/0268-1242/30/10/104002 (2015) (p. 125).

317. Yaacobi-Gross, N. *et al. Adv. Energy Mater.* **5,** 1401529. doi:10.1002/aenm.201401529 (2015) (pp. 125, 129, 130, 153).
318. Treat, N. D. *et al. Appl. Phys. Lett.* **107,** 013301. doi:10.1063/1.4926408 (2015) (pp. 125, 153).
319. Chaudhary, N., Chaudhary, R., Kesari, J. P., Patra, A. & Chand, S. *J. Mater. Chem. C* **3,** 11886–11892. doi:10.1039/c5tc03124a (2015) (p. 125).
320. Pattanasattayavong, P. *et al. Chem. Commun.* **49,** 4154–4156. doi:10.1039/c2cc37065d (2013) (pp. 125, 133, 136, 148).
321. Pattanasattayavong, P. *et al. Adv. Mater.* **25,** 1504–1509. doi:10.1002/adma.201202758 (2013) (p. 125).
322. Wijeyasinghe, N. *et al. Adv. Funct. Mater.* **27,** 1701818. doi:10.1002/adfm.201701818 (2017) (pp. 125, 128, 129, 130, 135, 136, 137, 153, 154).
323. Chaudhary, N., Chaudhary, R., Kesari, J. P. & Patra, A. *Opt. Mater.* **69,** 367–371. doi:10.1016/j.optmat.2017.04.063 (2017) (p. 125).
324. Pearson, R. G. *J. Am. Chem. Soc.* **85,** 3533–3539. doi:10.1021/ja00905a001 (1963) (p. 128).
325. Parr, R. G. & Pearson, R. G. *J. Am. Chem. Soc.* **105,** 7512–7516. doi:10.1021/ja00364a005 (1983) (p. 128).
326. Popova, T. V. & Aksenova, N. V. *Russ. J. Coord. Chem.* **29,** 743–765. doi:10.1023/b:ruco.0000003432.39025.cc (2003) (pp. 128, 129).
327. Kabešová, M., Dunaj-jurčo, M., Serator, M., Gažo, J. & Garaj, J. *Inorganica Chim. Acta* **17,** 161–165. doi:10.1016/s0020-1693(00)81976-3 (1976) (p. 131).
328. Smith, D. L. & Saunders, V. I. *Acta Cryst. B* **37,** 1807–1812. doi:10.1107/s0567740881007309 (1981) (pp. 131, 132).
329. Tsetseris, L. *J. Phys. Condens. Matter* **28,** 295801. doi:10.1088/0953-8984/28/29/295801 (2016) (pp. 131, 134, 148).
330. Sun, L. *et al. J. Electrochem. Soc.* **159,** D323–D327. doi:10.1149/2.028206jes (2012) (p. 131).
331. Ezealigo, B. N. *et al. Arab. J. Chem.* **13,** 346–356. doi:10.1016/j.arabjc.2017.04.013 (2020) (p. 131).
332. Tsuda, Y. *et al. Monatsh. Chem.* **148,** 845–854. doi:10.1007/s00706-017-1929-5 (2017) (p. 131).
333. Tsetseris, L. *Phys. Chem. Chem. Phys.* **18,** 7837–7840. doi:10.1039/c6cp00438e (2016) (p. 131).
334. Aldakov, D. *et al. J. Phys. Chem. C* **118,** 16095–16103. doi:10.1021/jp412499f (2014) (p. 131).

335. Bowmaker, G. A. & Hanna, J. V. *Z. Naturforsch. B* **64,** 1478–1486. doi:10.1515/znb-2009-11-1231 (2009) (pp. 131, 132).
336. Gates-Rector, S. & Blanton, T. *Powder Diffr.* **34,** 352–360. doi:10.1017/s0885715619000812 (2019) (pp. 133, 134).
337. Ayala, G. & Pike, R. D. *Polyhedron* **115,** 242–246. doi:10.1016/j.poly.2016.05.029 (2016) (p. 136).
338. Worakajit, P. *et al. Adv. Funct. Mater.* **30,** 2002355. doi:10.1002/adfm.202002355 (2020) (p. 136).
339. Schulz, K. H. & Cox, D. F. *J. Phys. Chem.* **97,** 3555–3564. doi:10.1021/j100116a020 (1993) (p. 136).
340. Thornburg, D. M. & Madix, R. J. *Surf. Sci.* **226,** 61–76. doi:10.1016/0039-6028(90)90154-z (1990) (p. 136).
341. Wijeyasinghe, N. *et al. Adv. Funct. Mater.* **28,** 1802055. doi:10.1002/adfm.201802055 (2018) (pp. 137, 146).
342. Wei, J. & Xue, Q. *Wear* **176,** 213–216. doi:10.1016/0043-1648(94)90149-x (1994) (p. 137).
343. Klein, J. C., Li, C. P., Hercules, D. M. & Black, J. F. *Appl. Spectrosc.* **38,** 729–734. doi:10.1366/0003702844555016 (1984) (p. 138).
344. Biesinger, M. C. *Surf. Interface Anal.* **49,** 1325–1334. doi:10.1002/sia.6239 (2017) (p. 138).
345. Dubé, C. E. *et al. J. Electrochem. Soc.* **142,** 3357–3365. doi:10.1149/1.2049987 (1995) (p. 139).
346. Zhang, D. K., Liu, Y. C., Liu, Y. L. & Yang, H. *Physica B Condens. Matter* **351,** 178–183. doi:10.1016/j.physb.2004.06.003 (2004) (p. 139).
347. Kim, J. *et al. ACS Appl. Energy Mater.* **3,** 7572–7579. doi:10.1021/acsaem.0c01001 (2020) (p. 139).
348. Chen, K. J., Laurent, A. D., Boucher, F., Odobel, F. & Jacquemin, D. *J. Mater. Chem. A* **4,** 2217–2227. doi:10.1039/c5ta10421a (2016) (p. 142).
349. Savikhin, V. *et al. iScience* **2,** 182–192. doi:10.1016/j.isci.2018.03.002 (2018) (p. 143).
350. Lombeck, F. *et al. Macromolecules* **49,** 9382–9387. doi:10.1021/acs.macromol.6b02216 (2016) (p. 149).
351. Walker, B. *et al. Appl. Phys. Lett.* **105,** 183302. doi:10.1063/1.4900933 (2014) (p. 150).
352. He, Z. *et al. Nat. Photon.* **6,** 591–595. doi:10.1038/nphoton.2012.190 (2012) (pp. 152, 176).

353. De Boer, B., Hadipour, A., Mandoc, M. M., van Woudenbergh, T. & Blom, P. W. M. *Adv. Mater.* **17,** 621–625. doi:10.1002/adma.200401216 (2005) (pp. 153, 180).
354. Nam, S. *et al. Adv. Electron. Mater.* **2,** 1600264. doi:10.1002/aelm.201600264 (2016) (pp. 153, 154).
355. Colella, R., Esposito, A., Catarinucci, L. & Tarricone, L. *IEEE Antennas Propag. Mag.* **58,** 109–119. doi:10.1109/map.2016.2520299 (2016) (p. 157).
356. Finkenzeller, K. *RFID Handbook: Fundamentals and Applications in Contactless Smart Cards, Radio Frequency Identification and Near-Field Communication* 3rd edn. (John Wiley & Sons, Chichester, UK, 2010) (pp. 157, 158, 173).
357. Tedjini, S. & Perret, E. *URSI Radio Sci. Bull.* **331,** 9–20. doi:10.23919/URSIRSB.2009.7909297 (2009) (pp. 157, 158).
358. Arias, A. C., MacKenzie, J. D., McCulloch, I., Rivnay, J. & Salleo, A. *Chem. Rev.* **110,** 3–24. doi:10.1021/cr900150b (2010) (p. 157).
359. Semple, J., Georgiadou, D. G., Wyatt-Moon, G., Gelinck, G. & Anthopoulos, T. D. *Semicond. Sci. Technol.* **32,** 123002. doi:10.1088/1361-6641/aa89ce (2017) (pp. 157, 158, 159, 162, 163).
360. Kraft, T. M., Berger, P. R. & Lupo, D. *Flex. Print. Electron.* **2,** 033001. doi:10.1088/2058-8585/aa8ac3 (2017) (p. 158).
361. Batarseh, I. & Harb, A. *Power Electronics: Circuit Analysis and Design* 2nd edn. (Springer, Cham, Switzerland, 2018) (p. 158).
362. Kang, C.-m., Shin, H. & Lee, C. *MRS Commun.* **7,** 755–769. doi:10.1557/mrc.2017.100 (2017) (pp. 159, 161, 175).
363. Krebs, F. C. *Sol. Energy Mater. Sol. Cells* **93,** 394–412. doi:10.1016/j.solmat.2008.10.004 (2009) (p. 159).
364. Kao, H. L. *et al. IEEE Electron Device Lett.* **26,** 489–491. doi:10.1109/led.2005.851238 (2005) (p. 159).
365. Steudel, S. *et al. Nat. Mater.* **4,** 597–600. doi:10.1038/nmat1434 (2005) (pp. 160, 164, 165, 166, 167, 173, 176).
366. *RFID Market with COVID-19 Impact Analysis by Product Type (Tags, Readers, and Software and Services), Wafer Size, Tag Type (Passive Tags and Active Tags), Frequency, Applications, Form Factor, Material, and Region—Global Forecast to 2026* https://www.researchandmarkets.com/reports/5292847/rfid-market-with-covid-19-impact-analysis-by (2021-04-15) (p. 160).
367. Sun, J., Pal, B. N., Jung, B. J. & Katz, H. E. *Org. Electron.* **10,** 1–7. doi:10.1016/j.orgel.2008.08.016 (2009) (p. 162).
368. Ali, S., Bae, J. & Lee, C. H. *Electron. Mater. Lett.* **12,** 270–275. doi:10.1007/s13391-015-5202-y (2016) (p. 162).

369. Kleemann, H. *et al. Org. Electron.* **13,** 1114–1120. doi:10.1016/j.orgel.2012.03.011 (2012) (p. 162).
370. Li, T. *et al. Nat. Commun.* **11,** 3592. doi:10.1038/s41467-020-17352-9 (2020) (p. 162).
371. Klauk, H. *Adv. Electron. Mater.* **4,** 1700474. doi:10.1002/aelm.201700474 (2018) (p. 162).
372. Waldrip, M., Jurchescu, O. D., Gundlach, D. J. & Bittle, E. G. *Adv. Funct. Mater.* **30,** 1904576. doi:10.1002/adfm.201904576 (2019) (p. 162).
373. Myny, K. *et al. Solid-State Electron.* **53,** 1220–1226. doi:10.1016/j.sse.2009.10.010 (2009) (p. 163).
374. Borchert, J. W. *et al. Sci. Adv.* **6,** eaaz5156. doi:10.1126/sciadv.aaz5156 (2020) (p. 163).
375. Perinot, A. & Caironi, M. *Adv. Sci.* **6,** 1801566. doi:10.1002/advs.201801566 (2019) (p. 163).
376. Perinot, A., Giorgio, M., Mattoli, V., Natali, D. & Caironi, M. *Adv. Sci.* **8,** 2001098. doi:10.1002/advs.202001098 (2021) (p. 163).
377. Im, D., Moon, H., Shin, M., Kim, J. & Yoo, S. *Adv. Mater.* **23,** 644–648. doi:10.1002/adma.201002246 (2011) (pp. 164, 179, 180, 184).
378. Sawatzki, M. F. *et al. Adv. Sci.* **8,** 2003519. doi:10.1002/advs.202003519 (2021) (pp. 164, 173).
379. Kim, S., Cho, H., Hong, Y. & Lee, C. *Mol. Cryst. Liq. Cryst.* **513,** 256–261. doi:10.1080/15421400903212034 (2009) (p. 164).
380. Heljo, P. S., Li, M., Lilja, K. E., Majumdar, H. S. & Lupo, D. *IEEE Trans. Electron Devices* **60,** 870–874. doi:10.1109/ted.2012.2233741 (2013) (p. 164).
381. Viola, F. A. *et al. Adv. Mater.* **32,** 2002329. doi:10.1002/adma.202002329 (2020) (pp. 164, 168, 173, 189).
382. Higgins, S. G., Agostinelli, T., Markham, S., Whiteman, R. & Sirringhaus, H. *Adv. Mater.* **29,** 1703782. doi:10.1002/adma.201703782 (2017) (pp. 164, 166, 173, 186, 189).
383. Semple, J. *et al. Small* **12,** 1993–2000. doi:10.1002/smll.201503110 (2016) (pp. 164, 189).
384. Altazin, S. *et al. J. Appl. Phys.* **115,** 064509. doi:10.1063/1.4865739 (2014) (p. 167).
385. Nicolai, H. T. *et al. Nat. Mater.* **11,** 882–887. doi:10.1038/nmat3384 (2012) (p. 170).
386. Arkhipov, V. I., Heremans, P., Emelianova, E. V. & Bässler, H. *Phys. Rev. B* **71,** 045214. doi:10.1103/physrevb.71.045214 (2005) (p. 170).

387. Bisoyi, H. K. & Li, Q. *Prog. Mater. Sci.* **104,** 1–52. doi:10.1016/j.pmatsci.2019.03.005 (2019) (p. 174).
388. Schott, S. *et al. Adv. Mater.* **27,** 7356–7364. doi:10.1002/adma.201502437 (2015) (p. 174).
389. Venkateshvaran, D. *et al. Nature* **515,** 384–388. doi:10.1038/nature13854 (2014) (p. 174).
390. Samuel, I. D. W. & Turnbull, G. A. *Chem. Rev.* **107,** 1272–1295. doi:10.1021/cr050152i (2007) (p. 175).
391. Abbaszadeh, D. *et al. Nat. Mater.* **15,** 628–633. doi:10.1038/nmat4626 (2016) (p. 175).
392. Nikolka, M. *et al. Nat. Mater.* **16,** 356–362. doi:10.1038/nmat4785 (2017) (p. 175).
393. Nikolka, M. *et al. Adv. Mater.* **30,** 1801874. doi:10.1002/adma.201801874 (2018) (p. 175).
394. Nikolka, M. *et al. Nat. Commun.* **10,** 2122. doi:10.1038/s41467-019-10188-y (2019) (p. 175).
395. Zuo, G., Linares, M., Upreti, T. & Kemerink, M. *Nat. Mater.* **18,** 588–593. doi:10.1038/s41563-019-0347-y (2019) (p. 175).
396. Michaelson, H. B. *J. Appl. Phys.* **48,** 4729–4733. doi:10.1063/1.323539 (1977) (p. 176).
397. Zhang, X.-H. & Kippelen, B. *J. Appl. Phys.* **104,** 104504. doi:10.1063/1.3020533 (2008) (p. 179).
398. Semenov, K. N. *et al. J. Chem. Eng. Data* **55,** 13–36. doi:10.1021/je900296s (2009) (p. 179).
399. Lin, H.-S. *et al. ACS Appl. Mater. Interfaces* **10,** 39590–39598. doi:10.1021/acsami.8b11049 (2018) (p. 179).
400. De Zerio Mendaza, A. D. *et al. Adv. Mater.* **27,** 7325–7331. doi:10.1002/adma.201503530 (2015) (p. 179).
401. Kröger, M. *et al. Appl. Phys. Lett.* **95,** 123301. doi:10.1063/1.3231928 (2009) (p. 180).
402. Kawata, S. *et al. J. Mater. Chem. C* **2,** 501–509. doi:10.1039/c3tc31719f (2014) (p. 182).
403. Lof, R. W., van Veenendaal, M. A., Koopmans, B., Jonkman, H. T. & Sawatzky, G. A. *Phys. Rev. Lett.* **68,** 3924–3927. doi:10.1103/physrevlett.68.3924 (1992) (p. 182).
404. Han, B.-y. *et al. J. Vac. Sci. Technol. A* **13,** 1606–1608. doi:10.1116/1.579736 (1995) (p. 182).

405. Li, W. *et al. J. Mater. Chem.* **22,** 11354–11363. doi:10.1039/c2jm30576c (2012) (pp. 182, 183).
406. Chen, H. *et al. Adv. Mater.* **29,** 1702523. doi:10.1002/adma.201702523 (2017) (pp. 184, 185, 186).
407. Boufflet, P. *et al. Adv. Funct. Mater.* **25,** 7038–7048. doi:10.1002/adfm.201502826 (2015) (p. 184).
408. Wadsworth, A. *et al. J. Am. Chem. Soc.* **142,** 652–664. doi:10.1021/jacs.9b09374 (2020) (pp. 185, 188).
409. Hurhangee, M. *Heteroatom and Bridged-Ring π-Conjugated Polymers and Their Use in Organic Electronics* PhD thesis (Imperial College London, London, UK, 2016) (p. 185).
410. Thomas, T. H. *et al. Nat. Commun.* **10,** 2614. doi:10.1038/s41467-019-10277-y (2019) (pp. 185, 188).
411. Yu, M.-N. *et al. J. Phys. Chem. Lett.* **9,** 364–372. doi:10.1021/acs.jpclett.7b03148 (2018) (p. 196).
412. Hamill, J. C. *et al. J. Phys. Chem. C* **124,** 14496–14502. doi:10.1021/acs.jpcc.0c03465 (2020) (p. 197).
413. *Mateial safety data sheet (MSDS) of N,N-dimethylthioformamide* https://www.sigmaaldrich.com/catalog/product/aldrich/163643 (2021-04-20) (p. 197).
414. Skrypnychuk, V. *et al. Adv. Mater.* **28,** 2359–2366. doi:10.1002/adma.201503422 (2016) (p. 198).
415. Yamada, K., Suwa, Y., Katagiri, C. & Nakayama, K.-i. *Org. Electron.* **53,** 320–324. doi:10.1016/j.orgel.2017.12.001 (2018) (p. 198).

Appendix

Publications and Presentations

Publications

1. **Bingjun Wang,** Hao Ye, Moritz Riede, and Donal D. C. Bradley. Chain conformation control of fluorene-benzothiadiazole copolymer light-emitting diode efficiency and lifetime. *ACS Appl. Mater. Interfaces* **13,** 2919–2931 (2021).

2. Yuping Shi, Paul N. Stavrinou, **Bingjun Wang,** Robert A. Taylor, Stephen M. Morris, and Donal D. C. Bradley. Fine-tuning the emission characteristics of conjugated polymers using photoalignment and liquid crystalline orientation. *Mater. Today (submitted).*

3. **Bingjun Wang,** Sungho Nam, Saurav Limbu, Ji-Seon Kim, Moritz Riede, and Donal D. C. Bradley. Properties and applications of copper(I) thiocyanate (CuSCN) hole-transport interlayers processed from different solvents. *(in preparation).*

4. **Bingjun Wang,** Moritz Riede, and Donal D. C. Bradley. Solution-processed organic Schottky diodes for high-frequency rectifiers operating at $> 200\,\mathrm{MHz}$. *(in preparation).*

Presentations

1. **Bingjun Wang,** Hao Ye, Moritz Riede, and Donal D. C. Bradley. Chain conformation control of a polyfluorene-based copolymer for improved OLED performance (poster presentation). *Materials Research Society (MRS) Spring Meeting.* online, November 2020.

2. **Bingjun Wang,** Hao Ye, Moritz Riede, and Donal D. C. Bradley. Chain conformation control of fluorene–benzothiadiazole copolymer light-emitting diode efficiency and lifetime (poster presentation). *International Workshop on Charge Transport and Excited State Processes in Organic Materials (IWOM).* online, June 2021.